Synthesis and characterization of dinuclear Fe(μ-CN)Co complexes exhibiting metal-to-metal electron transfer properties

Evangelia S. Koumousi

université de BORDEAUX

THÈSE

présentée pour obtenir le grade de

DOCTEUR DE

L'UNIVERSITÉ DE BORDEAUX

École doctorale des sciences chimiques

SPÉCIALITÉ : Physico-Chimie de la Matière Condensée

par Evangelia S. Koumousi

Synthesis and characterization of dinuclear {Fe(μ-CN)Co} complexes exhibiting metal-to-metal electron transfer properties

Sous la direction de : Corine Mathonière et Rodolphe Clérac

Soutenue le 4 Décembre 2015

Membres du jury :

Mme Anne Bleuzen	Professeur, Université Paris-Sud 11	Rapportrice
M. Jean-Pascal Sutter	Directeur de recherche, CNRS	Rapporteur
Mme Cécile Zakri	Professeur, Université de Bordeaux	Examinatrice
M. Spyridon P. Perlepes	Professeur, Université de Patras	Examinateur
Mlle Florence Volatron	Maître de Conférence, Université Paris 6	Membre invitée
M. Etienne Duguet	Professeur, Université de Bordeaux	Membre invité
Mme Corine Mathonière	Professeur, Université de Bordeaux	Directrice de thèse
M. Rodolphe Clérac	Directeur de recherche, CNRS	Directeur de thèse

- 2015 -

To the people who encourage us,

while we are trying to stand up after every fall…

Acknowledgements

Reaching the end of my PhD after three years, I am confident to say that I do understand now the meaning of the poem "Ithaka" (Konstantinos P. Kavafis, 1863-1933): "It's not only the destination that matters, but also the journey itself". Because during these three years, I was lucky to meet, collaborate and communicate with wonderful people on a scientific and personal level. Without their help, support and guidance, this thesis work wouldn't be completed, thus I would like to thank all of them for their valuable contribution.

First of all, I would like to thank ***Philippe Richetti*** *and* ***Mario Maglione*** *for welcoming me at the Centre de Recherche Paul Pascal (CRPP) and the Institut de Chimie de la Matière Condensée de Bordeaux (ICMCB), respectively. I thank* ***Prof. Anne Bleuzen*** *and* ***Dr. Jean-Pascal Sutter*** *for their time and consideration to review this thesis;* ***Prof. Cécile Zakri****,* ***Prof. Spyridon P. Perlepes*** *and* ***Dr. Florence Volatron*** *for their participation in the thesis defense jury. Thank you all for dedicating your precious time to evaluate my manuscript.*

I would like to express my heartfelt thanks to my supervisors, ***Corine Mathonière*** *and* ***Rodolphe Clérac*** *for their continuous support, guidance, encouragement and trust on me. Words are not enough in order to express my sincere gratitude for everything they have done during these three years of the thesis. I thank them for trusting me this project and offering me a tremendous amount of advices in every scientific aspect of this thesis work. Their dynamic and optimistic attitude, passion for research, research ethics, patience and motivation make them role models for every young scientist. They also allowed me a great freedom of research, but they were always there to answer all my questions, naive and not, in a pedagogic way and guide me at key moments. They always encouraged me to attend many conferences and communicate our work to the scientific community and they provided me access to several collaborations with "top-league" researchers in our field. For all these reasons,* ***Corine*** *and* ***Rodolphe****, thank you for offering me all the tools to become a complete and independent researcher. At last, I would like to thank you for your understanding and moral support during all the difficulties I faced these three years.*

I won't forget to thank my former supervisors in diploma and master thesis, ***Prof. Spyridon P. Perlepes*** *and* ***Dr. Theocharis C. Stamamatos****, who introduced me to the field of Molecular Magnetism, taught me synthetic coordination chemistry, encouraged me to study abroad and introduced me with warm words to my PhD thesis supervisors.*

Acknowledgements

I would like to express many thanks also to ***Prof. Claude Coulon*** *for his great contribution to this thesis work. Without him, we wouldn't be able to explain the results obtained by permittivity studies. His deep knowledge of physics and his great pedagogical skills were very precious for me during all my PhD. It is an honor to work and discuss with a scientist of this class. At last, without him during the team "wine-testing" sessions, I wouldn't be able to appreciate the good wine.*

At this point, I would like to thank many people who also participated on my thesis project. I would like to mention first and thank ***Florence Volatron*** *and then* ***Ie-Rang Jeon*** *and* ***Sergiu Calancea*** *who coordinated and initiated this project, respectively. Special thanks to the rest of the members of this project and my lab mates:* ***David Aguilà***, ***Yoann Prado*** *and* ***Abhishake Mondal***, *who were always there to help me and offered me their valuable scientific advices. I also thank: (a)* ***Pierre Dechambenoit*** *and* ***Daniel Woodruff*** *who helped me with the difficult organic synthesis and taught me crystallography the first year of my thesis.* ***Daniel Rosario-Amorin*** *for providing me also help with the organic synthesis of ligands during the second year of my thesis. For the single-crystal X-ray diffraction studies, I would like to thank also* ***Philippe Guionneau***, ***Olaf Stefanczyk*** *and* ***Ahmad Naim*** *from ICMCB; (b)* ***Elizabeth Hillard***, *who taught me how to use Schlenk line and glove box techniques during the first months of my thesis. Moreover, I would like to thank her for her invaluable contribution in the electrochemistry experiments of my thesis and all the pleasant, scientific and non- scientific discussions we had during these three years; (c)* ***Sadaf Fatima***, ***Marie-Anne Arrio***, ***Philippe Sainctavit***, ***Edwige Otero***, ***Christophe Cartier dit Moulin***, ***Andrei Rogalev***, ***Fabrice Wilhelm***, ***Philippe Ohresser*** *and* ***Loic Joly*** *for collaborating in three beam-times and introducing me to the synchrotron research; and (d)* ***Hitoshi Miyasaka*** *and* ***Wataru Kosaka*** *for collaborating on the permittivity experiments of my thesis work.*

I also thank the people from both laboratories who gave me scientific and technical support and especially ***Mathieu Rouzières*** *for the SQUID/PPMS,* ***Patrick Rosa*** *for the specrtoelectrochemisty studies,* ***Laeticia Etienne*** *for elemental analysis at ICMCB,* ***Stéphanie Exiga*** *for NMR and mass spectroscopies and elemental analysis,* ***Alan Dérre*** *and* ***Dominique Denux*** *for TGA analysis,* ***Xavier Brilland*** *for IR and UV-vis spectroscopies,* ***Eric Lebraud*** *for powder diffraction studies. Finally I would like to thank* ***Anne Facq***, ***Jean-Luc Laborde***,

Acknowledgements

***Natalie Touzé**, **Corine Amengual**, **Elisabeth Hortolland**, **Béatrice Dupin**, **Fréderic Louerat**, **Mbolotiana Rajaoarivelo**, **Stéphane Bechemin** and **Lionel Chevalier** for the administration, informatics, chemical and security support.*

*Many thanks to all my colleagues in both teams at CRPP and ICMCB, who contributed to the development of this warm and welcoming atmosphere at work. They were always available for fruitful, scientific and non-scientific discussions. They were always supporting and they inspired and motivated me until the end of this thesis. I used to liken our relationship to a family: Our postdocs **Daniel Woodruff**, **David Aguilà**, **Yoann Prado**, **Daniel Rosario-Amorin**, **Abhishake Mondal** and **Kasper Steen Pedersen** were like my older cousins and the PhD and master students by that time **Dmitri Mitcov**, **Mihail Secu**, **Vivien Pianet**, **Elena Darbinean**, **Vladimir Bulicanu**, **Dumitru Samohvalov**, **Petru Apostol**, **Anandi Srinivasan** and **Vianney Grau** as my older and younger brothers and sisters. Thank you all!*

*Now many thanks are oriented to my good friends inside and outside the laboratory, who shared with me all the good and bad moments during these three years: **Katerina**, **Elena**, **Angelo**, **Cintia**, **Paula**, **Miguel**, **Besira**, **Noelia**, **Dalice**, **Amalia**, **Petra**, **Sergio**, **Maria**, **Magdalena**, **Laura**, **Manu**, **Deniz**, **Liuba**, **Bierte** and **Alexandra**. I would like to thank a lot **Olivier** for his immense support, trust, patience and encouragement especially during the last year of my thesis.*

*Last but not least, I owe many thanks to my parents, **Mary** and **Sotiris**, and to my little sister, **Spyri**, for their encouragement, belief and eternal support throughout all my life.*

Merci à tous!

Evangelia S. Koumousi

Pessac, December 2015

TABLE OF CONTENTS

General Introduction

The relatively young and fast growing field of Material Science, which involves the study of the structure of materials and their properties, is driven by the demand of new technologies able to overcome the potential of the existing materials. Within this field, molecular-based materials have attracted great interest in the last two decades due to exciting and novel features originating at the molecular level. Moreover, these systems show synthetic advantages over traditional materials since they use well-designed precursors with known geometries, allowing an efficient control of the final structure and thus their related properties. In addition to the above mentioned features, their low energy-intensive production methods makes even more appealing the use of molecular-based systems for technological applications.

Systems built from molecular units containing spin centers (e.g. paramagnetic ions) allow interesting magnetic properties, which lead to the new and fascinating research area of Molecular Magnetism. Chemists and physicists rapidly realized the importance of this new research area, since it allows the study of basic concepts in magnetism at the molecular level. Moreover, the widespread use of magnetic materials in our ordinary life (e.g. **magnetic recording media**, credit cards, television, microphones, electric guitars, electric motors or medicine (Magnetic Resonance Imaging)) increases the need of an improvement of their properties regarding their size and efficiency. More specifically, in the context of growing demand of non volatile memories, more performing, robust and low cost, magnetic recording media are still very competitive.[1] This is explained by (i) the increase of the disks' capacity storage (from 2 kbits/in^2 in 1957 to a few Tbits/in^2 currently)[2,3] through the decreasing size of the information bit (100 nm^2 nowadays)[4] and by (ii) the improvement of addressing on one bit.[5]

Concerning the first point, considerable research efforts have been devoted to the synthesis of systems at the nanometer scale in order to reduce the size of the magnetic units for the storage information, and therefore the size of devices. In that sense, the discovery of Single-Molecule Magnets (SMMs)[6] in early 90s and the Single-Chain Magnets (SCMs)[7] a decade later, can be considered as the biggest contribution to the field of Molecular Magnetism. These paramagnetic coordination complexes and coordination polymers, respectively, have generated great expectations to encode information using single molecules and thus to reduce dramatically the size of magnetic storage units.

In respect to the improvement of the addressing on one bit, IBM in 1991 introduced the magneto-resistive read-head, exploiting the phenomenon of Anisotropic Magneto-Resistance (AMR), followed by the recently revealed Giant Magneto-Resistance (GMR) and Tunnel Magneto-Resistance (TMR) phenomena, which allowed a more precise reading of the bits and hence a considerable increase of the information storage density.[8] However, this approach will face fundamental limitations for the near future concerning the addressing of the bits. As the information bits are reducing and the bits density is increasing, the magnetic field employed for writing the information will have an influence on the neighboring bits, leading to systematic errors.[8] Hence, other ways of addressing bits are demanding, such as memories based on thermal assisted switching or spin transfer switching.[9,10] In conjunction with such development, industrial as well as basic research has focused on the control of magnetic

properties by an external stimulus different from the magnetic field such as temperature, light, pressure or electric field.[11,12]

In this respect, Fe/Co Prussian Blue Analogues (PBAs), with general formula $A_xCo_y[Fe(CN)_6]\bullet nH_2O$ (A: alkali ion),[13] have emerged as one of the most interesting systems, due to their outstanding photo-switchable physical properties. In such systems, a reversible transfer of one electron is occurring between two sites (metal ions) through temperature change and / or low temperature photo-excitation. The modification of the optical and magnetic states allows magneto-optical bistability. On the other hand, transferring this remarkable bistability into systems with lower dimensionality (2D, 1D or 0D) has emerged as an attractive research goal to develop new materials that can be easily manipulated and studied. Therefore, in the group of "Molecular Materials & Magnetism" (M_3) in Centre de Recherche Paul Pascal (CRPP) and group "Molécules et Matériaux Commutables" (group VI) in Institut de Chimie de la Matière Condensée de Bordeaux (ICMCB), it is becoming of great importance to dedicate part of our research to develop new magnetic molecular materials with the possibility to control their magnetization with temperature and light.[14-19] During her PhD thesis (2009-2012, CRPP/ICMCB), Ie-Rang Jeon designed through a rational building-block approach, a simple dinuclear cyanido-bridged Fe/Co complex that exhibits an unexpected temperature-dependent Spin CrossOver (SCO compounds: another important class of molecular switches which show modification of their spin state under external stimuli) in the solid state while an intramolecular electron transfer triggered by protonation is observed in solution.[15] Following the same aims, part of Sergiu Calancea's thesis work (2010-2013, ICMCB) was dedicated to the effect of functionalized organic ligands used in iron and cobalt molecular precursors on the redox properties of the building blocks, and subsequently of the new dinuclear Fe/Co complexes. This work afforded several new Fe/Co pairs, which unfortunately don't exhibit the expected bistable properties.[18]

Following the urgency of the field and guided by the valuable work of the two previous PhD students, we oriented to the synthesis of new dinuclear cyanido-bridged Fe/Co complexes, which will mimic on a single molecule the original properties of the coordination networks of PBAs,[13] i.e. intramolecular thermal and photo-induced electron transfer in solid state. We focus on the study of the physical properties of this simplest Fe/Co Prussian Blue analogue, with the hope to understand the fundamental concepts of this fascinating phenomenon. Chapter I contains the most representative examples of Fe/Co Prussian Blue analogues, focusing on the techniques used to understand their photomagnetic properties and the synthetic strategies employed in order to obtain Fe/Co Prussian Blue analogues of different dimensionalities. The theoretical background and characteristics of this important class of magnetic materials –the electron transfer systems– are described in the end. This chapter will help the readers from different fields to follow the subsequent chapters. Chapter II is devoted to the molecular building block approach we followed, in respect to the redox properties of the molecular precursors, in order to synthesize novel dinuclear cyanido-bridged Fe/Co complexes. These compounds aim to be the smallest {Fe(μ-CN)Co} moieties at the origin of the remarkable physical properties of the high dimensionality Fe/Co Prussian Blue. Combined structural, spectroscopic, magnetic and photomagnetic studies reveal that a metal-to-metal electron transfer that can be triggered in solid state by light and temperature, is

observed for the first time in a dinuclear complex.[19] Chapter III presents the influence of the environment content of the dinuclear Fe/Co complexes, such as the counter ions, on the occurrence of the thermally and/or photo-induced electron transfer in solid state, thus highlighting the versatility of these molecular materials. In the end of Chapter II and III advanced characterization techniques demonstrate our efforts to understand in depth the electron transfer phenomenon. Finally in Chapter IV, the possibility of transferring the electron transfer phenomenon of the studied Fe/Co pairs from solid state to solution was investigated. At the end, a conclusion to this work is provided, emphasizing the perspectives in order to complete it and further contribute to the field of molecular magnetism.

References

(1) Hilbert, M.; Lopez, P. *Science* **2011**, *332*, 60.
(2) "Sony develops magnetic tape technology with the world's highest[*1] areal recording density of 148 Gb/in^2" , *Sony*, Retrieved 5 May **2014**.
(3) http://storageservers.wordpress.com/2014/05/20/fujifilm-achieves-154tb-data-storage-record-on-tape/
(4) Moser, A.; Takano, K.; Marguiles, D.; Albrecht, M.; Sonobe, Y.; Ikeda, Y.; Sun, S.; Fullerton, E. *J. Phys. D: Appl. Phys.* **2002**, *35*, R157.
(5) Affronte, M. *J. Mater. Chem.* **2009**, **19**, 1731.
(6) (a) Boyd, P. D. W.; Li, Q.; Vincent, J. B.; Folting, K.; Chang, H. R.; Streib, W. E.; Huffman, J. C.; Christou, G.; Hendrickson, D. N. *J. Am. Chem. Soc.* **1988**, *110*, 8537; (b) Caneschi, A.; Gatteschi, D.; Sessoli, R.; Barra, A. L.; Brunel, L. C.; Guillot, M. *J. Am. Chem. Soc.* **1991**, *113*, 5873; (c) Sessoli, R.; Gatteschi, D.; Caneschi, A.; Novak, M. A. *Nature* **1993**, *365*, 141.
(7) (a) Caneschi, A.; Gatteschi, D.; Lalioti, N.; Sangregorio, C.; Sessoli, R.; Venturi. G.; Vindigni. A.; Rettori. A.; Pini, M. G.; Novak, M. A. *Angew. Chem. Int. Ed.* **2001,** *40*, 1760; (b) Clérac, R.; Miyasaka, H.; Yamashita, M.; Coulon, C. *J. Am. Chem. Soc.* **2002,** *124*, 12837.
(8) Chappert, C.; Fert, A.; Van Dau, F. N. *Nat. Mater.* **2007**, *6*, 813.
(9) Kahn, O.; Jay Martinez, C. *Science* **1998**, *279*, 44.
(10) Ralph, D. C.; Stiles, M. D. *Journal of Magnetism and Magnetic Materials* **2008**, *320*, 1190.
(11) Sato, O.; Tao, J.;. Zhang, Y.-Z *Angew. Chem., Int. Ed.* **2007**, *46*, 2152.
(12) Sato, O. *J. Photochem. Photobiol. C Photochem. Rev.* **2004**, *5*, 203.
(13) Sato, O.; Iyoda, T.; Fujishima, A.; Hashimoto, K. *Science* **1996**, *272*, 704.
(14) Codreanu-Siretanu, D. *PhD thesis, Bordeaux University* **2011**.
(15) Siretanu, D.; Li, D.; Buisson, L.; Bassani, D. M.; Holmes, S. M.; Mathonière, C.; Clérac, R. *Chem.-Eur. J.* **2011** *17*, 11704.
(16) Mitcov, D. *PhD thesis, Bordeaux University* **2014**.
(17) Jeon, I.-R.; Calancea, S.; Panja, A.; Piñero Cruz, D. M.; Koumousi, E. S.; Dechambenoit, P.; Coulon, C.; Wattiaux, A.; Rosa, P.; Mathonière, C.; Clérac, R. *Chem. Sci.* **2013**, *4*, 2463.
(18) Calancea, S. *PhD thesis, Bordeaux University* **2013**.
(19) Koumousi, E. S.; Jeon, I.-R.; Gao, Q.; Dechambenoit, P.; Merzeau, P.; Buisson, L.; Jia, B.; Li, D.; Woodruff, D. N.; Voltaron, F.; Mathonière, C.; Clérac, R. *J. Am. Chem. Soc*. **2014**, *136*, 15461.

Chapter I

Generalities and Context

Table of Contents for Chapter I:

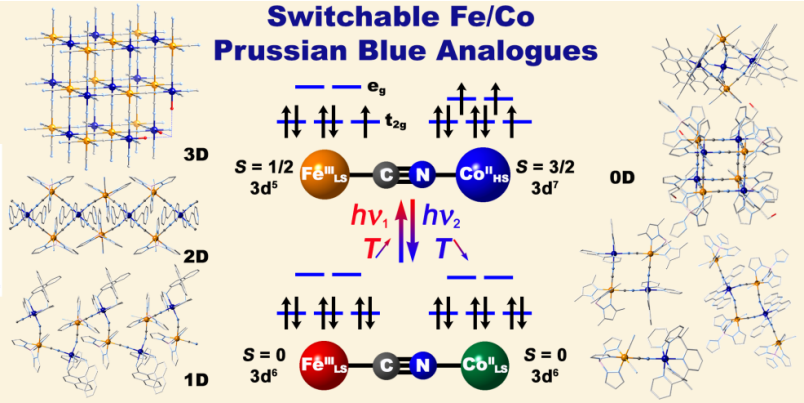

The field of molecular magnetism has rapidly developed with considerable steps, thanks to the possible interdisciplinary research between chemistry, physics and material science. Materials in this field are built through the bottom-up approach that allows a judicious choice of building blocks (metals and ligands, or the coordination complexes). In this way, we can predict and control not only the structural dimensionalities and geometries but also the related magnetic properties. Moreover, these materials are soluble in common solvents and their modular character opens ways to fine-tune their properties. One of the most important advantages of the molecular materials is that molecules are all identical to each other, therefore allowing relatively easy experiments on large assemblies of them, while still being able to probe, for example, quantum effects. This means that we can relate the macroscopic properties and the microscopic ones through studying the simple quantum mechanics and thermodynamics. These remarkable magnetic properties are often rare or unknown in traditional inorganic materials. For example, molecular systems with spin crossover phenomenon (SCO),[1] photomagnetism,[2] single-molecule magnet (SMM)[3] or single-chain magnet (SCM)[4] behaviors have been discovered. Furthermore, these molecule-based materials may exhibit additional features including transparency, thermo- or photochromism, solubility, conductivity/superconductivity, low density, biocompatibility and/or recyclability affording convenient solutions for new technological needs.[5] Therefore, an understanding of the underlying physics of the system is important for chemists in order to design magnetic materials with desired and enhanced properties. In this regard, we will discuss the theoretical tools in this chapter. Even though all details of physical concepts concerning molecular magnetic materials cannot be covered in this chapter, the basic and essential information that will be useful to help the readers in the following chapters are summarized here.

This thesis is focused on the synthesis and characterization of novel, molecular photoswitchable materials. Our objective is to develop photomagnetic materials based on their intramolecular metal-to-metal electron transfer properties. The literature review and the previously performed work in the "M_3" group from CRPP and "VI" group from ICMCB based on Fe/Co photoswitchable materials will be used for illustrating the motivation and the objectives of this thesis work in the end of the chapter.

I.1 Electron transfer (ET) systems

Molecule-based materials have attracted great interest in the last two decades due to exciting and novel features originating from the molecular level.[4c,6-8] In conjunction with such development, research has focused on the control of their optical and magnetic properties by an external stimulus different from the magnetic field such as temperature, light, pressure or electrical field.[9,10] The possibility to control magnetization with light is particularly appealing for potential applications in information storage, where magnetic molecules can be used as molecular bits and addressed by these stimuli. Amongst the molecules displaying such properties, Fe^{II} complexes exhibiting spin crossover phenomenon were the first to show a modification of their spin state through light irradiation at low temperature.[2a,8] Another important class of molecular switches allowing such control with light is based on

intramolecular electron transfer processes.[9] In such molecules, the presence of electronic donor and acceptor moieties promotes a reversible transfer of one electron between the two sites through temperature change and/or low temperature photo-excitation. As for spin crossover materials, the modification of the optical and magnetic states by light irradiation allows magneto-optical bistability. Different donor / acceptor couples have been considered in molecular compounds, such as radicals or complexes, implying an electron transfer (ET) between an organic moiety (radical/ligand) and a metal center[11] or between two metal ions.[12,13] In this later case, Fe/Co Prussian Blue Analogues (PBAs) have emerged as one of the most interesting systems, due to their outstanding photo-switchable physical properties. These cyanido-bridged bimetallic tridimensional coordination networks, with general formula $A_xCo_y[Fe(CN)_6]\bullet nH_2O$ (A: alkali ion), can display both optical and magnetic bistability due to a reversible metal-to-metal electron transfer process between the cobalt and iron centres, switching between paramagnetic (Fe^{III}_{LS}-CN-Co^{II}_{HS}) and diamagnetic (Fe^{II}_{LS}-CN-Co^{III}_{LS}) configurations (Scheme I-1; with LS: Low Spin and HS: High Spin). Due to the different electronic distribution within the cobalt center (HS or LS), this phenomenon has been named as charge-transfer-induced spin transition (CTIST), although the mechanism related to this electronic reorganization is under debate. This reversible process can be triggered by a change of the temperature (thermally induced electron transfer) as well as by irradiation at low temperatures (photo-induced electron transfer). On the other hand, transferring this remarkable magnetic and optical bistability into systems with lower dimensionality (2D, 1D or 0D) has emerged as an attractive research goal to develop new materials that can be easily manipulated and studied. The use of blocking ligands, which limit or impede the growth of the coordination network, allows a fine and controlled reduction of structural dimensionality resulting in discrete Fe/Co Prussian blue molecular analogues.[14-18] In most of the reported cases, these species are obtained from the reaction of cyanido/Fe^{III} and Co^{II} building blocks of general formula $[Fe^{III}L(CN)_p]^{n-}$ and $[Co^{II}L'(S)_q]^{m+}$ respectively (L, L': ligands and S: solvent molecules). The presence of the ligands affords also a good solubility of the final complexes in organic solvents, consequently allowing the study of electron transfer processes in solution. More importantly and in contrast to the 3D Prussian Blue materials, the design of discrete species guarantees a well-defined environment of the cobalt coordination sphere, which favours a full electron transfer in these molecular compounds. In addition, the versatility of coordination chemistry allows the fine-tuning of the building block redox potentials through ligand design and molecular engineering, and thus the control of the electron transfer properties. Hence, the reduction of the structural dimensionality in this family of Fe/Co Prussian Blue Analogues can obviously lead to interesting model systems essential to improve our comprehension of these metal-to-metal electron transfer processes.

In the following paragraphs, the most representative examples of tridimensional $A_xCo_y[Fe(CN)_6]\bullet nH_2O$ Prussian blue compounds are described, focusing on their photomagnetic switchable properties and how those are influenced by their chemical composition. Subsequently, the different strategies toward the design of new low dimensional Prussian blue systems based on a rational molecular building block approach are discussed emphasizing the advantages and potential applications of these functional molecular analogues.

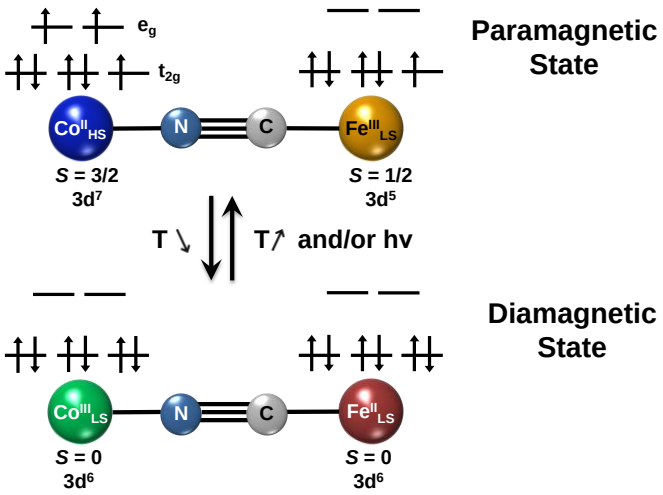

Scheme I-1. Interconversion between the paramagnetic (Fe^{III}_{LS}-CN-Co^{II}_{HS}) and diamagnetic (Fe^{II}_{LS}-CN-Co^{III}_{LS}) electronic configurations due to thermally and photo-induced metal-to-metal electron transfer processes.

I.1.1 Switchable Fe/Co Prussian Blue networks

The Prussian blue family of materials has been widely studied due to their appealing electronic and magnetic properties. The original Prussian Blue, $Fe^{III}_4[Fe^{II}(CN)_6]_3 \bullet 14H_2O$, is a Robin and Day's class II mixed-valence system.[19,20] The intense and characteristic blue colour of this pigment originates from a metal-to-metal charge transfer band around 700 nm due to the weak electron delocalization between the metallic centres through the cyanide bridge.[19] This electronic delocalization is also responsible for the superexchange interactions between high spin Fe^{III} ions, although separated by 10.166 Å through the diamagnetic $[Fe^{II}(CN)_6]^{4-}$ unit,[21,23] leading to a ferromagnetic order below 5.2 K. Intense research efforts in the 1990s have led to the rationalization of the magnetic properties of Prussian Blue Analogues (PBAs), allowing the synthesis of room temperature molecule-based magnets.[7]

The Fe/Co Prussian Blue materials have a general formula $A_xCo_y[Fe(CN)_6] \bullet nH_2O$ (A: Na^+, K^+, Cs^+, Rb^+) and form a neutral tridimensional network (Figure I-1) obtained from the reaction of hexacyanidoferrate(III) ($[Fe^{III}(CN)_6]^{3-}$) with cobalt(II) centres in water ($[Co^{II}(OH_2)_6]^{2+}$), in presence of alkali ions A^+. These coordination networks adopt a face-centred cubic (fcc) structure in the Fm3m space group, with a cell parameter close to 10 Å depending on the oxidation state of the metallic ions and the nature of alkali ions.[24-26] The vertices and the centres of the faces of the cubic unit cell are occupied by the Fe^{III} ions, while Co^{II} ions are located at the octahedral sites (Figure I-1). Both metal centres are linked by cyanide bridges with Fe^{III} and Co^{II} being coordinated by carbon and nitrogen, respectively. The corresponding ligand field of both donor atoms leads to low spin Fe^{III}_{LS} and high spin Co^{II}_{HS} configurations. Zeolitic water molecules form a hydrogen-bonded network in the interstitial sites, where alkali ions are also inserted. Depending on the amount of alkali ions introduced, the stoichiometry of the network can vary. The electro-neutrality of the network is ensured by adjusting the number of $[Fe^{III}(CN)_6]^{3-}$ vacancies (□), and the coordination sphere of the neighbouring Co^{II} sites is completed by water molecules (as shown on the right bottom

corner of structure in Figure I-1; note that each missing $[Fe^{III}(CN)_6]^{3-}$ unit is leading to the coordination of six additional water molecules). Hence, in the crystal, such vacancies (inhomogeneously distributed through the network) are responsible for a variety of coordination environments around the Co^{II} ions leading to an average $CoN_{6-x}O_x$ coordination sphere. These different environments around the Co^{II} site are of particular importance for the electron transfer properties, which are correlated to the redox potential of the two metal centres.[27] The replacement of a nitrogen atom from the cyanide ligand by a water molecule increases the redox potential of the cobalt centre. Therefore depending on the amount of water on the Co site, the Co redox potential can be significantly lower or higher than the Fe one, stabilizing Fe^{II}/Co^{III} or Fe^{III}/Co^{II} states respectively. This is only when the redox potential of the Co site is slightly lower than the Fe one that the Fe^{III}/Co^{II} paramagnetic excited state becomes thermally and optically accessible above the Fe^{II}/Co^{III} ground state.[27] Hence, the electron transfer phenomena in this Fe/Co Prussian blue analogue can be easily tuned through modification of the vacancies, directly in link with the quantity of alkali ions inserted in the network.

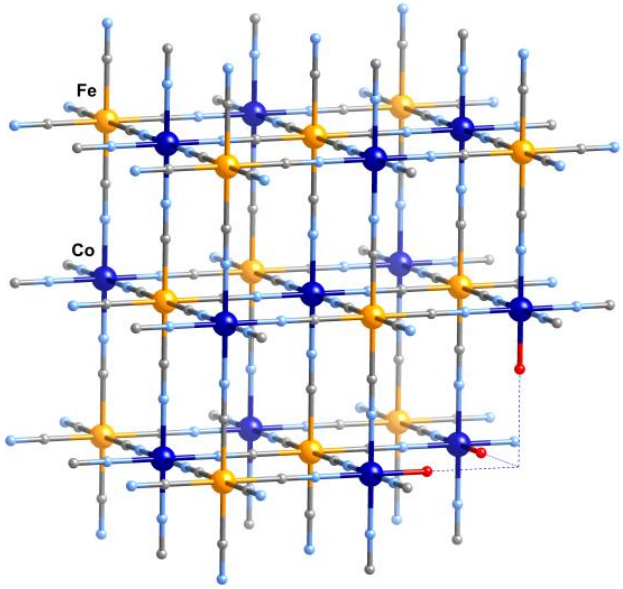

Figure I-1. Schematic representation of a Fe/Co Prussian blue network with formula $A_xCo_y[Fe(CN)_6]\bullet nH_2O$ (A: alkali ion; C: grey; N: light blue; Co: blue; Fe: yellow; O: red).

About twenty years ago, the control of the spontaneous magnetization of molecule-based materials by an optical stimulus was one of the main challenges within the molecular magnetism community. As previously discussed, the unique magnetic properties observed in some of the Prussian blue analogues make them potential candidates to develop such new systems with a light control of the magnetic properties. The breakthrough was achieved by Hashimoto, Fujishima and co-workers who synthesized a new Fe/Co Prussian Blue Analogue with the formula $K_{0.2}Co_{1.4}[Fe(CN)_6]\bullet 6.9H_2O$ (**1**).[24,28] As for other related PBAs,[21] a face-centred Fm3m cubic structure was observed by powder X-Ray diffraction, with a unit cell parameter a = 10.28 Å. The infrared spectrum carried out at 12 K showed two bands at 2162 and 2116 cm^{-1} that were ascribed to the cyanide stretching in Fe^{III}-CN-Co^{II} and Fe^{II}-CN-Co^{III} configurations, respectively. The higher intensity of the former band suggested the main

oxidation of both metal ions, while the presence of the diamagnetic Fe^{II}-CN-Co^{III} units was attributed to a spontaneous metal-to-metal electron transfer due to the introduction of K^+ ions in the structure. Magnetic susceptibility measurements revealed a tridimensional ferrimagnetic order in the compound with a Curie temperature of about 16 K. In order to investigate the photo-induced magnetic effect, the material was irradiated at 5 K with red light (660 nm), observing for the first time an enhancement of the magnetization, and an increase of the ordering temperature to 19 K. Interestingly, when the temperature was increased back to 150 K, the sample relaxed to its original state with a para/ferrimagnetic transition around 16 K. These unprecedented results demonstrated that the magnetization can be changed under light irradiation, and that the initial properties can be restored by thermal treatment. Accordingly, the infrared spectrum after irradiation at 12 K showed concomitantly a decrease of the peak at 2116 cm^{-1} and an increase of the peak at 2162 cm^{-1}. Taking into account the band ascription given before, these effects demonstrated that a photo-induced electron-transfer transformation from $Fe^{II}_{LS(S=0)}$-CN-$Co^{III}_{LS(S=0)}$ into $Fe^{III}_{LS(S=1/2)}$-CN-$Co^{II}_{HS(S=3/2)}$ was possible and induced an increase of the paramagnetic site number in the material, with a consequent enhancement of the magnetization value. Therefore, it was established that the presence of the diamagnetic Fe^{II}-CN-Co^{III} units were responsible of the photo-induced effect observed in **1**. Moreover, the authors also proved that the photo-enhancement of the magnetization was partially reversible irradiating the compound with a blue light (450 nm). Sequence of irradiation alternating red and blue lights was also reported to illustrate the remarkable bistability of this system at 5 K. The Science paper of Hashimoto, Fujishima and co-workers in 1996[24] that summarizes these outstanding results, is thus considered to be the first report of a tuneable magnetism based on a photo-induced metal-to-metal electron-transfer process.

After the discovery of the photo-induced magnetization in $K_{0.2}Co_{1.4}[Fe(CN)_6]\bullet 6.9H_2O$, several other Fe/Co Prussian Blue Analogues were synthesized and studied to further understand the phenomena.[29-34] Parallel to the developments carried out by Hashimoto and co-workers, an important work was done by other groups, especially by Bleuzen, Verdaguer and co-workers, in order to access the influence of different synthetic parameters in the photo-induced magnetization.[25,26,28,35-42] In the following section, some of the most representative results on this topic will be discussed.

One of the most relevant compounds studied by Hashimoto and co-workers was obtained by replacing potassium by rubidium: $Rb_{0.66}Co_{1.25}[Fe(CN)_6]\bullet 4.3H_2O$ (**2**).[34] To understand its photo-induced long-range magnetic order, the authors first characterized the compound by infrared and Mössbauer spectroscopy, and the results were compared with alkali free analogue, $Co_{1.5}[Fe(CN)_6]\bullet 6H_2O$ (**3**). Compound **2** was found to be composed mainly by Fe^{II}-CN-Co^{III} pairs, while clear evidence for a Fe^{III}-CN-Co^{II} configuration was found for **3**. Indeed, elemental analysis suggested the following stoichiometries, $Rb_{0.66}Co_{0.25}Co[Fe(CN)_6][\square]_{0.25}\bullet 4.3H_2O$ for **2** and $Co_{0.5}Co[Fe(CN)_6][\square]_{0.5}\bullet 6H_2O$ for **3**, which implies $CoN_{4.8}O_{1.2}$ and CoN_4O_2 average cobalt coordination spheres for **2** and **3**, respectively (note that the oxygen atoms originate from the six water molecules, which are present for each vacancy). Since the ligand field for the N atom from the cyanide ligand is higher than the O atom from the water molecule, the electronic structure of both compounds turns out to be

substantially different.[28] Thus, for a CoN_4O_2 environment (**3**), the ligand field of the cobalt is weak enough to stabilize the Fe^{III}_{LS}-CN-Co^{II}_{HS} configuration. In contrast, for **2**, where the average amount of nitrogen around the cobalt is higher ($CoN_{4.8}O_{1.2}$) due to fewer vacancies, the ligand field is stronger, thus stabilizing the diamagnetic Fe^{II}_{LS}-CN-Co^{III}_{LS} state. It is worth mentioning that these conclusions drawn from the ligand field theory are also perfectly in line with the discussion of the redox potentials reported by Bleuzen and co-worker in 2010 (*vide supra*).[27] The magnetic properties of both compounds further confirmed this scenario. For **3**, the ferrimagnetic order was observed below a Curie temperature of 16 K. In contrast, the χT values for **2** were much smaller, as the material is mostly composed by diamagnetic Fe^{II}_{LS}-CN-Co^{III}_{LS} pairs, and only a small amount of Co^{II} and Fe^{III} centers are responsible for the observed paramagnetism in the whole temperature range. Nevertheless when a sample of **2** was irradiated at 5 K, a remarkable increase of the magnetization was observed (Figure I-2).[34] This enhancement associated with a long-range magnetic order at 22 K confirmed the first studies on **1**[24] and the effect of the light illumination. When the sample was further heated to 150 K, the original value of the magnetization (before irradiation) was recovered. The same conclusions were obtained by infrared and Mössbauer spectroscopies after photo-excitation at 5 K and 25 K, respectively. Interestingly, no change in the infrared spectra after irradiation was observed in the thermal treatment until 70 K, demonstrating that the metastable photo-induced Fe^{III}_{LS}-CN-Co^{II}_{HS} configuration was kinetically trapped below this temperature. The recovery of the Fe^{II}_{LS}-CN-Co^{III}_{LS} configuration was observed only around 80 K, and the original spectrum was completely restored at *ca.* 120 K. Taking into account these results, the authors proposed a possible mechanism for the light induced electron-transfer based on the CTIST process, which can explain the long-life time of the metastable state.[34] Since the change from the Fe^{II}_{LS}-CN-Co^{III}_{LS} to Fe^{III}_{LS}-CN-Co^{II}_{HS} implies a spin-forbidden transition, a possible alternative pathway was contemplated considering an intermediate Fe^{III}_{LS}-CN-Co^{II}_{LS} state. The transition between Fe^{II}_{LS}-CN-Co^{III}_{LS} and Fe^{III}_{LS}-CN-Co^{II}_{LS} is spin-allowed and enables the following decay to Fe^{III}_{LS}-CN-Co^{II}_{HS} due to the large stability of Co^{II}_{HS}. Recovering the original Fe^{II}_{LS}-CN-Co^{III}_{LS} state turns out to be slow due to the large change in the bond distances and the spin-forbidden character of such transition. This mechanism suggests a high energy barrier, which would afford a long-lived metastable state.

From these results, Hashimoto and co-workers demonstrated the importance of the presence of diamagnetic Fe^{II}_{LS}-CN-Co^{III}_{LS} pairs in the compound to allow the photo-induced magnetization.[34] At the same time, they observed that this diamagnetic motif was favoured when the number of nitrogen atoms was sufficient to guarantee a sufficiently strong ligand field around the cobalt ion. Subsequently to Hashimoto's work, an extensive study was performed by Bleuzen, Verdaguer and co-workers through the study of three different compounds featuring different cobalt environment: $K_{0.04}Co_{1.48}[Fe(CN)_6]\bullet 6.8H_2O$ (**4**), $Rb_{0.55}Co_{1.2}[Fe(CN)_6]\bullet 13H_2O$ (**5**), and $CsCo_{1.03}[Fe(CN)_6]\bullet 3.3H_2O$ (**6**), displaying average coordination spheres close to CoN_4O_2, CoN_5O and CoN_6, respectively.[25] These environments correspond to different amount of vacancies in the material from 33 % for **4**, 17 % for **5**, to almost none for **6** (see Table I-1). Comparing the behaviour of these three compounds, the authors demonstrated that the enhancement of the ligand field produced by five nitrogen and one oxygen atom in **5** was enough to induce a spontaneous electron transfer during the

synthesis and thus to produce diamagnetic pairs in the material. Due to the existence of these diamagnetic pairs, a considerable increase of the magnetization was observed after irradiation due to the presence of a photo-induced ferrimagnetic phase. However, when compound **6** (with six nitrogen atoms around the cobalt and thus a maximum of diamagnetic pairs) was measured, the effect of the light was found to be very weak. Thus, the authors confirmed that the presence of diamagnetic pairs in the Prussian Blue Analogues was necessary to observe a photo-induced magnetization, but an excess of such diamagnetic pairs precludes the phenomena.[25] The hypothesis given by the authors to explain this result relies on the flexibility of the inorganic network that seems to be required to allow the necessary increase of the bond lengths during the photo-generation of the Fe^{III}_{LS}-CN-Co^{II}_{HS} pairs. When the number of diamagnetic units is too high (**6**), almost no $[Fe(CN)_6]^{3-}$ vacancies are present in the network, and thus the number of water molecules coordinated to the Co metal ions is very low. In these conditions, the network is probably relatively rigid and the photo-generation of the Fe^{III}_{LS}-CN-Co^{II}_{HS} phase is difficult to take place. This study was further complemented one year later by the same authors, who demonstrated that it was possible to induce and eventually tune the photo-induced magnetization of **6** by carefully controlling the amount of Cs^+ inserted in the structure.[26] Compounds with general formula $Cs_xCo_y[Fe(CN)_6][\square]_z.nH_2O$ were synthesized with different x values from 0.1 to 0.68 (see Table I-1). Elemental analysis showed an increase of the nitrogen amount, corresponding to mean environment of the cobalt center from $CoN_{4.2}O_{1.8}$ to $CoN_{5.1}O_{0.9}$ for x = 0.1, y = 1.43 and z = 0.43 to x = 0.68, y = 1.18 and z ≈ 0.18, respectively, due to the decrease of z (the number of vacancies [□]). Infrared spectroscopy, powder X-ray diffraction and X-ray absorption spectroscopy (see below) demonstrated the enhancement of the amount of diamagnetic Fe^{II}_{LS}-CN-Co^{III}_{LS} units with the increase of Cs^+ amount. This evidence was corroborated by measuring the magnetic susceptibility of the samples at room temperature, which was progressively reduced by the increase of Cs^+ quantity. When the Cs^+ content ranged in between x = 0.24 and 0.38, the required ligand field at the cobalt ion was empirically achieved resulting in the presence of a thermally induced electron transfer when decreasing the temperature. In contrast, when the samples were irradiated with light, the highest efficiency for the photo-induced process was observed for x between 0.38 and 0.68. Thus, this range turned out to be the best compromise between the amount of Fe^{II}_{LS}-CN-Co^{III}_{LS} diamagnetic pairs and the number of vacancies [□], providing the adequate network flexibility to allow the trapping of the photo-induced metastable state. Similar conclusions were obtained by Hashimoto and co-workers by studying the effect of the Na^+ content in the $Na_xCo_y[Fe(CN)_6][\square]_z.nH_2O$ Prussian blue analogues from x = 0.07 to 0.94.[30] The infrared and UV-Vis spectra of the different compounds within this series showed that lower contents of sodium imposed a main Fe^{III}_{LS}-CN-Co^{II}_{HS} phase, while an increase of the Na^+ content rather stabilized the Fe^{II}_{LS}-CN-Co^{III}_{LS} configuration. For intermediate doping of Na^+, the average ligand field around the cobalt ion allows the occurrence of a thermal electron transfer, as well as a photo-induced ferrimagnetic state at low temperature. It should be noticed that these compounds were the first Prussian Blue Analogues exhibiting a thermal hysteresis associated with the thermally induced electron-transfer phenomenon (i.e. a first order phase transition). This phase transition was shifted towards high temperatures increasing the amount of alkali metal ion. Additionally, it is

worth mentioning that the relaxation of the thermally quenched state was studied in details for one related compound of this series, $Na_{0.4}Co_{1.4}[Fe(CN)_6]\bullet 3.4H_2O$ (**7**).[43,44] This system was found to show a quasi-complete trapping of the high-temperature phase (when the sample was cooled down extremely fast), with a thermal decay of the quenched phase around 160 K. The mean-field analysis of the relaxation curves led to a relaxation time following a thermally activated behaviour (Arrhenius) with an energy barrier to electron transfer (E/k_B) of 3110(60) K and $\tau_0 = 6.7 \times 10^{-7}$ s. This work represents the first evaluation of the relaxation time (τ) in a Fe/Co PBA, with a τ value of ca. 33 hours at 120 K.[43,44] Similarly, the relaxation properties of the photo-induced state from other systems of this family have also been explored. As an example, the lifetime of the photo-induced state in $Na_{0.6}Co_{1.21}[Fe(CN)_6]\bullet 4.2H_2O$ was found to be about 3 hours at 120 K.[45]

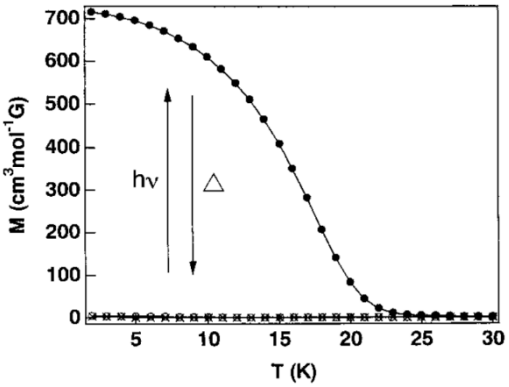

Figure I-2. Dependence of field-cooled magnetization of compound **2** with temperature under an applied field H = 0.5 mT before (empty dots) and after (black dots) light irradiation, and after the thermal treatment at 150 K (crosses). Reprinted with permission from ref. 34. Copyright 1999 American Chemical Society.

One of the main issues faced during the study of Prussian Blue Analogues was the difficulty of establishing the local structure of the materials. Since PBAs are obtained as amorphous or weakly crystalline powders, information from X-ray diffraction is not very instructive. On the other hand, the combination of infrared and UV-Vis spectroscopies, together with powder X-ray diffraction, has been very useful for determining the main oxidation state of the metal ions in the PBAs, as well as the unit cell parameter. However as discussed before, the coordination sphere of each metal ion is the key to understanding the electron-transfer properties of these systems. Thus, fundamental information on their geometry and the nature of coordinated atoms is required and therefore further analyses needs to be carried out. With these objectives, scientists have used X-ray absorption spectroscopy that offers the possibility to investigate the local structure/environment of a selected atom or metal ion. This technique is highly sensitive and provides information about the probed element's symmetry, nature of the coordinating atoms, metal-ligand distances but also its oxidation and spin states. In particular, Extended X-ray-Absorption Fine-Structure (EXAFS) and X-ray Absorption Near-Edge Structure (XANES) spectroscopies appeared to be the most efficient techniques for such characterizations. From EXAFS, the local geometries around the metal ions can be determined, while XANES is used to study their electronic structures. In

that sense, Hashimoto and co-workers, as well as Cartier dit Moulin, Bleuzen, Verdaguer and co-workers, demonstrated the efficiency of both techniques to characterize the PBAs.[23,46,48-51] Several compounds have been studied by EXAFS and XANES (see Table I-1), confirming and completing the information already obtained by the standard techniques mentioned above. As an example, a detailed comparison of six different compounds known to show different magnetic properties was carried out by Hashimoto and coworkers:[46] $Rb_{0.66}Co_{1.25}[Fe(CN)_6]\bullet 4.3H_2O$ (**2**) and $K_{0.4}Co_{1.3}[Fe(CN)_6]\bullet 5H_2O$ (**8**), which do not show any thermally-induced electron transfer but a ferrimagnetic ordered state upon irradiation; $Na_{0.4}Co_{1.3}[Fe(CN)_6]\bullet 5H_2O$ (**9**) and $K_{0.4}Co_{1.3}[Fe(CN)_6]\bullet 4.2H_2O$ (**10**), which display a thermally induced electron transfer transition; and $Na_{1.4}Co_{1.3}[Fe(CN)_6]\bullet 5H_2O$ (**11**) and $Co_{1.5}[Fe(CN)_6]\bullet 6H_2O$ (**3**), for which the cobalt ion was assumed to be Co^{II}_{HS} at all temperatures. XANES spectra obtained at the iron *K* edge (electronic transition from 1s to 4p orbitals; pre-edge from 1s to 3d orbitals) for all compounds and for the references $K_3[Fe(CN)_6]$ and $K_4[Fe(CN)_6]$ confirmed the octahedral environment $Fe(CN)_6$ around the iron ion (Figure I-3, left). Nevertheless, a small edge energy shift to higher energy from Fe^{II}_{LS} to Fe^{III}_{LS} can be observed. Under this consideration, the spectra observed in compounds **2**, **8** and **11** suggested an oxidation state of Fe^{II}_{LS}, while in sample **3**, the iron site was closer to Fe^{III}_{LS}. Accordingly, the spectra for samples **9** and **10** showed a thermal dependence, since slight differences were observed between the spectra at 296 and 30 K (Figure I-3, left, dashed and solid lines, respectively). Since the XANES signatures at the Fe *K*-edge of both Fe^{II}_{LS} and Fe^{III}_{LS} states are very similar, no quantitative analysis could be carried out. In contrast, marked differences can be observed in the Co *K*-edge XANES spectra as the results of the Co oxidation state change imposes a different spin state (Figure I-3, right). Similarly to the Fe *K*-edge spectra, temperature dependence of the Co XANES was observed for **9** and **10** due to the conversion between Co^{III}_{LS} and Co^{II}_{HS}. In this case, clear differences can be observed in the spectra at high and low temperatures (Figure I-3, right, dashed and solid lines, respectively), with resemblances to those related to $Co^{II}(NO_3)_2$ and $K_3Co^{III}(CN)_6$, respectively. As expected, much smaller differences were found for the other compounds.

Similar conclusions were obtained by analysing the results from the EXAFS measurements, proving the dominant oxidation states of each metal ion in the different compounds. Further analyses of the EXAFS data were also used to obtain specific structural information, such as the coordination number or interatomic distances around the metal ions. Interestingly, it was observed that Fe^{II}-C bond length distances are slightly shorter than in systems with Fe^{III}_{LS}-C bonds. This effect was attributed to the presence of an additional electron in the t_{2g} bonding orbital for Fe^{II}_{LS} site, that induces a slight shortening of the Fe-C bond compared to those involving Fe^{III}_{LS}. On the other hand, the EXAFS analysis for the Co^{II}_{HS}-N,O and Co^{III}_{LS}-N,O systems showed that the differences in the bond lengths were more similar to the ones found in Co/radical complexes showing valence tautomerism than in Co^{II} spin-crossover compounds. This study proved the change of Co valence within the studied materials and thus the electron transfer phenomena. In 1999, Hashimoto and co-workers went one step further and used EXAFS and XANES spectroscopies to study the local Fe and Co environments in the photo-excited state of $Na_{0.4}Co_{1.3}Fe(CN)_6\bullet 5H_2O$ (**9**).[50] This system was found to exhibit photo-induced electron transfer at low temperatures,[32] with a

metastable state possessing lifetimes large enough around 40 K to be studied by these spectroscopic techniques. The features observed in the Co *K*-edge and Fe *K*-edge XANES spectra after irradiating the sample with visible light at 36 K were similar to those at 300 K, showing that the dominant Co and Fe species were in the oxidation state +2 and +3, respectively. After heating the sample to 150 K, the Co *K*-edge spectra turned back to the low temperature one (for Co^{III}_{LS}), implying that the trapped excited state was thermally relaxed to the ground state at this temperature. A further increase of the temperature until 300 K confirmed the presence of the Fe^{III}_{LS}-Co^{II}_{HS} phase and thus that the thermally induced electron-transfer was still present as for the non irradiated sample. By comparing the estimated Co^{III}/Co^{II} composition ratio, it was shown that the amount of Co^{II} site was larger in the irradiated sample at 36 K than in the sample at 300 K, which evidenced the larger number of paramagnetic Fe^{III}_{LS}-Co^{II}_{HS} units in the photo-induced phase. Nevertheless, EXAFS spectroscopy proved that the local structure of the photo-induced state was very close to that of the high-temperature phase.

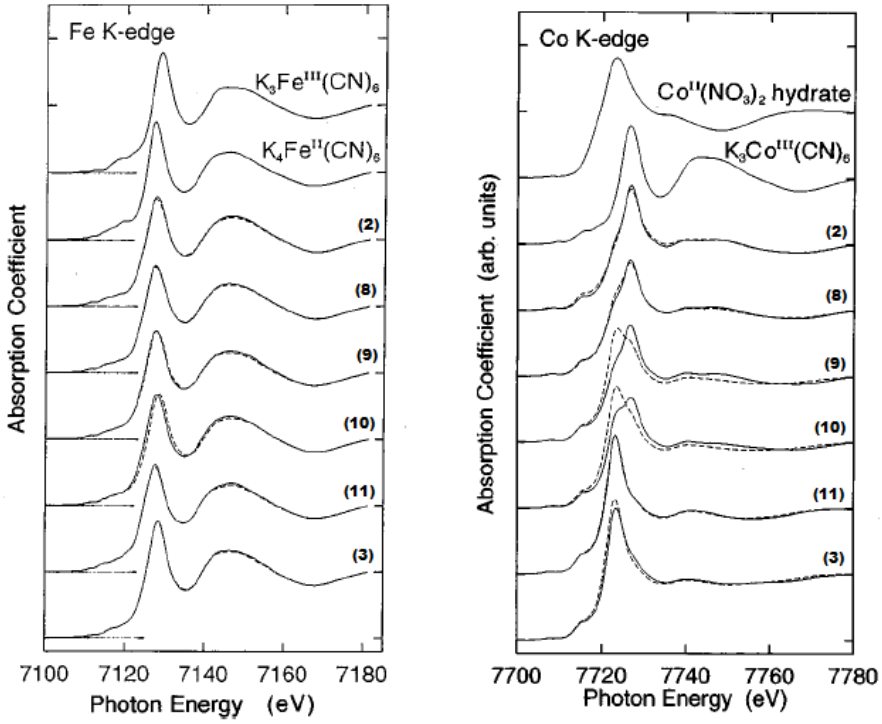

Figure I-3. Fe *K*-edge (left) and Co *K*-edge (right) XANES spectra for compounds **2**, **8**, **9**, **10**, **11** and **3** at 30 K (solid lines) and 296 K (dashed lines). Spectra for $K_3Fe^{III}(CN)_6$ and $K_4Fe^{II}(CN)_6$ (Fe *K*-edge) and for $K_3Co^{III}(CN)_6$ and $Co(NO_3)_2$ hydrate (Co *K*-edge) were added for comparison. Adapted with permission from Ref. 46. Copyrighted by the American Physical Society.

The influence of the alkali-metal ion in the thermally induced electron transfer phenomenon was also assessed by EXAFS spectroscopy. As an example, Bleuzen and co-workers studied $Cs_{0.24}Co_{1.38}[Fe(CN)_6]\bullet 5.5H_2O$ not only at the Fe and Co *K*-edges but also at the Cs L_3-edge.[47] The different EXAFS signals obtained at 300 and 20 K at Fe and Co *K*-edges were used to evidence the thermally induced electron transfer in this compound (see Table I-1). On the other hand, the analysis of EXAFS data at the Cs L_3-edge demonstrated

that at 300 K, the Cs ion is not centered on the Td site of the Prussian Blue network inducing a bend of the Co-CN-Fe motifs. This structural feature, that implies a less efficient orbital overlap than in the linear conformation, imposes a weaker ligand field around the cobalt centre and thus stabilizes the Co^{II}_{HS} state. In contrast, the EXAFS experiments carried out at 20 K showed that the Cs ion is localized on the Td site, inducing a linear Co-CN-Fe conformation in its neighbourhood. The stronger orbital interaction promoted by such linearity produces a stronger ligand field around the cobalt ion, and thus stabilizes its Co^{III}_{LS} configuration. With these instructive results, the authors showed that the cobalt ions surrounding the Cs ions are the ones involved in the thermal electron transfer phenomenon, thus proving the crucial role of the alkali metal ions in this process.

In order to study further the light-induced electron transfer process, Cartier dit Moulin, Bleuzen, Verdaguer and co-workers investigated the electronic and local structures of the ground and excited states of $Rb_{0.55}Co_{1.2}[Fe(CN)_6]\bullet 3.9H_2O$ (**5**) by EXAFS and XANES.[48] The comparison between the XANES spectra before and after irradiation below 30 K confirmed a decrease of the Co^{III}_{LS} and Fe^{II}_{LS} signals subsequent to the photo-induced conversion of some Co^{III}_{LS}-Fe^{II}_{LS} units into Co^{II}_{HS}-Fe^{III}_{LS} ones. However, it was estimated that about 46 % of diamagnetic pairs remained unaffected by the irradiation. Therefore, two types of diamagnetic Co^{III}_{LS}-Fe^{II}_{LS} pairs were described: (i) active ones, which are located in a more flexible network (close to iron vacancies [□]) and can be easily converted into the paramagnetic Co^{II}_{HS}-Fe^{III}_{LS} configuration through light irradiation; and (ii) inactive ones, which are thought to have less or a lack of vacancies [□] in their neighbourhood, being trapped in a more rigid network that precludes the light-induced electron transfer. These two kinds of Fe^{II}_{LS}-CN-Co^{III}_{LS} moiety are naturally induced by the inhomogeneous repartition of the vacancies in the material, which implies a variety of environments around the cobalt centres (*vide supra*). Interestingly, the authors tried to de-excite the photo-induced state with a blue light as seen before by Hashimoto and co-workers for **1**.[24] Against expectations, the effect was found to be inversed, resulting in a further increase of the paramagnetic Co^{II}_{HS}-Fe^{III}_{LS} pair population. This observation illustrates the complexity of the materials with the presence of a distribution of geometries for the Fe^{II}_{LS}-CN-Co^{III}_{LS} moiety that display different photo-activities.[48] These EXAFS experiments also evidenced that the photo-induced electron-transfer was associated to a local structure rearrangement of the coordination sphere of the cobalt ions with a bond increase of about 0.17 Å. This large modification needs to be absorbed by the tridimensional network, and thus the efficiency of the photo-conversion of the Fe^{II}_{LS}-CN-Co^{III}_{LS} pairs depends on a subtle compromise between the number of diamagnetic pairs and vacancies [□] in the material.

One of the remaining questions concerning the photo-induced phase of Fe/Co PBAs was the nature of the exchange interaction between the magnetic Co^{II}_{HS} and Fe^{III}_{LS} sites. Even if it was assumed that antiferromagnetic interactions between the centres led to ferrimagnetic ground state,[24-26,34] no macroscopic characterization of this photo-induced metastable state could be carried out. The main difficulties were (i) to know the amount of the photo-transformed phase[48] (as the photo-conversion of the sample is never complete; *vide supra*), (ii) the possible partial relaxation to the diamagnetic state at low temperatures, and (iii) the fact that two configurations (antiferromagnetic $Co^{II}_{(HS,3/2)}$/$Fe^{III}_{(LS,1/2)}$ or ferromagnetic

$Co^{II}_{(LS,1/2)}/Fe^{III}_{(LS,1/2)}$) cannot be easily discriminated as they generate a very similar resulting magnetic moment (around 2 μ_B).[49] However, Cartier dit Moulin, Bleuzen and co-workers showed that X-ray Magnetic Circular Dichroism experiments (XMCD) were able to probe therelative orientation of the magnetic moments of the metal ions, and thus to determine the sign of the magnetic interaction. With this technique, they characterized the magnetic interaction within the photo-induced metastable state of compound **5** ($Rb_{0.55}Co_{1.2}[Fe(CN)_6]\bullet 3.9H_2O$),[49] that was compared to $K_{0.04}Co_{1.48}[Fe(CN)_6]\bullet 6.8H_2O$ (**4**), known to exhibit antiferromagnetic interactions between Co and Fe ions.[25] For both compounds, a weak dichroic signal was obtained at the Co and Fe *K*-edges, with positive and negative signs, respectively. Since the antiferromagnetic coupling between magnetic $Co^{II}_{(HS,3/2)}$ and $Fe^{III}_{(LS,1/2)}$ centres in **4** was shown already by macroscopic magnetization data, it was concluded that the inversion of dichroic signal from cobalt to iron was a local evidence of the antiferromagnetic interaction in **4**. With this assumption, and taking into account that the same XMCD signature was observed for **5**, the authors evidenced for the first time the ferrimagnetic ground state of the photo-induced phase in Fe/Co PBAs.

Table I-1. Thermally and photo-induced electron-transfer (ET) for Fe/Co PBAs reported in the literature.

Compound (number in text)	% of vacancies [□]	ET with temperature	ET with light	EXAFS	XANES	References
$Co_{1.5}[Fe(CN)_6]\bullet 6H_2O$ (**3**)	33 %	-	non active	Yes	Yes	34,46
$K_{0.04}Co_{1.48}[Fe(CN)_6]\bullet 6.8H_2O$ (**4**)	33 %	-	non active	-	-	25
$K_{0.2}Co_{1.4}[Fe(CN)_6]\bullet 6.9H_2O$ (**1**)	29 %	-	active	-	-	24
$K_{0.4}Co_{1.3}[Fe(CN)_6]\bullet 4.2H_2O$ (**10**)	23 %	active (280 K)	-	Yes	Yes	46
$K_{0.4}Co_{1.3}[Fe(CN)_6]\bullet 5H_2O$ (**8**)	23 %	-	active	Yes	Yes	46
$Na_{0.07}Co_{1.5}[Fe(CN)_6]\bullet 6.3H_2O$	33 %	-	non active	-	-	30
$Na_{0.37}Co_{1.37}[Fe(CN)_6]\bullet 4.8H_2O$	27 %	active (180/220 K)	active	-	-	30
$Na_{0.4}Co_{1.3}[Fe(CN)_6]\bullet 5H_2O$ (**9**)	23 %	active (260 K)	-	Yes	Yes	46
$Na_{0.43}Co_{1.35}[Fe(CN)_6]\bullet 4.6H_2O$ (**7**)	26 %	active (213/232 K)	active	-	-	43,44
$Na_{0.53}Co_{1.32}[Fe(CN)_6]\bullet 4.4H_2O$	24 %	active (230/270 K)	active	-	-	30
$Na_{0.60}Co_{1.26}[Fe(CN)_6]\bullet 3.9H_2O$	21 %	active (260/300 K)	active	-	-	30,45
$Na_{0.94}Co_{1.15}[Fe(CN)_6]\bullet 3H_2O$	13 %	-	non active	-	-	30
$Na_{1.4}Co_{1.3}[Fe(CN)_6]\bullet 5H_2O$ (**11**)	23 %	-	-	Yes	Yes	46
$Rb_{0.55}Co_{1.2}[Fe(CN)_6]\bullet 3.9H_2O$ (**5**)	17 %	-	active	-	-	25
$Rb_{0.66}Co_{1.25}[Fe(CN)_6]\bullet 4.3H_2O$ (**2**)	20 %	-	active	Yes	Yes	34,46
$Cs_{0.1}Co_{1.43}[Fe(CN)_6]\bullet 6.4H_2O$	30 %	-	weak	-	Yes	26
$Cs_{0.24}Co_{1.38}[Fe(CN)_6]\bullet 5.5H_2O$	28 %	active (170 - 280 K)	active	Yes	Yes	26,47
$Cs_{0.38}Co_{1.25}[Fe(CN)_6]\bullet 5H_2O$	20 %	active (170 - 280 K)	active	-	Yes	26
$Cs_{0.68}Co_{1.18}[Fe(CN)_6]\bullet 4.1H_2O$	15 %	-	non active	-	Yes	26
$CsCo_{1.03}[Fe(CN)_6]\bullet 3.3H_2O$ (**6**)	3 %	-	weak	-	-	25

I.1.2 Introducing blocking ligands: reducing the dimensionality of the Prussian Blue Analogues

The previous section summarizes the research done in the past twenty years on tridimensional Fe/Co Prussian Blue Analogues, which display thermally and photo-induced electron transfer processes associated with optical and magnetic bistabilities between paramagnetic Fe^{III}_{LS}-CN-Co^{II}_{HS} and diamagnetic Fe^{II}_{LS}-CN-Co^{III}_{LS} configurations. In these systems, the amount of $[Fe(CN)_6]^{3-}$ vacancies can be modified through the nature and the quantity of the alkali ions (Na^+, K^+, Rb^+, Cs^+…). These modifications highly influence the

environment around the cobalt ion and its coordination sphere that is completed by water molecules. These chemical variations allow the change of the network flexibility, as well as the modification of the ligand field around the cobalt ion (and thus its local redox potential) influencing the electron transfer properties. Unfortunately, these vacancies and associated distortions of the network are inhomogeneously disseminated in the materials, resulting in a distribution of local environments around the cobalt ion. This feature promotes a distribution of electron transfer processes that coexist with inactive diamagnetic or paramagnetic Fe-CN-Co pairs. Moreover, the low solubility of these tridimensional materials precludes their manipulation and thus their easy shaping for technological applications. In that sense, materials with a lower structural dimensionality such as molecular, uni- or bi-dimensional systems, appeared to be an interesting strategy to face these challenges. These low dimensional systems allow not only a high control of the environment around the metal ions by a careful choice of the ligands, but also an increase of the solubility making easier the study of their structure and physico-chemical properties. These promising ideas encouraged several research groups in the world to design and search for low-dimensional Fe/Co cyanide complexes by using blocking ligands to limit the extension of the PBA framework. The most representative examples of this trend of research are described in the following paragraphs.

Although some low-dimensional Fe/Co cyanide complexes were reported during the emergence of the Fe/Co Prussian blue networks, none of these examples showed evidence of a thermally or photo-induced electron transfer phenomena.[52-56] However in 2004, the seminal works of Dunbar, Achim and co-workers reported for the first time a cyanido-bridged Fe/Co molecule exhibiting a thermally induced metal-to-metal electron transfer.[57-58] By reacting $[Fe(CN)_6]^{3-}$ and $[Co(tmphen)_2]^{2+}$ (tmphen: 3,4,7,8-tetramethyl-1,10-phenanthroline), a pentanuclear complex, $[\{Co(tmphen)_2\}_3\{Fe(CN)_6\}_2]$ (**12**), was obtained (Figure I-4, left). This molecule exhibits a trigonal bipyramidal geometry, with three $[Co(tmphen)_2]^{2+}$ units forming the central equatorial plane and two $[Fe(CN)_6]^{3-}$ moieties completing the apical positions. While the Fe-C bonds in the crystal structures at low and high temperatures did not exhibit significant differences, a decrease of the Co-N distances (ca. 0.12-0.14 Å) was observed for two of the three cobalt ions when lowering from 220 to 110 K. These results suggest the presence of Co centres experiencing a conversion from a divalent high spin configuration (Co^{II}_{HS}) to a trivalent low-spin one (Co^{III}_{LS}). At the same time, Mössbauer spectroscopy confirmed the presence of only Fe^{III} sites at high temperatures, while features for both Fe^{II} and Fe^{III} centres, in an approximate 1:1 ratio, were observed at low temperature. From these observations, the authors concluded on the oxidation state of the five metal ions for the complex **12** as $[Co^{II}_3Fe^{III}_2]$ at high temperature, while they proposed two possibilities at low temperature: a $[Co^{II}_2Co^{III}Fe^{II}Fe^{III}]$ configuration with a statistical disorder of the Co^{III} and Fe^{II} centres on two different Co and Fe sites respectively, or a mixture of $[Co^{II}Co^{III}_2Fe^{II}_2]$ and $[Co^{II}_3Fe^{III}_2]$ species. The temperature dependence of the magnetic susceptibility of **12** revealed a χT value of 8.3 cm^3 K mol^{-1} above 270 K, confirming the presence of three Co^{II}_{HS} (S = 3/2) and two Fe^{III}_{LS} (S = 1/2) ions (Figure I-4, right, red crystals). When cooling the sample, the χT product decreased significantly to reach a value of 3.3 cm^3 K mol^{-1} at 2 K,[59] in agreement with the author's first hypothesis (*vide supra*) and a $[Co^{II}_2Co^{III}Fe^{II}Fe^{III}]$ state at low temperature. These results showed for the first time the possibility to obtain a metal-to-metal

electron transfer within a discrete Fe/Co complex. It is worth mentioning that after a prolonged air exposure, this sample experienced a transformation from a red crystalline material to a blue powder due to water absorption. Mössbauer and magnetic susceptibility measurements of this new phase indicated the presence of a low temperature $[Co^{II}Co^{III}_2Fe^{II}_2]$ phase below 200 K. The gradual increase of the χT product above this temperature, together with the appearance of a small quadrupole doublet in the Mössbauer spectrum originated from a Fe^{III}_{LS} centre, supported an electron-transfer process from Fe^{II}_{LS} to Co^{III}_{LS} within the compound, suggesting the thermal population of a $[Co^{II}_3Fe^{III}_2]$ configuration (Figure I-4, right, blue solid). Interestingly, a third solid-state phase was obtained when the blue powder was exposed to high temperatures or vacuum, changing its colour to red. Mössbauer spectroscopy on this new phase revealed only the signature of Fe^{III}_{LS} centres independently of the temperature, and thus suggesting a stable $[Co^{II}_3Fe^{III}_2]$ configuration above 2 K. This hypothesis was confirmed by magnetic susceptibility measurements, which display only a smooth decrease attributed to the orbital contribution of both metal ions in the complex (Figure I-4, right, red solid). Even if compound **12** is not a molecular fragment of the original tridimensional Fe/Co Prussian Blue Analogue (*vide infra*, section 3.2), this complex should be considered as the first discrete Fe/Co cyanide-based species exhibiting a thermally induced intramolecular electron transfer.

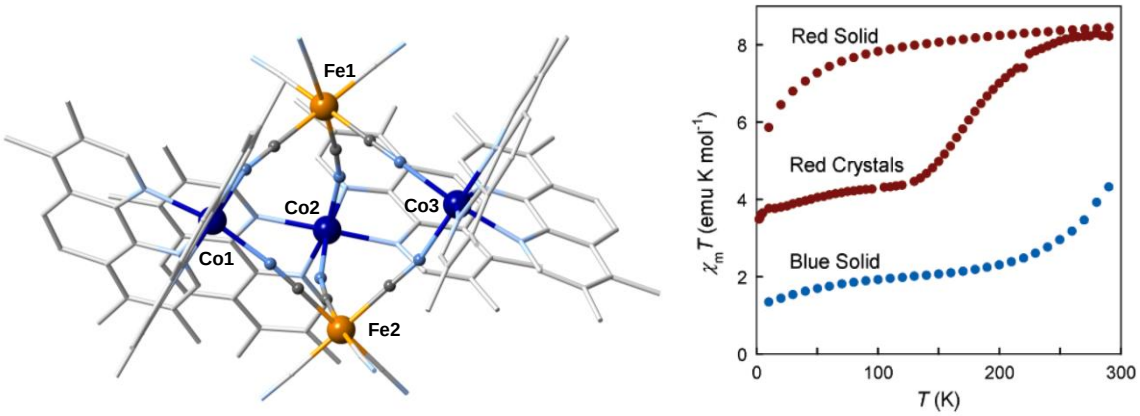

Figure I-4. (Left) Representation of the molecular structure of $[\{Co(tmphen)_2\}_3\{Fe(CN)_6\}_2]$ (**12**) at T = 220 K. Hydrogen atoms are omitted for clarity. Fe, Co, N and C atoms are indicated in orange, dark blue, light blue and light grey, respectively; (right) χT versus T data of **12** at a constant magnetic field of 0.1 T for the three solid-state phases obtained (red crystals, red and blue powders). Reprinted with permission from ref. 58. Copyright 2005 American Chemical Society.

A few years later in 2011, the photomagnetic properties of **12** were reported by Dunbar, Clérac, Mathonière and co-workers by measuring the temperature dependence of the magnetic susceptibility of compound **12** after exposure to the humidity (blue powder phase) before and after irradiation.[59] As expected[57-59] the magnetic properties agreed with a $[Co^{II}Co^{III}_2Fe^{II}_2]$ configuration at low temperatures (*vide supra*) that appeared to be photo-active as indicated by a fast increase of the magnetic response after irradiation at 10 K with white light. This effect was attributed to a partial photo-conversion (about 30 %) of the $[Co^{II}Co^{III}_2Fe^{II}_2]$ state to the $[Co^{II}_3Fe^{III}_2]$ one. The authors related the incomplete nature of the photomagnetic effect to the dark colour of the sample (which likely impeded the light penetration) or to the difficulty

to access to the [$Co^{II}_3Fe^{III}_2$] configuration from the blue solid phase. Above 50 K, the photo-excited state relaxed to the thermodynamic [$Co^{II}Co^{III}_2Fe^{II}_2$] phase, which reproducibly exhibits the same magnetic properties observed before irradiation.[59]

The studies carried out by Dunbar et al. demonstrated for the first time the possibility of observing an electron transfer phenomenon within a molecular Fe/Co system. However some years later in 2008, the first molecular fragment of the tridimensional Fe/Co Prussian Blue Analogue was reported by Clérac, Mathonière, Holmes and co-workers. This complex, [{(pzTp)$Fe^{III}(CN)_3$}$_4${Co^{II}(tpmCH_2OH)}$_4$][ClO_4]$_4$•13DMF•4H_2O (**13**, pzTp: tetrapyrazolylborate, tpmCH_2OH: 2,2,2,-tris(pyrazolyl)ethanol), is an octanuclear species which truly represents the elementary unit of the 3D PBA network.[60] This cationic [Fe_4Co_4] molecular cube was obtained by reacting [NEt_4][(pzTp)$Fe^{III}(CN)_3$] with $Co(ClO_4)_2$ in DMF, with the subsequent addition of $(pz)_3CCH_2OH$ ligand. Earlier to this work, it is worth mentioning that this synthetic strategy using blocking/capping ligands has been successfully applied by Long,[61] Rauchfuss[62] and co-workers to obtain other molecular homo- and hetero-metallic cyanido-bridged cubes. In the case of complex **13**, both cobalt and iron centers are located at the corners of the molecular cube (Figure I-5, left) that is surrounded in the crystal packing by perchlorate anions and solvent molecules. Crystallographic studies at 260 and 90 K first evidenced the occurrence of an electron transfer phenomenon in this complex. At high temperatures, bond analysis and charge compensation indicated the presence of four Fe^{III}_{LS}-Co^{II}_{HS} pairs within the cube. In contrast, when this compound is cooled down to 90 K, the Co-N bond distances fall in the range expected for a Co^{III}_{LS} site (average value: 1.905(7) Å) suggesting the occurrence of a thermal electron transfer converting four Fe^{III}_{LS}-Co^{II}_{HS} pairs (observed at 260 K) in four Fe^{II}_{LS}-Co^{III}_{LS} pairs (at 90 K). Differential scanning calorimetry (DSC) revealed the presence of an endothermic peak at 255 K indicating the presence of a phase transition associated with the intramolecular electron transfer that was also studied by temperature dependent infrared (IR) and UV-Vis spectroscopies. IR studies focused on the ν_{CN} stretching mode that is a good internal probe of the bridging mode of the cyanide groups. The formation of Fe^{II}_{LS}-CN-Co^{III}_{LS} units in temperature was monitored by following the reversible shift of this IR band from high to lower energies when decreasing the temperature. Similar temperature studies were also performed analysing the UV-visible spectra, both in solution (CH_3CN) and in solid state. The magnetic properties as a function of temperature and light irradiation were carried out to further study the physical properties of compound **13**. Magnetic susceptibility measurements revealed a constant χT product of 12.7 cm^3 K mol^{-1} from 300 to 265 K, in a good agreement with non-interacting Fe^{III}_{LS} and Co^{II}_{HS} magnetic centres in a 4:4 ratio (Figuer I-5, right). An abrupt and reproducible decrease of the χT value down to 0.57 cm^3 K mol^{-1} was observed when the sample was cooled below 255 K, evidencing the intramolecular electron transfer from the paramagnetic [$Fe^{III}_{LS}Co^{II}_{HS}$]$_4$ configuration into the diamagnetic [$Fe^{II}_{LS}Co^{III}_{LS}$]$_4$ one. Moreover, the authors demonstrated that the high temperature [$Fe^{III}_{LS}Co^{II}_{HS}$]$_4$ phase can be thermally trapped by rapidly cooling the sample, or photo-generated at 30 K after 20 hours of white light irradiation. A gradual increase of the temperature (at 0.4 K/min) allowed the complete relaxation of the metastable state toward the thermodynamic [$Fe^{II}_{LS}Co^{III}_{LS}$]$_4$ phase at about 180 K. This remarkably high relaxation temperature clearly evidenced the long lifetime of the metastable state, which was

further studied as a function of the temperature. For both thermally and photo-induced metastable states, the characteristic relaxation time (τ) followed the same Arrhenius law with an extremely large activation energy barrier of 4455 K and τ_0 = 2.6 x 10^{-8} s. In comparison to tridimensional PBAs, **7** or $Na_{0.6}Co_{1.21}[Fe(CN)_6]$•$4.2H_2O$, which possess τ values at 120 K of ca. 33 or 3 hours respectively,[43-45] this $[Fe_4Co_4]$ molecular cube possesses an exceptionally long relaxation time estimated at 10 years at 120 K.[60]

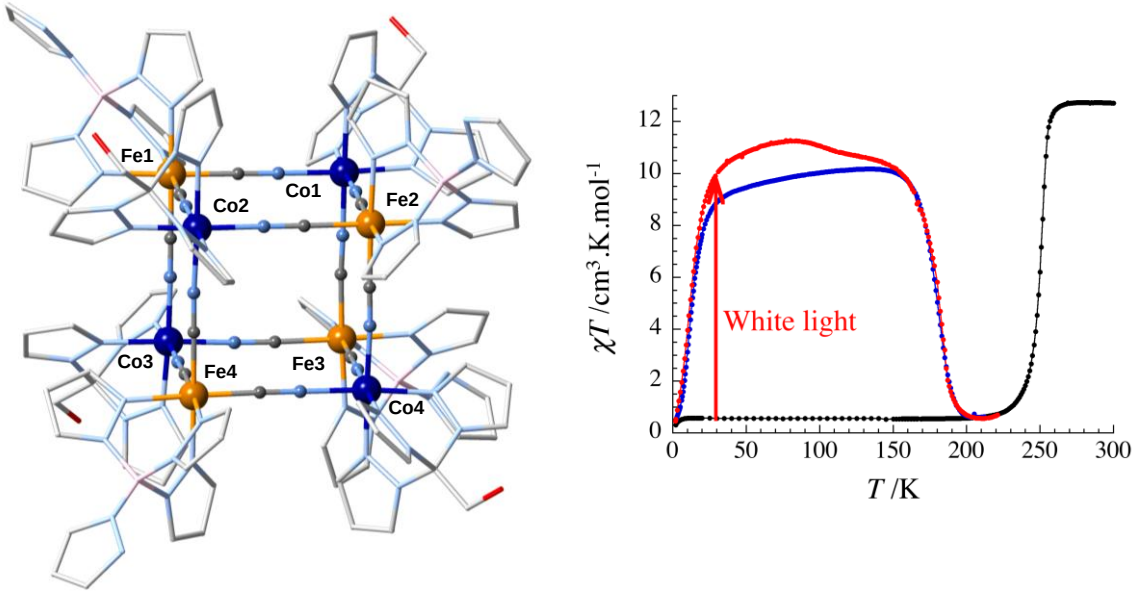

Figure I-5. (Left) Representation of the molecular structure of $[\{(pzTp)Fe^{III}(CN)_3\}_4\{Co^{II}(tpmCH_2OH)\}_4][ClO_4]_4$•$13DMF$•$4H_2O$ (**13**) at T = 260 K. Hydrogen atoms, perchlorate and lattice-solvent molecules are omitted for clarity. Fe, Co, N, C, O and B atoms are indicated in orange, dark blue, light blue, light grey, red and pink, respectively; (right) χT versus T data of **13** at 0.4 K/min and a constant magnetic field of 1 T before (black dots) and after (red dots) white light irradiation, and after thermal quenching (blue dots). Reprinted with permission from ref. 60. Copyright 2008 American Chemical Society.

The evaluation of the physical properties of compound **13** evidenced that i) both photo- and thermally induced electron transfer properties of the tridimensional Fe/Co PBAs were able to be transferred into molecular species, and ii) a diamagnetic molecular complex can be fully converted into a paramagnetic one through a photo-induced electron transfer. The next question in this field of research was obvious: is it possible to reduce the size of this photo-active molecular PBA to even smaller systems than this cube complex? This question was answered first by isolating a "face" of this octanuclear Fe/Co cube using again the successful building block approach. In fact, this kind of square complex was already described by Oshio and co-workers in 2000 by bridging iron and cobalt metal ions through cyanide groups, and capping them using bpy ligand (bpy = 2,2'-bipyridine).[63] Nevertheless, the two reported heterometallic compounds exhibited $[Fe^{II}_{LS}Co^{III}_{LS}]_2$ or $[Fe^{II}_{LS}Co^{II}_{HS}]_2$ configurations, and no evidence of electron transfer was found. In contrast in 2010, Clérac, Mathonière, Holmes and co-workers showed the occurrence of a reversible thermally and light-induced electron transfer in the tetranuclear $[Fe_2Co_2]$ complex $[\{(Tp^*)Fe^{III}(CN)_3\}_2\{Co^{II}(bpy)_2\}_2][OTf]_2$-•$4DMF$•$2H_2O$ (**14**, Tp*: tris(3,5-dimethyl)pyrazolyl borate, OTf: trifluoro-

methanesulfonate).[64] This compound was obtained by treating $[NEt_4][(Tp^*)Fe(CN)_3]$ with $Co(OTf)_2$ and bpy in DMF. The crystal structure at 230 K evidenced $\{(bpy)_2Co\}$ and $\{(Tp^*)Fe\}$ moieties located alternatively at the square corners and linked by cyanide ligands to afford Fe-CN-Co edges (Figure I-6, left). This molecule exhibited a nearly planar geometry, with a slightly distorted $[Fe_2(\mu\text{-}CN)_4Co_2]$ square core. At this temperature, the Co-N bond distances revealed the Co^{II} high spin configuration, suggesting the formation of $[Fe^{III}_{LS}Co^{II}_{HS}]_2$ paramagnetic species by charge balance consideration. This high temperature configuration was further confirmed by IR spectroscopy and the corresponding ν_{CN} stretches for Fe^{III}_{LS}-CN-Co^{II}_{HS} units. When the spectra were recorded at 130 K, characteristic bands for diamagnetic Fe^{II}_{LS}-CN-Co^{III}_{LS} pairs were observed. It is important to mention that these thermal variations were perfectly reversible upon cycling the temperature of the sample. Similarly, optical properties (solid state UV-Vis spectroscopy and optical reflectivity) were also found to be temperature dependent. In particular, the optical reflectivity was recorded between 260 and 10 K, exhibiting an abrupt and hysteretic change of the absolute value between 200 and 160 K. Moreover, the reflectivity spectrum at 10 K after irradiating the sample for 4 hours was similar to the high temperature one, thus evidencing the photo-activity of the compound. This photo-generated state relaxed to the thermodynamic configuration around 130 K when the sample was heated. For a deeper analysis and the identification of the different phases, the observed thermally and light-induced electron transfer phenomena were studied by magnetic measurements (Figure I-6, right). At high temperature, the χT value of 6.8 cm^3 K mol^{-1} agreed well with the presence of two Fe^{III}_{LS} and two Co^{II}_{HS} magnetic centres (Figure I-6, bottom). By decreasing the temperature, an abrupt decay of the χT product was observed around 168 K reaching 0.4 cm^3 K mol^{-1} at 120 K. This result confirmed the expected thermal electron transfer between Co^{II}_{HS} and Fe^{III}_{LS} leading to the conversion of paramagnetic $[Fe^{III}_{LS}Co^{II}_{HS}]$ pairs into diamagnetic $[Fe^{II}_{LS}Co^{III}_{LS}]$ ones. Upon increasing the temperature, the reversible phenomenon was observed at 186 K underlining a broad thermal hysteresis of 18 K (1 K min^{-1}) and thus the first order phase transition associated with the electron transfer process. This phase transition was further confirmed by the presence of enthalpic peaks in the DSC thermograms. The photomagnetic properties of **14** were also studied at 10 K by irradiation of the sample with white light. As anticipated from the reflectivity measurements, a sharp increase of the χT product was observed in agreement with the photo-generation of paramagnetic Fe^{III}_{LS}-CN-Co^{II}_{HS} pairs. This metastable $[Fe^{III}_{HS}Co^{II}_{HS}]_2$ state was also obtained by thermal quenching of the sample. Nevertheless, the lower χT values measured for the quenched phase demonstrate the higher efficiency of the light to generate this metastable paramagnetic phase. Both quenched and photo-induced metastable states were found to relax with relatively long characteristic times which follow an Arrhenius law with E/k_B = 2854 K and τ_0 = 9.1 x 10^{-9} s. For comparison with the previous systems (*vide supra*), this $[Fe_2Co_2]$ molecular square possesses a relaxation time estimated at 3 minutes at 120 K.[64]

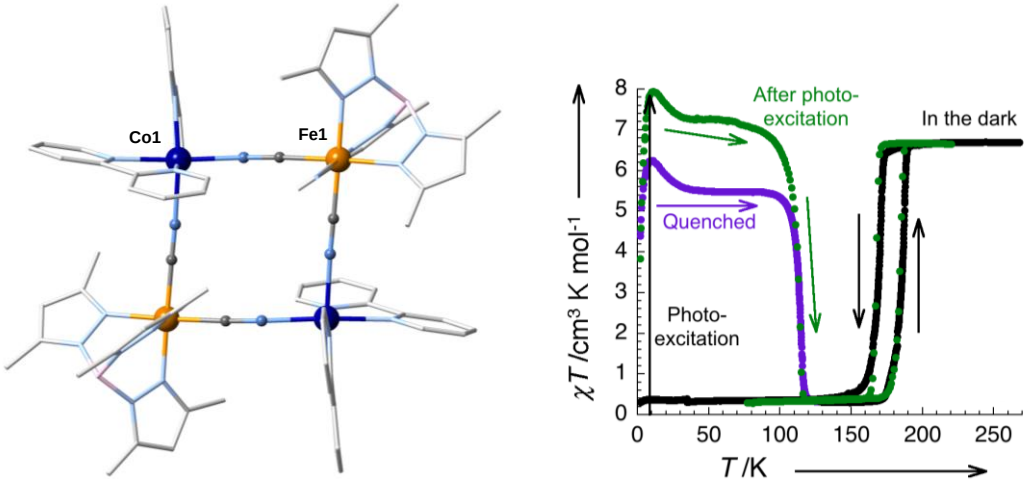

Figure I-6. (Left) Representation of the molecular structure of $[\{(Tp^*)Fe^{III}(CN)_3\}_2\{Co^{II}(bpy)_2\}_2][OTf]_2 \bullet 4DMF \bullet 2H_2O$ (**14**) at T = 230 K. Hydrogen atoms, triflate and lattice-solvent molecules are omitted for clarity. Fe, Co, N, C, and B atoms are indicated in orange, dark blue, light blue, light grey, and pink, respectively; (right) χT versus T data of **14** at 0.4 K min^{-1} before (black dots, 0.1 T) and after (green dots, 1 T) white light irradiation, and after thermal quenching (purple dots, 0.1 T). Reprinted with permission from ref. 64. Copyright 2010 Wiley-VCH.

After the discovery of **14**, several other Fe/Co molecular square complexes featuring thermally and/or photo-induced electron transfer have been reported.[65] Using a similar building block approach, different groups have obtained these new square complexes by the modification of the ligands capping the metal centres or by looking at the influence of the counter-ion or the synthesis/crystallization solvent mixture. Indeed, the functionalization of the 2,2'-bipyridine ligand (bpy) has been one of the main approaches to develop new tetranuclear $[Fe_2Co_2]$ square compounds. For example, the addition of alkyl *R* groups on bpy (bpy^R) tunes the electronic properties of the final complex, but also its solubility. The first related complexes were reported by Oshio and co-workers who synthesized and studied $[\{(Tp^*)Fe^{III}(CN)_3\}_2\{Co^{II}(bpy)_2\}_2][PF_6]_2 \bullet 2MeOH$ (**15**) and $[\{(Tp^*)Fe^{III}(CN)_3\}_2\{Co^{II}(dtbbpy)_2\}_2][PF_6]_2 \bullet 2MeOH$ (**16**, dtbbpy: 4,4'-di-*tert*-butyl-2,2'-bipyridine).[66,67] The former analogue was found to exhibit a paramagnetic $[Fe^{III}_{LS}Co^{II}_{HS}]_2$ state independently of the temperature. The absence of electron-transfer properties was attributed by the authors to the lack of donating group on the bpy ligand, which results in an increase of the redox potential at the cobalt site. This hypothesis, that was proposed comparing the redox properties of both **15** and **16** (*vide infra*),[67a] contrasts completely with the results observed for **14**,[64] which rather suggest a strong influence of the counter-ion within these systems and more generally the importance of the crystal packing on the electron transfer properties. Remarkably, complex **16** showed a two-step thermally induced electron transfer behaviour, with diamagnetic $[Fe^{II}_{LS}Co^{III}_{LS}]_2$ and paramagnetic $[Fe^{III}_{LS}Co^{II}_{HS}]_2$ configurations at low and high temperatures, respectively. In between at intermediate temperatures, the nature of the phase is still controversial. While infrared spectroscopy and X-ray diffraction studies suggest a 1:1 mixture of both $[Fe^{II}_{LS}Co^{III}_{LS}]_2$ and $[Fe^{III}_{LS}Co^{II}_{HS}]_2$ squares, DFT calculations strongly support the stabilization of a one-electron transfer species with a $[Fe^{II}_{LS}Co^{III}_{LS}Fe^{III}_{LS}Co^{II}_{HS}]$

configuration.[67b] The photo-generation of the paramagnetic phase was successfully carried out by irradiating the compound with an 808 nm laser at 5 K. The light-induced metastable state was found to relax to the $[Fe^{II}_{LS}Co^{III}_{LS}]_2$ state around 80 K when increasing the temperature, as well as by irradiating the sample with green light (532 nm) at 5 K.[68] The same authors have also recently characterized compound **16** before and after irradiation using X-ray diffraction and X-ray absorption spectroscopy.[68,69] Interestingly, the X-ray beam itself was also found to produce the paramagnetic $[Fe^{III}_{HS}Co^{II}_{HS}]_2$ state, since accumulating XAS measurements on the diamagnetic $[Fe^{II}_{LS}Co^{III}_{LS}]_2$ state at 15 K induced gradual changes in the XAS spectra with time toward the one observed at high temperature.[69]

Another important result was reported by Oshio and co-workers, who used compound **16** to demonstrate for the first time the possibility of transferring the electron transfer phenomenon and the associated properties from solid state to solution.[67] When **16** was dissolved in butyronitrile, significant changes were observed in temperature by UV-Vis spectroscopy. Reducing the temperature, the intensity of the UV-Vis band associated with the $[Fe^{III}_{LS}Co^{II}_{HS}]_2$ state described a S-shape variation and the signature of the $[Fe^{II}_{LS}Co^{III}_{LS}]_2$ state was observed below 200 K. Remarkably, the thermal equilibrium between the two $[Fe^{II}_{LS}Co^{III}_{LS}]_2$ and $[Fe^{III}_{LS}Co^{II}_{HS}]_2$ states and their respective populations in solution were determined for the first time in temperature by UV-Vis spectroscopy. It is also important to mention that the intermediate state detected in solid state was absent in solution likely due to the lack of intermolecular interactions in solution.[67] Furthermore, UV-Vis spectroscopy was also used to monitor the electron transfer process upon addition of trifluoroacetic acid at fixed temperature. This remarkable result demonstrated for the first time the possibility of inducing an electron transfer in these molecular Fe/Co PBAs by protonation. The same authors also explored the possibility of changing the ligand capping the iron centre by using the Tp ligand (Tp: hydrotris(pyrazol-1-yl)borate) to synthesize the related compound $[\{(Tp)Fe^{III}(CN)_3\}_2\{Co^{II}(dtbbpy)_2\}_2][PF_6]_2 \bullet 4H_2O$ (**17**).[67] The absence of methyl groups on the Tp ligand stabilizes the Fe^{II} low spin state, thus leading to a diamagnetic $[Fe^{II}_{LS}Co^{III}_{LS}]_2$ electronic configuration for **17** in the whole temperature range. The good solubility of these $[Fe_2Co_2]$ systems permitted the study of their electron transfer by electrochemical measurements. Four redox processes attributed to the $[Fe_2Co_2]^{2+}$ moiety were observed by cyclic voltammetry experiments permitting (i) the simple comparison of the redox potentials of each metal centre for complexes **15**, **16** and **17**, and (ii) to probe the influence of the ligand functionalization by alkyl groups. The authors concluded that the addition of electron donating groups on the bpy and Tp* ligand offers a control of the redox potential at the Co and Fe sites, respectively, allowing the stabilisation of a thermally induced electron transfer phenomenon in **16**.

The influence of the bpy functionalization was also studied by Clérac, Mathonière, and co-workers in particular with complex **18**, $[\{(Tp^*)Fe^{III}(CN)_3\}_2\{Co^{II}(bpy^{Me})_2\}_2][OTf]_2 \bullet DMF \bullet H_2O$, for which the bpy ligand of complex **14** is replaced by bpy^{Me} (bpy^{Me}: 4,4'-dimethyl-2,2'-bipyridine).[70] This simple modification influenced dramatically the thermally induced electron transfer mechanism and the associated properties. While complex **14** exhibited a first order transition with a significant thermal hysteresis associated with the electron transfer process (*vide supra*; Figure I-6), a thermal conversion (i.e. a thermal equilibrium between the

two $[Fe^{II}_{LS}Co^{III}_{LS}]_2$ and $[Fe^{III}_{LS}Co^{II}_{HS}]_2$ states) was observed for **18**. Similarly to spin-crossover systems, the electron transfer transition in **14** is converted in an electron transfer conversion in **18** by decreasing the elastic interactions between the molecules (i.e. decreasing the cooperativity) thanks to weaker π-π interactions between bpy^{Me} moieties in **18** than between bpy ligands in **14**.[70]

Combined UV-Vis spectroscopy and magnetic measurements of **14** and **18** in the different solvents were used to confirm that the occurrence of the intramolecular electron transfer was preserved in solution.[70] While the electron transfer process was detected only in methanol and acetonitrile for **14**, the physical properties of **18** were transferred to dilute solutions using a larger number of solvents. Interestingly, the thermally induced electron transfer conversion was found to be strongly influenced by the nature of the used solvent. For example, a shift of about 60 K was observed when comparing $T_{1/2}$ (temperature where the ratio between the paramagnetic and diamagnetic configurations is 1:1) for **18** in CH_3OH (240 K) and CH_2Cl_2 (180 K). A general tendency showed that $T_{1/2}$ values increased with the solvent polarity, allowing a fine tuning of the electron transfer properties simply by a judicious choice of the solvent or adjusting the composition of a solvent mixture. For comparison, the authors also reported the solution properties of the related compound **19**, $[\{(Tp^*)Fe^{III}(CN)_3\}_2\{Co^{II}(DMF)_4\}_2][OTf]_2 \cdot 2DMF$, possessing cobalt ions capped by only coordinating DMF molecules and not bpy type ligands like in the analogues described above.[64,70,71] In this case, the complex stays paramagnetic in solid state[71] but also in all the solvents tested,[70] confirming the influence of the ligand environment on the redox potential of the Co site and thus the occurrence of an intramolecular electron transfer process. Recently, Oshio and co-workers obtained a similar complex $[\{(Tp^*)Fe^{III}(CN)_3\}_2\{Co^{II}(dmbpy)_2\}_2][PF_6]_2 \cdot 4MeCN$ (**20**, dmbpy: 5,5'-dimethyl-2,2'-bipyridine), by changing the position of the methyl group on the bpy ligand in comparison to complex **18**.[72] Like for **19**, X-ray diffraction and magnetic measurements in the solid state evidenced that **20** is stabilised in its paramagnetic $[Fe^{III}_{LS}Co^{II}_{HS}]_2$ configuration independently of the temperature. These results highlight how sensitive is the electron transfer process for these $[Fe_2Co_2]$ square complexes in the solid state and solutions, regarding the functionalization of the bpy ligand, as well as the choice of the counter-anions and the solvent molecules surrounding the complex.[63-72] The effect of the crystallisation solvent molecules was also illustrated by the appearance of both thermally and photo-induced electron transfer phenomena when **20** is desolvated.[72]

The influence of the ancillary ligands and the effect of the intermolecular interactions within these kinds of Fe/Co molecular squares were also recently studied by Holmes, Clérac, Mathonière and co-workers.[73] Two new complexes of this family, $[\{(Tp^{Me})Fe^{III}(CN)_3\}_2\{Co^{II}(bpy)_2\}_2][(Tp^{Me})Fe^{III}(CN)_3]_2 \cdot 12H_2O$ (**21**, Tp^{Me}: hydrotris(3-methylpyrazol-1-yl) borate) and $[\{(Tp^{Me})Fe^{III}(CN)_3\}_2\{Co^{II}(bpy)_2\}_2][BPh_4]_2 \cdot 6MeCN$ (**22**) were synthesized using $[EtN_4][(Tp^{Me})Fe^{III}(CN)_3] \cdot 9H_2O$ as a new iron building block. As their analogues, these $[Fe_2Co_2]$ systems show thermally and photo-induced electron transfer properties with a metastable paramagnetic state relaxing at 90 K and 120 K for **21** and **22**, respectively. The obtained $T_{1/2}$ values were 244 K for **21**, and 230 K for **22**. These values are higher than those observed for the related Tp*-based complexes (i.e., 177 K for **14**, 174 K for **18**), demonstrating that the weaker σ donor character of the Tp^{Me} ligand stabilizes the low

spin state of the Fe^{II} sites. This conclusion is corroborated by the properties of the related Tp-based complexes such as **17** (vide supra), which is diamagnetic due to an even weaker σ donor character of Fe capping ligand.[67] With this study, the authors demonstrated how the functionalization of the Tp ligand can also tune the electron transfer properties of the Fe/Co molecular squares. In contrast, no clear influence on $T_{1/2}$ was observed from the different intermolecular interactions detected in **21** and **22**. On the other hand, Li and co-workers synthesized and studied another example of a Fe/Co molecular square using the Tp ligand to chelate the iron sites and 4,4'-bis(ethoxycarbonyl)-2,2'-bipyridine (4,4'-bcbpy) as capping ligand for the cobalt centres: $[\{(Tp)Fe(CN)_3\}_2\{Co(4,4'\text{-bcpby})_2\}_2][ClO_4]_2 \bullet 2MeOH$ (**23**•2MeOH).[74a] Accordingly, only the diamagnetic $[Fe^{II}_{LS}Co^{III}_{LS}]_2$ configuration was observed up to 300 K for **23**•2MeOH. However when the methanol molecules were removed from the lattice, complex **23** exhibited an incomplete thermally induced electron transfer to the paramagnetic $[Fe^{III}_{LS}Co^{II}_{HS}]_2$ state around 200 K. The authors attributed this effect to the loss of the hydrogen bonding network present between these molecular squares that is supposed to induce a negative shift of the redox potentials of the iron ions, thus promoting the electron transfer.[74a] Under external pressure (up to 8.35 kbar), the $T_{1/2}$ value increased slightly and the electron transfer process became almost complete. Remarkably when the crystals of **23** were soaked in methanol, the diamagnetic state was fully recovered, and this "crystal-to-crystal" transformation was found to be reversible. Interestingly, the same group recently published a related compound featuring similar ligands for both metal centres: $[\{(MeTp)Fe(CN)_3\}_2\{Co(4,4'\text{-bmbpy})_2\}_2][PF_6]_2 \bullet 2MeOH$ (**24**•2MeOH, MeTp: methyltris(pyrazolyl)borate, 4,4'-bmbpy: 4,4'-bis(methoxycarbonyl)-2,2'-bipyridine).[74b] While the metal precursors exhibit similar redox potentials to the ones in **23**•2MeOH, both thermal and photo-induced electron transfer processes were observed for compound **24**•2MeOH. The authors justified this behaviour regarding the remarkable distortion of the molecular square's core and the bend exhibited by the cyanide linkers in **24**•2MeOH, which induce a decrease of the transition temperature of the electron transfer process.[74b] Thus, Li's work introduces the influence of the square topology and demonstrates once more the importance of the lattice environment in the electron transfer properties of these $[Fe_2Co_2]$ compounds.

Lescouëzec and co-workers also reported a Fe/Co cyanido-based square complex using the pzTp iron derivative and the bis(1-methylimidazol-2-yl)ketone) (bik) ligand to coordinate at the cobalt centres: $[\{(pzTp)Fe(CN)_3\}_2\{Co(bik)_2\}_2][ClO_4]_2 \bullet 2H_2O$ (**25**).[75] While the magnetic measurements clearly indicates the diamagnetic nature of **25** between 2 and 300 K, the irradiation of the $[Fe^{II}_{LS}Co^{III}_{LS}]_2$ state (with white light at 20 K) led to a photo-induced electron transfer engendering paramagnetic $[Fe^{III}_{LS}Co^{II}_{HS}]_2$ species. In 2013, the same authors demonstrated that this metastable paramagnetic state in **25** could also be photo-generated using laser sources, with a high efficiency at 808 nm.[76] Interestingly, this photo-excited state was found to photo-relax to the diamagnetic one after irradiation at 532 nm, showing for the first time a bidirectional photomagnetic effect for a Fe/Co molecular PBA at a fixed temperature.

For comparison, the previously discussed $[Fe_2Co_2]$ systems are gathered in Table I-2, mentioning the ligands occupying the iron (L_{Fe}) and cobalt (L_{Co}) coordination spheres, the

used anion, the state of the compound for the study, the temperature at which the thermally induced electron transfer occurs and the temperature at which the system relaxes after a photo-induced electron transfer.

Table I-2. Characteristics of the $[\{(L_{Fe})Fe^{III}(CN)_3\}_2\{Co^{II}(L_{Co})_n\}_2][X]_2$ molecular squares described in the text

Compound	L_{Fe}	L_{Co}	Anion	ET Temp., $T_{1/2}$ [(b)] (K)	ET light, T_{relax} (K)	State studied	Ref.
14	Tp*	bpy	OTf^-	168/186	120	Solid/Solution	64,70
15	Tp*	bpy	PF_6^-	paramagnetic	-	Solid	67
16	Tp*	dtbbpy	PF_6^-	275 and 310 (two steps)	80	Solid/Solution	66,67
17	Tp	dtbbpy	PF_6^-	diamagnetic	-	Solid/Solution	67
18	Tp*	bpy^{Me}	OTf^-	174	120	Solid/Solution	70
19	Tp*	$(DMF)_4$	OTf^-	paramagnetic	-	Solid/Solution	70
20[(a)]	Tp*	dmbpy	PF_6^-	240	100	Solid	72
21	Tp^{Me}	bpy	$[(Tp^{Me})Fe(CN)_3]^-$	244	100	Solid	73
22	Tp^{Me}	bpy	BPh_4^-	230	120	Solid	73
23[(a)]	Tp	4,4'-bcbpy	ClO_4^-	120	-	Solid	74a
24	MeTp	4,4'-bmbpy	PF_6^-	177/184	65	Solid	74b
25	pzTp	bik	ClO_4^-	diamagnetic	100	Solid	75,76

(a) Data obtained from the desolvated form of the compound
(b) Temperature where the ratio between the paramagnetic and diamagnetic configurations is 1:1

In the previous paragraphs, we reviewed almost chronologically the switchable Fe/Co Prussian blue networks and how their thermally and photo-induced electron transfer properties have been implemented in molecular objects, decreasing the nuclearity from an octanuclear cube, pentanuclear complexes to a tetranuclear square. The next obvious episode of this scientific adventure was naturally pointing toward the design of a simple dinuclear [FeCo] complex with electron transfer properties. Indeed, many dinuclear Fe/Co molecular complexes were reported in the literature by Bernhardt and co-workers.[52,54,77] Most of these complexes were obtained in a diamagnetic $[Fe^{II}_{LS}Co^{III}_{LS}]$ configuration, and none showed a thermally or photo-induced electron transfer phenomena. Only in 2005, Bernhardt, Hauser and co-workers studied by visible pump-probe spectroscopy the short-lived metal-to-metal electron transfer excited states of some of these dinuclear compounds.[78] By studying $[Fe^{II}_{LS}Co^{III}_{LS}]$ complexes, the authors were able to detect two different excited states with $[Fe^{III}_{LS}Co^{II}_{LS}]$ and $[Fe^{III}_{LS}Co^{II}_{HS}]$ configurations depending on the experimental time scale and pulse-width. While the former de-excited very fast (picosecond time scale), the back-electron transfer from the latter was found to be slower due to the required spin rearrangement and Co-N bond changes.

It was only in 2013 that the first dinuclear Fe/Co complex exhibiting electron transfer phenomena was finally synthesized and studied.[79] By using $PY5Me_2$ (2,6-bis(1,1-di(pyridine-2- yl)ethyl)pyridine) and bbp^{2-} (2,6- bis(benzimidazol-2-yl)pyridine) as capping ligands, Clérac, Mathonière and co-workers obtained a new dinuclear Fe/Co complex, $[(bbp)Fe(CN)_3Co(PY5Me_2)]\bullet 2.5CH_3OH$ (**26**).[79] The bulky $PY5Me_2$ ligand around the cobalt precursor, $[Co(PY5Me_2)(OH_2)]^{2+}$, allowed only one accessible position in the Co coordination sphere for a cyanide ligand of the iron partner, $[Fe(bpp)(CN)_3]^{2-}$ thus stabilizing a dinuclear species in stoichiometric conditions (Figure I-7, left).

At 370 K, the Co-N and Fe-C bond distances agreed well with Co^{II}_{HS} and Fe^{III}_{LS} sites, evidencing the paramagnetic $[Fe^{III}_{LS}Co^{II}_{HS}]$ state of the molecular pair. Magnetic susceptibility measurements revealed a gradual decrease of the χT value from high to low temperatures. While the high temperature χT value was in concordance with the paramagnetic $[Fe^{III}_{LS}Co^{II}_{HS}]$ configuration, also established by X-ray diffraction, the value found at lower temperatures was incompatible with a diamagnetic $[Fe^{II}_{LS}Co^{III}_{LS}]$ pair. In contrast, single-crystal X-ray diffraction, ^{57}Fe Mössbauer and magnetic studies revealed for the first time the presence of a different paramagnetic ground state with a $[Fe^{III}_{LS}Co^{II}_{LS}]$ configuration that was previously identified using visible pump-probe spectroscopy as an excited state in the dinuclear systems reported by Bernhardt, Hauser and co-workers.[78] Unexpectedly, **26** exhibits a spin-crossover process occurring at the cobalt site in the solid state.[79] Nevertheless when **26** was studied in solution, different physical properties were observed. DMSO solutions of **26** were studied by magnetic susceptibility measurements to show that the spin-crossover behaviour is lost and only the paramagnetic $[Fe^{III}_{LS}Co^{II}_{HS}]$ configuration is observed above 1.8 K. However, when DMSO solutions were treated with an acid (trifluoroacetic or trifluoromethanesulfonic acids), their colour changed from dark green to purple. This proton-induced evolution was proven to be associated with a change of the [FeCo] pair electronic configuration by UV-vis spectroscopy, following the concomitant disappearance of the ligand-to-metal charge transfer band and the appearance of the metal-to-ligand charge transfer absorption centred on the iron moiety upon acid addition (Figure I-7, right). Moreover, the ^{1}H NMR spectra measured before and after acidifying the solution demonstrated the conversion of the paramagnetic $[Fe^{III}_{LS}Co^{II}_{HS}]$ complexes into diamagnetic species which can only be $[Fe^{II}_{LS}Co^{III}_{LS}]$ pairs.

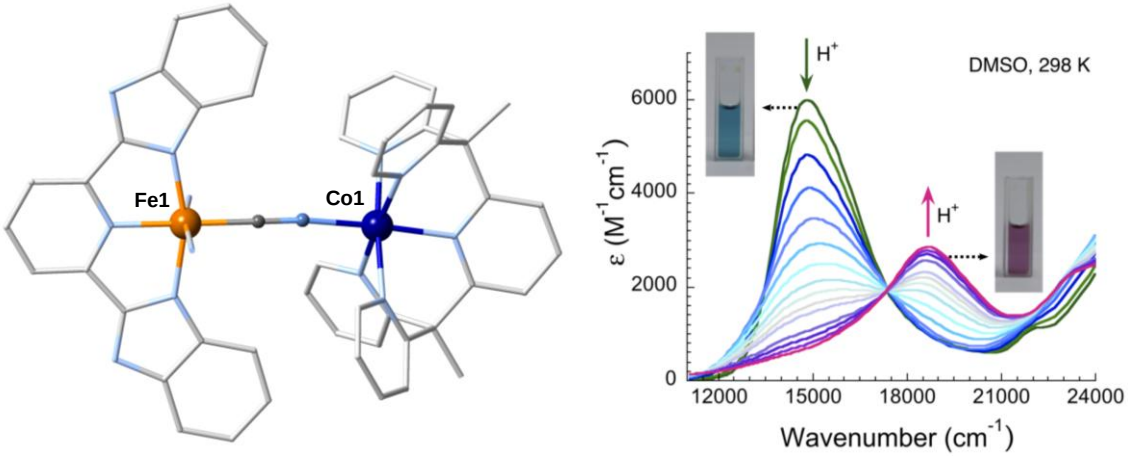

Figure I-7. (Left) Representation of the molecular structure of $[(bbp)Fe(CN)_3Co(PY5Me_2)]$•2.5MeOH (**26**) at T = 370 K. Hydrogen atoms, triflate and lattice-solvent molecules are omitted for clarity. Fe, Co, N and C atoms are indicated in orange, dark blue, light blue and light grey, respectively; (right) Evolution of the UV-Vis spectra upon TFA (TFA: trifluoroacetic acid) addition to a solution of **26** in DMSO, showing the colour change from dark green (paramagnetic, $[Fe^{III}_{LS}Co^{II}_{HS}]$) to purple (diamagnetic, $[Fe^{II}_{LS}Co^{III}_{LS}]$). Reproduced from ref. 79 with permission from The Royal Society of Chemistry.

Using combined cyclic voltammetry and UV-vis spectroscopy on **26** and its molecular precursors, it was shown that the proton addition only affects the iron redox properties, shifting its potential toward the unaffected Co one and thus promoting the electron transfer mechanism. By crystallizing the iron precursor after protonation ($[Fe(H_2bbp)(CN)_3]\bullet 2H_2O$), the authors revealed that added protons were indeed doubly protonating the bpp ligand affecting only the redox properties of the Fe site. Remarkably, complex **26** is the first dinuclear [FeCo] PBA to exhibit a metal-to-metal electron transfer, and this process is not triggered by temperature or light but by protonation.[79]

I.1.3 Other molecular Fe/Co cyanide-based complexes with high nuclearity and electron transfer properties

The molecular systems reviewed in section I.1.2 feature the characteristics of "extracted" molecular units (cube, square and pair) from the tridimensional Fe/Co Prussian blue networks.[60,63-70,72-76,79] These different Fe/Co cyanide-based complexes illustrate beautifully how, nowadays, coordination chemistry is able to design step-by-step model systems with targeted physical properties from bulk materials. A few other discrete polynuclear Fe/Co compounds exhibiting similar properties have been reported, even if they are not strictly a fragment of the 3D PBA network. In that sense, the pentanuclear complex **12**, described in section I.1.2, should be considered as the first example of this subgroup.

Oshio and co-workers reported a tetradecanuclear $[Fe_8Co_6]$ complex $[Fe_8Co_6(\mu\text{-}CN)_{14}(CN)_{10}(Tp)_8(HL)_{10}(CH_3CN)_2][PF_6]_4\bullet 14CH_3CN\bullet 5H_2O$ (**27**•$14CH_3CN\bullet 5H_2O$, HL: 3-(2-pyridyl)-5-[4-(diphenylamino)phenyl]-1*H*-pyrazole),[80] by reacting $[NBu_4][(Tp)Fe(CN)_3]$ with $Co(BF_4)_2\bullet 6H_2O$ in the presence of HL and $[NBu_4]PF_6$. A crown-like complex was obtained, exhibiting a twelve-membered ring with alternated Fe and Co metal ions decorated with two dangling $[(Tp)Fe(CN)_3]^-$ moieties. Independently of the temperature, coordination bond lengths, magnetic measurements and Mössbauer spectroscopy revealed the paramagnetic $[(Fe^{III}_{LS})_8(Co^{II}_{HS})_6]$ configuration of **27**•$14CH_3CN\bullet 5H_2O$. However, when this compound was left at ambient temperature for several days, the magnetic properties changed drastically. Elemental analysis and TGA data established the total loss of the acetonitrile solvated molecules leading to formulate this compound as **27**•$5H_2O$. In this "aged" sample, a decrease of the χT product was observed from 250 to 150 K before levelling to a value of about 9.4 cm^3 K mol^{-1}. From these magnetic measurements, the authors concluded to the presence of a $[(Fe^{III}_{LS})_5(Fe^{II}_{LS})_3(Co^{II}_{HS})_3(Co^{III}_{LS})_3]$ configuration below 150 K in **27**•$5H_2O$. This low temperature phase was stabilized by a Co^{II} to Fe^{III} electron transfer in three Fe^{III}-CN-Co^{II} pairs from the high temperature $[(Fe^{III}_{LS})_8(Co^{II}_{HS})_6]$ state. Remarkably, this compound in its $[(Fe^{III}_{LS})_5(Fe^{II}_{LS})_3(Co^{II}_{HS})_3(Co^{III}_{LS})_3]$ configuration at 20 K was efficiently converted (at about 76 %) in its fully paramagnetic $[(Fe^{III}_{LS})_8(Co^{II}_{HS})_6]$ state using laser irradiations (at 405 or 808 nm). Increasing the temperature, the photo-generated phase relaxed to its thermodynamic state above 150 K.[80]

Recently, the same group synthesized a new decanuclear Fe/Co complex containing six cobalt ions and four iron centers: $[NEt_4]_2[\{Co(L^R)\}_6\{Fe(CN)_6\}_4][BF_4]\bullet 17CH_3OH\bullet 12H_2O$ (**28**, Figure I-8, left).[81] For its synthesis, the authors used the L^R ligand that was obtained *in situ* by

reacting 2-pyridinecarbaldehyde and *R*-(+)-phenylethylamine, together with the metal ion precursors ($Co(BF_4)_2$•$6H_2O$ and $[NEt_4]_3[Fe(CN)_6]$). This serendipitous synthetic strategy led to a cage-type species, featuring six $[Co(L^R)_2]$ and four hexacyanoferrate units, encapsulating one tetraethylammonium cation (Figure I-8, left). Structural studies and Mössbauer spectroscopy evidenced the presence of a thermally induced electron transfer in **28** from a $[(Co^{II}_{HS})_5Co^{III}_{LS}(Fe^{II}_{LS})_2(Fe^{III}_{LS})_2]$ configuration at high temperatures to a $[(Co^{II}_{HS})_3(Co^{III}_{LS})_3(Fe^{II}_{LS})_4]$ state at 100 K. This conclusion was corroborated by magnetic susceptibility studies (Figure I-8, right) which detected a characteristic thermal variation of the χT product from 12.4 cm^3 K mol^{-1} at 300 K (close to the expected value for five Co^{II}_{HS} and two Fe^{III}_{LS} centers) down to 6.8 cm^3 K mol^{-1} below 180 K (in agreement with the value expected for three Co^{II}_{HS} ions) clearly associated with the metal-to-metal electron transfer process. As already observed for other compounds of this family, the desolvated version of **28** led to different physical properties with, in this case, a loss of the thermally induced electron transfer.[81]

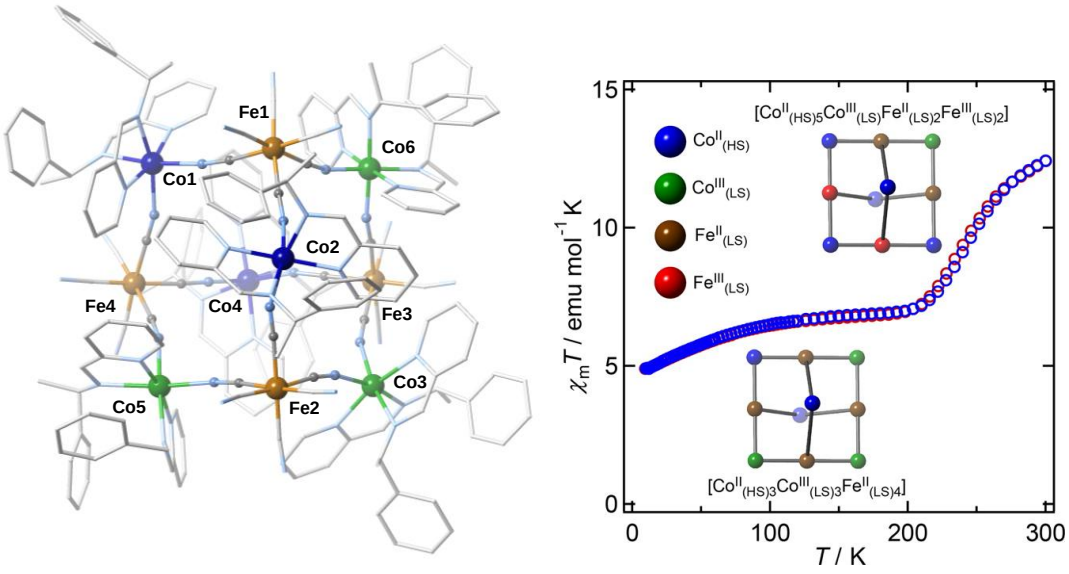

Figure I-8. (Left) Representation of the molecular structure of $[NEt_4]_2[\{Co(L^R)\}_6\{Fe(CN)_6\}_4][BF_4]$•$17CH_3OH$•$12H_2O$ (**28**) at T = 100 K. Hydrogen atoms, tetrafluoroborate and lattice-solvent molecules are omitted for clarity. Fe(II), Co(III), Co(II), N and C atoms are indicated in brown, green, dark blue, light blue and light grey, respectively; (right) χT versus T data cooling (blue dots) and heating (red dots) the sample, together with the diagrams of the spin state of each metal ion. Reprinted with permission from ref. 81. Copyright (2014) American Chemical Society.

I.1.4 Multifunctional molecular Fe/Co cyanide-based complexes with electron transfer properties

One of the most ambitious goals when synthesizing molecular cyanido-bridged Fe/Co complexes is to obtain multifunctional materials with a combination of the electron transfer behaviour and another physical property.

A remarkable example was reported by Oshio and co-workers in a complex showing Single-Molecule Magnet (SMM)[6] properties due to a light-induced electron transfer.[82] By reacting $[NBu_4][(pzTp)Fe(CN)_3]$ with $Co(OTf)_2 \cdot 6H_2O$ and bimpy in 1-PrOH, the authors obtained an hexanuclear compound: $[Co_2Fe_4(bimpy)_2(CN)_6(\mu\text{-}CN)_6(pzTp)_4] \cdot 2(1\text{-}PrOH) \cdot 4H_2O$ (**29**, bimpy: 2,6-bis(benzimidazol-2-yl)pyridine). The complex exhibited a square core composed of two $[(pzTp)Fe(CN)_2(\mu\text{-}CN)]^-$ and two $[Co(bimpy)]^{2+}$ moieties decorated by two more $[(pzTp)Fe(CN)_2(\mu\text{-}CN)]^-$ modules linked to each cobalt centre (Figure I-9, left). By using the tridentate bimpy ligand, one position around the cobalt ion coordination sphere is left available consenting the targeted square motif to be kept and at the same time allowing the coordination of the two additional iron units. As for the previous complexes, the high and low temperature configurations were assessed by single-crystal X-ray diffraction and ^{57}Fe Mössbauer spectroscopy. While cobalt and iron sites at 250 K were found to be Co^{II}_{HS} and Fe^{III}_{LS}, respectively, the study carried out at 100 K revealed a Co^{III}_{LS} configuration for the two cobalt centers, and two different oxidation/spin states for the iron centers: Fe^{II}_{LS} for the metal ions belonging to the central square (Fe1), and Fe^{III}_{LS} for the external ones (Fe2). In other words, these measurements suggested the occurrence of a thermally induced electron transfer between the iron and cobalt centres only within the central square core. This thermal conversion from $[Fe^{III}_{LS}(Co^{II}_{HS}Fe^{III}_{LS})_2Fe^{III}_{LS}]$ to $[Fe^{III}_{LS}(Co^{III}_{LS}Fe^{II}_{LS})_2Fe^{III}_{LS}]$ states was confirmed by magnetic susceptibility measurements, showing a characteristic decrease of the χT product centred around 220 K from high to low temperatures. When the sample was irradiated at 5 K (808-nm laser light), the χT value increased and reached saturation after about 150 minutes due to the intramolecular photo-induced electron transfer generating $[Fe^{III}_{LS}(Co^{II}_{HS}Fe^{III}_{LS})_2Fe^{III}_{LS}]$ species as confirmed by the 20-K crystal structures obtained before and after light irradiation. It is worth mentioning that the static magnetic properties of this photo-induced phase evidenced the presence of intramolecular ferromagnetic interactions between Co^{II}_{HS} and Fe^{III}_{LS} magnetic sites in contrast with the observation made in the three dimensional PBAs.[25,26,34] Below 4 K, the two accessible electronic configurations, the thermodynamics $[Fe^{III}_{LS}(Co^{III}_{LS}Fe^{II}_{LS})_2Fe^{III}_{LS}]$ and the photo-induced $[Fe^{III}_{LS}(Co^{II}_{HS}Fe^{III}_{LS})_2Fe^{III}_{LS}]$ ones, were studied by alternative current (ac) magnetic susceptibility measurements. While no evidence for slow dynamics of the magnetization was observed before irradiation, frequency dependence of the in-phase and out-of-phase signals under an external magnetic field of 500 Oe was clearly seen in the photo-induced phase (Figure I-9, right). From these measurements revealing the SMM properties of the light induced $[Fe^{III}_{LS}(Co^{II}_{HS}Fe^{III}_{LS})_2Fe^{III}_{LS}]$ phase in **29**, the relaxation time of the magnetization was estimated and found to follow a thermally activated law (i.e. Arrhenius law) with $\tau_0 = 5.7 \times 10^{-9}$ s and $\Delta_{eff}/k_B = 26$ K. Complex **29** is thus the first discrete molecule exhibiting slow relaxation of the magnetization in the light-induced phase.[82]

Another interesting example of multifunctional molecular cyanido-bridged Fe/Co complex exhibiting an electron transfer phenomenon was reported by Liu, Sato, Duan and coworkers.[83] In this case, the authors described a linear trinuclear compound, $[\{(Tp)Fe(CN)_3\}_2\text{-}Co(Meim)_4] \cdot 6H_2O$ (**30**, Meim: *N*-methylimidazole), with the aim of controlling concomitantly the dielectric and the magnetic properties of the system.

The reaction of $[NBu_4][(Tp)Fe(CN)_3]$ with $Co(NO_3)_2 \cdot 6H_2O$ in the presence of Meim led to **30**, where a cobalt centre is inserted between two iron metal ions in a linear cyanido-bridged skeleton. At 240 K, the bond lengths around the metal ions observed in the crystal structure agreed well with a $[Fe^{III}_{LS}Co^{II}_{HS}Fe^{III}_{LS}]$ configuration. After cooling the sample at 150 K, a significant decrease of the bond distances around the Co site suggested a thermally induced electron transfer from the cobalt metal ion to one of the two iron centres (likely occurring randomly between the two iron sites) leading to a low temperature $[Fe^{II}_{LS}Co^{III}_{LS}Fe^{III}_{LS}]$ state. This conclusion was also supported by infrared and ^{57}Fe Mössbauer spectroscopies, from which the characteristics of the two iron configurations, Fe^{II}_{LS} and Fe^{III}_{LS}, were clearly observed.

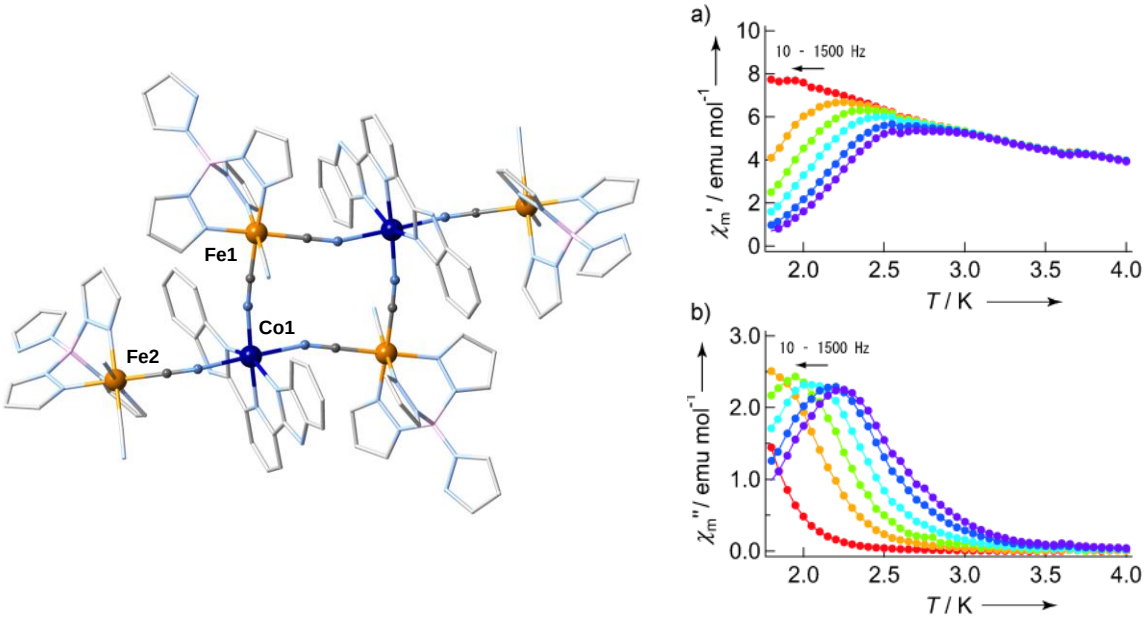

Figure I-9. (Left) Representation of the molecular structure of $[Co_2Fe_4(bimpy)_2(CN)_6(\mu\text{-}CN)_6(pzTp)_4] \cdot 2(1\text{-}PrOH) \cdot 4H_2O$ (**29**) at T = 100 K. Hydrogen atoms and lattice-solvent molecules are omitted for clarity. Fe, Co, N, C, and B atoms are indicated in orange, dark blue, light blue, light grey, and pink, respectively, (right) χ' versus T (a) and χ'' versus T (b) data for compound **29** after light irradiation (H_{ac} = 3 Oe oscillating at 10-1500 Hz and H_{ext} = 500 Oe) demonstrating the slow relaxation of the magnetization in the light-induced paramagnetic phase. Reprinted with permission from ref. 82. Copyright 2012 Wiley-VCH.

The thermal dependence of the magnetic susceptibility confirmed a reversible electron transfer transition (i.e. a first order phase transition) centered around 225 K with a small thermal hysteresis of about 10 K at 0.5 K/min. The χT values at high and low temperatures were found to be in good agreement with the expected electronic configurations. The possibility to light-induce the electron transfer process was also demonstrated at 5 K by irradiating the sample with a laser source at 535 nm. This effect was found to be relatively inefficient in **30** with only about 20% of photo-conversion. The magnetic susceptibility measurements showed that this photo-induced $[Fe^{III}_{LS}Co^{II}_{HS}Fe^{III}_{LS}]$ fraction of the sample relaxed completely to the $[Fe^{III}_{LS}Co^{III}_{LS}Fe^{II}_{LS}]$ phase upon heating above 90 K.[83] In both thermally or photo-induced electron transfer processes for **30**, one electron from the single

Co^{II}_{HS} site was transferred to one of the two Fe^{III}_{LS} centres. This phenomenon was thus imposing a change from a centrosymmetric nonpolar [$Fe^{III}_{LS}Co^{II}_{HS}Fe^{III}_{LS}$] molecule into an asymmetric [$Fe^{III}_{LS}Co^{III}_{LS}Fe^{II}_{LS}$] polar one, demonstrating the possibility to switch the polarity of a given complex by a "directional" electron transfer mechanism. Based on the X-ray crystal structures, DFT calculations were used to estimate the permanent electric dipole moment of the low temperature phase (18.4 D), and to demonstrate the absence of dipole moment for the high temperature configuration. With this example, the authors demonstrated for the first time that it is possible to trigger a polar/nonpolar conversion of a molecular system by thermally and photo-induced electron transfer mechanisms.[83]

I.1.5 One- and two-dimensional cyanido-bridged Fe/Co Prussian blue analogues with electron transfer properties

One and two-dimensional cyanido-bridged Fe/Co systems featuring metal-to-metal electron transfer properties have also been reported even if the number of examples in the literature is still very scarce.

The first example, [{(Tp)Fe(CN)$_3$}$_2$Co(bpe)]•5H$_2$O (**31**•5H$_2$O), was described by Sato and co-workers in 2010.[84] This compound was synthesized by reacting Li[(Tp)Fe(CN)$_3$] with Co(NO$_3$)$_2$ and 1,2-bis(4-pyridyl)ethane (bpe). This compound contains cyanido-bridged Fe/Co double zigzag chains (Figure I-10, left) with each cobalt centre linked to four [(Tp)Fe(CN)$_3$]$^-$ moieties which themselves act as a bidentate metallo-ligand between Co ions (Figure I-10, top). In the crystal structure, these chains are interconnected by the bpe ligands to form a two-dimensional framework. In addition, uncoordinated water molecules are located between the cyanido-bridged Fe/Co layers, interacting with them by significant hydrogen bonding interactions. At 223 K, the red crystals of **31**•5H$_2$O exhibit a structure with metal-ligand bond distances indicating only paramagnetic Co^{II}_{HS} and Fe^{III}_{LS} sites. Lowering the temperature to 123 K, the structure of the thermochromic dark green crystals revealed the presence of randomly distributed Fe^{II}_{LS}, Fe^{III}_{LS}, Co^{II}_{HS} and Co^{III}_{LS} metal ions. This conclusion based on the metal-ligand bond distances was attributed to a partial intramolecular electron transfer as also supported by temperature-dependent IR spectroscopy, which showed reversibly the expected ν_{CN} bands at the different temperatures. The metal-to-metal electron transfer process was further confirmed by magnetic susceptibility studies. Above 220 K, the obtained χT value agreed well with only Fe^{III}_{LS} (two sites) and Co^{II}_{HS} (one site) magnetic centres (5.1 cm^3 K mol^{-1}; Figure I-10, bottom). Lowering the temperature, the χT product experienced a marked decrease around 180 K, before stabilizing down to about 1.9 cm^3 K mol^{-1} below 120 K. This low temperature value suggested that only two-thirds of the Co^{II}_{HS} metal ions are transformed into Co^{III}_{LS} sites. In addition to the thermally induced electron transfer phenomenon, the authors demonstrated that the high-temperature configuration can also be photo-generated at 5 K. After 12 hours of 532-nm light irradiation, the χT product raised notably. The resulting photo-induced phase was shown to relax to the original thermodynamic state upon heating the sample above 150 K. Interestingly, these thermally and photo-induced electron transfer phenomena exhibited by **31**•5H$_2$O vanished after

dehydrating the sample (Figure I-10, right). In both materials, **31**•5H_2O and **31**, the magnetic properties revealed the occurrence of dominant ferromagnetic interactions between the paramagnetic metal ions (Figure I-10, bottom) as observed in **29**,[82] and again in contrast with the three dimensional PBAs.[25,26,34] Based on the crystal structure of **31** that established the complete removal of the water molecules observed in **31**•5H_2O, the authors attributed the absence of electron transfer properties in **31** to the lack of the water hydrogen bonding interactions toward terminal cyanido groups. This scenario suggests that the hydrogen bond network produced by the water molecules in **31**•5H_2O, pushes the redox potentials of the two metal ion sites to be close enough to favour the metal-to-metal electron transfer.[87] This "water-switchable" electron transfer system highlights once more the extreme sensitivity of the electron transfer process likely in link with redox potentials of the metal centers.

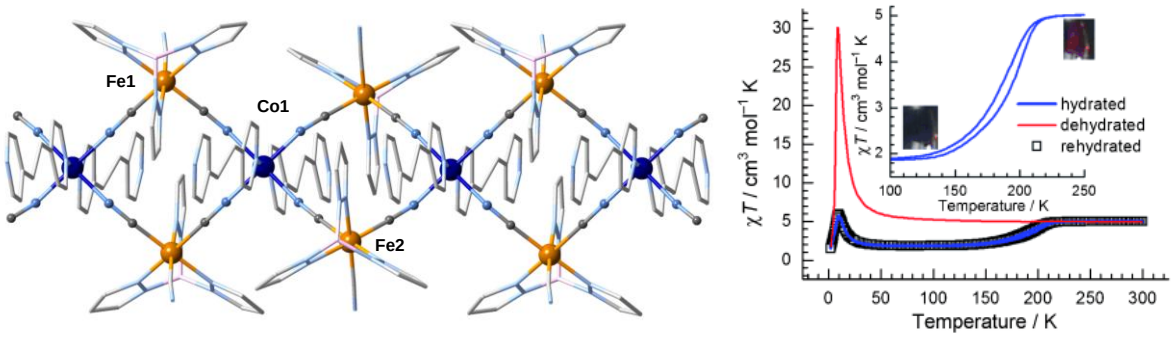

Figure I-10. (Left) Representation of the molecular structure of {[(Tp)Fe(CN)$_3$]$_2$Co(bpe)}•5H_2O (**31**•5H_2O) at T = 123 K. Hydrogen atoms and lattice-solvent molecules are omitted for clarity. Fe, Co, N, C, and B atoms are indicated in orange, dark blue, light blue, light grey, and pink, respectively; (right) χT versus T data of the hydrated (blue line), dehydrated (red line) and rehydrated (squares) of **31**. Reprinted with permission from ref. 84. Copyright 2010 Wiley-VCH.

By changing the environment of the iron centre, the same group reported another two-dimensional compound **32**, [{Fe(bpy)(CN)$_4$}$_2$Co(4,4'-bipyridine)]•4H_2O, exhibiting thermally and photo-induced electron transfer properties.[85] In this case, the authors used Li[Fe(bpy)(CN)$_4$] as the iron precursor, while Co(ClO_4)$_2$ and 4,4'-bipyridine were chosen to assemble the cobalt counterpart. As in **31**•5H_2O (Figure I-10, left), the crystal structure shows a double zigzag chain conformation, with the cobalt metal ions connected by four cyanide groups to four [Fe(bpy)(CN)$_4$] moieties. Two 4,4'-bipyridine ligands complete the Co coordination sphere and connect the chains into a 2D network. As already observed in **31**•5H_2O**,** water molecules are intercalated between the cyanido/bpy-bridged Fe/Co layers. Partial thermally (around 215 K) and light-induced electron transfer phenomena were characterized by X-ray diffraction, infrared spectroscopy, magnetic measurements and recently by X-ray absorption spectrocopy.[85b] Interestingly, strong frequency dependence of the ac susceptibility (for both in-phase and out-of-phase components) was observed in the photo-induced metastable state of **32**. The relaxation time of the dynamics was shown to follow an Arrhenius law with an energy barrier of 29 K and a pre-exponential factor of 1.4 10^{-9} s. Based on a qualitative analysis of the magnetic data, the authors attributed the observed

slow dynamics of the magnetization to the intrinsic Single-Chain Magnet (SCM)[86] properties of the chains in the antiferromagnetically ordered phase (T_N = 3.8 K).

In order to minimize the inter-chain magnetic interactions and obtain a SCM system, the authors recently proposed to use other ligands able to separate more efficiently the $\{Fe_2Co\}_\infty$ chains. This strategy is well illustrated by complex **33**, $[\{(pzTp)Fe(CN)_3\}_2Co(4\text{-styrylpyridine})_2]\bullet 2H_2O\bullet 2CH_3OH$.[87] In this case, Liu, Sato, Duan and co-workers used a bulkier pzTp ligand to block the iron centre, while a monodentate ligand (4-styrylpyridine) was chosen to complete the coordination of the cobalt ion. Consequently, **33** exhibits an one-dimensional structural organization with double zigzag chains (similar to **31**•$5H_2O$ in Figure I-10, top), which are not connected (in contrast to **31**•$5H_2O$ and **32**) but just separated by uncoordinated water molecules. In this case, crystallographic, spectroscopic and magnetic techniques confirmed a full thermally induced electron transfer around 230 K from Fe^{III}_{LS}-CN-Co^{II}_{HS} pairs to Fe^{II}_{LS}-CN-Co^{III}_{LS} ones while decreasing the temperature. As the stoichiometry of compound **33** is one cobalt for two Fe centres, only half of the iron metal ions are involved in the electron transfer process with all Co sites. Surprisingly, this phenomenon engaged specifically one of the two iron sites instead of randomly involving both iron centres as described for example in the trinuclear complex **30**.[83] The authors attributed this ordered electron transfer to the presence of different hydrogen bonding interactions around the two $[(pzTp)Fe(CN)_3]^{2-}$ units with the solvent molecules in the crystal packing. The photo-induced electron transfer was first shown in **33** by infrared spectroscopy and the decrease of the bridging ν_{CN} absorption peaks from the $Fe^{II/III}_{LS}$-CN-Co^{III}_{LS} units after a 532-nm laser irradiation of the sample. Magnetic measurements further confirmed the photoactivity of the sample. After an irradiation of 12 hours at 5 K, the χT product was significantly increased as expected for the photoconversion of a material composed essentially of isolated paramagnetic Fe^{III}_{LS} centres to an one-dimensional magnetically correlated $\{(Fe^{III}_{LS})_2Co^{II}_{HS}\}_\infty$ system. The magnetization dynamics of these metastable photo-induced chains was studied by ac magnetic susceptibility measurements, which revealed a thermally activated relaxation time with an energy barrier of 27 K ($\tau_0 = 1.4\ 10^{-10}$ s). Based solely on the study of the magnetization dynamics, the authors concluded to the photo-induced SCM properties of **33**. In addition, the thermal relaxation of the metastable photo-induced state was studied by monitoring the time decay of the magnetization at different temperatures. Above 40 K, the photo-generated phase relaxed with an Arrhenius behaviour and an energy barrier of 1348 ± 200 cm^{-1} (1926 ± 286 K) ($\tau_0 = 8.4\ 10^{-12}$ s). In contrast at lower temperatures (< 40 K), a temperature independent tunnelling relaxation of the excited paramagnetic $\{(Fe^{III}_{LS})_2Co^{II}_{HS}\}_\infty$ state to the diamagnetic $\{Fe^{III}_{LS}Fe^{II}_{LS}Co^{III}_{LS}\}_\infty$ ground state was observed. Overall, this remarkable compound constitutes the first evidence of the possibility to design photo-switchable single-chain magnets from one-dimensional cyanido-bridged Fe/Co Prussian Blue Analogues based on a metal-to-metal electron transfer mechanism.[87]

In 2012, Oshio and co-workers reported another type of one dimensional cyanido-bridged Fe/Co compound with a chiral square-wave chain topology: $[Co^{II}((R)\text{-pabn})][(Tp)Fe^{III}(CN)_3](BF_4)\bullet MeOH\bullet 2H_2O$ (**34*R***•$MeOH•2H_2O$; (*R*)-pabn: (*R*)-*N*(2),*N*(2')-bis(pyridine-2-ylmethyl)-1,1'-binaphtyl-2,2'-diamine), and $[Co^{II}((S)\text{-pabn})][(Tp)Fe^{III}(CN)_3](BF_4)\bullet 2H_2O$ (**34*S***•$2H_2O$).[88] By reacting $[NBu_4][(Tp)Fe(CN)_3]$ with the corresponding cobalt building block ($[Co^{II}((R)$-

pabn)]$^{2+}$ or [Co^{II}((*S*)-pabn)]$^{2+}$), the authors were able to synthesize both enantiomerically pure materials. These cyanido-bridged Fe/Co chain systems crystalized in the chiral $P2_12_12_1$ space group, with the cobalt metal ions chelated by four N atoms from the pabn ligand and linked to two cyanide N atoms from the iron [(Tp)Fe$(CN)_3$]$^-$ units (Figure I-11, left). Compound **34*R***•MeOH•2H_2O was found to lose the solvated methanol molecules and evolved to **34*R***•H_2O (when dried under N_2) or to **34*R***•3H_2O (when dried in air). While the magnetic properties of both *R* and *S* enantiomers were found, as expected, to be the same, the different solvated systems showed a thermally induced electron transfer phenomenon with a thermal hysteretic behaviour differing only by the $T_{1/2}$ values (above 250 K). These materials appeared to be fully diamagnetic at low temperatures in agreement with the {$Fe^{II}_{LS}Co^{III}_{LS}$}$_\infty$ ground state and exhibited χT values (ca. 3.4 cm^3 K mol^{-1}) coherent with the paramagnetic {$Fe^{III}_{LS}Co^{II}_{HS}$}$_\infty$ phase above the thermal hysteresis.[88] These metal-to-metal electron transfer properties were also confirmed by Mössbauer spectroscopy and single-crystal X-ray diffraction experiments. In addition, the temperature dependence of the electrical properties of **34*R***•H_2O was probed. Below 250 K, the value of the electrical conductivity was found to be around 10^{-12} S m^{-1}, suggesting an insulating state.

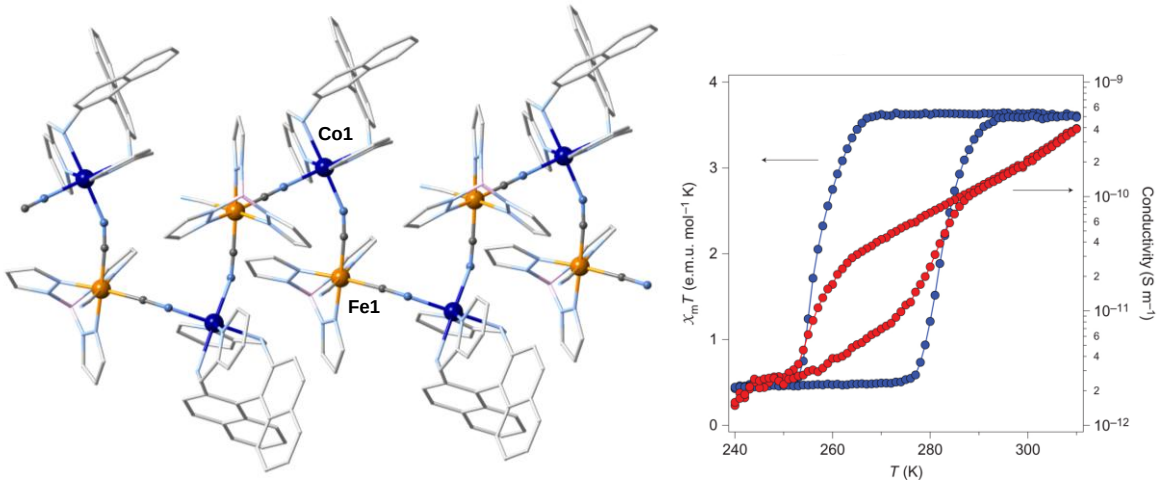

Figure I-11. (Left) Representation of the one-dimensional structure of [Co^{II}((*R*)-pabn)]-[(Tp)$Fe^{III}(CN)_3$](BF_4)•MeOH•2H_2O (**34*R***•MeOH•2H_2O) shown at 360 K. Hydrogen atoms, tetrafluoroborate and lattice-solvent molecules are omitted for clarity. Fe, Co, N, C, and B atoms are indicated in orange, dark blue, light blue, light grey, and pink, respectively; (right) Temperature dependence of the χT product (blue dots) and the dc conductivity (red dots) of **34*R***•H_2O. Reprinted with permission from ref. 88. Copyright (2012) Nature Chemistry, McMillan Publishers Ltd.

By increasing the temperature above the electron transfer temperature, the conductivity raised to about 10^{-9} S m^{-1} with semiconducting properties in the paramagnetic phase. Similarly to the magnetic properties, conductivity measurements exhibited a thermal hysteresis associated to the electron transfer process, thus demonstrating that **34*R***•H_2O possessed not only magnetic but also electric bistability (Figure I-11, right). As well, the photomagnetic properties of **34*R***•H_2O were studied by irradiating the sample with an 808-nm laser at 5 K. Under light, a fast increase of the χT values (up to ca 300 cm^3 K mol^{-1}) was detected suggesting the photo-generation of the metastable paramagnetic {$Fe^{III}_{LS}Co^{II}_{HS}$}$_\infty$

state. The χT vs T data revealed the presence of ferromagnetic interactions between Fe^{III}_{LS} and Co^{II}_{HS} magnetic sites within the photo-induced state, which relaxed to the diamagnetic ground state when the temperature exceeded 72 K. Furthermore, the characterization of the photo-generated $\{Fe^{III}_{LS}Co^{II}_{HS}\}_\infty$ state was carried out by ac susceptibility measurements showing a strong frequency-dependence of both in-phase and out-of-phase signals. Two thermally activated relaxation processes of the magnetization were identified with energy barriers of 65.5 K ($\tau_0 = 3.1x10^{-10}$ s^{-1}) and 33.3 K ($\tau_0 = 1.1x10^{-8}$ s^{-1}). Without further analysis of the static magnetic susceptibility, the authors concluded from this dynamic study that the photo-induced state displayed single-chain magnet properties. Thanks to thermally and light-induced electron transfer processes, this astonishing multifunctional material displays above 250 K both magnetic and conductivity bistabilities in temperature, while below 10 K, a photo-induced "tristability" (from the diamagnetic state and the field-induced ±M states from the SCM properties) is also described.[88]

Recently, Nojiri, Oshio and co-workers showed that the solid state grinding of **34*R***•MeOH•$2H_2O$ could also provoked an electron transfer and thus switched its diamagnetic state to the paramagnetic phase.[89] This new way of inducing the metal-to-metal electron transfer was indeed associated to the partial dehydration of the sample (i.e. the loss of only one water molecule) as deduced by thermogravimetric experiments. L-edge XAS and XMCD measurements were performed to characterize the different phases before and after grinding the sample and confirmed the observed effect. This study highlighted once more the key role of the interstitial solvent molecules on the metal-to-metal electron transfer process.

I.1.6 Theoretical background

As described above, ET complexes show experimentally interconversion between two different states (diamagnetic and paramagnetic), or eventually a phase transition leading often bistability. Therefore the following part is dedicated to the understanding of the mechanism of conversion and transition based on simple thermodynamic models for binary solutions.[90]

Given the fact that the ET process occurs between two different metal ions, we will consider an isolated pair to describe the occurrence of this process. The ET phenomenon involves two states (paramagnetic and diamagnetic labeled A and B, respectively) that are energetically close and, therefore it can be described as an equilibrium between these two states. The two different phases can be easily identified by measuring the temperature dependence of the χT product (as shown in Figures I-4 to I-6, I-8 and I-10), since each state is expected to be diamagnetic or paramagnetic that follows more or less a Curie law. Thus, the χT product corresponds to the Curie constants (C) of each state (C = 0 for a diamagnetic species) and is related to their molar fraction, x, according to the following equation:

$$\chi T = x_A \cdot (\chi T)_A + x_B \cdot (\chi T)_B \qquad \text{I.1}$$

where x_A and x_B represent the paramagnetic and diamagnetic fractions of a given system, respectively. Assuming that $x_A = x$, then Eq. I. becomes:

$$\chi T = x\cdot(\chi T)_A + (1 - x)\cdot(\chi T)_B \qquad \text{I.2}$$

For the paramagnetic *A* and diamagnetic *B* states, the $(\chi T)_A$ and $(\chi T)_B$ products are in most cases temperature independent. Therefore the investigation of the $\chi T = f(T)$ gives a direct access to $x = f(T)$. Experimental observations have shown that ET may occur as a conversion or a transition. Therefore it was decided to describe the temperature dependence of *x* by both ideal and regular solution models, and finally to construct a phase diagram with the aim to highlight the difference between a conversion and a transition.

The electron transfer phenomenon may be described as equilibrium between two states:

$$A \rightleftarrows B$$

with a Gibbs energy change:

$$\Delta G = \Delta H - T\Delta S \qquad \text{I.3}$$

This energy change ($\Delta G = G_B\text{-}G_A = \Delta H - T\Delta S = (H_B\text{-}H_A)\text{-}T(S_B\text{-}S_A)$) is positive below a temperature named T^* and negative above it. When $T = T^*$ ($\Delta G = 0$), the following relationship is verified:

$$\Delta H = T^*\Delta S \qquad \text{I.4}$$

According to the ideal solution model, we assume that A and B states are mixed without any interaction. If *N* is the total number of molecules, then $N_A = x_A\cdot N = x\cdot N$ is the number of molecules in the A state, while $N_B = x_B\cdot N = (1\text{-}x)\cdot N$ is the number of molecules in the B state. In statistical thermodynamics, the Gibbs energy of the system can be written:

$$G = N_A G_A + N_B G_B + G_{mix} \qquad \text{I.5}$$

where, G_A and G_B are the molar Gibbs energy for molecules in A and B states, whereas the G_{mix} is the energy of the mixture:

$$G_{mix} = - TS_{mix} = Nk_BT[x\ln x + (1\text{-}x)\ln(1\text{-}x)] \qquad \text{I.6}$$

hence:

$$G = xN(H_A\text{-}k_BT\ln g_A) + (1\text{-}x)N(H_B\text{-}k_BT\ln g_B) + Nk_BT\,[x\ln x + (1\text{-}x)\ln(1\text{-}x)] \qquad \text{I.7}$$

This relationship allows describing the Gibbs energy per molecule, g_N, as following:

$$g_N = \frac{G}{N} = x\left[\Delta H - k_B T \ln\frac{g_A}{g_B}\right] + k_B T[x\ln x + (1-x)\ln(1-x)] + G_B \qquad \text{I.8}$$

Introducing the logarithmic degeneracy ratio, $a = \ln\left(\frac{g_A}{g_B}\right)$:

$$g_N = \frac{G}{N} = x[\Delta H - k_B T a] + k_B T[x\ln x + (1-x)\ln(1-x)] + G_B = g'_N(x) + G_B \qquad \text{I.9}$$

The condition for equilibrium requires

$$\left(\frac{\partial g'_N}{\partial x}\right)_{T,N} = 0 \qquad \text{I.10}$$

as G_B is a constant. So we get the following relation with x_{min} being the fraction of A at equilibrium:

$$\left(\frac{\partial g'_N}{\partial x}\right)_{T,N} = \Delta H - k_B T a + k_B T \ln\frac{x_{min}}{1-x_{min}} = 0 \qquad \text{I.11}$$

The equation can be rearranged in the form of

$$\frac{1-x_{min}}{x_{min}} = exp\left(\frac{\Delta H}{k_B T} - a\right) \qquad \text{I.12}$$

and:

$$x_{min} = \frac{1}{1+exp\left(\frac{\Delta H}{k_B T} - a\right)} \qquad \text{I.13}$$

For $T = T^*$, $x_A = x_B = x^* = 0.5$ and thus $\ln\frac{x^*}{1-x^*} = 0$. Then, $\Delta H - k_B T^* \cdot a = 0$ and $a = \frac{\Delta H}{k_B T^*}$.

The expression I.13 changes in:

$$x_{min} = \frac{1}{1+exp\left(\frac{\Delta H}{k_B}\left(\frac{1}{T} - \frac{1}{T^*}\right)\right)} = \frac{1}{1+exp\left(a\left(\frac{T^*}{T} - 1\right)\right)} \qquad \text{I.14}$$

or

$$\frac{T}{T^*} = \frac{a}{a + \ln\frac{1-x_{min}}{x_{min}}} \qquad \text{I.15}$$

This allows the plotting of the $x_{min} = f(\frac{T}{T^*})$ dependence (Figure I-12), where $T^* = \frac{\Delta H}{k_B \cdot a}$. Whatever is the value of a, the function x_{min} increases when T/T^* increases. This model predicts that at low temperature ($T/T^* << 1$), the system is in B state, so x_{min} = 0. We can observe that all curves pass through a common point, $T/T^* = 1$, and x_{min} = 0.5. So we can

conclude that T^* is a characteristic temperature of the system. At this point, the system contains 50 % of molecules in state A and 50 % of molecules in state B. Note that in the literature, T^* is often noted $T_{1/2}$ to reflect the composition of the system.

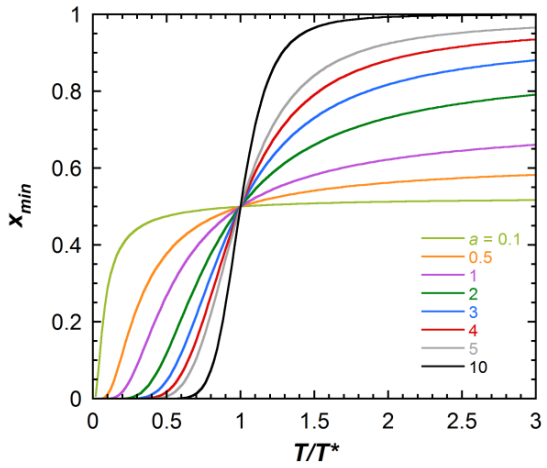

Figure I-12. Temperature dependence of the paramagnetic molar fraction $\boldsymbol{x_{min}}$ for different values of the degeneracy ratio, *a*, in ideal solution model.

Now let's consider a real case, for example a couple of Fe and Co ions, both in an octahedral environment. The paramagnetic state (A) consists of an Fe^{III}_{LS} ion (S = 1/2, $^2T_{2g}$ spectroscopic term, so the spin degeneracy is 2 and the orbital degeneracy, $2L + 1$, is 3) and a Co^{II}_{HS} ion (S = 3/2, $^4T_{2g}$, the spin degeneracy is 4, and the orbital degeneracy is 3). The diamagnetic state (B) consists of Fe^{II}_{LS} (S = 0) and Co^{III}_{LS} (S = 0) ions that are both corresponding to the $^1A_{1g}$ spectroscopic term for which the spin degeneracy is 1 and the orbital degeneracy also 1. So $g_A = (2\times3)\times(4\times3)$, $g_B = (1\times1)\times(1\times1)$ or $g_A/g_B = 72$, which gives $a = ln72 = 4.28$. According to the simulation plot in Figure I-12, the most similar case is for $a = 4$, where x_{min} tends to 0.90 at $T/T^* > 2$. In real systems, the limit of x is, indeed, very close to 1. The entropy change in {FeCo}-based ET systems can be experimentally measured by calorimetric methods or deduced from optical and/or magnetic measurements, thus the value of a could be experimentally estimated between 6.0 and 7.1.[60,64,70] This shows that in real complexes not only the electronic contributions to the degeneracy are present, but also the vibrational contributions for paramagnetic and diamagnetic states, which are different due to the different geometry of the states.

In a solid phase, in the crystalline lattice, the ET is directly influenced by intermolecular interactions (mostly of elastic origin). They play an important role in the macroscopic properties of the systems. Therefore we can add the interaction energy, which is responsible for the cooperative effects, in the regular solution mode. Hence, the Gibbs energy of the system can be written as:

$$G = N_A G_A + N_B G_B + G_{mix} + I \qquad \text{I.16}$$

where, the interaction energy term (I) is given by the formula:

$$I(x) = Wx(1-x) \qquad \text{I.17}$$

with W being the intermolecular interaction parameter (in units of energy) that is independent of temperature. Note that $I(x)$ is a simple exchange term in the mean-filed approximation: $Wx(1-x) = Wx_Ax_B$. Insertion of this term in the molar Gibbs energy gives:

$$G = xN(H_A - k_\mathrm{B}T\ln g_A) + (1-x)N(H_B - k_\mathrm{B}T\ln g_B) + \\ +Nk_\mathrm{B}T[x\ln x + (1-x)\ln(1-x)] + Wx(1-x) \qquad \text{I.18}$$

then:

$$g'_N(x) = x[\Delta H - k_\mathrm{B}Ta] + k_\mathrm{B}T[x\ln x + (1-x)\ln(1-x)] + Wx(1-x) \qquad \text{I.19}$$

and from the condition of equilibrium (Eq. I.10):

$$\Delta H - k_\mathrm{B}Ta + k_\mathrm{B}T\ln\frac{x_{min}}{1-x_{min}} + W(1-2x_{min}) = 0 \qquad \text{I.20}$$

or

$$k_\mathrm{B}T = \frac{\Delta H + W(1-2x_{min})}{a + \ln\frac{1-x_{min}}{x_{min}}} \qquad \text{I.21}$$

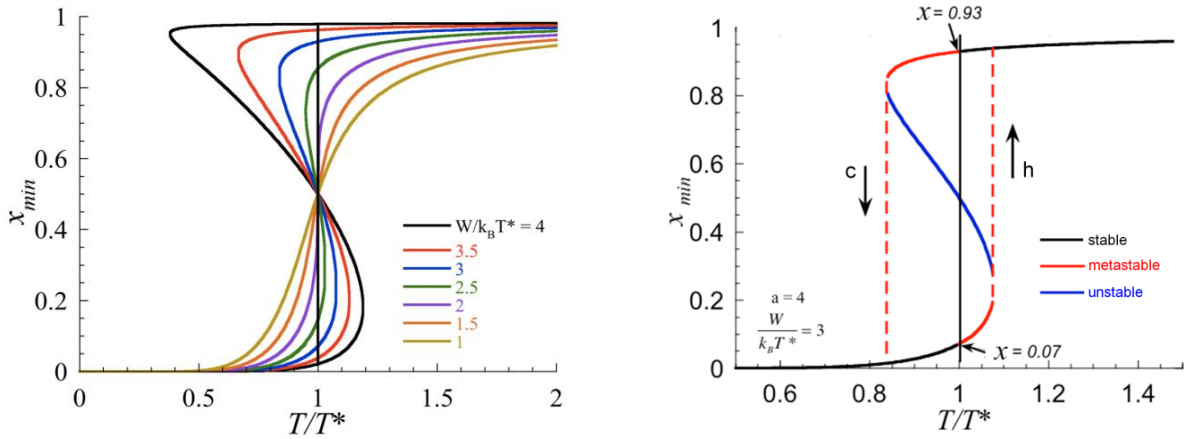

Figure I-13. (left) Temperature dependence of the paramagnetic molar fraction x for different values of $W/(k_\mathrm{B}T^*)$ at fixed a = 4, in a regular solution model; (right) thermal hysteresis when a = 4 and $W/(k_\mathrm{B}T^*)$ = 3, c – cooling mode, h – heating mode.

For given values of a, $\frac{T}{T^*} = f(x_{min})$ can be plotted (Figure I-13) and the function is defined by:

$$\frac{T}{T^*} = \frac{a+\frac{W}{k_B T^*}(1-2x_{min})}{a+\ln\frac{1-x_{min}}{x_{min}}} \qquad \text{I.22}$$

As shown in Figure I-13 (left), the inter-molecular interaction (W) plays an important role to define the stable state depending on the temperature. Therefore, three cases can be discussed:

- $W/(k_B T^*) < 2$, so x_{min} is increasing when T/T^* increases, and the corresponding curves are more and more steep for higher values of $W/(k_B T^*)$, but possess the same inflection point given by $T/T^* = 1$ and $x_{min} = 0.5$. This phenomenon is a conversion.
- $W/(k_B T^*) = 2$, there is a vertical gap of x_{min} at $T/T^* = 1$, and the corresponding curve is abrupt. This gives a first order transition at $T = T^* = T_C$ and the spin transition temperature is given by the relationship $W/(k_B T^*) = T_C$. This phenomenon is a transition at the critical point.
- $W/(k_B T^*) > 2$ the curve has an "S" shape, and for $T/T^* = 1$, not only the $x_{min} = 0.5$ solution is possible, but the Gibbs energy adopts two other local minimum values. A transition corresponding to a first order transition is observed then.

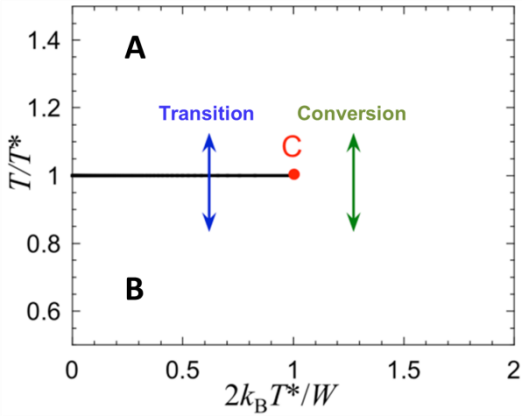

Figure I-14. Phase diagram for the regular solution model with $W > 0$ in the plane ($2k_B T^*/W$, T/T^*).

In the last case, a first order transition is associated with a thermal hysteresis (Figure I-13, right). The blue branch of the curve corresponds to unstable points, but in fact the system describes a hysteresis, drawn in dashed lines in Figure I-13 (right). It is noteworthy to mention that, in the general case, T^* is not at the center of the thermal hysteresis. Note also that the hysteresis width does not depend on the thermodynamics but on kinetic criteria and thus on the experimental scanning rate of the temperature.

From this analysis, we can construct a phase diagram that describes the system at any temperature and any value of W. The phase diagram consists in a line of first order phase transition at $\frac{T}{T^*} = 1$ that ends with a critical point, C (red point from Figure I-14). From this phase diagram, we can predict if real system will present a conversion or a transition. If $2k_B T^*/W \leq 1$, the system crosses the transition line (blue arrow from Figure I-14) and a transition will be observed; otherwise if $2k_B T^*/W > 1$, the system is beyond the critical point (green arrow from Figure I-14) and a conversion will be observed.

In this section, the thermal ET process could be described by binary solution models. This simple approach tells us that the interactions between the motifs responsible for the interconversion phenomena are crucial to exhibit a transition, and therefore to display bistability.

I.2 Conclusions and Motivation

The different examples presented in this introduction chapter illustrate the diversity of Fe/Co Prussian Blue Analogues from extended networks to molecular systems, which have been synthesized from serendipitous or by-design coordination chemistry. The remarkable research work on the tridimensional cyanido-bridged Fe/Co PBA networks has been essential to improve the comprehension of the metal-to-metal electron transfer process but also to access to a certain degree of control of their physical properties. In that sense, the subtle compromise between the number of diamagnetic Fe^{II}_{LS}-CN-Co^{III}_{LS} units present in these 3D systems and the network flexibility, modulated by the iron vacancies, can be considered as the first important conclusion of these studies in order to explain and fine tune the thermally and photo-induced electron transfer phenomena. However, the disordered nature and heterogeneity of these materials together with their low solubility reflect the difficulties that must be overcome to envisage some possible applications. These aspects are absent, or almost absent, in the molecular or low dimensional cyanido-bridged Fe/Co systems. Then the detailed study of the electron transfer phenomena appears always easier in these molecule-based compounds by simply analysing their structures from a single crystal at different temperatures or before/after irradiation, but also by probing in solution the redox properties (of the building blocks and/or the final product), which turned to be the most important information to understand and control the observed physical behaviours. As the redox potentials at each metal ion site are highly influenced by their respective coordination spheres and thus by the organic capping ligands, chemists have used this knowledge to develop new synthetic strategies with custom-made ligands. As a result, these designed molecular or low dimensional systems display adjustable physical properties with improved characteristics in comparison to their tridimensional analogues. In the last few years, the scientific community has made an important effort of research on these Fe/Co PBAs reporting more and more examples, which demonstrate the interest and potential behind these new molecular or low dimensional complexes. Consequently, the understanding of the metal-to-metal electron transfer process in these systems has progressed tremendously. Following this emerging research field, the ultimate challenge is the design of the smallest molecule being able to switch thermally and optically between states using a metal-to-metal electron transfer through a bridging cyanido ligand, in other words a simple dinuclear [Fe–CN–Co] complex. The simplicity of a dinuclear system will allow systematic studies of electron transfer properties depending on the structure and the redox potential of each metal-containing building block, and consequently lead to developing systems with optimized switching properties at the molecular level. Moreover, an Fe/Co dinuclear system which will mimic the properties of the 3-D network of PBAs **in solid state**, will allow the study in depth of the mechanism of the photo-induced electron transfer phenomenon at low temperatures with advanced physical

techniques and reveal the states involved in it. Apart from the fundamental interest provided by these systems, they also offer technological promises, since the combination of their magnetic and optical bistabilities induced by an electron transfer, together with other physical properties will allow the thermal or light control of the latter properties and thus, leading to a new generation of multifunctional materials.

This thesis is devoted to the synthesis and detailed characterization of a family of novel Fe/Co pairs, which exhibit intramolecular metal-to-metal electron transfer properties in solid state, observed for the first time in a dinuclear complex. This phenomenon can be triggered by light and temperature (Chapters II and III), solvent contents (Chapter II) and counter ions (Chapter III), characterized by structural, optical, magnetic, electric and photomagnetic measurements in the bulk and advanced characterization techniques at the local level. Moreover, the possibility of transferring the electron transfer phenomenon and the associated properties of the studied Fe/Co pairs from solid state to solution was also investigated (Chapter IV).

I.3 References

(1) Gütlich, P.; Goodwin, H. A. *Spin Crossover in Transition Metal Compounds I−III*, *Topics in Current Chemistry*; Springer-Verlag: Berlin, **2004**; *Vols. 233*.
(2) (a) Decurtins, S.; Gütlich, P.; Köhler, C.P.; Spiering, H.; Hauser, A. *Chem. Phys. Lett.*, **1984**, *105*, 1; (b) Sato, O.; Iyoda, T.; Fujishima, A.; Hashimoto, K. *Science*, **1996**, *272*, 704; (c) Sato, O.; Einaga, Y.; A. Fujishima, A.; K. Hashimoto, K. *Inorg. Chem.*, **1999**, *38*, 4405.
(3) (a) Caneschi, A.; Gatteschi, D.; Sessoli, R.; Barra, A. L.; Brunel, L. C.; Guillot, M. *J. Am. Chem. Soc.*, **1991**, *113*, 5873; (b) Sessoli, R.; Tsai, H. L.; Schake, A. R.; Wang, S. Y.; Vincent, J. B.; Folting, K.; Gatteschi, D.; Christou, G.; Hendrickson, D. N.; *J. Am. Chem. Soc.*, **1993**, *115*, 1804; (c) Sessoli, R.; Gatteschi, D.; Caneschi, A.; Novak, M. A. *Nature*, **1993**, *365*, 141.
(4) (a) Caneschi, A.; Gatteschi, D.; Lalioti, N.; Sangregorio, C.; Sessoli, R.; Venturi, G.; Vindigni, A.; Rettori, A.; Pini, M. G.; Novak, M. A. *Angew. Chem., Int. Ed.*, **2001**, *40*, 1760; (b) Clérac, R.; Miyasaka, H.; Yamashita, M.; Coulon, C. *J. Am. Chem. Soc.*, **2002**, *124*, 12837; (c) Coulon, C.; Miyasaka, H.; Clérac, R. *Struct. Bond.*, **2006**, *122*, 163.
(5) Linert, W.; Verdaguer, M. (Eds) *Molecular Magnets Recent Highlights*, Springer-Verlag Wien: New York, **2003**.
(6) Gatteschi, D.; Sessoli, R. *Angew. Chem., Int. Ed.*, **2003**, *42*, 268.
(7) Verdaguer, M.; Girolami, G. in *Magnetism - Molecules to Materials*, ed. J. S. Miller and M. Drillon, Wiley-VCH, Weinheim, **2004**, *5*, 283.
(8) Gütlich, P.; Hauser, A.; Spiering, H. *Angew. Chem., Int. Ed.*, **1994**, *33*, 2024.
(9) Sato, O.; Tao, J.; Zhang, Y.-Z. *Angew. Chem., Int. Ed.*, **2007**, *46*, 2152.
(10) Sato, O. *J. Photochem. Photobiol. C Photochem. Rev.*, **2004**, *5*, 203.
(11) Natali, M.; Campagna, S.; Scandola, F. *Chem. Soc. Rev.*, **2014**, *43*, 4005.
(12) Bleuzen, A.; Marvaud, V.; Mathonière, C. ; Sieklucka, B.; Verdaguer, M. *Inorg. Chem.*, **2009**, *48*, 3453.
(13) Ohkoshi, S.-i.; Tokoro, H.; *Acc. Chem. Res.*, **2012**, ***45***, 1749.
(14) Mallah, T.; Auberger, C.; Verdaguer, M.; Veillet, P. *J. Chem. Soc., Chem. Commun.*, **1995**, 61.
(15) Rebilly, J.-N.; Mallah, T. *Struct. Bonding*, **2006**, *122*, 103.
(16) Beltran, L. M. C.; Long, J. R. *Acc. Chem. Res.*, **2005**, *38*, 325.
(17) Lescouëzec, R.; Toma, L. M.; Vaissermann, J.; Verdaguer, M.; Delgado, F. S.; Ruiz-Pérez, C.; Lloret, F.; Julve, M. *Coord. Chem. Rev.*, **2005**, *249*, 2691.
(18) Pedersen, K. S.; Bendix, J.; Clérac, R.; *Chem. Commun.*, **2014**, *50*, 4396.
(19) Robin, M. B. *Inorg. Chem.*, **1962**, *1*, 337.
(20) Robin, M. B.; Day, P. in *Adv. Inorg. Chem. Radiochem.*, eds. H. J. Emeléus and A. G. Sharpe, Academic Press, **1968**, *10*, 247.
(21) Ludi, A.; Güdel, H. U. *Struct. Bonding*, **1973**, *14*, 1.
(22) Buser, H. J.; Schwarzenbach, D.; Petter W.; Ludi, A. *Inorg. Chem.*, **1977**, *16*, 2704.
(23) Herren, F.; Fischer, P.; Ludi A.; Haelg, W.; *Inorg. Chem.*, **1980**, *19*, 956.
(24) Sato, O.; Iyoda, T.; Fujishima, A.; Hashimoto, K. *Science*, **1996**, *272*, 704.

(25) Bleuzen, A.; Lomenech, C.; Escax, V.; Villain, F.; Varret, F.; Cartier dit Moulin, C.; Verdaguer, M. *J. Am. Chem. Soc.*, **2000**, *122*, 6648.
(26) Escax, V.; Bleuzen, A.; Cartier dit Moulin, C.; Villain, F.; Goujon, A.; Varret, F.; Verdaguer, M. *J. Am. Chem. Soc.*, **2001**, *123*, 12536.
(27) Cafun, J.-D.; Champion, G.; Arrio, M.-A.; Cartier dit Moulin, C.; Bleuzen, A. *J. Am. Chem. Soc.*, **2010**, *132*, 11552.
(28) Verdaguer, M. *Science*, **1996**, *272*, 698.
(29) Sato, O.; Einaga, Y.; Iyoda, T.; Fujishima A.; Hashimoto, K. *J. Electrochem. Soc.*, **1997**, *144*, L11.
(30) Shimamoto, N.; Ohkoshi, S.-i.; Sato, O.; Hashimoto, K. *Inorg. Chem.*, **2002**, *41*, 678.
(31) Einaga, Y.; Sato, O.; Iyoda, T.; Kobayashi, Y.; Ambe, F.; Hashimoto, K.; Fujishima, A. *Chem. Lett.*, **1997**, 289.
(32) Sato, O.; Einaga, Y.; Iyoda, T.; Fujishima A.; Hashimoto, K. *J. Phys. Chem. B*, **1997**, *101*, 3903.
(33) Einaga, Y.; Ohkoshi, S.-i.; Sato, O.; Fujishima A.; Hashimoto, K. *Chem. Lett.*, **1998**, 585.
(34) Sato, O.; Einaga, Y.; Fujishima A.; Hashimoto, K. *Inorg. Chem.*, **1999**, *38*, 4405.
(35) Pejaković, D. A.; Manson, J. L.; Miller, J. S.; Epstein, A. J. *J. Appl. Phys.*, **2000**, *87*, 6028.
(36) Pejaković, D. A.; Manson, J. L.; Miller, J. S.; Epstein, A. J. *Phys. Rev. Lett.*, **2000**, *85*, 1994.
(37) Goujon, A.; Varret, F.; Escax, V.; Bleuzen A.; Verdaguer, M. *Polyhedron*, **2001**, *20*, 1339.
(38) Bleuzen A.; Lomenech, C.; Dolbecq, A.; Villain, F.; Goujon, A.; Roubeau, O.; Nogues, M.; Varret, F.; Baudelet, F.; Dartyge, E.; Giorgetti, C.; Gallet, J.-J.; Cartier dit Moulin, C.; Verdaguer, M. *Mol. Cryst. Liq. Cryst.*, **1999**, *335*, 253.
(39) Goujon, A.; Roubeau, O.; Varret, F.; Dolbecq, A.; Bleuzen A.; Verdaguer, M. *Eur. Phys. J. B*, **2000**, *14*, 115.
(40) Goujon, A.; Varret, F.; Escax, V.; Bleuzen A.; Verdaguer, M. *Polyhedron*, **2001**, *20*, 1347.
(41) Cartier dit Moulin, C.; Champion, G.; Cafun, J.-D.; Arrio, M.-A.; Bleuzen, A. *Angew. Chem., Int. Ed.*, **2007**, *46*, 1287.
(42) Escax, V.; Bleuzen, A.; Itié, J. P.; Munsch, P.; Varret, F.; Verdaguer, M. *J. Phys. Chem. B*, **2003**, *107*, 4763.
(43) Shimamoto, N.; Ohkoshi, S.; Sato, O.; Hashimoto, K. *Mol. Cryst. Liq. Cryst.*, **2000**, *344*, 95.
(44) Gawali-Salunke, S.; Varret, F.; Maurin, I.; Enachescu, C.; Malarova, M.; Boukheddaden, K.; Codjovi, E.; Tokoro, H. Ohkoshi, S.-i.; Hashimoto, K. *J. Phys. Chem. B*, **2005**, *109*, 8251.
(45) Le Bris, R.; Cafun, J.-D.; Mathonière, C.; Bleuzen A.; Létard, J.-F. *New J. Chem.*, **2009**, *33*, 1255.
(46) Yokoyama, T.; Ohta, T.; Sato, O.; Hashimoto, K. *Phys. Rev. B*, **1998**, *58*, 8257.

(47) Bleuzen, A.; Escax, V.; Ferrier, A.; Villain, F.; Verdaguer, M.; Münsch, P.; Itié, J.-P. *Angew. Chem., Int. Ed.*, **2004**, *43*, 3728.
(48) Cartier dit Moulin, C.; Villain, F.; Bleuzen, A.; Arrio, M.-A.; Sainctavit, P.; Lomenech, C.; Escax, V.; Baudelet, F.; Dartyge, E.; Gallet, J.-J.; Verdaguer, M. *J. Am. Chem. Soc.*, **2000**, *122*, 6653.
(49) Champion, G.; Escax, V. ; Cartier dit Moulin, C.; Bleuzen, A.; Villain, F.; Baudelet, E.; Dartyge, F.; Verdaguer, M. *J. Am. Chem. Soc.*, **2001**, *123*, 12544.
(50) Yokoyama, T.; Kiguchi, M.; Ohta, T.; Sato, O.; Einaga, Y.; Hashimoto, K. *Phys. Rev. B*, **1999**, *60*, 9340.
(51) Dujardin, E.; Ferlay, S.; Phan, X.; Desplanches, C.; Cartier dit Moulin, C.; Sainctavit, P.; Baudelet, F.; Dartyge, E.; Veillet, P.; Verdaguer, M. *J. Am. Chem. Soc.*, **1998**, *120*, 11347.
(52) Bernhardt, P. V.; Martinez, M. *Inorg. Chem.*, **1999**, *38*, 424.
(53) Hester, R. E.; Nour, E. M. *J. Chem. Soc., Dalton Trans.*, **1981**, 939.
(54) Bernhardt, P. V.; Macpherson, B. P.; Martinez, M. *J. Chem. Soc., Dalton Trans.*, **2002**, 1435.
(55) Vogler, A.; Kunkely, H.; *Ber. Bunsenges. physik. Chem.*, **1975**, *79*, 301.
(56) Shu-zhong, Z.; Xiao-yuan, C.; Qing-jin, C. M.; Wei, X.; *Synth. React. Inorg. Met. Org. Chem.*, **1996**, *26*, 277.
(57) Berlinguette, C. P.; Dragulescu-Andrasi, A.; Sieber, A.; Galán-Mascarós, J. R.; Güdel, H.-U.; Achim, C.; Dunbar, K. R. *J. Am. Chem. Soc.*, **2004**, *126*, 6222.
(58) Berlinguette, C. P.; Dragulescu-Andrasi, A.; Sieber, A.; Güdel, H.-U.; Achim, C.; Dunbar, K. R. *J. Am. Chem. Soc.*, **2005**, *127*, 6766.
(59) Funck, K. E.; Prosvirin, A. V.; Mathonière, C.; Clérac, R.; Dunbar, K. R. *Inorg. Chem.*, **2011**, *50*, 2782.
(60) Li, D.; Clérac, R.; Roubeau, O.; Harté, E.; Mathonière, C.; Le Bris, R.; Holmes, S. M. *J. Am. Chem. Soc.*, **2008**, *130*, 252.
(61) Heinrich, J. L.; Berseth, P. A.; Long, J. R. *Chem. Commun.*, **1998**, 1231.
(62) Klausmeyer, K. K.; Rauchfuss, T. B.; Wilson, S. R. *Angew. Chem., Int. Ed.*, **1998**, *37*, 1694.
(63) Oshio, H.; Onodera, H.; Tamada, O.; Mizutani, H.; Kikichi, T.; Ito, T. *Chem.–Eur. J.*, **2000**, *6*, 2523.
(64) Zhang, Y.; Li, D.; Clérac, R.; Kalisz, M.; Mathonière, C.; Holmes, S. M. *Angew. Chem., Int. Ed.*, **2010**, *49*, 3752.
(65) Newton, G. N.; Nihei, M.; Oshio, H. *Eur. J Inorg. Chem.*, **2011**, *20*, 3031.
(66) Nihei, M.; Sekine, Y.; Suganami, N.; Oshio, H.; *Chemistry Chem. Lett.*, **2010**, 978.
(67) (a) Nihei, M.; Sekine, Y.; Suganami, N.; Nakazawa, K.; Nakao, A.; Nakao, H.; Murakami, Y.; Oshio, H. *J. Am. Chem. Soc.*, **2011**, *133*, 3592; (b) Kitagawa, Y.; Asaoka, M.; Miyagi, K.; Matsui, T.; Nihei, M.; Oshio, H.; Okumura, M.; Nakano, M. *Inorg. Chem. Front.*, **2015**, *2*, 771.
(68) Sekine, Y.; Nihei, M.; Kumai, R.; Nakao, H.; Murakami, Y.; Oshio, H. *Inorg. Chem. Front.*, **2014**, *1*, 540.

(69) Y Sekine, Y.; Nihei, M.; Kumai, R.; Nakao, H.; Murakami, Y.; Oshio, H. *Chem. Commun.*, **2014**, *50*, 4050.
(70) Siretanu, D.; Li, D.; Buisson, L.; Bassani, D. M.; Holmes, S. M.; Mathonière, C.; Clérac, R. *Chem.-Eur. J.*, **2011**, *17*, 11704.
(71) Li, D.; Parkin, S.; Wang, G.; Yee, G. T.; Prosvirin, A. V.; Holmes, S. M. *Inorg. Chem.*, **2005**, *44*, 4903.
(72) Sekine, Y.; Nihei, M.; Oshio, H. *Chem. Lett.*, **2014**, 1029.
(73) Zhang, Y.-Z.; Ferko, P.; Siretanu, D.; Ababei, R.; Rath, N. P.; Shaw, M. J.; Clérac, R.; Mathonière, C.; Holmes, S. M. *J. Am. Chem. Soc.*, **2014**, *136*, 16854.
(74) (a) Cao, L.; Tao, J.; Gao, Q.; Liu, T.; Xia, Z.; Li, D. *Chem. Commun*., **2014**, *50*, 1665; (b) Zheng, C.; Xu, J.; Yang, Z.; Tao, J.; Li, D. *Inorg. Chem*., 10.1021/acs.inorgchem.5b02272
(75) Mercurol, J.; Li, Y.; Pardo, E.; Risset, O.; Seuleiman, M.; Rousselière, H.; Lescouëzec, R.; Julve, M. *Chem. Commun.*, **2010**, *46*, 8995.
(76) Mondal, A.; Li, Y.; Seuleiman, M.; Julve, M.; Toupet, L.; Buron-Le Cointe, M.; Lescouëzec, R. *J. Am. Chem. Soc.* **2013**, *135*, 1653.
(77) Bernhardt, P. V.; Macpherson, B. P.; Martinez, M. *Inorg. Chem.*, **2000**, *39*, 5203.
(78) Macpherson, B. P.; Bernhardt, P. V.; Hauser, A.; Pagès, S.; Vauthey, E. *Inorg. Chem.*, **2005**, *44*, 5530.
(79) Jeon, I.-R.; Calancea, S.; Panja, A.; Piñero Cruz, D. M.; Koumousi, E. S.; Dechambenoit, P.; Coulon, C.; Wattiaux, A.; Rosa, P.; Mathonière, C.; Clérac, R. *Chem. Sci*., **2013**, *4*, 2463.
(80) Mitsumoto, K.; Oshiro, E.; Nishikawa, H.; Shiga, T.; Yamamura, Y.; Saito, K.; Oshio, H. *Chem.–Eur. J.*, **2011**, *17*, 9612.
(81) Shiga, T.; Tetsuka, T.; Sakai, K.; Sekine, Y.; Nihei, M.; Newton, G. N.; Oshio, H. *Inorg. Chem.*, **2014**, *53*, 5899.
(82) Nihei, M.; Okamoto, Y.; Sekine, Y.; Hoshino, N.; Shiga, T.; Liu, I. P.-C.; Oshio, H. *Angew. Chem., Int. Ed.*, **2012**, *51*, 6361.
(83) Liu, T.; Dong, D.-P.; Kanegawa, S.; Kang, S.; Sato, O.; Shiota, Y.; Yoshizawa, K.; Hayami, S.; Wu, S.; He, C.; Duan, C.-Y. *Angew. Chem., Int. Ed.*, **2012**, *51*, 4367.
(84) Liu, T.; Zhang, Y.-J.; Kanegawa, S.; Kang, S.; Sato, O. *Angew. Chem., Int. Ed.*, **2010**, *49*, 8645.
(85) (a) Liu, T.; Zhang, Y.-J.; Kanegawa, S.; Kang, S.; Sato, O. *J. Am. Chem. Soc.*, **2010**, *132*, 8250; (b) Yang, J.; Zhou, L.; Cheng, J.; Hu, Z.; Kuo, C.; Pao, C.-W.; Jang, L.; Lee, J.-F.; Dai, J.; Zhang, S.; Feng, S.; Kong, P.; Yuan, Z.; Yuan, J.; Uwatoko, Y.; Liu, T.; Jin, C.; Long, Y. *Inorg. Chem.*, **2015**, *54*, 6433.
(86) Coulon, C.; Miyasaka, H. ; Clérac, R. *Struct. Bond.*, **2006**, *122*, 163; Coulon, C.; Pianet, V.; Urdampilleta, M.; Clérac, R. *Struct. Bond.*, **2015**, *164*, 143.
(87) Dong, D.-P.; Liu, T.; Kanegawa, S.; Kang, S.; Sato, O.; He, C.; Duan, C.-Y. *Angew. Chem., Int. Ed.*, **2012**, *51*, 5119.
(88) Hoshino, N.; Iijima, F.; Newton, G. N.; Yoshida, N.; Shiga, T.; Nojiri, H.; Nakao, A.; Kumai, R.; Murakami, Y.; Oshio, H. *Nat. Chem.*, **2012**, *4*, 921.

(89) Baker, M. L.; Kitagawa, Y.; Nakamura, T.; Tazoe, K.; Narumi, Y.; Kotani, Y.; F. Iijima, F.; Newton, G. N.; Okumura, M.; Oshio, H.; Nojiri, H. *Inorg. Chem.*, **2013**, *52*, 13956.
(90) Slichter, C. P.; Drickamer, H. G. *J. Chem. Phys*., **1972**, *56*, 2142.

Chapter II

Towards the miniaturization of the 3-D network of Prussian Blue Analogue: The {Fe(μ-CN)Co} elementary unit

Table of Contents for Chapter II:

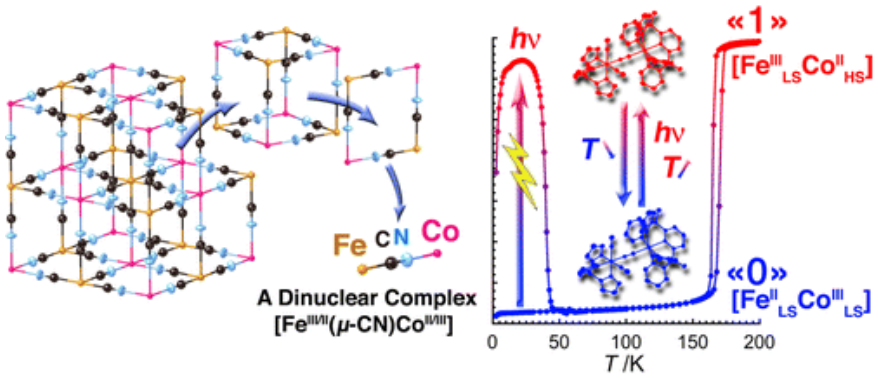

II.1 Introduction

The discovery in 1996 of the first photoswitchable Prussian Blue analogue,[1] $K_{0.2}Co_{1.4}[Fe(CN)_6]\bullet 6.9H_2O$, opened a new field of research in material science. The versatile molecule-based chemistry used to synthesize this Prussian Blue system motivated chemists to obtain a family of three dimensional (3D) cyanido-bridged Co/Fe networks with different electronic behaviors tunable by external stimuli such as light and/or temperature.[2–7] The origin of the remarkable physical properties of these materials is found in the elementary {Fe(μ-CN)Co} moiety that exhibits a reversible thermally induced and photoinduced metal-to-metal electron transfer. As a consequence, this constitutive bimetallic pair can adopt two different valence states: $\{Fe^{II}_{LS}(\mu\text{-}CN)Co^{III}_{LS}\}$ and $\{Fe^{III}_{LS}(\mu\text{-}CN)Co^{II}_{HS}\}$ being diamagnetic and paramagnetic respectively (LS: low spin; HS: high spin). Recently, both thermally and light induced electron transfer has been reported in two dimensional (2D) and one-dimensional (1D) cyanido-bridged Co/Fe materials containing {Fe(μ-CN)Co} motifs,[8–10] but so far most of the reported synthetic work in this field has been oriented toward the design of molecular complexes, able to mimic the physical properties of the 3D Prussian Blue compounds.[11-19] The last decade, several groups around the world designed, isolated and studied molecular analogues (fragments of various geometry) of Prussian blue by rational selection of various capping ligands, which "decorated" the metal centers and stopped the polymerization.

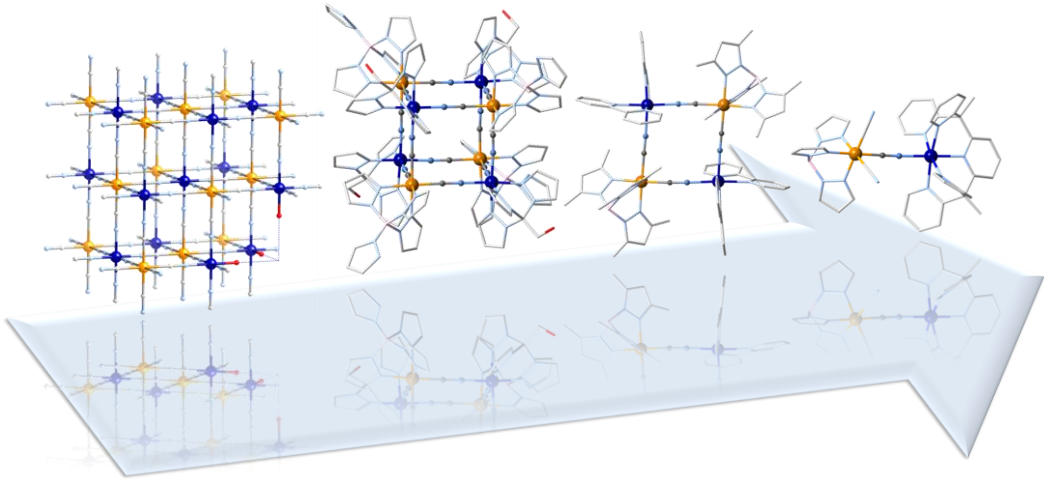

Scheme 1. Scheme illustrating the different Fe/Co systems exhibiting electron transfer properties: from the 3D network of the Fe/Co Prussian Blue Analogue in 1996, to its unit cell, an Fe/Co cube, to a face of the a cubic unit cell, an Fe/Co square and finally to the fundamental unit of the previous mentioned compounds, an Fe/Co pair, in 2013.

The preparation of these discrete molecules, rather than extended networks, is of fundamental and technological interests. The high dimensionality of bimetallic assemblies of Prussian blue analogues and their non-stoichiometric lattice defects make difficult the systematic structure-property correlation investigations. Moreover, the reduced solubility of

these inorganic 3D polymers limits their potential applications as future molecule-based electronic devices and requires elaboration of synthetic strategies towards nanoparticles, to increase their solubility and to create multi-functionalities at nano-scale.[20]

Following this emerging research field, the ultimate challenge was to design the smallest molecule being able to switch thermally and optically between states using a metal-to-metal electron transfer through a bridging cyanido ligand, in other words a simple dinuclear [Fe–CN–Co] complex. The simplicity of a dinuclear system will allow systematic studies of electron transfer properties depending on the structure and the redox potential of each metal-containing building block, and consequently lead to developing systems with optimized switching properties at a molecular level. In the recent past, a series of dinuclear complexes involving $\{Fe^{III}(\mu\text{-}CN)Co^{III}\}$ and $\{Fe^{II}(\mu\text{-}CN)Co^{III}\}$ motifs were reported in respect of their redox and catalytic properties. [21-23]

In 2013, our group reported a new dinuclear complex, $[\{(BBP)Fe(CN)_3\}\{Co(PY5Me_2)\}]$ ($PY5Me_2$ = 2,6-bis(1,1-bis(2-pyridyl)ethyl)pyridine; H_2BBP = 2,6-bis(benzimidazol-2-yl)pyridine) that was described as the smallest cyanido-bridged Fe/Co unit with switchable optical and magnetic properties depending on its physical state.[24] In solid state, it is displaying a thermally induced spin crossover at the Co^{II} ion confirmed by single-crystal X-ray diffraction and magnetic measurements, while an intramolecular electron transfer triggered by protonation was revealed in solution by extended studies with cyclic voltammetry, NMR and UV-vis spectroscopies (see Chapter I).

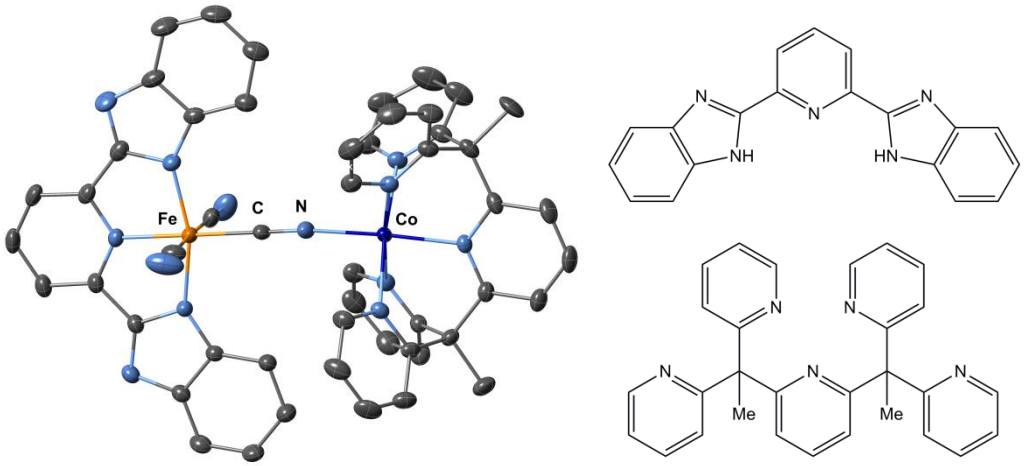

Figure II-1. (Left) ORTEP-type view of the molecular structure of $[\{(BBP)Fe(CN)_3\}\{Co(PY5Me_2)\}]$ at 370 K.[24] Thermal ellipsoids are depicted at the 30% probability level. All lattice solvents and hydrogen atoms are omitted for clarity. Fe, Co, N, and C atoms are indicated in orange, dark blue, light blue and gray, respectively; (top, right) The tridentate capping ligand 2,6-bis(benzimidazol-2-yl)pyridine ligand (H_2BBP) and (bottom, right) the pentadentate capping ligand 2,6-bis(1,1-di(pyridin-2-yl)ethyl)pyridine ($PY5Me_2$).

To direct the rational formation of this dinuclear cyanido-bridged complex (Figure II-1, left), the coordination chemistry of preformed molecular precursors was exploited. This

synthetic approach includes the use of solvated metal cations with cyanido-metallate ions. In order to prevent polymerization, it was necessary to employ capping ligands, which dictate the number and relative position of the available binding sites on the metal ions. In the case of compound [{(BBP)Fe(CN)$_3$}{Co(PY5Me$_2$)}],[24] the pentadentate ligand, 2,6-bis(1,1-di(pyridin-2-yl)ethyl)pyridine (PY5Me$_2$),[25] was chosen as a capping ligand in order to leave only one accessible site on the Co^{II} precursor for the cyanido bridge. For the Fe^{III} precursor, the tridentate planar 2,6-bis(benzimidazol-2-yl)pyridine ligand (H$_2$BBP)[26] was selected to allow free cyanide groups in a meridional configuration. Although the success of this synthetic approach, the electron transfer process was found to be triggered by protonation of the pair in solution. Now the question arises of how to induce the electron transfer phenomenon by temperature and/or light in solid state within a Fe/Co dinuclear system.

II.2 Synthesis, Characterization and Physical Properties of a New Dinuclear {Fe(μ-CN)Co} Complex Mimicking the Properties of the Prussian Blues

II.2.1 Synthetic Strategy

In order to develop new Fe/Co pairs with electron transfer properties in solid state, the evaluation of the protonation effect in compound [{(BBP)Fe(CN)$_3$}{Co(PY5Me$_2$)}][24] is required. Thus, the electrochemical studies previously performed in both the pair and its metal ion precursors upon controlled acid addition were deeply analyzed. We remind that the electron transfer phenomenon is directly dependent on the redox potential difference between the donor D+ / D (Co(II) moiety) and the acceptor A / A- (Fe(III) moiety) species ($\Delta E_{1/2} = E_{D+/D} - E_{A-/A}$). Two cases are possible when $\Delta E_{1/2} > 0$: when this difference is large, even at low temperature, no electron transfer occurs (Figure II-2, case I). On the other hand, when $\Delta E_{1/2}$ is of the order of magnitude of the thermal energy, an electron transfer can be observed by a decrease of temperature (Figure II-2, case II). When $\Delta E_{1/2} < 0$, an electron transfer is occurring at room temperature (Figure II-2, case III). Thus, the coordination environment of the species (donor / acceptor) must be perfectly controlled and tuned in order to adjust the relative position of their redox potential.

Figure II-3 shows that the ligand protonation induces a marked increase of the redox potential for the Fe^{III} precursor (donor site) (Figure II-3, top, blue and light blue cyclic voltammograms), which led finally to a significant decrease of the redox potential difference between the Fe and Co precursors of the pair [{(BBP)Fe(CN)$_3$}{Co(PY5Me$_2$)}][24] (Figure II-3, top, orange, blue and light blue cyclic voltammograms). This decrease was efficient to trigger a spontaneous electron transfer within the dinuclear complex and the stabilization of the diamagnetic pair in solution at room temperature.[24]

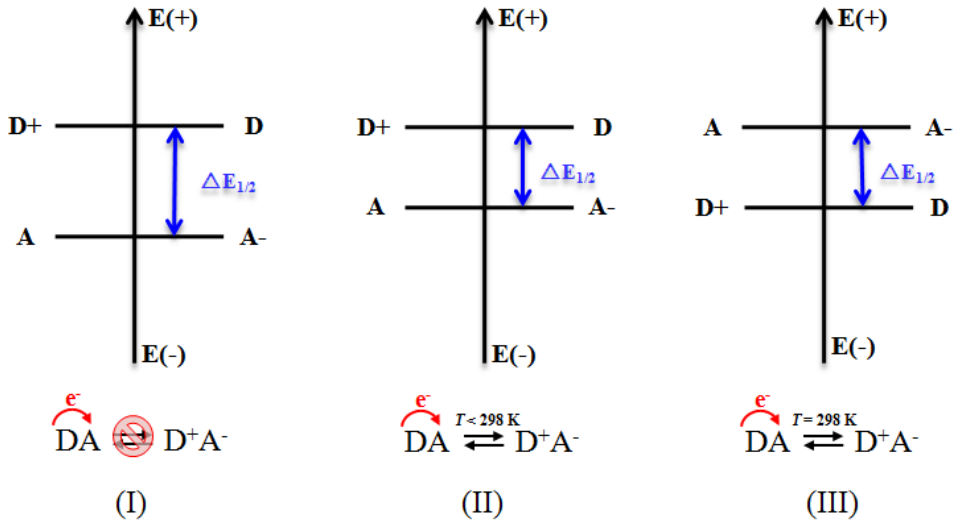

Figure II-2. Electron transfer originating from the relative redox potentials value of the donor D and the acceptor A (see text).

This result motivated us to design new dinuclear [FeCo] complexes exhibiting both thermally and light induced electron transfer by altering the redox potentials of the molecular precursors, as done by Bernhardt,[23] Oshio,[16] and Mallah[27] in mixed-valence compounds. Starting with the same Co^{II} molecular module, $\{Co^{II}(PY5Me_2)\}^{2+}$, we selected the $\{(Tp)Fe^{III}(CN)_3\}^{-}$ building block (Tp = hydridotris(pyrazol-1-yl)borate, (Figure II-3, bottom), which can be reduced in $\{(Tp)Fe^{II}(CN)_3\}^{2-}$ around −0.81 V (vs Fc^{+}/Fc), a redox potential that falls between those previously reported for $\{(BBP)Fe(CN)_3\}^{2-}$ and $\{(H_2BBP)Fe(CN)_3\}$ (−1.1 vs −0.46 V, respectively); which led to paramagnetic $\{Fe^{III}_{LS}(\mu\text{-}CN)Co^{II}_{HS}\}$ and diamagnetic $\{Fe^{II}_{LS}(\mu\text{-}CN)Co^{III}_{LS}\}$ complexes, respectively (Figure II-3, top).[24] The choice of acetonitrile as solvent for the electrochemistry experiments was based on the Co^{II} precursor and the fact that the coordination of this solvent on the Co^{II} ion is mimicking the –CN environment observed in the dinuclear Co/Fe cyanido-bridged complexes. However, the cyclic voltammogram of the $(Bu_4N)_2[(BBP)Fe^{III}(CN)_3]$ (blue) is presented in DMSO solvent while in MeCN solvent, it gives an irreversible redox wave at -0.92 V.

The room-temperature equimolar reaction of $[Co^{II}(PY5Me_2)(H_2O)](CF_3SO_3)_2$ with $(Bu_4N)[(Tp)Fe^{III}(CN)_3]$ in DMF gives a dark red solution. Slow diffusion of diethyl ether vapor into this solution affords orange needles of $[\{(Tp)Fe(CN)_3\}\{Co(PY5Me_2)\}](CF_3SO_3)$•2DMF (**1**•2DMF; 10% yield).[28] The low yield of the reaction was overcome by preparing the Co precursor in situ by reacting equimolar quantity of $PY5Me_2$ and $Co^{II}(CF_3SO_3)_2$ with $(Bu_4N)[(Tp)Fe^{III}(CN)_3]$ in DMF. Slow diffusion of diethyl ether vapor into the dark red solution affords orange needles of $[\{(Tp)Fe(CN)_3\}\{Co(PY5Me_2)\}](CF_3SO_3)$•2DMF (**1**•2DMF) in 70% yield.[28] The identity of compound **1**•2DMF was revealed by IR spectroscopy and Single-crystal X-ray diffraction (See section II.2.2).

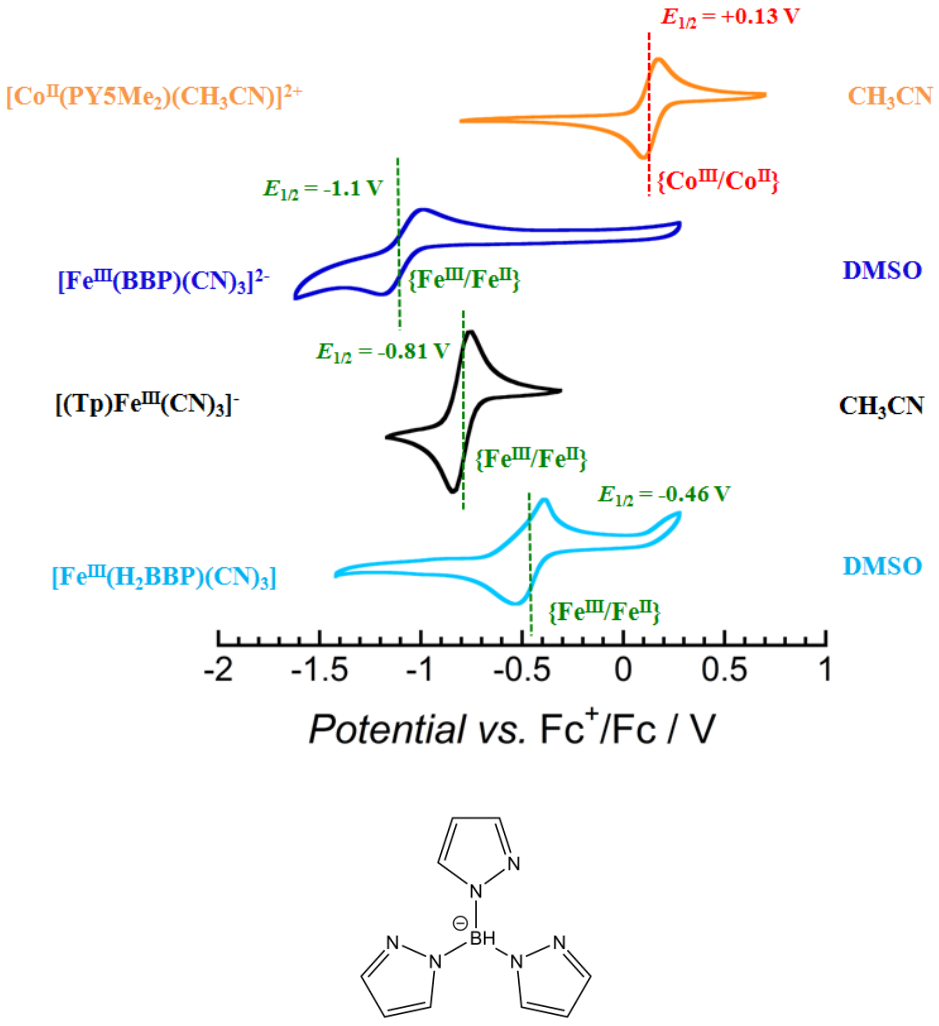

Figure II-3. (Top) Cyclic voltammograms of $(Bu_4N)_2[(BBP)Fe^{III}(CN)_3]$ (blue) and $[(H_2BBP)Fe^{III}(CN)_3]$ (light blue) in DMSO solution (~1 mM), $[(PY5Me_2)Co^{II}(MeCN)](BF_4)_2$ (orange) and $(Bu_4N)[(Tp)Fe^{III}(CN)_3]$ (black) in MeCN solutions (~1 mM), collected in a 0.1 M solution of $Bu_4N(BF_4)$ in DMSO and MeCN respectively, with a scan rate of 0.1 V s^{-1}. Potentials were referenced to the $[Cp_2Fe]^{1+/0}$ couple, (bottom) scheme of the anion of the tridentate capping ligand hydridotris(pyrazol-1-yl)borate (Tp^-).

II.2.2 Characterization of $[\{(Tp)Fe(CN)_3\}\{Co(PY5Me_2)\}](CF_3SO_3)$•2DMF (1•2DMF)

The stretching bands specific to cyanide groups ($\tilde{\nu}_{CN}$) are sensitive to their coordination mode (bridging or terminal) and the oxidation states of the coordinated metal ions.[31] The FT-IR spectrum of the tricyanido-metallate precursor, $(Bu_4N)[(Tp)Fe^{III}(CN)_3]$, exhibits one medium $\tilde{\nu}_{CN}$ stretching at 2117 cm^{-1} and another one of weak intensity corresponding to $\tilde{\nu}_{BH}$ at 2511 cm^{-1}. The stretching band of the cyanide groups in **1**•2DMF (Figure II-4, red color spectrum) at room temperature is shifted to higher energies in comparison to its iron precursor and splitted into two bands: one at 2155 cm^{-1} characteristic of bridging cyanides within $\{Fe^{III}_{LS}(\mu\text{-}CN)Co^{II}_{HS}\}$ units and a second one at 2120 cm^{-1} assigned to terminal cyanides. The

energy of $\tilde{\nu}_{BH}$ stretching band remained unchanged (2512 cm^{-1}) suggesting that the electronic state of the Fe^{III} ion remained the same as the tricyanido-metallate precursor. The FT-IR spectra of the final compound contains a strong C=O band (1674 cm^{-1}) suggesting the presence of co-crystallized DMF molecules.

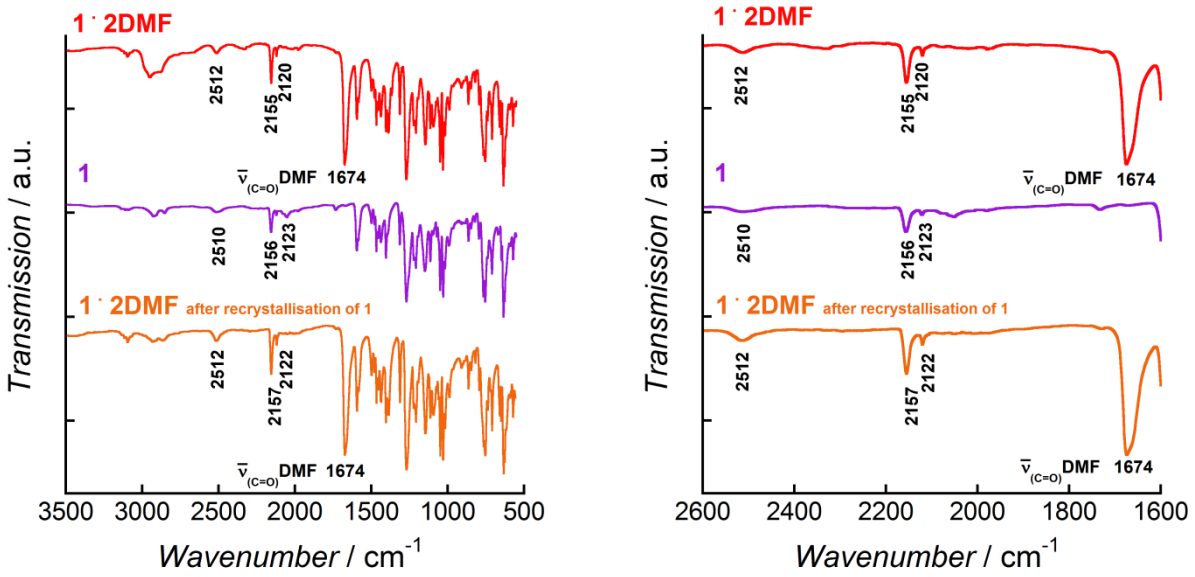

Figure II-4. The FT-IR spectra of **1**•2DMF (left, red), **1** (left, purple) and **1**•2DMF after recrystallization of **1** from a solution of DMF/Et_2O (left, orange), a portion of all spectra between 2600 and 1600 cm^{-1} for the comparison of **1**•2DMF and **1** (right) at 298 K.

Single-crystal X-ray diffraction studies at 180 and 90 K reveal that **1**•2DMF crystallizes in the orthorhombic *Pnma* space group (Figures II-5 and II-6, and Table II-1). In the cationic $[\{(Tp)Fe(CN)_3\}\{Co(PY5Me_2)\}]^+$ complex that resides on a mirror plane, the Fe and Co metal ions are hexacoordinated with distorted octahedral geometries (Table II-2), and their separation (Fe···Co) is 5.063(1) Å at 180 K, which is slightly longer than 4.987(2) Å found at 90 K.

At 180 K, the two metal centers are linked by one, almost linear, cyanide ligand (Fe1−C22−N8 and C22−N8−Co1 angles are 177.6(5)° and 170.9(4)°, respectively, see Table II-2) to form a [FeCo] pair (Figure II-5, top). The Fe site bears two terminal cyanide ligands, and its coordination sphere is completed by three N atoms from the Tp^- ligand in facial configuration. On the other hand, the Co center completes its coordination sphere with the five N donor atoms from the $PY5Me_2$ ligand. The average Fe−C and Fe−N bonds are 1.947(5) and 1.975(4) Å, respectively, while the average Co− N_{NC} and Co−N_{py} bonds are 2.047(5) and 2.135(3) Å, respectively (Table II-2). In addition to the bond valence analysis and the charge compensation, these structural features confirm the presence of LS Fe^{III} and HS Co^{II} metal ions in **1**•2DMF leading to a paramagnetic dinuclear complex at 180 K.

At 90 K (Figure II-5, down), the cyanide bridge between Fe and Co centers is slightly more linear, with Fe1−C22−N8 and C22−N8−Co1 angles of 178.3(8)° and 171.9(8)°, respectively (Table II-2). The average Co−N_{NC} and Co−N_{py} bond distances are notably shorter than those

observed at 180 K, with values of 1.968(8) and 2.080(6) Å, respectively. However, these bond distances are too long for only diamagnetic Co^{III} ions,[14–19] but are in good agreement with a mixture of both paramagnetic $[Fe^{III}_{LS}(\mu\text{-CN})Co^{II}_{HS}]$ and diamagnetic $[Fe^{II}_{LS}(\mu\text{-CN})Co^{III}_{LS}]$ dinuclear species with an approximate 1:1 ratio, as confirmed by the magnetic measurements (vide infra).

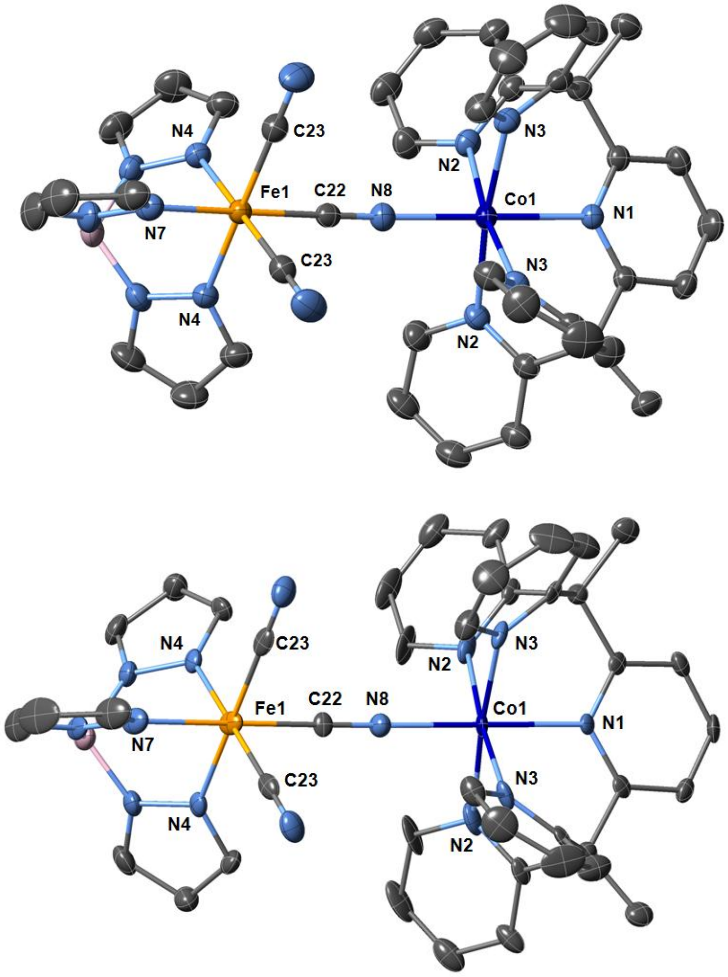

Figure II-5. ORTEP-type view of the cationic complex in **1**•2DMF at 180 K (top) and at 90 K (bottom). Thermal ellipsoids are depicted at the 30% probability level. All anions, lattice solvents, and hydrogen atoms are omitted for clarity. Fe, Co, N, C, and B atoms are indicated in orange, dark blue, light blue, gray, and pink, respectively.

Table II-1. Crystallographic data for **1**•2DMF at 180 and 90 K.

Compound	**1**•2DMF	
Formula	$C_{48}H_{49}BCoF_3FeN_{16}O_5S$	
FW / g·mol^{-1}	1144.68	
Crystal color	Orange	
Crystal size / mm	0.14 x 0.04 x 0.02	
Crystal system	orthorhombic	
Space group	Pnma	
Temperature / K	180	90
***a* / Å**	18.843(3)	18.6572(9)
***b* / Å**	15.396(2)	15.2008(8)
***c* / Å**	17.670(3)	17.5964(9)
***V* / Å^3**	5126.3(14)	4990.4(4)
Z	4	
d_{calc}	1.483	1.524
μ / mm^{-1}	0.722	0.742
Absorp. Correction	SADABS	
$\theta_{min} - \theta_{max}$	1.754° - 26.083°	1.770° - 25.415 °
Refl. Coll. / unique	137247 / 5262	47235 / 4772
Completeness to 2θ	0.999	0.997
R_{int}	0.0451	0.0746
Refined param./restr.	395 / 0	405 / 60
[a]R_1 ($I > 2\sigma(I)$)	0.0595	0.0992
[b]wR_2 (all data)	0.1737	0.2431
Goodness-of-fit	1.069	1.228

[a] $R_1 = \Sigma||F_0|-|F_C||/\Sigma|F_0|$, [b] $wR_2 = [\Sigma w(F_0^2-F_C^2)^2/\Sigma w(F_0^2)^2]^{1/2}$

Table II-2. Selected bond lengths, distances [Å] and angles [°] for **1**•2DMF at 180 K and 90 K.

Compound	**1**•2DMF	
Temperature / K	180	90
Average (Fe-C)	1.947(5)	1.920(8)
Fe1-C23	1.932(4)	1.942(8)
Fe1-C22	1.982(5)	1.875(9)
Average (Fe-N)	1.975(4)	1.933(7)
Fe1-N4	1.974(3)	1.933(6)
Fe1-N7	1.978(5)	1.933(9)
Co-N_{NC}	2.047(5)	1.968(8)
Average (Co-N_{py})	2.135(3)	2.080(6)
Co1-N1	2.145(3)	2.047(7)
Co1-N2	2.111(4)	2.081(6)
Co1-N3	2.138(3)	2.079(6)
Fe1-C22-N8	177.6(5)	178.3(8)
C22-N8-Co1	170.9(4)	171.9(8)
Fe1…Co1	5.063(1)	4.987(2)

The charge of the complex is compensated by one disordered $CF_3SO_3^-$ anion located on an inversion center (Figure II-6). As a consequence, the CF_3 and SO_3 parts occupy almost the same crystallographic position and are not distinguishable. The asymmetric unit also contains two disordered dimethylformamide (DMF) molecules per formula unit. At 180 K, one DMF was found to be disordered over two positions with equal occupancies whereas the second DMF is disordered over four positions with equal occupancies. At 90 K, both DMF molecules were found to be disordered over four positions. It is worth mentioning that the positional disorder of $CF_3SO_3^-$ anion and DMF molecules is also present when solving the crystal structure in the lower symmetry space groups, P-1 and P1, as well as with larger unit cells. The packing of the molecular components occurs via weak interactions (Figure II-7). The shortest contacts between the complex and the DMF molecules and triflate anion were found between O5 and C4 (3.19 Å), O4B and C14 (3.19 Å), and O3 and C12 (3.09 Å). Each of the oxygen atoms involved in these weak interactions have a partial occupancy due to the disorder (1/2 for O3 and O5 and 1/4 for O4B).

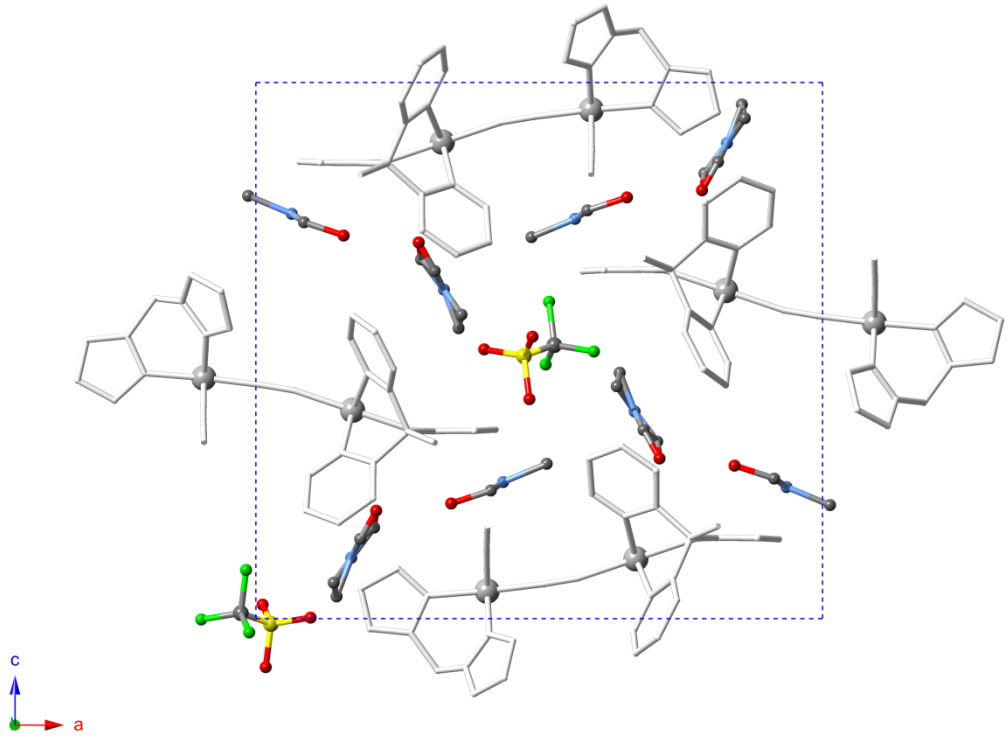

Figure II-6. Projection view of the crystal structure of **1**•2DMF at 180 K showing the packing of the cationic complexes, the $CF_3SO_3^-$ anions and the lattice DMF molecules in the (*ac*) plane. All the atoms of the cationic complexes are in light grey color for clarity. The $CF_3SO_3^-$ anions, the lattice DMF molecules and the metal centers are visualized in balls and sticks for clarity. N, C, S, O and F atoms are indicated in light blue, dark grey, yellow, red and green, respectively.

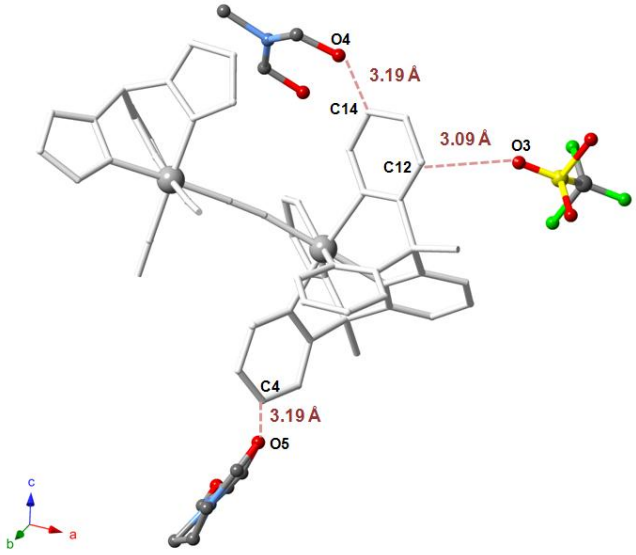

Figure II-7. View of the crystal structure of **1**•2DMF at 180 K showing the weak interactions between the cationic complex, the $CF_3SO_3^-$ anion and the lattice DMF molecules. All the atoms of the cationic complex are in light grey color for clarity. N, C, S, O and F atoms are indicated in light blue, dark grey, yellow, red and green, respectively.

II.2.3 Magnetic measurements of 1•2DMF

Before studying the magnetic properties of compound **1**•2DMF, the presence and the thermal stability of these two DMF molecules in the lattice of **1**•2DMF, were confirmed by thermogravimetric analysis (TGA). The measurements were carried out using freshly filtrated crystals of the sample, in air atmosphere at heating rate of 5 °C /min. The weight loss of 13 ± 1% in the 60−200 °C temperature range corresponds well to the loss of two DMF molecules (Figure II-8; at higher temperatures until 500 °C, **1**•2DMF gradually decomposes).

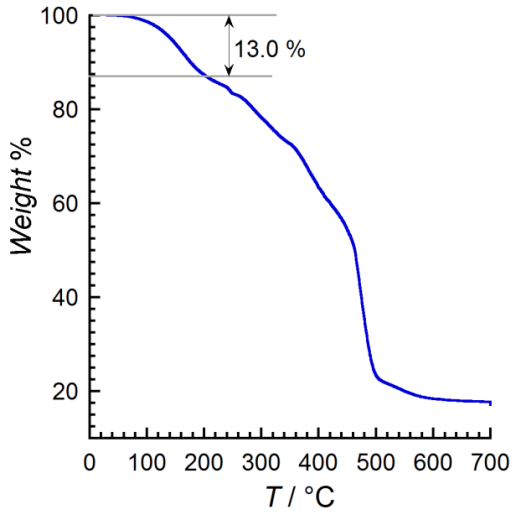

Figure II-8. TGA of **1**•2DMF in an air atmosphere at a heating rate of 5 °C / min.

As **1**•2DMF loses its DMF molecules rapidly, the magnetic susceptibility measurements were performed on fresh crystals kept in their mother liquor (DMF/Et_2O; Figure II-9) between 1.8 and 250 K. At 250 K, the χT product is 3.43 cm^3 K mol^{-1}, which corresponds to isolated magnetic centers, i.e., one LS Fe^{III} (S = 1/2) and one HS Co^{II} (S = 3/2) in octahedral coordination environments. Indeed, this value is close to the value measured for the related dinuclear [{(BBP)Fe$(CN)_3$}{Co$(PY5Me_2)$}] complex (3.1 cm^3 K mol^{-1}).[24] Lowering the temperature, the χT product is constant down to 165 K and then decreases sharply in two steps (at 161 and 152 K), until it reaches and stabilizes around 1.7 cm^3 K mol^{-1} at 90 K. As already suggested by single-crystal X-ray data (vide supra), this χT value corresponds to exactly half the χT product measured above 165 K, confirming, as shown by the crystal structure at 90 K (Table II-2), that, in a bulk sample, only 50% of the paramagnetic [Fe^{III}_{LS}(μ-CN)Co^{II}_{HS}] pairs convert into diamagnetic [Fe^{II}_{LS}(μ-CN)Co^{III}_{LS}] ones. As the temperature decreases below 70 K, the χT product decreases again to reach 0.91 cm^3 K mol^{-1} at 1.8 K, as expected in the presence of the combined effect of Co^{II} and Fe^{III} spin−orbit couplings[32,33] and possible antiferromagnetic coupling between LS Fe^{III} and HS Co^{II} magnetic centers through the cyanido bridge.[3] When the temperature is increasing up to 130 K, the χT product increases, following the same variation as seen in the cooling mode. Above 130 K, the two-step intramolecular electron transfer is observed (at 161 and 171 K) with the occurrence of a thermal hysteresis of about 10 K (0.67 K/min), indicating the presence of a first-order phase transition. The reversibility of the electron transfer is confirmed above 175 K when the magnetic susceptibility recovers its initial values.

As previously observed in related systems,[8,10,11b,19] the lattice solvents can strongly influence the electron-transfer properties of a compound. This fact encourage us to study the properties not only of compound **1**•2DMF, but as well as its desolvated form, **1**.

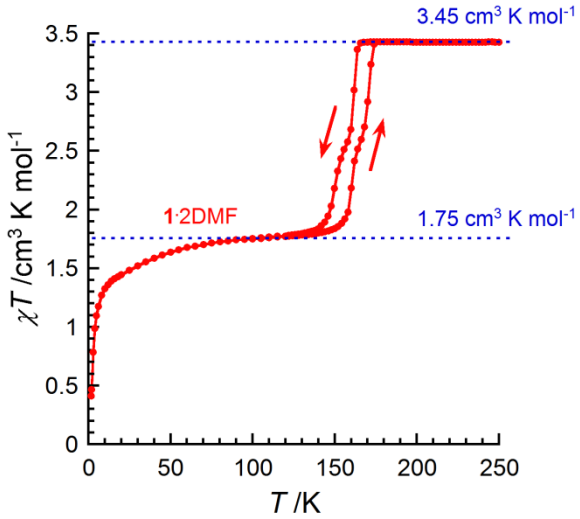

Figure II-9. χT versus T plots for polycrystalline samples of **1**•2DMF (in red, from 250 to 100 K at 1 T and below 100 K at 0.1 T) at 0.67 K/min (the blue dashed lines are guides for the eyes).

II.2.4 Preparation and Characterization of [{(Tp)Fe(CN)$_3$}{Co(PY5Me$_2$)}](CF$_3$SO$_3$) (1)

The preparation of the desolvated form of compound **1**•2DMF was based on its stability at high temperatures, thus new TGA experiments were designed and performed (Figure II-10). In air atmosphere and at heating rate 1°C / min, **1**•2DMF warmed up to 200 °C, where the expected weight loss of two DMF molecules (in the 60−200 °C temperature range) was observed. Then, the compound was kept in this temperature for 8 h (480 min) and a small decomposition of 4% was observed, before it decomposes totally with increasing more the temperature.

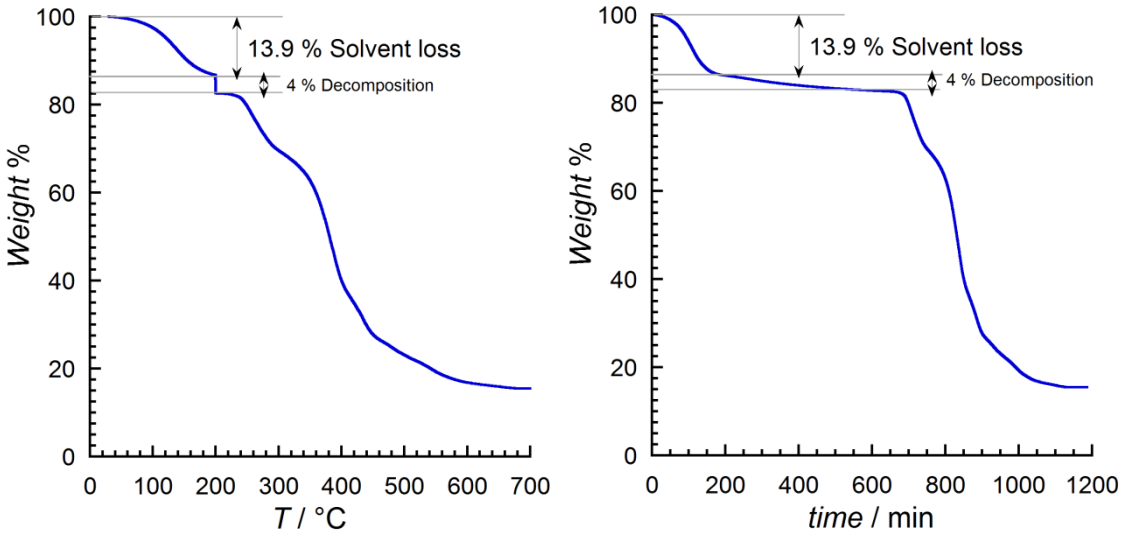

Figure II-10. TGA of **1**•2DMF in an air atmosphere at heating rate of 1 °C / min and as function of the temperature (left) and time (right).

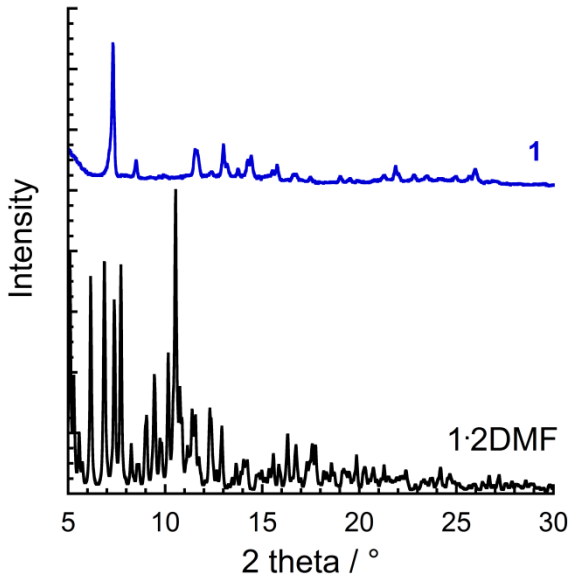

Figure II-11. Simulated powder diffraction pattern of **1**•2DMF at 180 K by Mercury version 3.3 (bottom) and powder diffraction pattern of **1** at 298 K (top).

To avoid any decomposition during the desolvation process, **1**•2DMF was successively sonicated in diethyl ether (30 min) and kept for 24 h under vacuum at 50 °C. Complete removal of the lattice DMF solvent was confirmed by the disappearance of the intense $\tilde{\nu}_{C=O}$ stretching absorption band at 1674 cm^{-1} in the solid-state IR spectrum at room temperature (Figure II-4, purple color spectrum). The rest of the spectrum is almost identical with the spectrum collected for **1**•2DMF (Figure II-4, red color spectrum). Unfortunately, based on powder X-ray diffraction, **1** is poorly crystalline, preventing its structure determination (Figure II-11). IR spectroscopy was also used to demonstrate that compound **1**•2DMF could be recovered, when **1** is re-dissolved in DMF and layered by Et_2O (Figure II-4, orange color spectrum).

However, the lattice DMF can be "gently", but only partially, removed by keeping **1**•2DMF in its mother liquor (DMF/Et_2O) for several days or weeks after crystallization. At a given temperature, different crystals of **1**•*n*(solv) ($n \leq 1.3$) display systematically smaller unit cells than **1**•2DMF as a consequence of DMF loss (Figures II-12 and II-13, Tables II-3 and II-4). The analysis of their crystal structures and bond distances reveals the occurrence of a partial or, in some cases (for low n numbers), a total thermally induced electron transfer. These observations confirm that **1**•2DMF can easily lose DMF molecules while maintaining the integrity of the dinuclear Fe/ Co complex and favoring the occurrence of a full electron transfer process.

Many crystals were measured but only two of them were selected in this work to illustrate our scientific conclusions. A first crystal (Crystal 1) was collected at 200 and 120 K (Figure II-12). The same orthorhombic *P*nma space group was found. As in **1**•2DMF, the $CF_3SO_3^-$ anion resides on an inversion center making impossible the distinction between CF_3 and SO_3 parts. The packing of the cationic and anionic parts is exactly the same as observed in **1**•2DMF. The unit cells are however significantly smaller than the comparable structures of **1**•2DMF at comparable temperatures. Disordered lattice solvent molecules are also present in the void space of the channels along the *a* axis, but their exact nature, localization and number of these molecules cannot be determined univocally based on the difference Fourier map. On the basis of the electronic density and void space volume calculated by PLATON, and assuming that only DMF molecules are present, the compound can be formulated as **1**•1.3DMF. Nevertheless, the exact nature and number of lattice solvent molecules must be taken with caution. At 200 K, the average Fe-C, Fe-N, Co-N_{py} and Co-N_{NC} bond distances are 1.988(5), 1.981(3), 2.122(3) and 2.046(5) Å respectively, suggesting that the crystal contains only paramagnetic $[Fe^{III}_{LS}(\mu\text{-CN})Co^{II}_{HS}]$ complexes (Table II-4). At 120 K, these average bond distances are 1.884(4), 1.947(4), 2.086(3) and 2.020(4) Å respectively, revealing the presence of a statistical mixture of paramagnetic $[Fe^{III}_{LS}(\mu\text{-CN})Co^{II}_{HS}]$ and diamagnetic $[Fe^{II}_{LS}(\mu\text{-CN})Co^{III}_{LS}]$ complexes in an approximate 1:1 ratio (Table II-4). Indeed, the average Co-N distance (2.07 Å) at 120 K is between the average Co-N bond length (2.12 Å) at 200 K for only paramagnetic species and the one expected (≤ 1.9 Å) at low temperatures for only diamagnetic species.

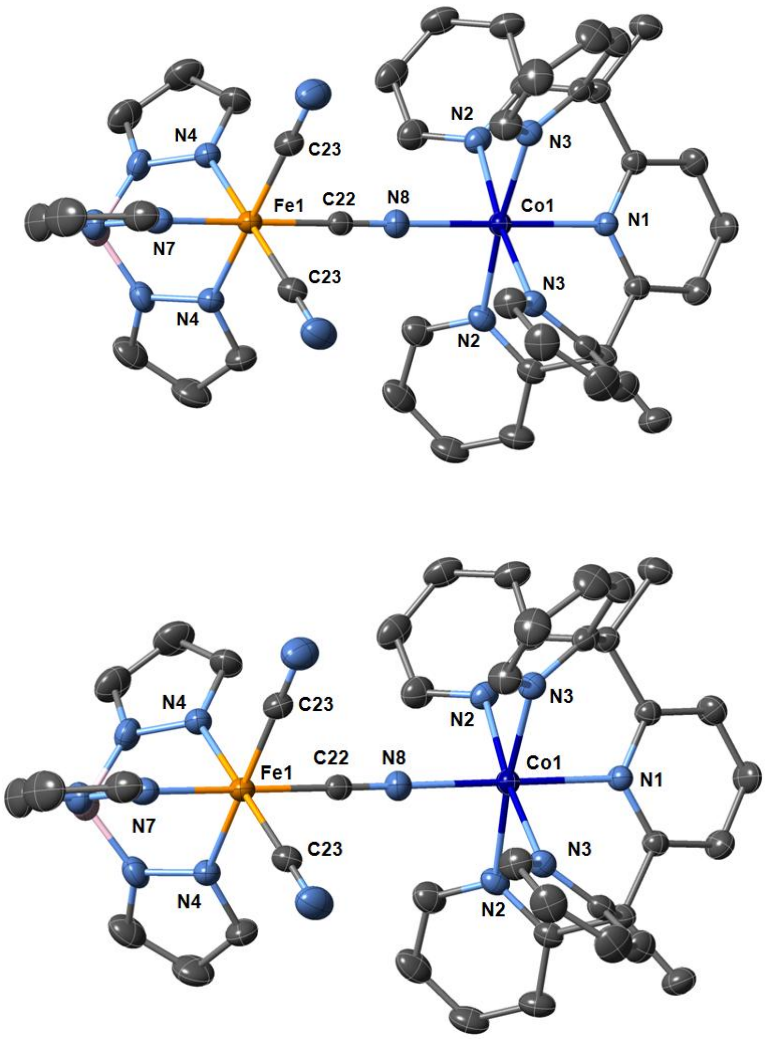

Figure II-12. ORTEP-type view of the cationic complex in **1**•*n*(solv) (Crystal 1) at 200 K (top) and at 120 K (bottom) . Thermal ellipsoids are depicted at the 30 % probability level. All anions, lattice solvents and hydrogen atoms are omitted for clarity. Fe, Co, N, C and B atoms are indicated in orange, dark blue, light blue, grey and pink, respectively.

A second crystal of **1**•*n*(solv) (Crystal 2) was collected at 120 K (Figure II-13). It crystallizes in the same orthorhombic *P*nma space group, but has a slightly smaller unit cell compared to the previous crystal of **1**•*n*(solv), indicating a slightly lower degree of solvation (see Table II-1 and Table II-3). As in **1**•2DMF, the $CF_3SO_3^-$ anion resides near an inversion center, but in this crystal, it appears to be disordered over six positions. It is worth mentioning that for crystals with a low amount of DMF in their crystal structure, the DMF molecules were extremely disordered, even more for some cases than this crystal 2 of **1**•*n*(solv). Except this higher disorder of the $CF_3SO_3^-$ anion, the packing of the cationic and anionic parts is same as observed in **1**•2DMF. Disordered lattice solvent molecules are also present in the void space of the channels along the *a* axis, but their exact nature, localization and number cannot be determined univocally based on the difference Fourier map. The average Fe-C, Fe-

N, Co-N_{py} and Co-N_{NC} bond distances are 1.892(3), 2.011(2), 1.983(2) and 1.878(3) Å respectively, suggesting the presence of only the diamagnetic [Fe^{II}_{LS}(μ-CN)Co^{III}_{LS}] complexes (Table II-4). Those features suggest therefore a full electron transfer process within the [Fe(μ-CN)Co] complexes for this type of crystal. It is worth mentioning that although the degree of solvation cannot be controlled precisely within this system, these single crystal results suggest a strong influence of the van der Waals interactions between the solvent molecules and the [Fe(μ-CN)Co] complexes on the electron transfer process.

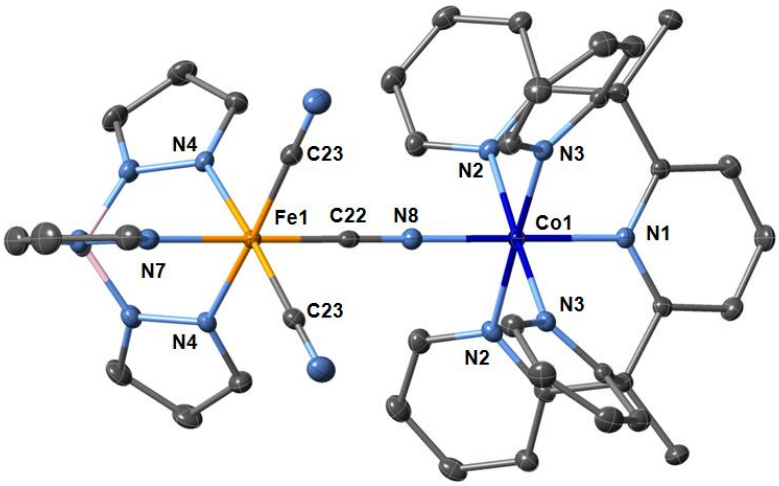

Figure II-13. ORTEP-type view of the cationic complex in **1**•*n*(solv) (Crystal 2) at 120 K. Thermal ellipsoids are depicted at the 30 % probability level. All anions, lattice solvents and hydrogen atoms are omitted for clarity. Fe, Co, N, C and B atoms are indicated in orange, dark blue, light blue, grey and pink, respectively.

Table II-3. Crystallographic data for **1**•*n*(solv) (Crystal 1 and Crystal 2) at 200 and 120 K.

Compound	**1**•*n*(solv) (Crystal 1)		**1**•*n*(solv) (Crystal 2)
Formula	$C_{42}H_{35}BCoF_3FeN_{14}O_3S$		
FW / g·mol^{-1}	998.49		
Crystal color	orange [1]		
Crystal size / mm	0.42 x 0.10 x 0.02		
Crystal system	orthorhombic		
Space group	Pnma		
Temperature / K	200	120	120
***a* / Å**	18.5561(17)	18.3266(15)	18.253(4)
***b* / Å**	15.1628(13)	14.8980(11)	14.801(3)
***c* / Å/**	17.7800(16)	17.4326(14)	17.422(3)
***V* / Å^3**	5002.6(8)	4759.6(6)	4707(2)
Z	4		
d_{calc}	1.326	1.393	1.409
μ / mm^{-1}	0.725	0.762	0.771
Absorp. Correction	SADABS		
$\theta_{min} - \theta_{max}$	1.586° - 26.774°	1.612° - 28.959°	1.805° - 29.194°
Refl. Coll. / unique	199842 / 5541	213849 / 6458	150858 / 6579
Completeness to 2θ	0.999	0.998	0.996
R_{int}	0.0409	0.0421	0.0419
Refined param./restr.	371 / 0	317 / 0	396 / 10
[a] R_1 ($I > 2\sigma(I)$)	0.0649	0.0656	0.0520
[b] wR_2 (all data)	0.1828	0.1840	0.1430
Goodness-of-fit	1.183	1.161	1.176

[a] $R_1 = \Sigma||F_0|-|F_C||/\Sigma|F_0|$, [b] $wR_2 = [\Sigma w(F_0^2-F_C^2)^2/\Sigma w(F_0^2)^2]^{1/2}$

Table II-4. Selected bond lengths, distances [Å] and angles [°] for **1**•*n*(solv) (Crystal 1 and Crystal 2) at 200 K and 120 K.

Compound	**1**•*n*(solv) (Crystal 1)		**1**•*n*(solv) (Crystal 2)
Temperature / K	200	120	120
Average (Fe-C)	1.988(5)	1.884(4)	1.892(3)
Fe1-C23	1.929(4)	1.892(3)	1.912(3)
Fe1-C22	1.985(5)	1.872(5)	1.851(4)
Average (Fe-N)	1.981(3)	1.947(4)	2.011(2)
Fe1-N4	1.976(3)	1.939(3)	2.012(2)
Fe1-N7	1.991(3)	1.963(4)	2.008(3)
Co-N_{NC}	2.046(5)	2.020(4)	1.878(3)
Average (Co-N_{py})	2.122(3)	2.086(3)	1.983(2)
Co1-N1	2.134(3)	2.070(4)	1.994(2)
Co1-N2	2.097(4)	2.086(3)	1.968(3)
Co1-N3	2.123(3)	2.093(3)	1.980(2)
Fe1-C22-N8	177.3(5)	177.4(4)	176.0(3)
C22-N8- Co1	174.9(5)	174.8(4)	175.3(3)
Fe1…Co1	5.079(1)	5.015(9)	4.883(1)

[1] No significant change of the color observed in low temperature measurements.

II.2.5 Magnetic measurements of 1

The magnetic properties of compound **1** were measured between 1.8 and 300 K in applied external field 1 T. In Figure II-14, the magnetic properties of **1** (in black) and **1**•2DMF (in red) are compared. At 300 K, the χT product of **1** is 3.44 cm^3 K mol^{-1}, corresponding well to the paramagnetic [Fe^{III}_{LS}(μ-CN)Co^{II}_{HS}] complex observed in **1**•2DMF. Upon lowering the temperature, the χT product is almost constant down to 175 K and decreases abruptly at 165 K (see, Figure S.II-3) before reaching a value of 0.21 cm^3 K mol^{-1} at 145 K, confirming the stabilization of the diamagnetic {Fe^{II}_{LS}(μ-CN)Co^{III}_{LS}} state by a quasi-full electron transfer. The small residue of 0.21 cm^3 K mol^{-1} equates with the 94% of the sample which converted from paramagnetic to diamagnetic though the electron transfer process. In heating mode, **1** displays a sharp transition at 170 K (see, Figure S.II-3), revealing a thermal hysteresis of about 5 K at 0.67 K/min and thus a first-order phase transition associated with the full electron transfer in solid state.

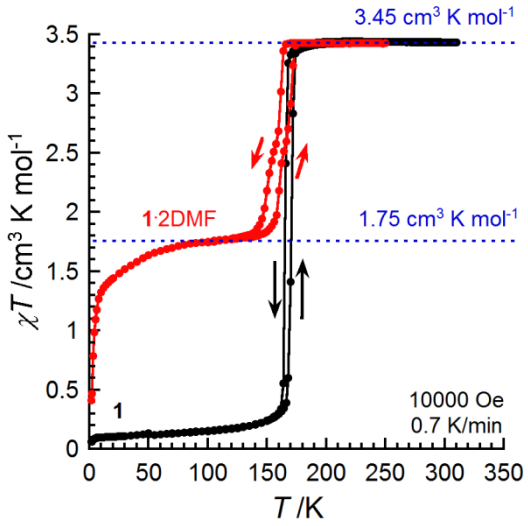

Figure II-14. χT versus T plots for polycrystalline samples of **1**•2DMF (in red, from 250 to 100 K at 1 T and below 100 K at 0.1 T) and **1** (in black, from 300 to 1.8 K at 1 T) at 0.67 K/min (the blue dashed lines are guides for the eyes).

II.2.6 Optical measurements of 1

The signature of the electron transfer in **1** can also be studied by solid-state optical reflectivity measurements. This set-up uses a white light source, and collects the light reflected by surface of the sample (that is the sum of direct and diffuse reflected light). Thus, it wasn't possible to perform the same studies for **1**•2DMF kept in its mother liquor.

The first set of measurements consists in studying the thermal dependence of the reflectivity spectra. To limit photoexcitation effects, the power of the white light is fixed at 0.08 mW, and the light is only switched on for 1 second to record at one temperature the reflectivity spectrum, and then the light is switched off during the next temperature step. Figure II-15 presents the reflectivity spectra of the compound **1** between 310 and 10 K on

cooling (top, left) and then on heating (top, right) modes with a sweeping temperature rate of 4 K/min. At 310 K, the spectrum of the paramagnetic [Fe^{III}_{LS}(μ-CN)Co^{II}_{HS}] complex is composed of two bands at 490 and 850 nm. Upon cooling, this spectrum is strongly modified in the 200−140 K temperature region, with a significant decrease in the reflectivity above 700 nm, as expected when diamagnetic [Fe^{II}_{LS}(μ-CN)Co^{III}_{LS}] species are stabilized at low temperature.[11−14,17] The reflectivity spectra are very similar to the ones of the Fe/Co square complexes reported in reference 14 using the same reflectivity set-up. Thus, the optical bands of **1** may be attributed by analogy with the spectra of these square analogues.[14,16-17] At room temperature, the strong absorption observed around 500 nm can be the superposition of the LMCT band of the Fe(III) moiety (as the reflectivity spectrum of the Fe(III) precursor suggests in Figure S.II-5, left (orange color spectrum)) and the Co(II) → Fe(III) MMCT band. They are not well resolved in solid state due to their strong intensity and indeed only the feet of these bands are observed. The band around 850 nm is likely corresponding the d-d transitions of the Co(II) site, based on the reflectivity spectrum of the Co(II) precursor in Figure S.II-5, left (blue color spectrum).

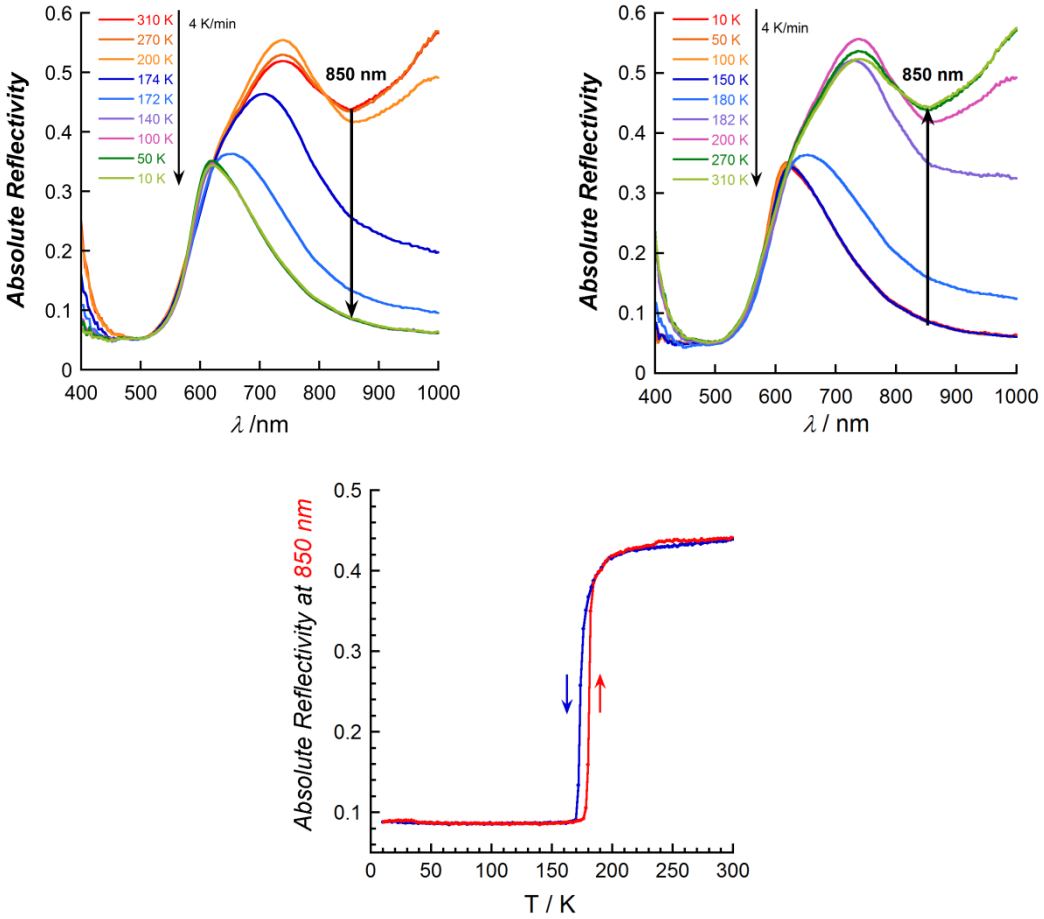

Figure II-15. Reflectivity spectra between 310 and 10 K as function of wavelength in cooling (top, left) and heating mode (top, right); (bottom) thermal evolution of reflectivity signal recorded at λ= 850 ± 5 nm (R_{850}) in cooling mode (310-10 K, blue curve), and heating mode (10-300 K, red curve) at 4 K/min for **1**.

At low temperatures, a strong absorption is observed with a maximum above 900 nm that corresponds to the MMCT Fe(II) → Co(III) band as observed in related Co/Fe cyanido-base complexes.[14,16-17] The thermal evolution of the absolute reflectivity at 850 nm helps to visualize the optical properties (Figure II-15, bottom) and reveals, as observed by magnetic measurements, a thermal hysteresis (ca. 9 K at 4 K/min) associated with the thermally induced electron transfer in **1**.

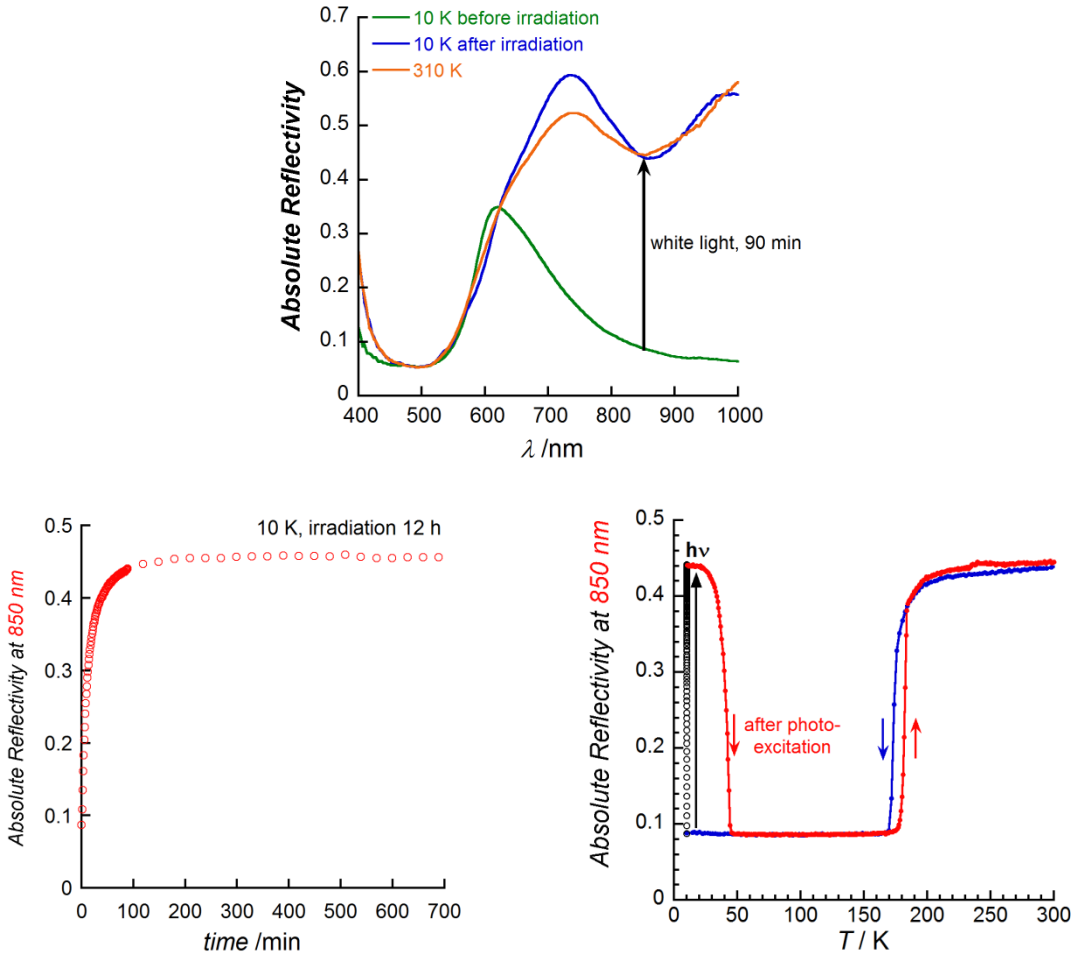

Figure II-16. (top) Reflectivity spectra at 310 K (orange), 10 K (green) before irradiation and at 10 K (blue) after white light irradiation 90 minutes; (bottom, left) time evolution of absolute reflectivity at 850nm (R_{850}) under white-light irradiation (0.4 mW/cm^2) 12 hours at 10 K; (bottom, right) thermal evolution of reflectivity signal recorded at λ= 850 ± 5 nm (R_{850}) in cooling mode (310-10 K, blue curve), during white white-light irradiation (0.4 mW/cm^2, at 10 K, black circle markers) and in heating mode (10-300 K, red curve) at 4 K/min for **1**.

A second set of measurements was realized in order to probe the photo-induced electron transfer: the compound is cooled to 10 K in the dark, and when the temperature is stable, the white light irradiation starts. After 90 min of white-light irradiation of the sample at 10 K (0.4 mW/cm^2), the resulting spectrum is nearly identical to the one recorded at 310 K (Figure II-16, top), demonstrating the possibility to photoinduce the paramagnetic [Fe^{III}_{LS}(μ-CN)Co^{II}_{HS}]

state, at least at the surface of the sample. Upon heating, the photo-induced state relaxes around 45 K to the thermodynamic diamagnetic state (Figure II-16, bottom).

The reflectivity properties of **1** were further investigated using specific wavelengths for photoexcitation experiments. Compared to the above optical measurements, the white light is still used as a light probe for spectroscopy, but a set-up of 14 different LEDs was used for irradiations. Detailed measurements were performed in order (i) to find the most efficient wavelength for irradiation, (ii) at this optimum wavelength, to study the effect of the light power under a fixed irradiation time. To test the different LEDs, the following protocol was applied: the compound is placed at 10 K in its diamagnetic state after a cooling at 10 K/min in the dark, and a spectrum is first collected. Then the compound is irradiated with one LED for 20 minutes with a power of 0.8 mW/cm^2. A new spectrum is recorded. To recover the diamagnetic state, the compound is reheated at 100 K, and then placed again in the dark at 10 K at 10 K/min, before finally being irradiated with another LED. This procedure is repeated for each LED. The results for the different LEDs are shown in Figure II-17. The most important changes in the spectra before and after 20 minutes of irradiation are observed with the 1050- and 940-nm LEDs.

An alternative way to visualize the changes induced by the LED irradiations is to plot the difference of absolute reflectivity (ΔAR) at 850 nm as shown in Figure II-18. These plots show clearly the ability of all 14 LEDs to excite the compound with the most efficient lying in the 850-1050 nm range.

The influence of the irradiation power was studied for the most efficient LED at 1050 nm. The following experimental protocol was applied: the sample is placed at 10 K in its diamagnetic state after a cooling at 10 K/min in the dark, and a spectrum is first collected (named “before irradiation”). Then the sample is irradiated with the 1050 nm LED for 70 min with a selected power. Spectra are recorded each minute, the LED being switched off during the spectra collection. Then, when the 70-minute irradiation is finished, the sample is reheated at 300 K, and then placed again at 10 K at 10 K/min in the dark, and finally irradiated with the same LED with a different power. The Figure II-19 shows the result of this experiment as the time evolution of AR_{850} during the successive irradiations. The different sets of data have similar shapes and reach a saturation value. When the power is increased, the saturation value is higher and is reached faster. This can be interpreted as a better light penetration at the surface of the sample when the power is increased. It is worth noting that the spectrum obtained after the 1050 nm irradiation clearly shows a band appearing around 860 nm, which is also observed in the spectrum at 310 K (Figure II-20, left).

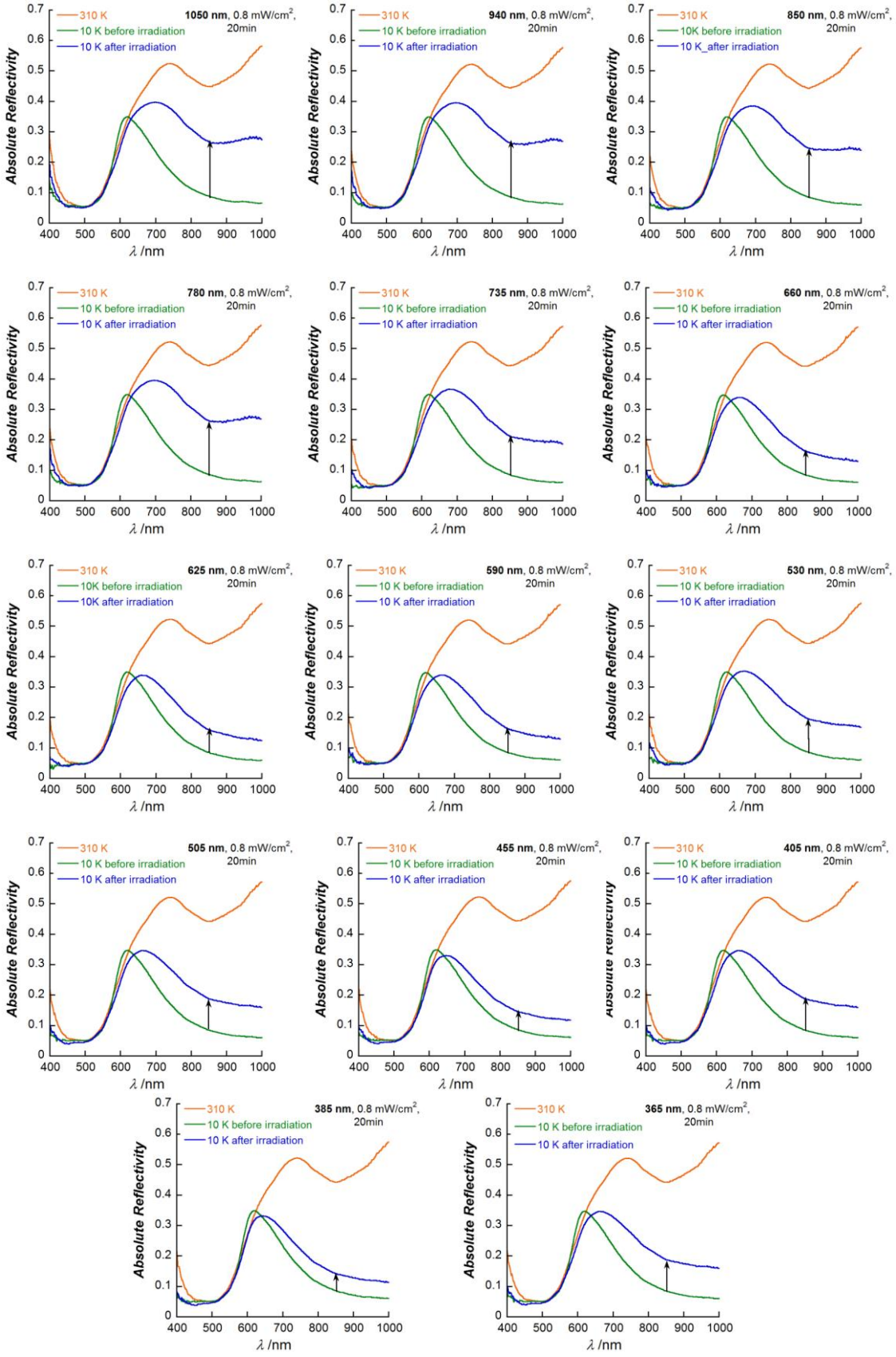

Figure II-17. Reflectivity spectra of **1** at 310 and 10 K obtained before irradiation and at 10 K after 20 min of irradiation (0.8 mW/cm^2) at different wavelengths delivered by 14 LEDs.

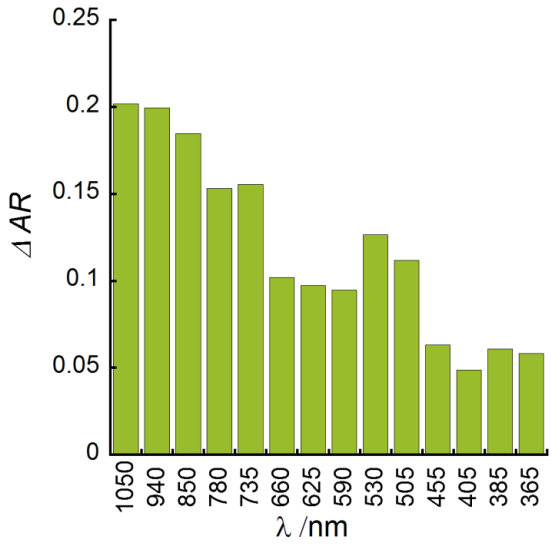

Figure II-18. Difference in absolute reflectivity (*ΔAR*) at 850 nm for **1**, obtained before irradiation and after 20 min of irradiation with the 14 different LEDs (P = 0.8 mW/cm^2) at 10 K.

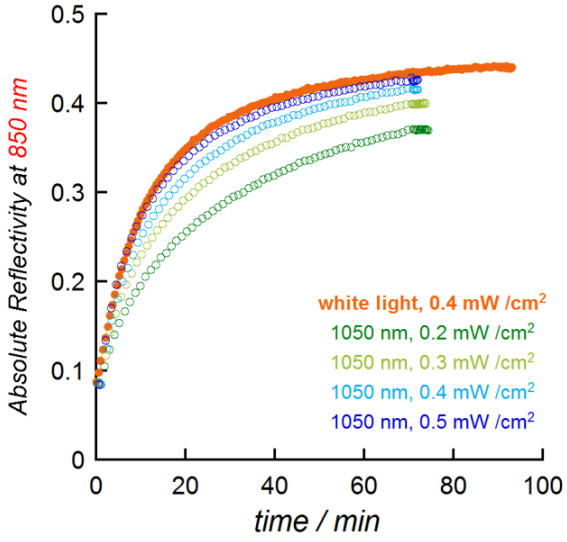

Figure II-19. Time evolution of reflectivity signal recorded at λ = 850± 5 nm (AR_{850}) during successive irradiations at 1050 nm with different power irradiations between 0.2 and 0.5 mW/cm^2 in comparison with the white-light irradiation for **1**.

Finally, the thermal evolution of AR_{850} after the photoexcitation with the 1050 nm LED at 0.5 mW/cm^2 is shown in Figure II-20, right. AR_{850} is nearly constant until 30 K, and shows a decrease from this temperature to reach 0.085 at 50 K. This decrease corresponds to the thermal-activated relaxation from the photo-excited state. Above 50 K, the same behavior for AR_{850} than the other measurements is observed. This shows again the good reversibility after the photoinduced electron transfer in the sample in **1**.

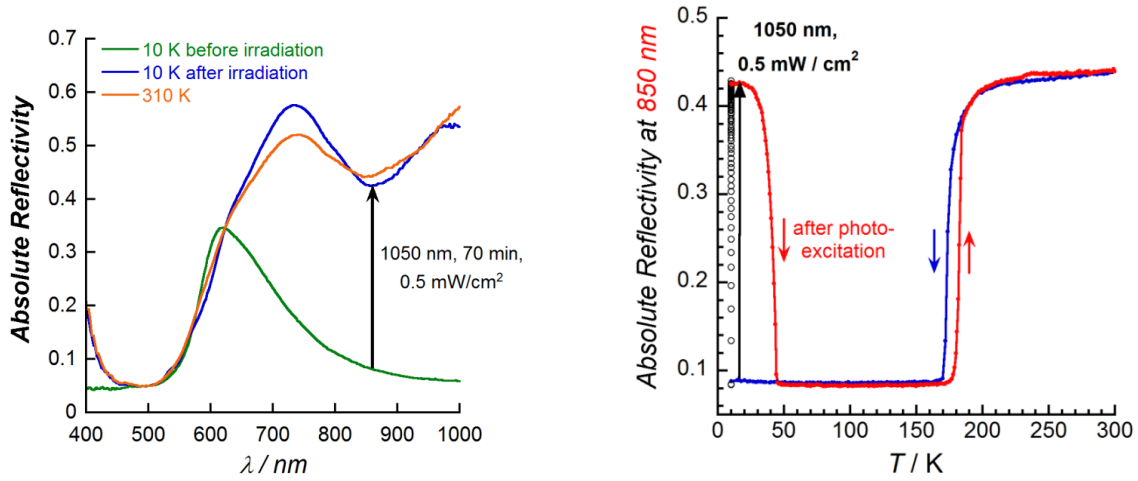

Figure II-20. (Left) Reflectivity spectra of **1**, obtained at 10 K before (green) and after 70 min of 1050 nm irradiation (blue), and at 310 K (orange); (right) thermal evolution of reflectivity signal of **1**, recorded at λ = 850 ± 5 nm (AR_{850}) in cooling mode (310-10 K, blue curve), under 1050 nm irradiation (0.5 mW/cm^2) during 70 min at 10 K (dark points) and after irradiation in heating mode (10-310 K, red curve).

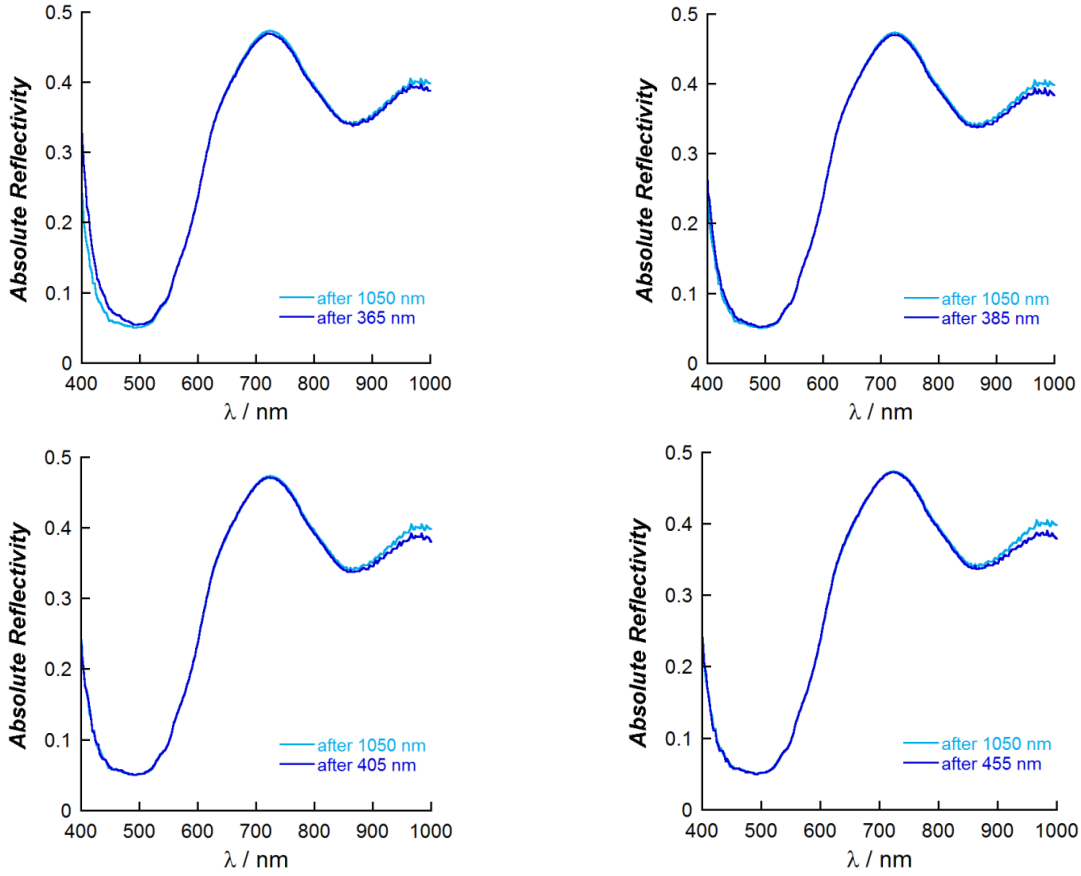

Figure II-21. Reflectivity spectra at 10 K for **1**, obtained after irradiation at 1050 nm (0.5 mW/cm^2, 20 min, in light blue) and after irradiation at 365, 385, 405 and 455 nm (0.5 mW/cm^2, 10 min, in dark blue).

To finish this reflectivity study with the LEDs, the eventual photoreversibility at 10 K by cycling a photo-excitation at 1050 nm (20 min with a power at 0.5 mW/cm^2) and a second irradiation (possible photo-deexcitation) with other LEDs (each irradiation for 10 min with a power at 0.5 mW/cm^2). Four LEDs at 365, 385, 405 and 455 nm (the less efficient to photo-excite the diamagnetic state; see Figure II-17 and Figure II-18) were selected for this deexcitation test. As shown by figure II-21, no photoreversibility has been observed for this compound. In summary, the optical reflectivity studies demonstrate well the reversible thermally-induced electron transfer process within compound **1.** Moreover, it was shown the possibility to fully photo-excite compound **1** by white light and 1050-nm irradiation at least in the surface of the sample.

II.2.7 Photomagnetic measurements of 1

In order to confirm and further investigate the photoinduced electron transfer phenomenon observed at low temperatures photomagnetic studies for compound **1** were performed (Figure II-22). Under white-light irradiation, the χT product at 10 K quickly increases and reaches a maximum of 2.97 cm^3 K mol^{-1} after 4 h, thus demonstrating that paramagnetic [Fe$^{III}_{LS}$(μ-CN)Co$^{II}_{HS}$] complexes are photogenerated at the bulk level. From 2 to 21 K in the dark, the χT product of the photoinduced phase increased from 1.8 to 3.2 cm^3 K mol^{-1}, most likely due to the Co^{II} and Fe^{III} spin−orbit coupling[32,33] and/or antiferromagnetic interactions between LS Fe^{III} and HS Co^{II} magnetic sites[3] in the [Fe$^{III}_{LS}$(μ-CN)Co$^{II}_{HS}$] complex (as already observed in the low-temperature phase of **1**•2DMF, Figure II-14). Upon further heating (0.4 K / min), this metastable state relaxes rapidly into the thermodynamic diamagnetic phase at 45 K (Figure II-22), consistent with optical reflectivity studies (Figure II-16, bottom right).

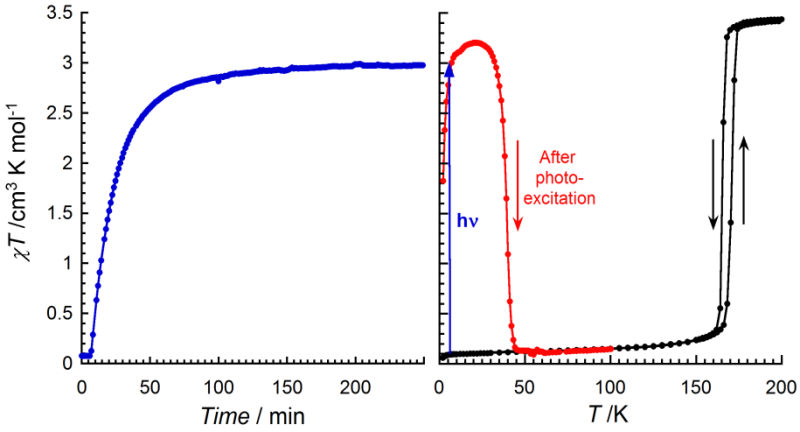

Figure II-22. (Left) χT versus time at 1 T under white-light irradiation (3 mW/cm^2) at 10 K; (right) χT versus temperature plots at 1 T and 0.4 K/min for **1** before (black) and after (red) white-light irradiation (3 mW/cm^2) at 10 K (the arrows are guides for the eye).

II.3 Preliminary XAS and XMCD Investigations for [{(Tp)Fe(CN)$_3$}{Co(PY5Me$_2$)}](CF$_3$SO$_3$) (1)

II.3.1 Introduction

Since the discovery of the remarkable properties of Prussian Blues (PBs) in 1996,[1] the need of understanding deeply the thermally and light-induced electron transfer phenomenon became important. X-ray Absorption Spectroscopy (XAS) and X-ray Magnetic Circular Dichroism (XMCD) are advanced characterization techniques, which can explain the change of the macroscopic magnetic properties of PBs and give local information about the metal centers existing in the structure. These experiments are carried out at synchrotron installations, where circularly polarized X-rays are used to probe the spin states of the measured elements (Figure II-23).

XAS is an element and orbital selective spectroscopic tool for geometric and electronic structure elucidation, which measures the absorption due to a transition from an initial state (core level) to a final empty state (above the Fermi level).[34] XAS data are obtained by tuning the photon energy using a monochromator to a range where core electrons can be excited (0.1-100 keV photon energy). The "name" of the edge depends upon the core electron which is excited: the principle quantum numbers n = 1, 2 and 3, correspond to the *K*-, *L*- and *M*-edges, respectively. For instance, excitation (~ 1.0 keV) of a *1s* electron to *4p* or *3d* level occurs at the *K*-edge, while excitation (~ 0.1 keV) of a *2s* or *2p* electron to a *3d* level occurs at the *L*-edges. The XAS of an element is sensitive to its local environment (symmetry, nature of the ligands, metal-ligand distances, and bonding), and to its oxidation and spin states. Depending on which edge we focus our studies, different information can be obtained. For example, it is well known that the *K* absorption edges of 3d metal compounds display an extended X-ray absorption fine structure (EXAFS) due to the scattering of the excited electron by the potential field of the neighbouring atoms. This effect can be used to determine bond distances and ligand coordination numbers. The information contained in the $L_{2,3}$ edges is of a completely different nature. The absorption spectrum is dominated by dipole transitions from the core *2p* level to the empty *3d* states, and because of the large Coulomb interaction (spin-orbit coupling, crystal field) between these two levels, it depends on the local electronic structure. Thus, analysis of the $L_{2,3}$ absorption structure may provide information about the oxidation state and the symmetry of the 3d transition metal ions.[40]

XMCD is the difference spectrum of two X-ray absorption spectra (XAS) taken in a magnetic field, one taken with left circularly polarized x-rays, and one with right circularly polarized ones.[34] Considering that the area of the XMCD signal is directly proportional to the local orbital magnetic moment carried by the absorber atom, information can be obtained on the magnetic properties of the atom, such as its spin, orbital magnetic moment and relative orientations of the neighboring magnetic moments.[34,35]

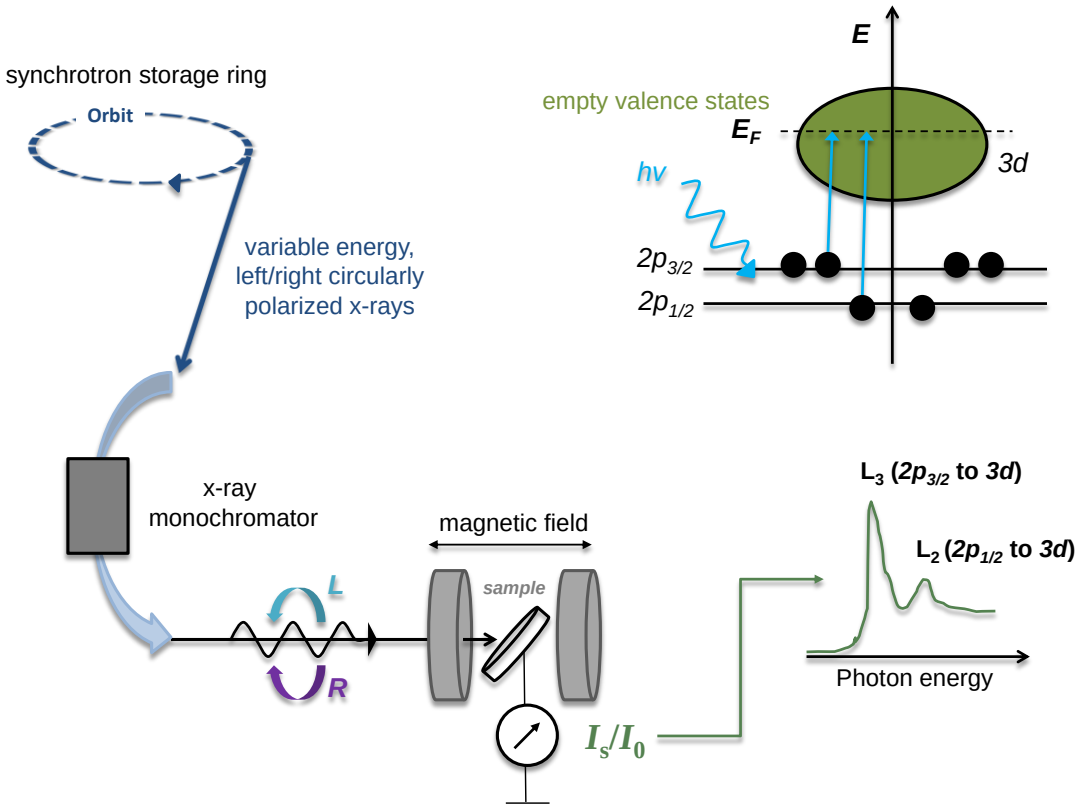

Figure II-23. Illustrated route of the X-rays from the source (synchrotron storage ring) to the sample and its response (I_s). On the right bottom the XAS spectrum at the M^{x+} $L_{2,3}$ edges obtained after the X-ray irradiation of the sample, and on the right top, the excitations that correspond to the spectrum beneath.

Detailed studies by XAS at the Co and Fe $L_{2,3}$ edges ($2p^2_{1/2}\,2p^4_{3/2}\,3d^{\,n} \rightarrow 2p^5 3d^{\,n+1}$) and Fe and Co *K*-edge were carried out for the 3D networks of PBAs, which presented a significant photoinduced magnetization, in order to investigate the electronic and local structures of the ground and excited states.[36] The comparison between the XAS spectra before and after irradiation confirmed the photoinduced transition from Co^{III}_{LS}-Fe^{II}_{LS} to Co^{II}_{HS}-Fe^{III}_{LS}. Moreover, XMCD studies suggested the presence of antiferromagnetic exchange interactions (*J*) between the magnetic moment of Co(II) and Fe(III) ions in the photoinduced state.[37]

Recently, XAS and XMCD investigations were reported for a 1D $\{FeCo\}_n$ coordination polymer (XAS and XMCD at *L*-edges)[38] and a cyanido-bridged molecular $\{Fe_2Co_2\}$ square (XAS at K edges)[39,45] that exhibit thermally and light-induced ET. In both cases only the changes in electronic states associated with thermally induced ET were investigated. No XAS and XMCD investigations of the metastable light-induced paramagnetic state were performed.

II.3.2 Experimental results

X-ray absorption spectroscopy (XAS) and X-ray magnetic circular dichroism (XMCD) investigations were carried out at DEIMOS beamline of SOLEIL synchrotron (Paris, France) for compound **1** in collaboration with Sadaf Fatima, Marie-Anne Arrio and Philippe

Sainctavit from IMPMC (University of Paris VI), and Philippe Ohresser (SOLEIL). Circularly polarized photons delivered by an Apple II undulator were monochromatised by a plane grating monochromator. The XMCD spectra recorded here have been obtained by inverting the direction of the magnetic field, keeping the same given circular polarization each time (right (+) or left (—)). The magnetic field was delivered by an electromagnet that could alternate the field between +6.5 and –6.5 T and its direction was set parallel to the X-ray beam. This method minimizes most spurious residual signals that might pollute the XMCD signal. The XMCD signal is obtained by $\sigma_{XMCD} = \sigma^- - \sigma^+$ where $\sigma^- = \frac{(\sigma^{-,6.5T} + \sigma^{+,-6.5T})}{2}$ and $\sigma^+ = \frac{(\sigma^{+,6.5T} + \sigma^{-,-6.5T})}{2}$.

The studies were performed at the $L_{2,3}$ edges (soft X-rays) of cobalt (~ 791-797 eV) and iron (~ 719-721 eV) ions with the following aims: (a) to observe the thermally and photo-induced ET in the dinuclear cyanido-bridged {FeCo} complex **1** using these techniques; (b) to determine/confirm the spin and oxidation states of the Co and Fe ions in the different phases; and (c) to determine the exact nature of the magnetic coupling between Fe and Co ions in the metastable light-induced paramagnetic state. The investigation of the photo-induced state is particularly interesting because macroscopic investigations of molecular cyanido-bridged $\{Fe_2Co_2\}$ squares suggest the presence of ferromagnetic interactions between Co^{II} HS and Fe^{III} LS ions.[14-17] Whereas previous reports on XMCD measurements at the Co and Fe K edges of the 3D Co/Fe PBAs have shown an antiferromagnetic coupling between Co^{II} HS and Fe^{III} LS ions and offered experimental evidence of the ferrimagnetic nature of the photo-induced metastable state in these 3D materials.[37]

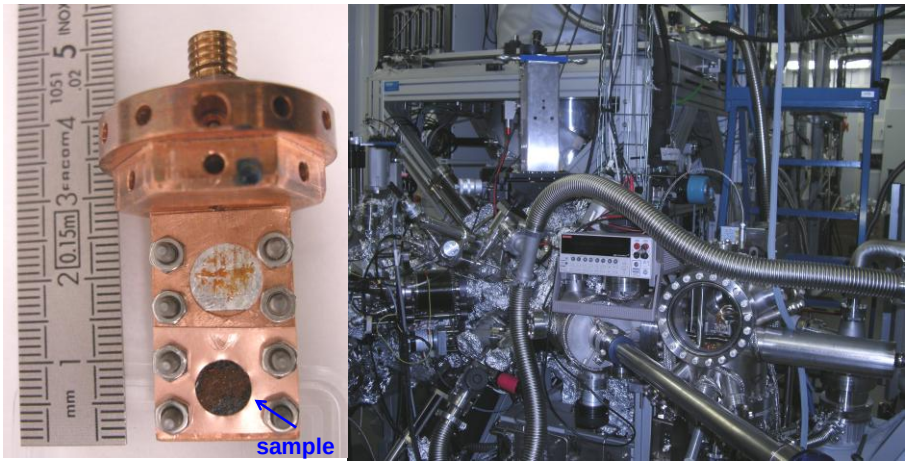

Figure II-24. (Left) The sample holder where compound **1** is deposited on graphite surface; (right) the experimental chamber under ultra-high vacuum conditions.

Prerequisite of a systematic study of **1** by XAS/XMCD constitutes the detailed study of Fe(III) and Co(II) precursors used for the synthesis of it. Thus, studies at the $L_{3,2}$ edges of cobalt and iron ions for the precursors were performed. These XAS spectra and the XMCD signals obtained will be used for comparison with those obtained by **1**. Microcrystalline powders of $[(PY5Me_2)Co^{II}(H_2O)](BF_4)_2$ and $(Bu_4N)[(Tp)Fe^{III}(CN)_3]$ were deposited by

dropcasting on silicon wafers on the sample holder and inserted to the experimental chamber under ultra-high vacuum conditions (UHV: 10^{-10} mbar range) (Figure II-24, right). XAS spectra at Co L_3-edges for $[(PY5Me_2)Co^{II}(H_2O)](BF_4)_2$ (Figure II-25, left) and Fe L_3-edges for $(Bu_4N)[(Tp)Fe^{III}(CN)_3]$ (Figure II-25, right) were recorded at 4 K; in order to avoid X-ray damaging, we focused on the L_3-edges (Figure II-25), since the information given in this part of the spectra is the most important for us (electronic information).

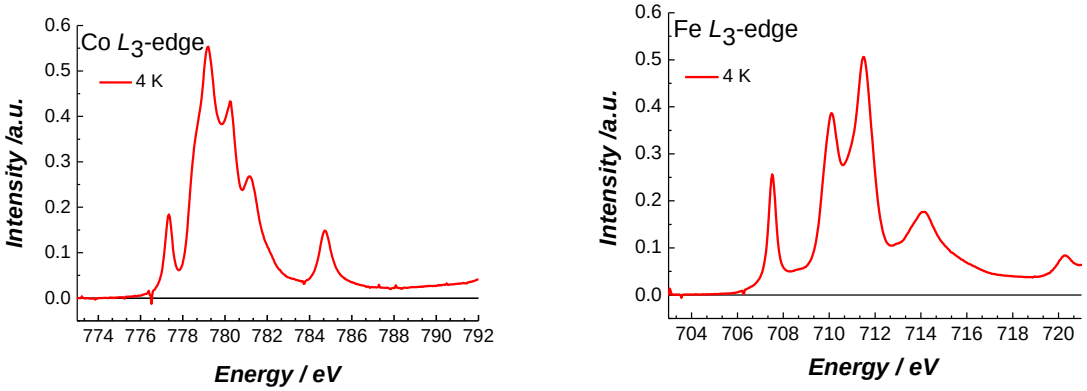

Figure II-25. XAS at Co L_3-edge (left) for $[(PY5Me_2)Co^{II}(H_2O)](BF_4)_2$ and Fe L_3-edge (right) for $(Bu_4N)[(Tp)Fe^{III}(CN)_3]$ at 4 K.

In the cobalt L_3-edge absorption spectrum of $[(PY5Me_2)Co^{II}(H_2O)](BF_4)_2$ at 4 K (Figure II-25, left), the energies of the absorption maximum at 777.3, 779.2 and 780.3 eV, which may correspond to the excitation $2p^63d^7 \longrightarrow 2p^53d^8$, indicate the presence of HS Co^{II} ions in a distorted octahedral symmetry.[36] In the iron L_3-edge absorption spectrum of $(Bu_4N)[(Tp)Fe^{III}(CN)_3]$ at 4 K (Figure II-25, right), a first peak at 707.5 eV is observed, which corresponds to the excitation $2p^6t_{2g}{}^5 \longrightarrow 2p^5t_{2g}{}^6$. This peak is the signature of the LS Fe^{III} configuration, when the metal is surrounded by cyanide ligands. The other peaks between 710 and 714 eV may correspond to multiplet structures arising from transitions from *2p* to *eg* orbitals.[36,41] XMCD signals were observed at the same temperature by applying external magnetic field of +/- 6.5 T, which were found to present several negative and positive peaks (Figure II-26, red curves) for both precursors. From these data, valuable information about the electronic and magnetic properties of the cobalt and iron precursors can be deduced, such as their spin and orbit magnetic moments. The meaning of the sign of the XMCD data and the information about the spin and orbital magnetic moment are part of Sadaf Fatima's Ph.D. work at IMPMC.

Having in mind the above mentioned spectra, we will focus on the results obtained for compound **1**. Microcrystalline powder of $[\{(Tp)Fe(CN)_3\}\{Co(PY5Me_2)\}](CF_3SO_3)$ (**1**) was deposited on graphite tape on the sample holder (Figure II-24, left, bottom hole) and inserted to the experimental chamber under ultra-high vacuum conditions (UHV: 10^{-10} mbar range) (Figure II-24, right).

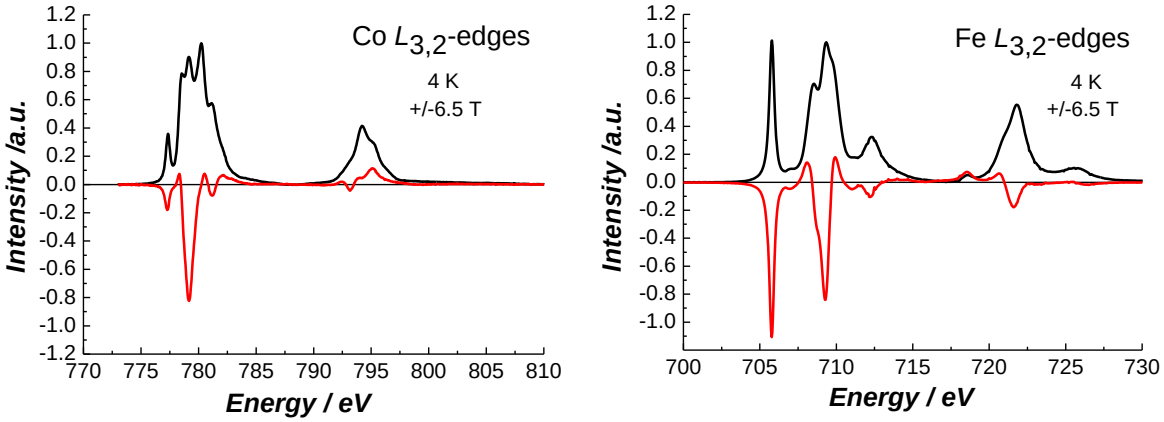

Figure II-26. Isotropic (average of *left* and *right* polarization XAS spectra, black) and dichroic (XMCD, red) absorption spectra at Co $L_{3,2}$-edges for $[(PY5Me_2)Co^{II}(H_2O)](BF_4)_2$ (left) and at Fe $L_{3,2}$-edges for $(Bu_4N)[(Tp)Fe^{III}(CN)_3]$ (right) at 4 K.

The first series of experiment include the investigation of the thermal induced electron transfer process, as well as its reversibility probed by X-ray absorption spectroscopy. Co and Fe L_3-edge XAS spectra were recorded for the complex **1** at 300 K and 100 K in order to obtain the signature of the paramagnetic and the diamagnetic state of the pair, respectively, as suggested by the magnetic measurements (Figure II-14). The cobalt L_3-edge absorption spectrum of **1** at 300 K (Figure II-27, left) shows maximum absorption at 779, 780.7 and 782 eV, corresponding to HS Co^{II} ions in octahedral symmetry.[36] At 100 K, the Co L_3-edge maximum at 779 eV has decreased, the maximum at 780.7 and 782 eV disappeared and a new maximum has appeared at higher energy (783 eV) compared to the spectrum at 300 K, which is characteristic of the absorption spectrum of Co^{III} ions.[36] The very intense band at 783 eV is the signature of the presence of -*CN* π* orbitals.[36] The shift of maximum at higher energy is due to the increase of the oxidation state and to the strong shortening of the Co-ligand distances in Co^{III} compared to Co^{II}.[36] The iron L_3-edge absorption spectrum of **1** at 300 K (Figure II-27, right) shows a first peak at 708.9 eV, which is typical of the LS Fe^{III} configuration, when the metal is surrounded by cyanide ligands.[36,41] At 100 K, the intensity of the peak at 708.9 eV is drastically reduced, evidencing the conversion from the LS Fe^{III} to the LS Fe^{II} configuration. Except from this peak, the transitions of Fe^{II} and Fe^{III} are located in overlapped energy ranges and the electron transfer appeared less clearly than at the Co *L*-edges.[36,41]

The second series of experiments concern the investigation of the photo-induced paramagnetic state at low temperature. The Co and Fe L_3-edge XAS spectra at 100 K before irradiation and at 4 K after irradiation with LED at 660-nm (P = 19 mW for 2 hours) are compared in Figure II-28. The choice of the 660-nm LED for irradiation was based on its ability to photo-excite compound **1** (see Figure II-18) and the high power that this LED can provide. The Co and Fe L_3-edge XAS spectra at 4 K after the irradiation of **1** are similar with those obtained at 300 K, confirming the photo-induced electron transfer between the diamagnetic $\{Fe^{II}_{LS}(\mu\text{-CN})Co^{III}_{LS}\}$ state of the pair at low temperature to the paramagnetic $\{Fe^{III}_{LS}(\mu\text{-CN})Co^{II}_{HS}\}$ state after irradiation (Figure II-28). The small variation observed in the

spectra after irradiation in comparison with the high temperature spectra may be attributed to temperature effects (4 K *vs* 300 K). After the photo-excitation experiment, the reversibility of the photo- and thermally induced intramolecular ET was verified. The system recovered its diamagnetic state at 100 K and its initial paramagnetic state when it was warmed up to 300 K.

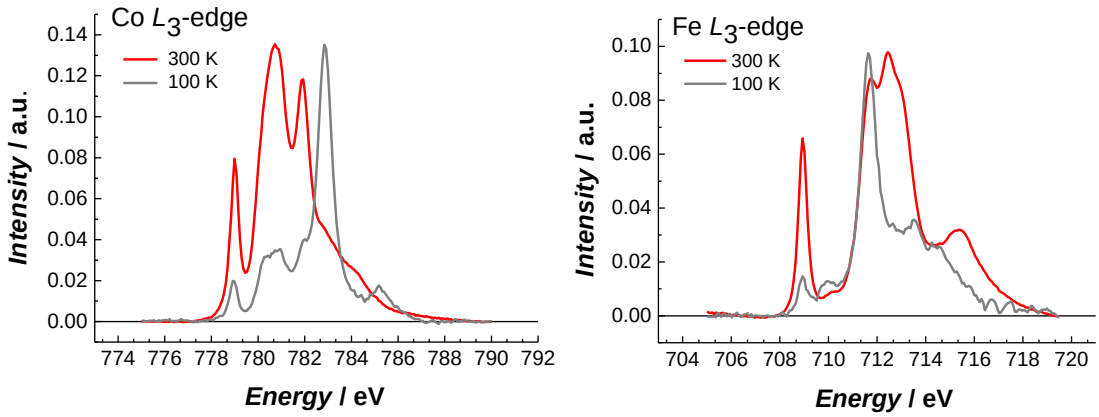

Figure II-27. XAS at Co (left) and Fe (right) L_3-edge at 300 K (red) and 100 K (gray) for **1**.

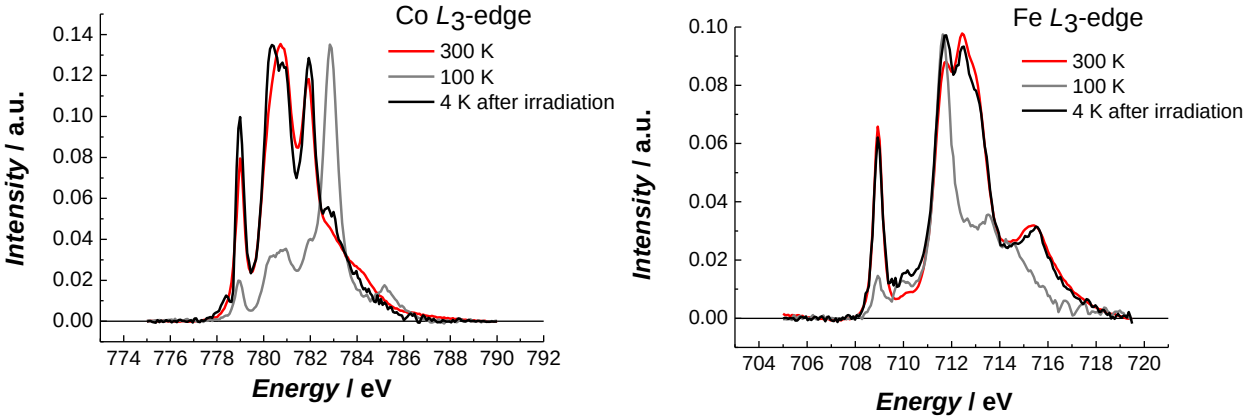

Figure II-28. XAS at Co (left) and Fe (right) L_3-edge at 300 K (red), 100 K (gray) and at 4 K after irradiation of LED 660 nm (black) for **1**.

The electron transfer phenomenon was also followed as a function of temperature by XAS at Co and Fe L_3 edges measurements. The Co L_3 XAS spectra at a given temperature were analyzed by linear combination of Co^{II} L_3 XAS (measured at 300 K or at 4 K after photo-excitation) and Co^{III} spectra (measured at 100 K). The Fe L_3 XAS at a given temperature were analyzed by linear combination of Fe^{III} L_3 XAS spectra (measured at 300 K or at 4 K after photo-excitation) and Fe^{II} spectra (measured at 100 K).The obtained data (blue stars in Figure II-29) correlate well with the data obtained from the magnetic susceptibility measurements (solid line in Figure II-29).

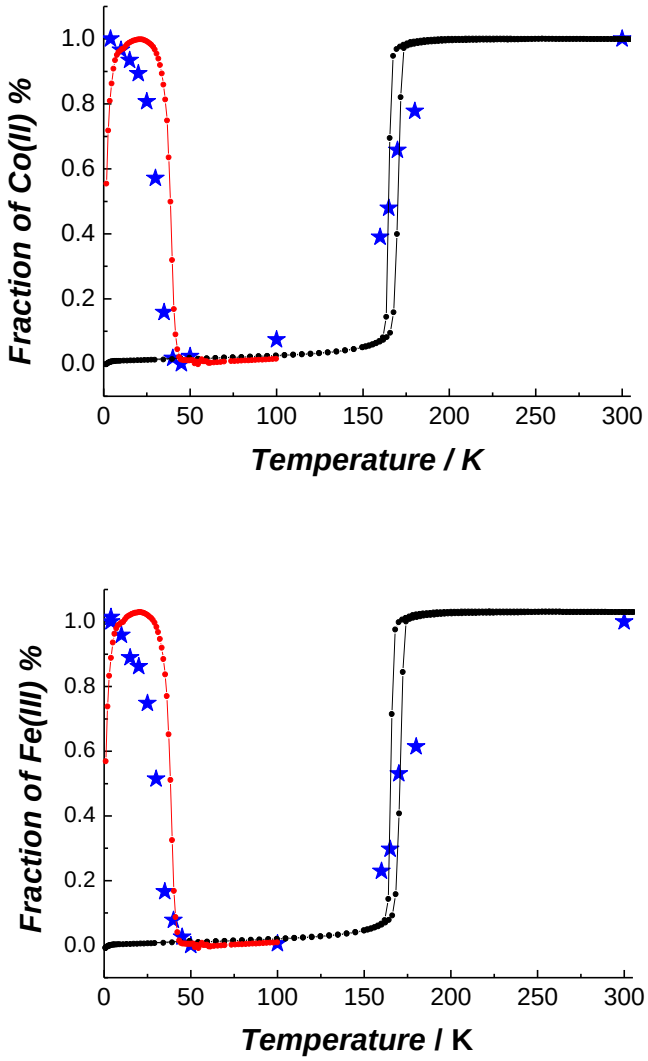

Figure II-29. Normalized fraction of Co(II) (top, blue stars) and Fe(III) (bottom, blue stars) as a function of temperature by XAS at 780.7 eV and 708.9 eV, respectively in comparison with the normalized photomagnetic data for **1**.

Since the light-induced metastable state in compound **1** is paramagnetic, weak XMCD signals were observed at Co and Fe $L_{3,2}$-edges at 4 K under applied magnetic field of +/- 6.5 T, exhibiting several negative and positive peaks. The sign of the XMCD signals indicates that Co and Fe ions are both oriented along the applied magnetic field. Unfortunately, irradiation damage was detected for the sample, which doesn't allow us to study further these results. Nevertheless, the antiferromagnetic Fe-Co coupling constant is expected to be weak, thus the coupling is likely to be inversed by the strong applied magnetic field at 4 K.[37] In order to determine this coupling, experiment at very low temperature (below 1 K) were initiated at SLS in Switzerland, where a specific cryostat can reach this temperature. Unfortunately, during the beam time attributed, technical problems prevented to reach the desired temperature. Finally, weak XMCD signals were observed at Co and Fe $L_{3,2}$-edges at

1.05 K under applied magnetic field of +/- 6.5 T, exhibiting several negative and positive peaks (Figure II-30). At this temperature, the XMCD-detected magnetization curves showed a ferromagnetic coupling, indicating that the temperature was likely to be too high. Therefore, these experiments will be repeated at SLS synchrotron at lower temperatures. The output of this study is of great importance, since the nature of the interaction was difficult to be extracted from the photomagnetic properties (Figure II-22), most likely due to (i) the Co^{II} and Fe^{III} spin−orbit coupling[32,33] and (ii) the relaxation of the metastable paramagnetic state around 50 K. Combining the experimental data with Ligand Field Multiplet (LFM)[42] theoretical calculations, we aim to deduce valuable information about the electronic and magnetic properties of the cobalt and iron site in the pair, such as their spin and orbit magnetic moments. These results will be compared with the results obtained from the XMCD signals of the Co(II) and Fe(III) precursors (Figures II-25 and II-26) for further analysis. This will be part of the Ph.D. work of Sadaf Fatima at IMPMC.

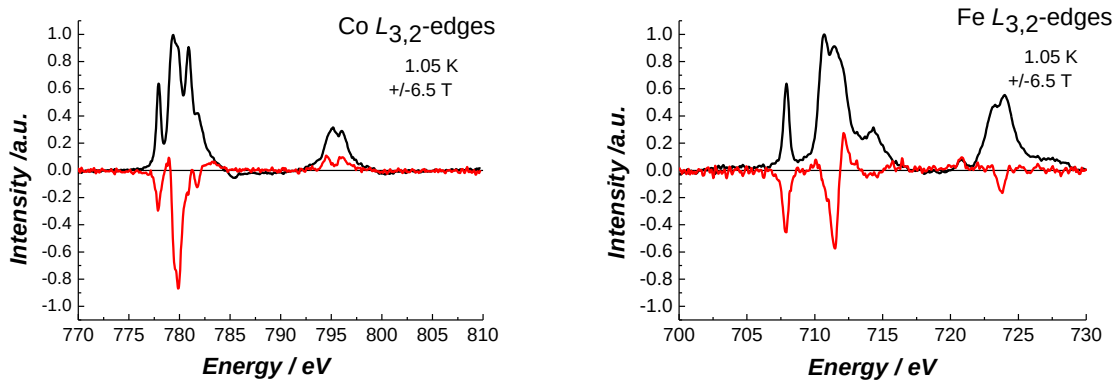

Figure II-30. Isotropic (average of σ^- and σ^+ XAS spectra, black) and dichroic (XMCD, red) absorption spectra at Co $L_{3,2}$-edges (top) and Fe $L_{3,2}$-edges (bottom) at 1.05 K for **1**.

II.4 Conclusions and Perspectives

A new dinuclear cyanido-bridged complex $[\{(Tp)Fe^{III}(CN)_3\}\{Co^{II}(PY5Me_2)\}](CF_3SO_3)\bullet 2DMF$ (**1**•2DMF)[28] was synthesized by following a rational building-block approach and its properties in respect to the metal-to-metal electron transfer phenomenon were investigated in solid state by structural, spectroscopic, bulk magnetic and photomagnetic methods, as well as with XAS and XMCD measurements. The choice of the ideal Fe(III) and Co(II) building-blocks arises from the fact that we need i) at least one bridging cyanide ligand, which favors the electronic delocalization between the metallic centers (electron transfer), ii) N-donor capping ligands, which direct the rational formation of a dinuclear complex, and iii) the appropriate difference of the redox potential between the two building blocks, based on our experience with compound

[{(BBP)Fe(CN)$_3$}{Co(PY5Me$_2$)}],[24] which finally led to the desired electron transfer properties (Figure II-31).

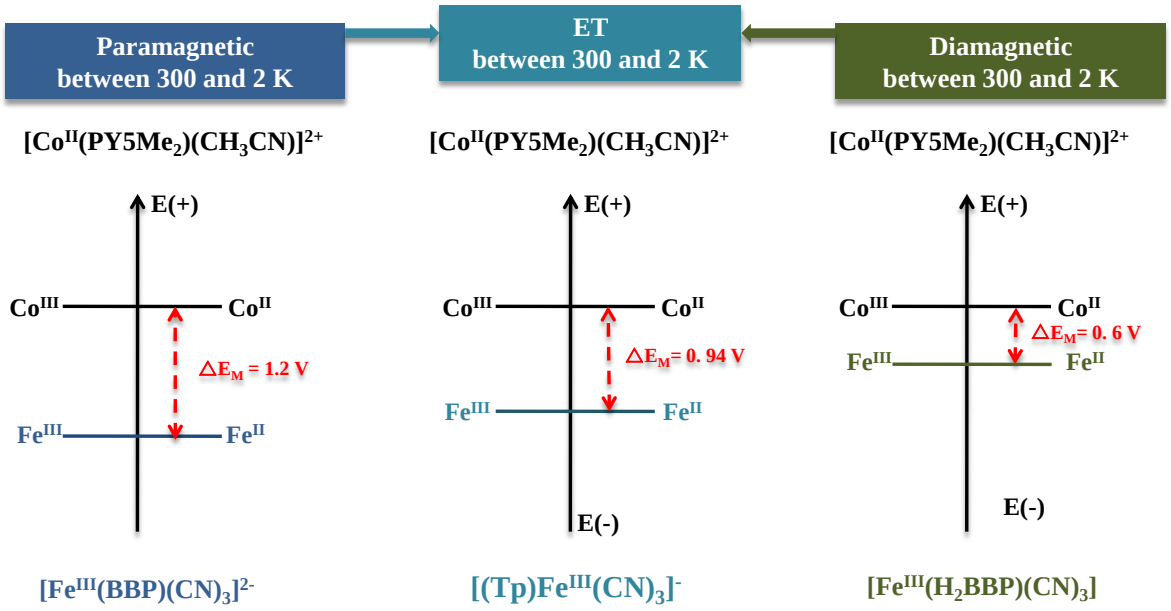

Figure II-31. The difference of the redox potential between the: (left) [(PY5Me$_2$)Co^{II}(MeCN)](BF$_4$)$_2$ and (Bu$_4$N)$_2$[(BBP)Fe^{III}(CN)$_3$]; (right) [(PY5Me$_2$)Co^{II}(MeCN)](BF$_4$)$_2$ and [(H$_2$BBP)Fe^{III}(CN)$_3$] by cyclic voltammetry (~1 mM), collected in a 0.1 M solution of Bu$_4$N(BF$_4$) in MeCN (for the Co(II) precursor) and DMSO (for the Fe(III) precursors), with a scan rate of 0.1 V s^{-1}; and (middle) [(PY5Me$_2$)Co^{II}(MeCN)](BF$_4$)$_2$ and (Bu$_4$N)[(Tp)Fe^{III}(CN)$_3$] by cyclic voltammetry (~1 mM), collected in a 0.1 M solution of Bu$_4$N(BF$_4$) in MeCN (for both precursors), with scan rate of 0.1 V s^{-1}. Potentials were referenced to the [Cp$_2$Fe]$^{1+/0}$ couple.

Single crystal X-ray diffraction and magnetic studies revealed that the thermal transition of the paramagnetic [Fe$^{III}_{LS}$(μ-CN)Co$^{II}_{HS}$] complex into its diamagnetic [Fe$^{II}_{LS}$(μ-CN)Co$^{III}_{LS}$] analogue is only 50% in **1**•2DMF (between 152 and 171 K). By looking closer the crystal structure of **1**•2DMF, we observed weak interactions between the solvent molecules of DMF and the pairs, which can affect the properties of the compound. Thus, the desolvated form of the pair, **1**, was studied, after the confirmation of its stability by TGA measurements and IR spectroscopy. The complete and reversible thermal induced electron transfer process (between 165 and 170 K) was revealed by magnetic studies in **1**. This is the first time that electron transfer is observed in a dinuclear cyanido-bridged complex in solid state. Unfortunately, the lack of crystallinity of **1**, didn't allow us to confirm the ET by single crystal X-ray diffraction. Photomagnetic and optical reflectivity studies demonstrated unambiguously that the diamagnetic state of **1** can be photoconverted into the paramagnetic one by applying a simple white-light irradiation at 10 K. When the light is switched off and the temperature is increased, the compound is relaxing around 45 K, back to the thermodynamically diamagnetic state. Additional optical reflectivity measurements employing different light wavelengths revealed that the diamagnetic [Fe$^{II}_{LS}$(μ-CN)Co$^{III}_{LS}$] state in **1** can be converted into the paramagnetic [Fe$^{III}_{LS}$(μ-CN)Co$^{II}_{HS}$] one by a photo-induced ET using 1050 to 365 nm

irradiation wavelengths (with an optimal wavelength of 1050 nm, and the less efficient one of 405 nm). X-ray absorption spectroscopy (XAS) and X-ray magnetic circular dichroism (XMCD) performed in synchrotron installations for compound **1** gave us local information about the oxidation state of the Co and the Fe metal centers at high and low temperatures, as well as under irradiation at 4 K. As expected, the obtained XAS data correlated well with the data obtained from the magnetic and photomagnetic susceptibility measurements, confirming once more the electron transfer phenomenon occurring between the two metal centers. The study of XMCD signal of the light-induced metastable state in compound **1** was performed in order to reveal the nature of the coupling between the cobalt and iron ions.[37] Additional experiments at low temperatures (T < 1 K) and analysis through theoretical calculations are necessary to be done. Combining the experimental data with Ligand Field Multiplet (LFM)[43] theoretical calculations, our collaborators from IMPMC will be able to deduce valuable information about the electronic and magnetic properties of the cobalt and iron sites in the pair, such as their spin and orbit magnetic moments.

The effect of the solvent around the pairs on the electron transfer properties opens new possibilities to manipulate the phenomenon by changing their chemical environment quite easily. The crystallization of the **1** from different reaction/crystallization solvents and the investigation of its properties in respect the metal-to-metal electron transfer in solid state are required in order to understand deeper the origin of the phenomenon.

II.5 Supporting Material

II.5.1 Experimental protocols

The ligands PY5Me2 and KTp were prepared using a procedure described in the literature.[25,29] The $(Bu_4N)[(Tp)Fe^{III}(CN)_3]$ precursor was synthesized by slightly modifying the procedure reported by Kim et al.[30] The synthesis of **1**•2DMF was performed under an argon atmosphere using standard Schlenk and glovebox techniques. The MeOH and DMF solvents were used as received from Aldrich. Diethylether was dried on and collected from a solvent purification system (PSMD5(2012)/Innovative Technology) before being stored under an argon atmosphere prior to use. Distilled water used as solvent for the synthesis of $Co^{II}(CF_3SO_3)_2$.

Preparation of $Co^{II}(CF_3SO_3)_2$. 0.2 g of $CoCO_3$ (1.6 mmol) were added in 10 ml of trifluoromethanesulfonic acid (0.5 g, 3.2 mmol) solution in water (30 ml). The mixture was stirred until CO_2 gas stopped to form. Then the solution was filtered and concentrated under reduced pressure, where $Co^{II}(CF_3SO_3)_2$ was precipitated as a pink solid. The compound was collected and dried in vacuum at 383 K. Yield: 0.46 g (82 %); MW = 465.16 g/mol; FT-IR (ATR, cm^{-1}): 1225 (vs), 1191 (vs), 1023 (vs), 626 (m), 593 (m).

Synthesis of $(Bu_4N)[(Tp)Fe^{III}(CN)_3]•3H_2O$. KTp (126 mg, 0.5 mmol) and KCN (160 mg, 2.5 mmol) were added to a mixture of MeOH (20 ml) and distilled water (10 ml). The solution was stirred, under aerobic conditions, until a clear colorless solution was obtained. This solution was added dropwise to a clear orange solution of 81.1 mg (0.5 mmol) of $FeCl_3$ in MeOH (40 ml). The color of the solution changed immediately to dark red and a red brown powder precipitated. After stirring at 70°C for 2 hours, the solution was filtered to remove insoluble KCl. Under reduced pressure, the orange solution was evaporated until dry, and the resulting orange powder was dissolved in 50 ml of hot water. Orange microcrystalline product was collected after filtration of the treated orange aqueous solution with 692 mg (2.5 mmol) of Bu_4NCl. Yield: 30 %; MW = 643.94 g/mol; FT-IR (ATR, cm^{-1}): 3445 (m), 2966 (m), 2937 (m), 2879 (m), 2511 (w), 2117 (m), 1661 (m), 1501 (w), 1486 (w), 1461 (w), 1433 (w), 1410 (m), 1381(w), 1313 (s), 1213 (s), 1153 (w), 1116 (s), 1077 (w), 1046 (s), 1006 (w), 986 (w), 879 (w), 822 (w), 797 (w), 775 (m), 756 (w), 712 (m), 659 (m), 615 (w).

Synthesis of $[\{(Tp)Fe^{III}(CN)_3\}\{Co^{II}(PY5Me_2)\}](CF_3SO_3)$•2DMF (1•2DMF). To a DMF solution (4 ml) of $PY5Me_2$ (40 mg, 0.09 mmol) was added 42 mg (0.12 mmol) of $Co^{II}(CF_3SO_3)_2$. The resulting pale yellow solution was stirred for 1 hour before adding 53 mg (0.09 mmol) of $(Bu_4N)[(Tp)Fe^{III}(CN)_3]$. The solution turned dark red and was stirred for four additional hours and then filtrated. Slow diffusion of diethylether vapor afforded orange needles of **1**•2DMF. Yield 70 %; MW = 1144.68 g/mol; FT-IR (ATR, cm^{-1}): 3095 (m), 2953 (m), 2512 (w), 2155 (m) 2120 (w), 2050 (w), 1674 (s), 1595 (m), 1499 (w), 1479 (m), 1437(m), 1403 (m), 1387 (m), 1313 (m), 1269 (s), 1208 (m), 1146 (m), 1114 (m), 1092 (m),

1049 (m), 1030 (s), 1017 (m), 988 (w), 909 (w), 864 (w), 754 (m), 709 (m), 634 (m), 572 (w); Elemental analysis calc. for C48H49N16CoFeO5BF3S (**1**•2DMF): C 50.4, H 4.3, N 19.6; found: C 49.6, H 4.3, N 19.2 %.

Preparation of [{(Tp)$Fe^{III}(CN)_3$}{$Co^{II}(PY5Me_2)$}](CF_3SO_3) (1). Orange needles of **1**•2DMF were kept in diethylether and sonicated for 30 minutes. The resulting orange microcrystalline powder was filtered and dried in a vacuum oven (at a few mbars and 50°C) for 24 hours, resulting in a dark orange powder. MW = 998.50 g/mol; FT-IR (ATR, cm^{-1}): 3095 (w), 2953 (w), 2510 (w), 2156 (m) 2123 (w), 2049 (w), 1730 (w), 1595 (m), 1499 (w), 1479 (m), 1437 (m), 1403 (m), 1387 (m), 1313 (m), 1269 (s), 1208 (m), 1146 (m), 1114 (m), 1092 (m), 1049 (m), 1030 (s), 1017 (m), 988 (w), 909 (w), 864 (w), 754 (m), 709 (m), 634 (m), 572 (w); Elemental analysis calc. for C42H41N14CoFeO6BF3S (**1**+$3H_2O$): C 47.9, H 3.9, N 18.6; found: C 47.9, H 4.1, N 18.3. As **1** is highly hygroscopic, the three water molecules considered in the elemental analysis are most likely the result of the solvatation of **1** by the atmosphere during the preparation of the sample for elemental analysis.

II.5.2 Physical methods of characterization

Elemental analysis. Elemental analysis for C, H and N were performed following the classical Pregl-Dumas technique for fluorine samples on a Thermo Fischer Flash EA 1112 equipment at Institut de Chimie de la Matière Condensée de Bordeaux (ICMCB).

FT-IR spectroscopy. FT-IR spectra were recorded in the 400–4000 cm^{-1} range on a Thermal Scientific Nicolet 6700 ATR (attenuated total reflection) spectrometer equipped with a smart iTR diamond window, housed at the Centre de Recherche Paul Pascal.

Crystallographic data. Single crystals of **1**•2DMF and **1**•*n*(solv) were mounted in CargilleTM NHV immersion oil on a 50 mm MicroMounts™ rod at different temperatures 200, 180, 120 and 90 K. The crystallographic data were collected with a Bruker APEX II Quasar diffractometer, housed at the Centre de Recherche Paul Pascal, and equipped with a graphite monochromator centered on the MoK_α path. Single crystal of (Bu_4N)[(Tp)$Fe^{III}(CN)_3$]•$3H_2O$ was mounted in CargilleTM NHV immersion oil on a 50 mm MicroMounts™ rod at 120 K. The crystallographic data were collected with a Bruker APEX II Quasar diffractometer, housed at the Institut de Chimie de la Matière Condensée de Bordeaux, and equipped with a graphite monochromator centered on the MoK_α path. The program SAINT was used to integrate the data, which were thereafter corrected for absorption using SADABS.[43] All structures were solved by direct methods and refined by a full-matrix least-squares method on F^2 using SHELXL-2013.[44] All non-hydrogen atoms were refined anisotropically. Hydrogen atoms were assigned to ideal positions and refined isotropically using suitable riding models. Reflections were merged by SHELXL according to the crystal class for the calculation of statistics and refinement. Figures II-5 to II-7, II-12 and II-13 were generated using CrystalMaker® (CrystalMaker Software Ltd, www.crystalmaker.com). The

crystallographic information files are available free of charge via the Internet at http://pubs.acs.org. The crystallographic data have also been deposited at the Cambridge Crystallographic Data Centre under deposition numbers CCDC 1017849-1017853 and are available via www.ccdc.cam.ac.uk/data_request/cif).

Table S.II-1. Crystallographic data, selected bond lengths and distances [Å] and angles [°] for $(Bu_4N)[(Tp)Fe^{III}(CN)_3]\bullet 3H_2O$ at 120 K.

Compound	$(Bu_4N)[(Tp)Fe^{III}(CN)_3]\bullet 3H_2O$
FW / g·mol^{-1}	643.94
Crystal color	orange
Crystal system	triclinic
Space group	*P*-1
Temperature / K	120
***a* / Å**	11.1956(4)
***b* / Å**	11.2191(4)
***c* / Å**	15.9740(6)
***α* / °**	87.2840(10)
***β* / °**	76.7360(10)
***γ* / °**	60.8650(10)
***V* / Å^3**	1700.91(11)
Z	2
Fe1-C1 / Å	1.931(8)
Fe1-C2 / Å	1.920(7)
Fe1-C3 / Å	1.939(8)
Fe1-N4 / Å	1.977(6)
Fe1-N6 / Å	1.975(8)
Fe1-N8 / Å	1.973(6)
N1...O3 / Å	2.934(6)
N2...O2 / Å	3.008(6)
[a]R_1 ($I > 2\sigma(I)$)	0.0630
[b]wR_2 (all data)	0.1801
R_{int}	0.0277

[a] $R_1 = \Sigma||F_0|-|F_C||/\Sigma|F_0|$, [b] $wR_2 = [\Sigma w(F_0^2-F_C^2)^2/\Sigma w(F_0^2)^2]^{1/2}$

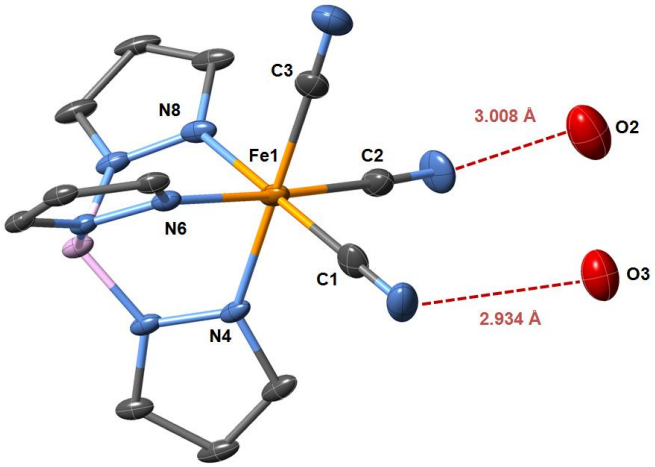

Figure S.II-1. ORTEP-type view of the anionic complex $(Bu_4N)[(Tp)Fe^{III}(CN)_3]\bullet 3H_2O$ at 120 K. Thermal ellipsoids are depicted at the 50 % probability level. All anions and hydrogen atoms are omitted for clarity. With red dashed lines are shown the H-bonds between the –CN groups of the anionic complex, and the lattice water molecules. Fe, N, C, B and O atoms are indicated in orange, light blue, grey, pink and red respectively.

Thermogravimetric Analysis (TGA). The TGA measurements were carried out on freshly filtered crystals of **1**•2DMF and dried sample of **1** (dried at 50°C under vacuum for 24 hours) using the thermogravimetric analyser SETARAM TAG 16, housed at the Centre de Recherche Paul Pascal. The TG measurements were carried out using 8.7 and 15.9 mg of **1**•2DMF and 25.57 mg of **1**. In Figure S.II-2, the weight loss of 13 % in the 60-200 °C temperature region in **1**•2DMF (blue) corresponds well to the loss of two DMF molecules, fact that it is supported by the almost unchanged TGA data for the desolvated compound **1** (red) in the same temperature region. Moreover, compound **1** seems to be stable up to 150°C.

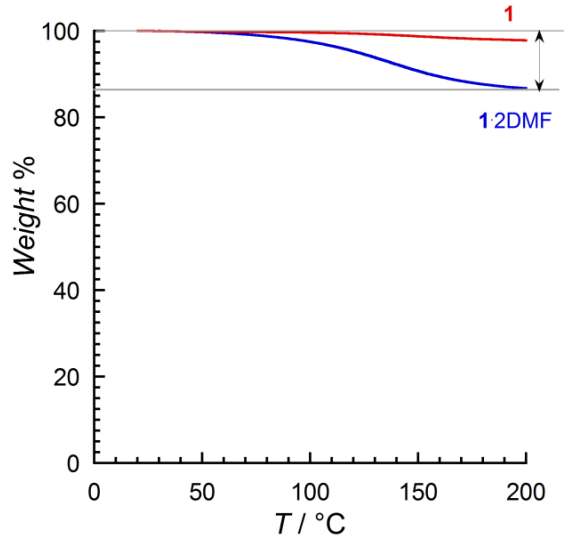

Figure S.II-2. TGA of **1**•2DMF and **1** at a heating rate of 1 and 2 °C / min respectively as function of the temperature under Ar atmosphere between 30 and 200 °C.

Magnetic measurements. Magnetic susceptibility measurements were performed on a Quantum Design SQUID magnetometer MPMS-XL housed at the Centre de Recherche Paul Pascal at temperatures between 1.8 and 400 K and dc magnetic fields ranging from -7 to 7 T. In the absence of light, measurements were reproducibly performed using polycrystalline samples. Crystals of **1**•2DMF were covered and thus restrained in a minimum amount of frozen mother liquor within a sealed straw to prevent their desolvation. No evaporation of the mother liquor was observed during the measurements. The mass of the sample was estimated at 19.43 mg after the measurements and after the mother liquor removal/evaporation. Complex **1** was measured on a sample obtained by keeping **1**•2DMF in diethylether with sonication for 30 minutes, before filtering and drying in a vacuum oven (at a few mbars and 50°C) for 24 hours. The resulting dark orange powder (10.97 mg) was then introduced in a sealed polyethylene bag (3 × 0.5 × 0.02 cm). Microcrystalline powder of $(Bu_4N)[(Tp)Fe^{III}(CN)_3]\bullet 3H_2O$ (13.24 mg) introduced in sealed polyethylene bag, which was containing 10.88 mg of paraton oil. Prior to the experiments, the field-dependent magnetization was measured at 100 K on each sample in order to detect the presence of any bulk ferromagnetic impurities. In fact, paramagnetic or diamagnetic materials should exhibit a perfectly linear dependence of the magnetization that extrapolates to zero at zero dc field. The samples appeared to be free of any significant ferromagnetic impurities. The magnetic data were corrected for the sample holder, solvent and the intrinsic diamagnetic contributions.

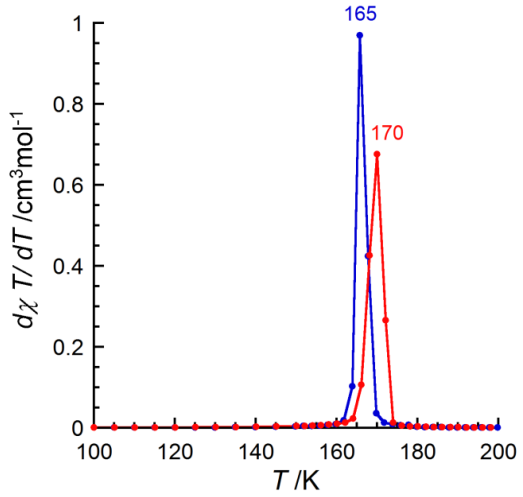

Figure S.II-3. The derivative of the χT (i.e. $d\chi T/dT$) versus T curve at 1 T for **1** in cooling (blue) and heating (red) modes at 0.67 K/min.

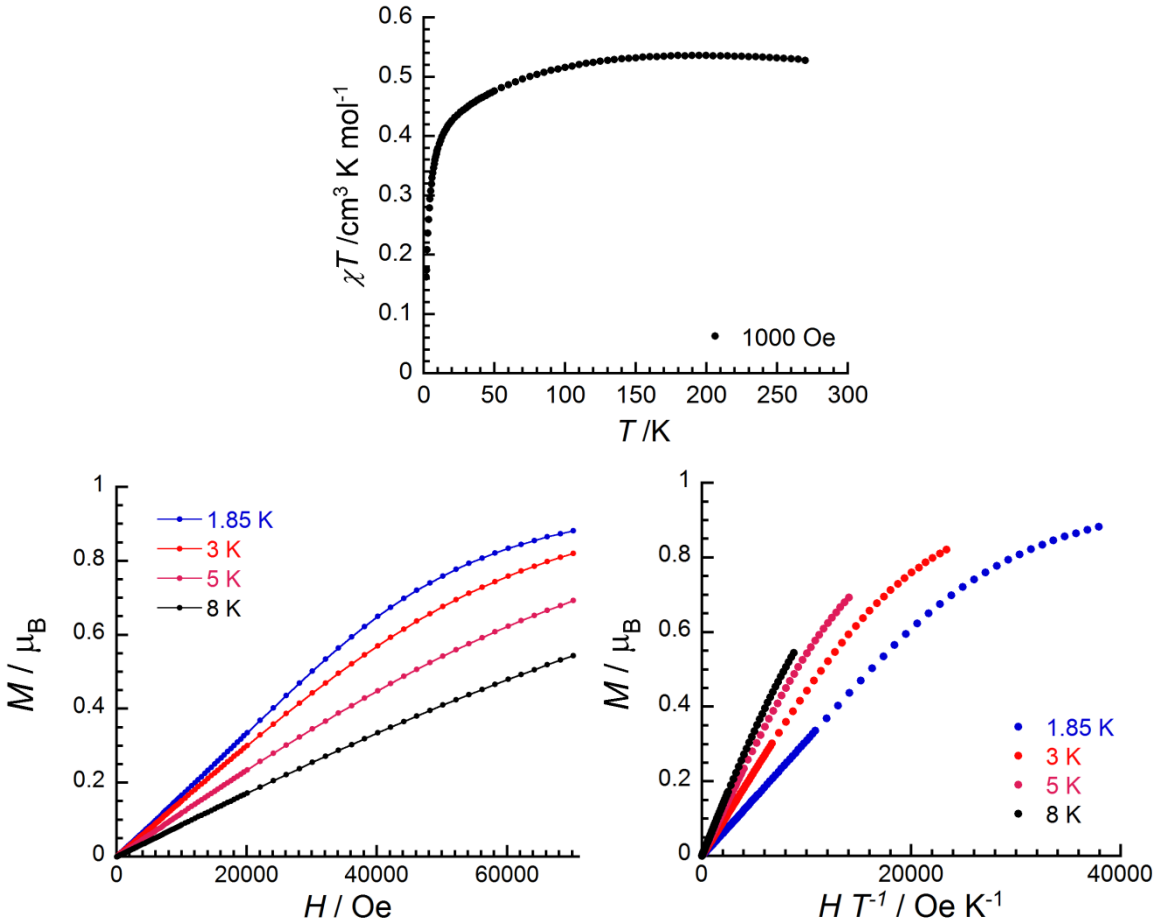

Figure S.II-4. (top) The χT versus T curve at 0.1 T, (bottom left) the magnetization versus field H, and (bottom right) the reduced magnetization curve for $(Bu_4N)[(Tp)Fe^{III}(CN)_3]\bullet 3H_2O$ at different temperatures; blue, 1.85 K; red, 3 K; pink, 5 K; black, 8 K.

Optical measurements. Surface reflectivity measurements were performed on a home built system, housed at the Centre de Recherche Paul Pascal, at temperatures ranging between 10 and 300 K. A tungsten-halogen light source was used (Leica CLS 150 XD, adjustable up to 1 W/cm^2) at wavelengths between 400 and 1000 nm. All measurements were calibrated against a NIST traceable reflectance standard (sphereOptics, ref SG3054).

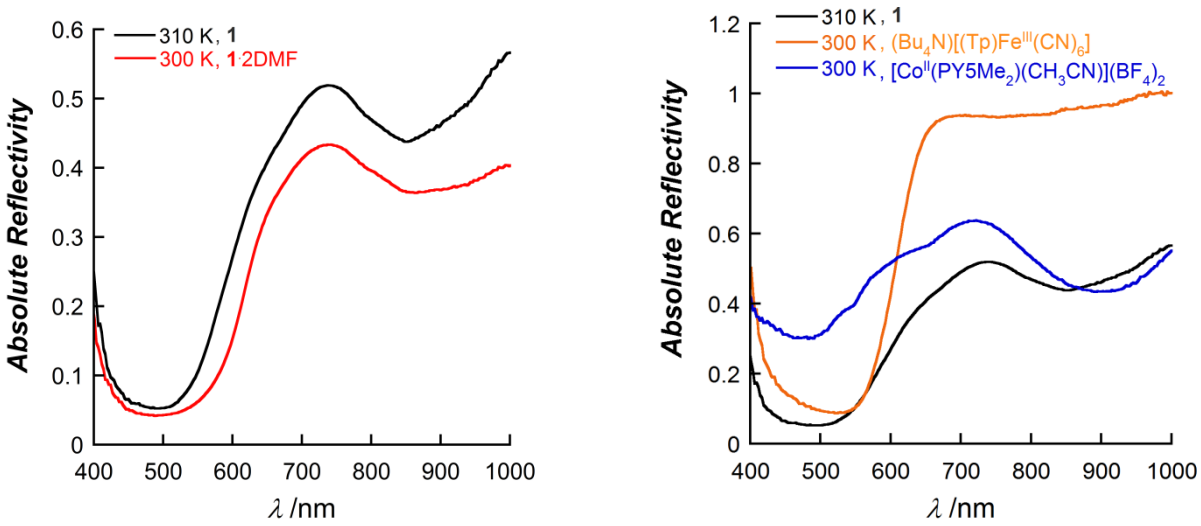

Figure S.II-5. (left) Reflectivity spectra of **1**•2DMF (red) and **1** (black) as function of wavelength at room temperature; (right) reflectivity spectra of **1** (black), $(Bu_4N)[(Tp)Fe^{III}(CN)_3]\bullet 3H_2O$ (orange) and $[(PY5Me_2)Co^{II}(MeCN)](BF_4)_2$ (blue), as function of wavelength at room temperature.

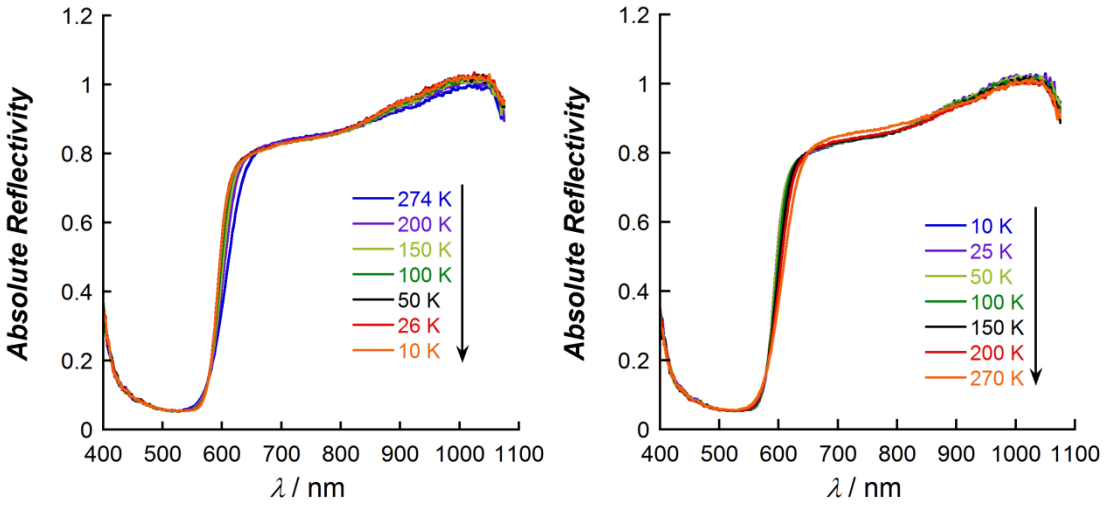

Figure S.II-6. Reflectivity spectra between 270 and 10 K as function of wavelength in cooling (left) and heating mode (right) for $(Bu_4N)[(Tp)Fe^{III}(CN)_3]\bullet 3H_2O$.

Photomagnetic measurements. Photomagnetic experiments were carried out at Institut de Chimie de la Matière Condensée de Bordeaux (ICMCB) and utilized a Quantum Design SQUID magnetometer MPMS-XL and a 150 W halogen lamp (LEICA CLS 150 XD) coupled to an optical fiber that was directed into the magnetometer cavity. A 4.6 mg sample of **1** was introduced into a preformed straw at a distance of 3 cm from the optical fiber end [incident light flux = 3 mW/cm^2]. Sample temperatures were corrected for light-induced heating (avg. +2 K with white light of 3 mW/cm^2) by calibrating the experimental sample temperatures to the data collected in the absence of light.

XAS/XMCD studies. X-ray Absorption Spectroscopy (XAS) and X-ray Magnetic Circular Dichroism (XMCD) investigations were carried out at SIM beamline of SLS synchrotron (Paul Scherrer Institut, Villigen, Switzerland) for compound **1** in collaboration with Sadaf Fatima, Marie-Anne Arrio and Philippe Sainctavit from IMPMC (University of Paris VII), and Edwige Otero and Loic Joly (Soleil).

II.6 References

(1) Sato, O.; Iyoda, T.; Fujishima, A.; Hashimoto, K. *Science* **1996**, *272*, 704.
(2) Bleuzen, A.; Lomenech, C.; Escax, V.; Villain, F.; Varret, F.; Cartier dit Moulin, C.; Verdaguer, M. *J. Am. Chem. Soc.* **2000**, *122*, 6648.
(3) (a) Champion, G.; Escax, V.; Cartier dit Moulin, C.; Bleuzen, A.; Verdaguer, M. *J. Am. Chem. Soc.* **2001**, 123, 12544. (b) Goujon, A.; Roubeau, O.; Varret, F.; Dolbecq, A.; Bleuzen, A.; Verdaguer, M. *Eur. Phys. J. B* **2000**, *14*, 115.
(4) Cartier dit Moulin, C.; Villain, F.; Bleuzen, A.; Arrio, M.-A.; Sainctavit, P.; Lomenech, C.; Escax, V.; Baudelet, F.; Dartyge, E.; Gallet, J.-J.; Verdaguer, M. *J. Am. Chem. Soc.* **2000**, *122*, 6653.
(5) Escax, V.; Bleuzen, A.; Cartier dit Moulin, C.; Villain, F.; Goujon, A.; Varret, F.; Verdaguer, M. *J. Am. Chem. Soc.* **2001**, *123*, 12536.
(6) Sato, O.; Einaga, Y.; Fujishima, A.; Hashimoto, K. *Inorg. Chem.* **1999**, *38*, 4405.
(7) Shimamoto, N.; Ohkoshi, S.-i.; Sato, O.; Hashimoto, K. *Inorg. Chem.* **2002**, *41*, 678.
(8) Liu, T.; Zhang, Y.-J.; Kanegawa, S.; Sato, O. *Angew. Chem., Int. Ed.* **2010**, *49*, 8645.
(9) Liu, T.; Zhang, Y.-J.; Kanegawa, S.; Sato, O. *J. Am. Chem. Soc.* **2010**, *132*, 8250.
(10) Hoshino, N.; Iijima, F.; Newton, G. N.; Yoshida, N.; Shiga, T.; Nojiri, H.; Nakao, A.; Kumai, R.; Oshio, H. *Nat. Chem.* **2012**, *4*, 921.
(11) (a) Berlinguette, C.; Dragulescu-Andrasi, A.; Sieber, A.; Galàn- Mascaròs, J. R.; Güdel, H.-U.; Achim, C.; Dunbar, K. R. *J. Am. Chem. Soc.* **2004**, *126*, 6222. (b) Berlinguette, C.; Dragulescu-Andrasi, A.; Sieber, A.; Güdel, H.-U.; Achim, C.; Dunbar, K. R. *J. Am. Chem. Soc.* **2005**, *127*, 6766.
(12) Later, in 2011, this complex was reported to display a photoinduced intramolecular electron transfer: Funck, K. E.; Prosvirin, A. V.; Mathonière, C.; Clérac, R.; Dunbar, K. R. *Inorg. Chem.* **2011**, *50*, 2782.
(13) Li, D.; Clérac, R.; Roubeau, O.; Harté, E.; Mathonière, C.; Le Bris, R.; Holmes, S. M. *J. Am. Chem. Soc.* **2008**, *130*, 252.
(14) Zhang, Y.; Li, D.; Clérac, R.; Kalisz, M.; Mathonière, C.; Holmes, S. M. *Angew. Chem., Int. Ed.* **2010**, *49*, 3752.
(15) Mercurol, J.; Li, Y.; Pardo, E.; Risset, O.; Seuleiman, M.; Rousselière, H.; Lescouëzec, R.; Julve, M. *Chem. Commun.* **2010**, *46*, 8995.
(16) Nihei, M.; Sekine, Y.; Suganami, N.; Nakazawa, K.; Nakao, A.; Nakao, H.; Murakami, Y.; Oshio, H. *J. Am. Chem. Soc.* **2011**, *133*, 3592.
(17) (a) Siretanu, D.; Li, D.; Buisson, L.; Bassani, D. M.; Holmes, S. M.; Mathonière, C.; Clérac, R. *Chem.-Eur. J.* **2011**, *17*, 11704. (b) Zhang, Y.-Z.; Ferko, P.; Siretanu, D.; Ababei, R.; Rath, N. P.; Shaw, M. J.; Clérac, R.; Mathonière, C.; Holmes, S. M. *J. Am. Chem. Soc.* **2014**, *136*, 16854.
(18) Mondal, A.; Li, Y.; Seuleiman, M.; Julve, M.; Toupet, L.; Buron-Le Cointe, M.; Lescouëzec, R. *J. Am. Chem. Soc.* **2013**, *135*, 1653.
(19) Cao, L.; Tao, J.; Gao, Q.; Liu, T.; Xia, Z.; Li, D. *Chem. Commun*. **2014**, *50*, 1665.
(20) Catala, L.; Volatron, F.; Brinzei, D.; Mallah, T. *Inorg. Chem.* **2009**, *48*, 3360.

(21) Bernhardt, P. V.; Martinez, M. *Inorg. Chem.* **1999**, *38*, 424.
(22) Bernhardt, P. V.; Macpherson, B. P.; Martinez, M. *Inorg. Chem.* **2000**, *39*, 5203.
(23) Bernhardt, P. V.; Macpherson, B. P.; Martinez, M. *J. Chem. Soc., Dalton Trans.* **2002**, 1435.
(24) Jeon, I.-R.; Calancea, S.; Panja, A.; Piñero Cruz, D. M.; Koumousi, E. S.; Dechambenoit, P.; Coulon, C.; Wattiaux, A.; Rosa, P.; Mathonière, C.; Clérac, R. *Chem. Sci.* **2013**, *4*, 2463.
(25) Bechlars, B.; D'Alessandro, D. M.; Jenkins, D. M.; Iavarone, A. T.; Glover, S. D.; Kubiak, C. P.; Long, J. R. *Nat. Chem.* **2010**, *2*, 362.
(26) (a) Addison, A. W.; Burke, P. J. *J. Heterocycl. Chem.* **1981**, *18*, 803; (b) Panja, A.; Guionneau, P. ; Jeon, I.-R. ; Holmes, S. M.; Clérac, R.; Mathonière, C. *Inorg. Chem.* **2012**, *51*, 12350.
(27) Rogez, G.; Marvillers, A.; Sarr, P.; Parsons, S.; Teat, S. J.; Ricard, L.; Mallah, T. *Chem. Commun.* **2002**, *14*, 1460.
(28) Koumousi, E. S.; Jeon, I.-R.; Gao, Q.; Dechambenoit, P.; Merzeau, P.; Buisson, L.; Jia, B.; Li, D.; Woodruff, D. N.; Voltaron, F.; Mathonière, C.; Clérac, R. *J. Am. Chem. Soc.*, **2014**, *136*, 15461**.**
(29) Trofimenko, S. *Inorg. Synth.* **1970**, *12*, 99.
(30) Kim, J. I.; Han, S.; Cho, I.-K.; Choi, K. Y.; Heu, M.; Yoon, S.; Suh, B. *Polyhedron* **2004**, *23*, 1333.
(31) Nakamoto, K. *Infrared and Raman Spectra of Inorganic and Coordination Compounds*, 5th Ed. John Wiley and Sons: New York, **1997**.
(32) Zadrozny, J. M.; Freedman, D. E.; Jenkins, D. M.; Harris, T. H.; Iavarone, A. T.; Mathonière, C.; Clérac, R.; Long, J. R. *Inorg. Chem.* **2010**, *49*, 8886.
(33) (a) Lescouëzec, R.; Vaissermann, J.; Lloret, F.; Julve, M.; Verdaguer, M. *Inorg. Chem.* **2005**, *41*, 5943. (b) Li, D.; Parkin, S.; Wang, G.; Yee, G. T.; Holmes, S. M. *Inorg. Chem.* **2006**, *45*, 1951.
(34) Stöhr, J.; Siegmann, H. C. *Magnetism – From Fundamentals to Nanoscale Dynamics, Part III, Polarized Electron and X-Ray Techniques*, Springer Berlin Heidelberg: Berlin; **2006**, 351.
(35) Brouder, C.; Kappler, J. P. in Beaurepaire, E., Carrière, B., Kappler, J. P. (Eds.) *Magnetism and Synchrotron Radiation*, Editions de Physique, Les Ulis, Springer: New York; **1997**, 19.
(36) Cartier dit Moulin, C.; Villain, F.; Bleuzen, A.; Arrio, M.-A.; Sainctavit, P.; Lomenech, C.; Escax, V.; Baudelet, F.; Dartyge, E.; Gallet, J.-J.; Verdaguer, M. *J. Am. Chem. Soc.* **2000**, *122*, 6653.
(37) Champion, G.; Escax, V.; Cartier dit Moulin, C.; Bleuzen, A.; Villain, F.; Baudelet, F.; Dartyge, E.; Verdaguer, M. *J. Am. Chem. Soc.* **2001**, *123*, 12544.
(38) Baker, M. L.; Kitagawa, Y.; Nakamura, T.; Tazoe, K.; Narumi, Y.; Kotani, Y.; Iijima, F.; Newton, G. N.; Okumura, M.; Oshio, H.; Nojiri, H. *Inorg. Chem.* **2013**, *52*, 13956.
(39) Sekine, Y.; Nihei, M.; Kumai, R.; Nakao, H.; Murakami Y.; Oshio, H. *Chem. Commun.* **2014**, *50*, 4050.

(40) (a) van der Laan, G.; Kirkman, I. W. *J. Phys: Condens. Matter* **1992**, *4*, 4189. (b) van der Laan, G.; Thole, B. T. *Phys Rev. Lett.* **1988**, *60*, 1977. (c) van der Laan, G. *Physica B* **1989**, *158*, 395.
(41) Cartier dit Moulin, C.; Rudolf, P.; Flank, A.-M.; Chen, C. T. *J. Phys. Chem.* **1992**, *96*, 6196.
(42) Thole, B.; Vanderlaan, G.; Fuggle, J.; Sawatzky, G.; Karnatak, R.; Esteva, J. *Phys. Rev. B* **1985**, *32*, 5107.
(43) Sheldrick, G. M. SADABS, version 2.03, Bruker Analytical X-Ray Systems, Madison, WI, **2000**.
(44) Sheldrick, G. M. *Acta Cryst.* **2008**, *A64*, 112.
(45) Mitcov, D. *PhD thesis, Bordeaux University*, **2014**.

Chapter III

Modulating the electron transfer properties of the {Fe(μ-CN)Co} elementary unit in solid state via anion exchange

Table of Contents for Chapter III:

III.1 Introduction

The study of the two first switchable pairs described in the previous chapters, [{(BBP)Fe(CN)$_3$}{Co(PY5Me$_2$)}][1] and [{(Tp)Fe(CN)$_3$}{Co(PY5Me$_2$)}](CF$_3$SO$_3$)•2DMF (**1**•2DMF),[2] shows the important role of i) the capping ligands on both metal centers and, ii) the environment of the molecular object, associated with the switching of the magnetic and optical properties. More specifically, in the first compound the change of the capping ligands modify the redox potentials of the concerned sites allowing a thermally and light-induced intramolecular ET. In the second compound, the elimination of the lattice solvent changes the degree of the completion and the characteristic temperature of the electron transfer phenomenon. By analyzing closely the crystal packing of **1**•2DMF (Figure III-1), we observed weak interactions between the disordered DMF solvents and the pairs, that can explain the different properties between the compound **1**•2DMF and its desolvated form, **1** (Chapter II, Figure II-14). Moreover, weak interactions between the pairs in **1**•2DMF were revealed by two ways: a) directly, by weak interactions between the free –CN groups of one pair and the methyl groups in the PY5Me$_2$ ligand of a second pair and b) indirectly, by weak interactions through the lattice solvents and the disordered $CF_3SO_3^-$ counter ion. Therefore, by only changing the environment of these molecular objects, it is possible to obtain new systems showing interesting thermally- and/or light-induced intramolecular electron transfer.

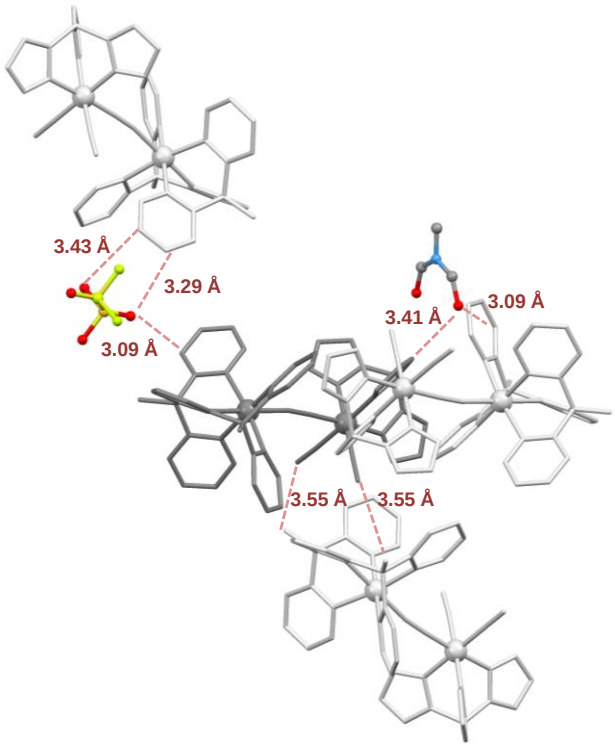

Figure III-1. View of the crystal structure of **1**•2DMF at 180 K showing the weak interactions between the cationic complexes, the disordered $CF_3SO_3^-$ anion and the disordered lattice DMF molecule. All the atoms of the cationic complex are in light and dark grey color for clarity. N, C, S, O and F atoms are indicated in light blue, dark grey, yellow, red and green, respectively.

In this direction, we searched for small modifications accessible in compound **1**•2DMF, that can alter its properties. The cationic unit $[(Tp)Fe(CN)_3Co(PY5Me_2)]^+$ in **1**•2DMF, which is compensated by one $CF_3SO_3^-$ anion, inspired us to exchange the counter ions. Two new cyanide-bridged {Fe(μ-CN)Co} pairs have been prepared:

- $[\{(Tp)Fe(CN)_3\}\{Co(PY5Me_2)\}](PF_6)$•2DMF (**2**•2DMF)

- $[\{(Tp)Fe(CN)_3\}\{Co(PY5Me_2)\}](AsF_6)$•2DMF (**3**•2DMF)

The synthesis and the structural, optical, magnetic and photomagnetic properties in solid state of **2**•2DMF and **3**•2DMF, as well as their desolvated forms **2** and **3**, respectively, are described in this chapter.

III.2 Synthesis, Characterization and Physical Properties of two New Dinuclear {Fe(μ-CN)Co} Complexes

III.2.1 Synthesis and FT-IR characterization of $[\{(Tp)Fe(CN)_3\}\{Co(PY5Me_2)\}](PF_6)$•2DMF (2•2DMF) and $[\{(Tp)Fe(CN)_3\}\{Co(PY5Me_2)\}](AsF_6)$•2DMF (3•2DMF)

Complexes **2**•2DMF and **3**•2DMF were synthesized and crystallized according to the procedure followed for the preparation of **1**•2DMF (see section II.5.1) with a slight modification in order to perform the anion exchange. In this case, $Co^{II}(CF_3SO_3)_2$ is added in a solution of $PY5Me_2$ in DMF, together with the desired counter ion hexaflurophospate (PF_6^-) for **2**•2DMF and hexafluoroarsenate (AsF_6^-) for **3**•2DMF (the detailed preparation is described in section III.6.1). The orange color of the needle-like products obtained from both reactions, combined with the high energy values of cyanide (bridging at 2158 cm^{-1} and terminal at 2122 cm^{-1}) and B-H (at 2514 cm^{-1}) stretching bands observed in the FT-IR spectra (Figure III-2, bottom left) suggest that at room temperature compounds **2**•2DMF and **3**•2DMF are indeed cyanido-bridged pairs in their paramagnetic $\{Fe^{III}_{LS}(\mu\text{-CN})Co^{II}_{HS}\}$ state. The FT-IR spectra of both compounds show a strong C=O band (1678 cm^{-1}) suggesting the presence of co-crystallized DMF molecules, as it was observed in **1**•2DMF (Figure III-2, bottom left). The comparison of the full range FT-IR spectra (from 3500 to 500 cm^{-1}) of **2**•2DMF and **3**•2DMF with the corresponding of compound **1**•2DMF (Figure III-2, top) demonstrates the strong similarities between them due to the presence of the same organic ligands ($PY5Me_2$ and Tp^-). The main differences are the characteristic bands of each counter ion used for the synthesis of each compound (Figure III-2, bottom right). In the spectra of **2**•2DMF and **3**•2DMF, the characteristic stretching vibrations at 837 cm^{-1} in the PF_6^- anions and 695 cm^{-1} in the AsF_6^- anions are appearing, respectively, whereas the characteristic stretching vibrations for the $CF_3SO_3^-$ anions at 1270, 1030 and 638 cm^{-1} are absent.

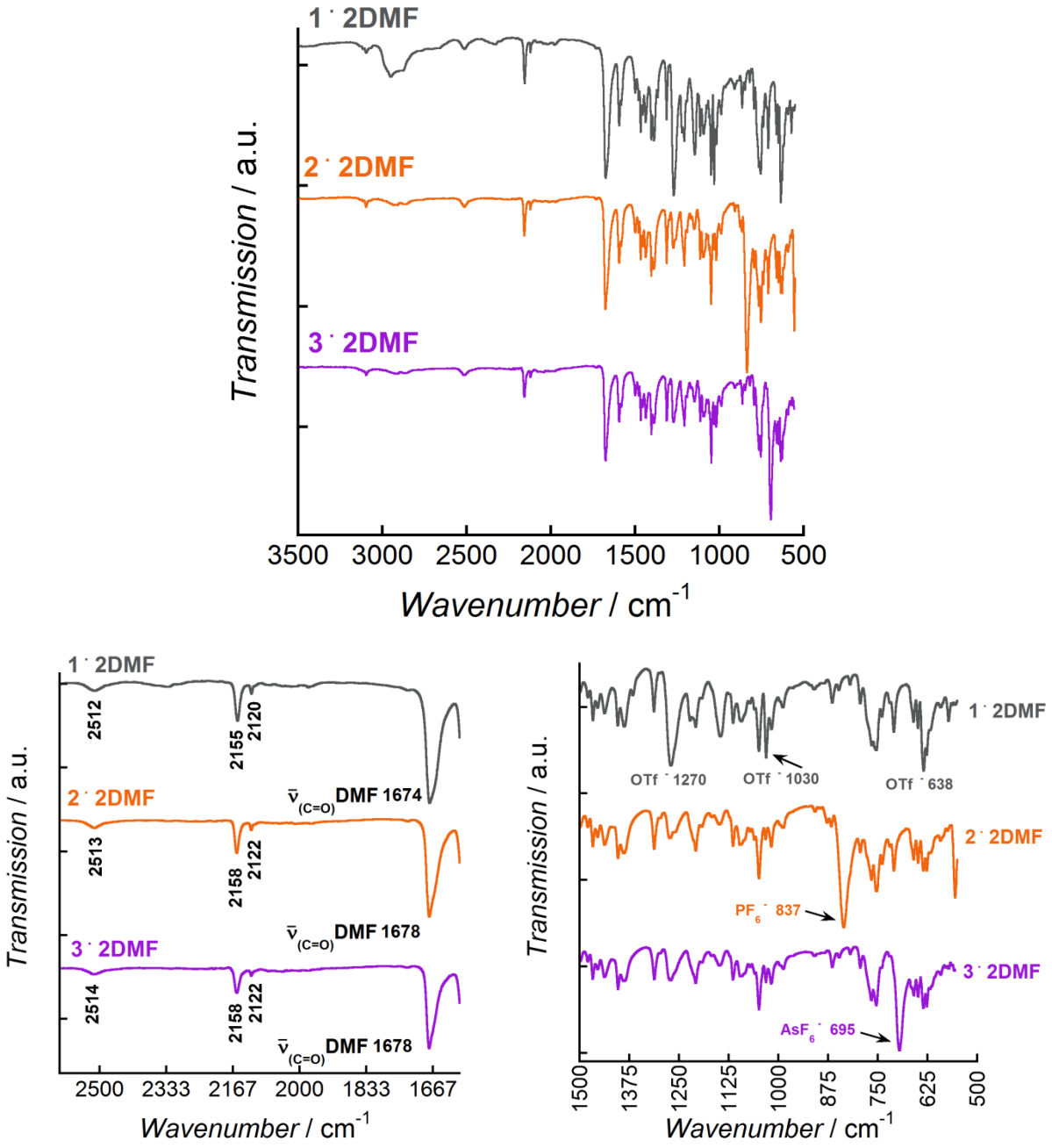

Figure III-2. The FT-IR spectra of **1**•2DMF (top, gray), **2**•2DMF (top, orange) and **3**•2DMF (top, purple), a portion of all spectra between 2600 and 1600 cm^{-1} for the comparison of **1**•2DMF, **2**•2DMF and **3**•2DMF (bottom, left) and a portion of all spectra between 1500 and 500 cm^{-1} for the comparison of **1**•2DMF, **2**•2DMF and **3**•2DMF (bottom, right) at 298 K.

III.2.2 Structural investigations for compounds 2•2DMF and 3•2DMF

Single-crystal X-ray diffraction studies at 220 and 250 K for **2**•2DMF and **3**•2DMF, respectively, reveal that the complexes crystallize in the orthorhombic *Pnma* space group (Figures III-3 and III-4, and Table III-1). The cationic $[\{(Tp)Fe(CN)_3\}\{Co(PY5Me_2)\}]^+$ units, that reside on a mirror plane, contain one Fe and one Co metal ions, which are hexacoordinated with distorted octahedral geometries (Figures III-3 and III-4, and Table III-2). Their separation (Fe···Co) is 5.056(1) Å at 220 K for **2**•2DMF and 5.068(2) at 250 K for **3**•2DMF.

In each complex, the two metal centers (Fe and Co) are linked by one, almost linear, cyanide ligand (Fe1−C1−N1 and C1−N1−Co1 angles are 177.3(16)° and 172.3(9)°, respectively for **2**•2DMF, and 177.4(3)° and 172.0(8)°, respectively for **3**•2DMF, see Table III-2) to form a [FeCo] pair (Figures III-3 and III-4). The Fe site bears two terminal cyanide ligands, and its coordination sphere is completed by three N atoms from the Tp^- ligand in facial configuration. On the other hand, the Co center completes its coordination sphere with the five N donor atoms from the $PY5Me_2$ ligand. The average Fe−C and Fe−N bonds are 1.917(4) and 1.982(4) Å, respectively for **2**•2DMF, and 1.929(6) and 1.984(6) Å, respectively for **3**•2DMF, while the average $Co-N_{NC}$ and $Co-N_{py}$ bonds are 2.042(4) and 2.135(2) Å, respectively for **2**•2DMF, and 2.058(8) and 2.140(5) Å, respectively for **3**•2DMF (Table III-2). These structural features confirm the presence of LS Fe^{III} and HS Co^{II} metal ions in **2**•2DMF and **3**•2DMF and thus the stabilization of paramagnetic dinuclear complexes at 220 and 250 K, respectively.

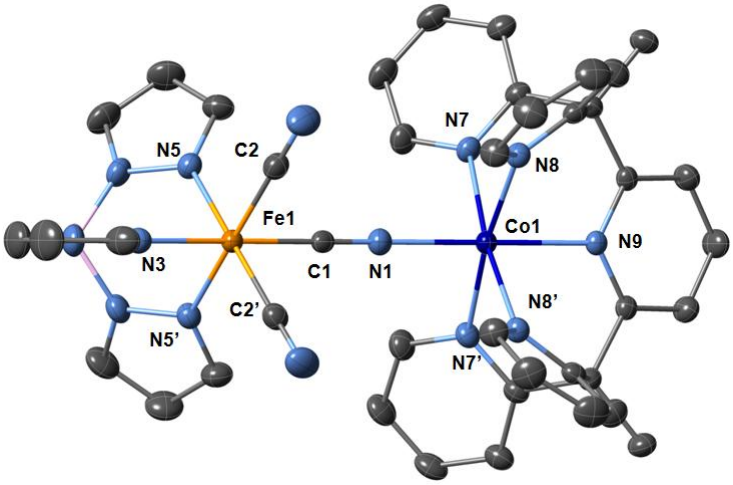

Figure III-3. ORTEP-type view of the cationic complex in **2**•2DMF at 220 K. Thermal ellipsoids are depicted at the 40% probability level. All anions, lattice solvents, and hydrogen atoms are omitted for clarity. Fe, Co, N, C, and B atoms are indicated in orange, dark blue, light blue, gray, and pink, respectively.

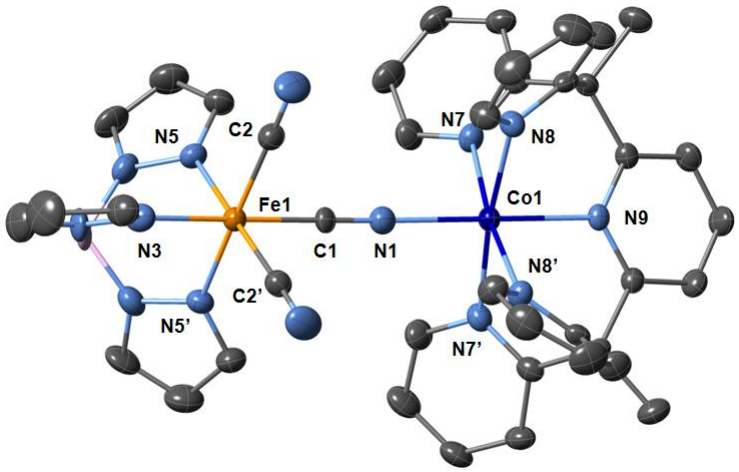

Figure III-4. ORTEP-type view of the cationic complex in **3**•2DMF at 250 K. Thermal ellipsoids are depicted at the 40% probability level. All anions, lattice solvents, and hydrogen atoms are omitted for clarity. Fe, Co, N, C, and B atoms are indicated in orange, dark blue, light blue, gray, and pink, respectively.

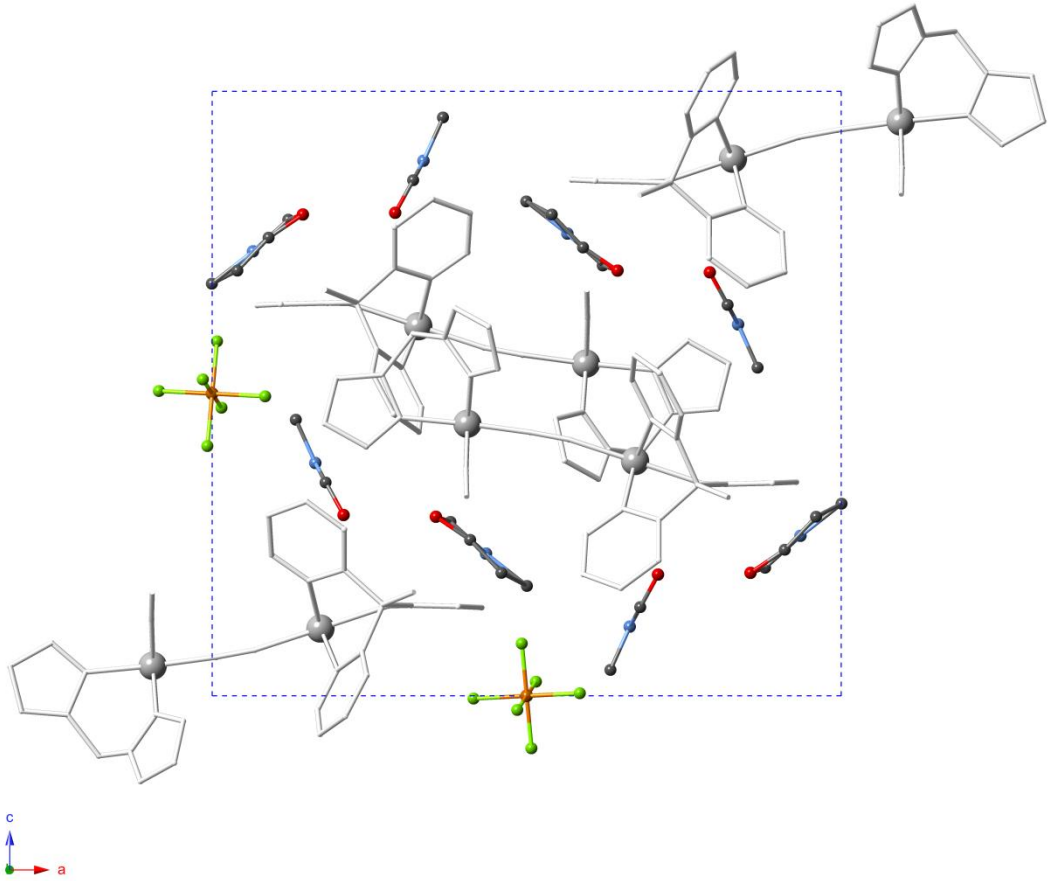

Figure III-5. Projection view of the crystal structure of **2**•2DMF at 220 K showing the packing of the cationic complexes, the PF_6^- anions and the lattice DMF molecules in the (*ac*) plane. All the atoms of the cationic complexes are in light gray color for clarity. The PF_6^- anions, the lattice DMF molecules and the metal centers are visualized in balls and sticks for clarity. N, C, P, O and F atoms are indicated in light blue, dark gray, orange, red and green, respectively.

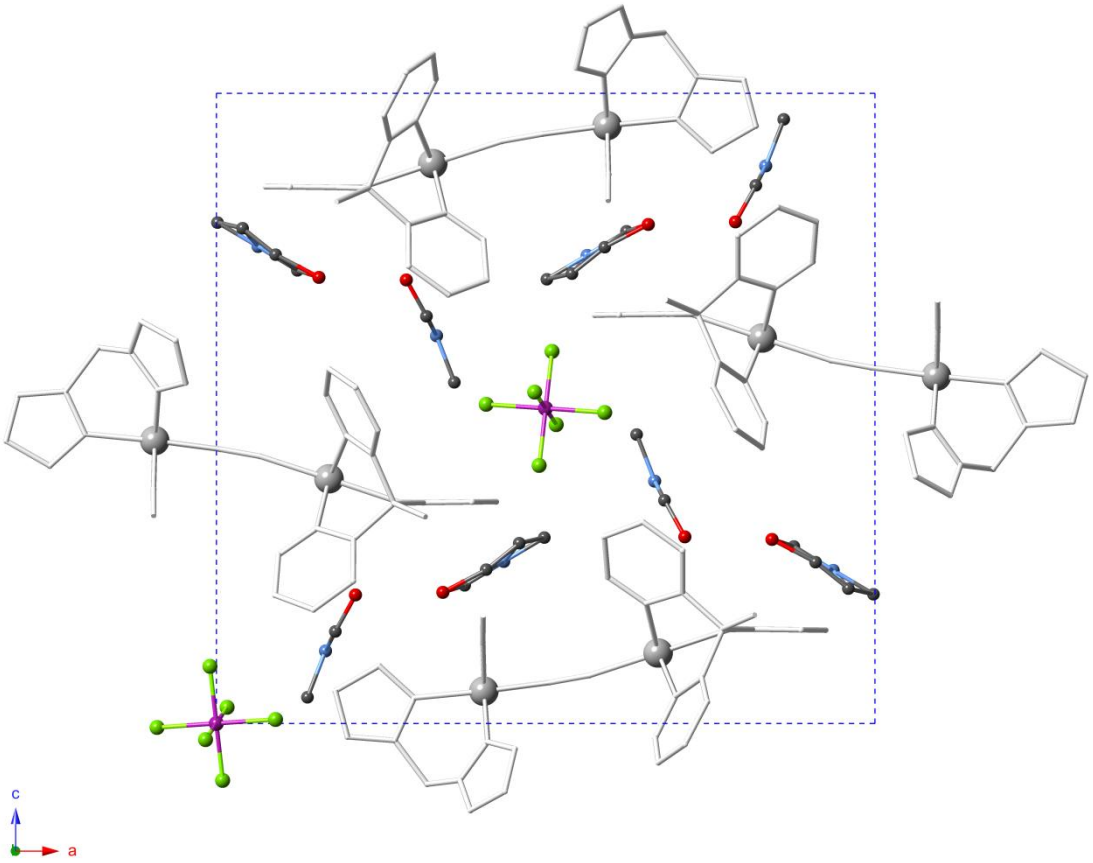

Figure III-6. Projection view of the crystal structure of **3**•2DMF at 250 K showing the packing of the cationic complexes, the AsF_6^- anions and the lattice DMF molecules in the (*ac*) plane. All the atoms of the cationic complexes are in light gray color for clarity. The AsF_6^- anions, the lattice DMF molecules and the metal centers are visualized in balls and sticks for clarity. N, C, As, O and F atoms are indicated in light blue, dark gray, purple, red and green, respectively.

The charge of the complexes is compensated by one PF_6^- anion in **2**•2DMF and by one AsF_6^- anion in **3**•2DMF, which are located on an inversion center (Figures III-5 and III-6). The asymmetric unit, for each complex, contains also two disordered dimethylformamide (DMF) molecules per formula unit, as observed for **1**•2DMF. At 220 K for **2**•2DMF and at 250 K for **3**•2DMF, the degree of disorder of the DMF molecules were found to be the same. Actually, one DMF was found to be disordered over two positions with equal occupancies whereas the second DMF is disordered over four positions with equal occupancies.

The packing of the molecular components occurs via weak interactions, as observed for compound **1**•2DMF (Figure III-1). At 220 K in **2**•2DMF, the shortest contacts between the complex and the DMF molecules and the hexafluorophosphate anion were found between O1 and C8 (3.40 Å), O1 and C17 (3.13 Å), and F2 and C18 (3.30 Å). The shorter contacts between the complexes were found between N2 and C15 (3.52 Å) (Figure III-7). Similarly, for **3**•2DMF at 250 K, the shortest contacts between the complex and the DMF molecules and the hexafluoroarsenate anion were found between O1 and C8 (3.40 Å), O1 and C17 (3.10 Å), F1 and C15 (3.34 Å) and F3 and C16 (3.46 Å). The shorter contacts between the complexes

were found between N2 and C20 (3.56 Å) (Figure III-8). By comparing the short contacts between the molecules in **2**•2DMF and **3**•2DMF, we observed that they differ only by one extra weak interaction between a fluorine atom of the hexafluoroarsenate anion (F3) and the carbon of the pyridine ring of $PY5Me_2$ ligand (C16). It is worth mentioning that the overlay of the packing of compounds **1**•2DMF (Figures III-9 and III-10, gray), **2**•2DMF (Figures III-9 and III-10, orange) and **3**•2DMF (Figures III-9 and III-10, purple) at high temperatures in the direction of the b and the c axis (Figures III-9 and III-10, respectively) reveals their isostructural character.

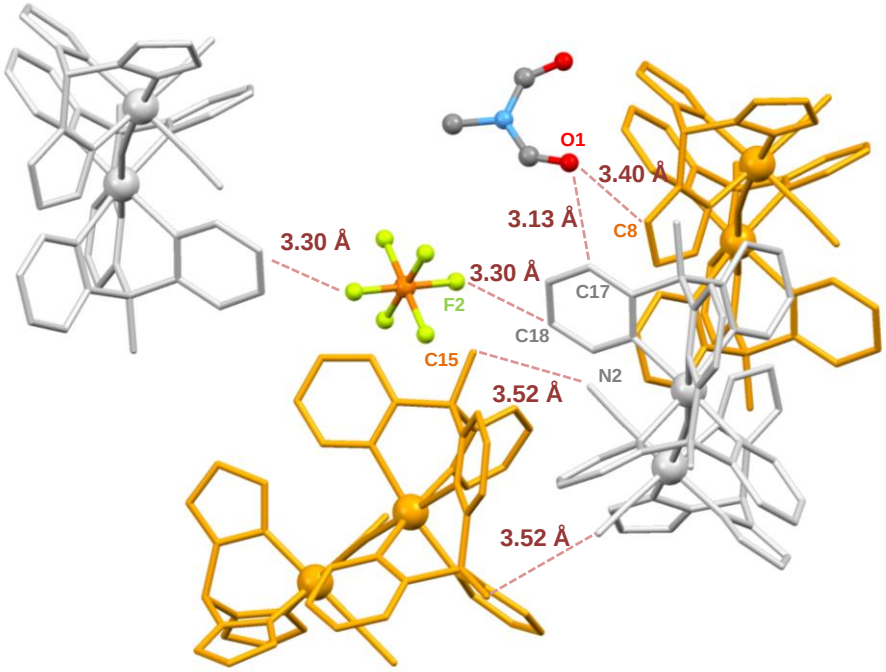

Figure III-7. View of the crystal structure of **2**•2DMF at 220 K showing the weak interactions between the cationic complexes, the PF_6^- anion and the disordered lattice DMF molecule. All the atoms of the cationic complex are in light gray and orange color for clarity. N, C, P, O and F atoms are indicated in light blue, dark gray, orange, red and green, respectively.

Before evaluating the crystal structures of compounds **2**•2DMF and **3**•2DMF at low temperatures, the investigation of their magnetic properties is necessary. This technique can give a direct answer regarding the effect of the different counter ions on the electron transfer properties of this dinuclear moiety.

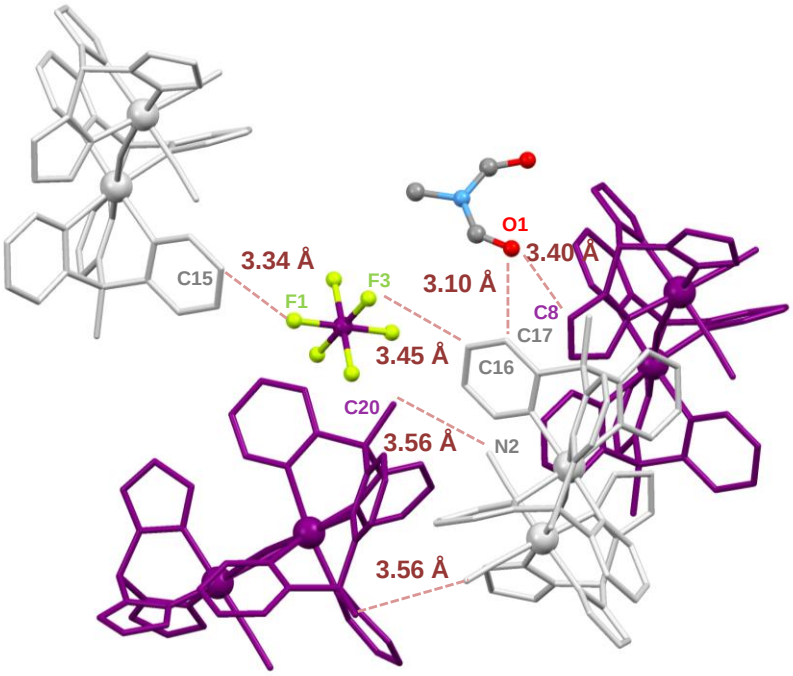

Figure III-8. View of the crystal structure of **3**•2DMF at 250 K showing the weak interactions between the cationic complexes, the AsF_6^- anion and the disordered lattice DMF molecule. All the atoms of the cationic complex are in light gray and purple color for clarity. N, C, As, O and F atoms are indicated in light blue, dark gray, purple, red and green, respectively.

Table III-1. Crystallographic data for **2**•2DMF at 220 K and for **3**•2DMF at 250 K.

Compound	**2**•2DMF	**3**•2DMF
Formula	$C_{47}H_{49}BCoF_6FeN_{16}O_2P$	$C_{47}H_{49}BCoF_6FeN_{16}O_2As$
FW / g·mol^{-1})	1140.58	1184.53
Crystal color	Orange	
Crystal size / mm	0.37 x 0.07 x 0.02	0.18 x 0.04 x 0.02
Crystal system	orthorhombic	
Space group	*P*nma	
Temperature / K	220	250
***a* / Å**	18.5449(5)	18.7088(10)
***b* / Å**	15.4092(5)	15.4040(9)
***c* / Å/**	17.8174(5)	17.9082(10)
***V* / Å^3**	5091.5(3)	5161.0(5)
Z	4	
d_{calc}	1.488	1.524
μ / mm^{-1}	0.721	1.316
Absorp. Correction	SADABS	
$\theta_{min} - \theta_{max}$	2.21° - 25.40°	2.27° - 21.28°
Completeness to 2θ	0.999	0.999
R_{int}	0.0535	0.0934
Refined param./restr.	389 / 21	389 / 63
[a] R_1 ($I > 2\sigma(I)$)	0.0457	0.0855
[b] wR_2 (all data)	0.1302	0.2455
Goodness-of-fit	1.049	1.030

[a] $R_1 = \Sigma||F_0|-|F_C||/\Sigma|F_0|$, [b] $wR_2 = [\Sigma w(F_0^2-F_C^2)^2/\Sigma w(F_0^2)^2]^{1/2}$

Table III-2. Selected bond lengths, distances [Å] and angles [°] for **2**•2DMF at 220 K and for **3**•2DMF at 250 K.

Compound	**2**•2DMF	**3**•2DMF
Temperature / K	220	250
Average (Fe-C)	1.917(4)	1.929(6)
Fe1-C1	1.885(4)	1.872(8)
Fe1-C2	1.930(3)	1.957(5)
Average (Fe-N)	1.982(4)	1.984(6)
Fe1-N3	1.991(4)	1.987(8)
Fe1-N5	1.978(3)	1.982(5)
Co-N_{NC}	2.042(4)	2.058(8)
Average (Co-N_{py})	2.135(2)	2.140(5)
Co1-N7	2.135(2)	2.139(5)
Co1-N8	2.148(2)	2.154(5)
Co1-N9	2.108(3)	2.113(6)
Fe1-C1-N1	177.3(16)	177.4(3)
C1-N1-Co1	172.3(9)	172.0(8)
Fe1…Co1	5.056(4)	5.068(8)

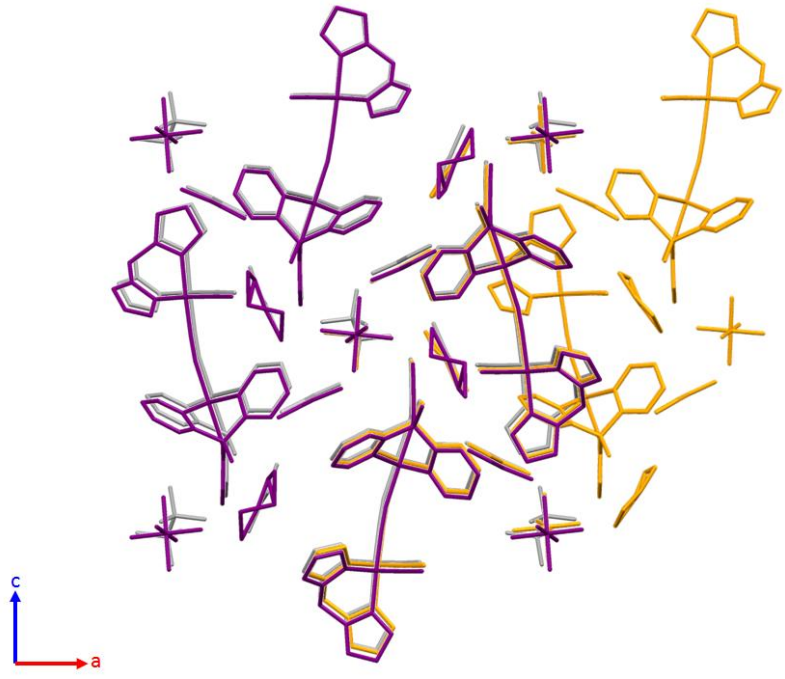

Figure III-9. Overlay of the packing of the crystal structure of **1**•2DMF at 180 K (gray), **2**•2DMF at 220 K (orange) and **3**•2DMF at 250 K (purple) in the (*ac*) plane.

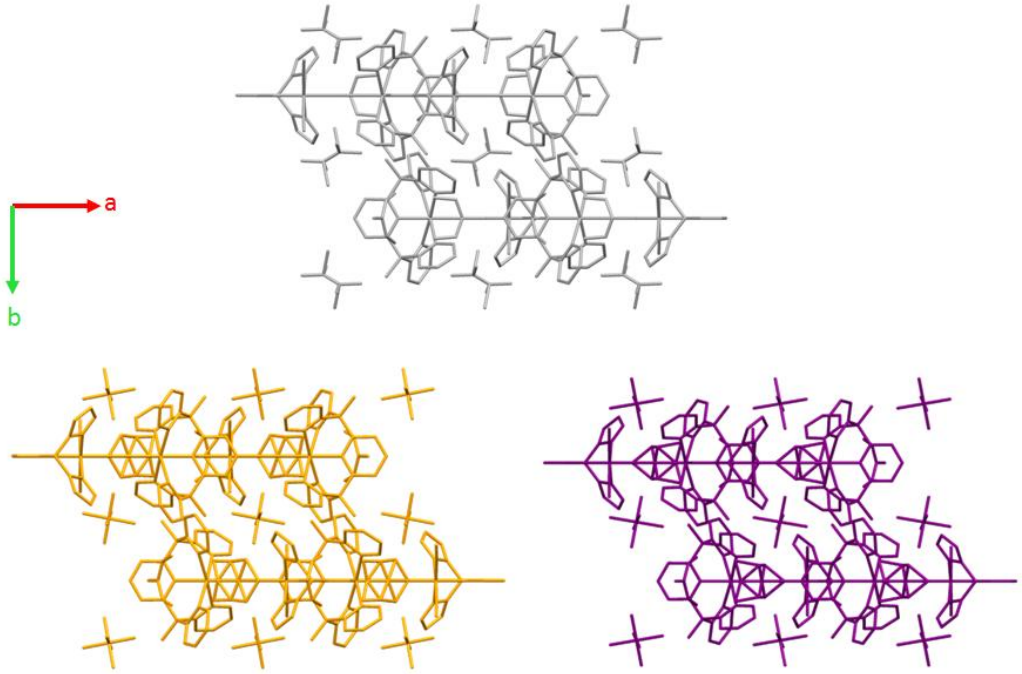

Figure III-10. Projection view of the crystal structure of **1**•2DMF at 180 K (gray), **2**•2DMF at 220 K (orange) and **3**•2DMF at 250 K (purple) in the (*ab*) plane.

III.2.3 Magnetic measurements and differential scanning calorimetry studies of compounds 2•2DMF and 3•2DMF

Magnetic susceptibility measurements were performed on fresh crystals (filtrated from their mother liquor (DMF/Et_2O) right before the measurement) between 1.8 and 250 K for compounds **2**•2DMF and **3**•2DMF (Figures III-11 and III-12, respectively). At 250 K, the χT product is 3.35 cm^3 K mol^{-1} and 3.32 cm^3 K mol^{-1} for **2**•2DMF and **3**•2DMF, respectively, which corresponds to the isolated magnetic centers, i.e., one LS Fe^{III} (S = 1/2) and one HS Co^{II} (S = 3/2) in an octahedral coordination environment. Indeed, this value is close to the value measured for the related dinuclear [{(BBP)Fe$(CN)_3$}{Co$(PY5Me_2)$}] complex (3.1 cm^3 K mol^{-1})[1] and for **1**•2DMF (3.43 cm^3 K mol^{-1})[2]. Lowering the temperature, the χT product is constant down to 150 K and then decreases sharply in one step (at 94 and 88 K for **2**•2DMF and **3**•2DMF, respectively; Figures III-11 and III-12, right), until 0.13 cm^3 K mol^{-1} at 79 K for **2**•2DMF and 0.36 cm^3 K mol^{-1} at 68 K for **3**•2DMF. The value of 0.13 cm^3 K mol^{-1} at 79 K for **2**•2DMF, confirms the stabilization of the diamagnetic {Fe^{II}_{LS}(μ-CN)Co^{III}_{LS}} state due to an almost full electron transfer process, with ≈ 4 % of the pairs remaining in the paramagnetic state. On the other hand, the value of 0.37 cm^3 K mol^{-1} at 68 K for **3**•2DMF, suggests the stabilization of the diamagnetic {Fe^{II}_{LS}(μ-CN)Co^{III}_{LS}} state by a quasi-full electron transfer, with ≈ 11 % of the pairs remaining in the paramagnetic state. In heating mode, a sharp transition at 112 K for **2**•2DMF (Figure III-11, right) and at 101 K for **3**•2DMF

(Figure III-12, right), reveals a thermal hysteresis of about 18 and 13 K, respectively, at 0.3 K/min. The reversibility of the magnetic properties for both compounds is confirmed above these temperatures, when the magnetic susceptibility recovers its initial value. It is worth mentioning that the width of the hysteresis loop for both compounds is not changing by increasing the sweeping rate of temperature from 0.3 to 0.6 and 1.2 K /min (Figure S.III-5).

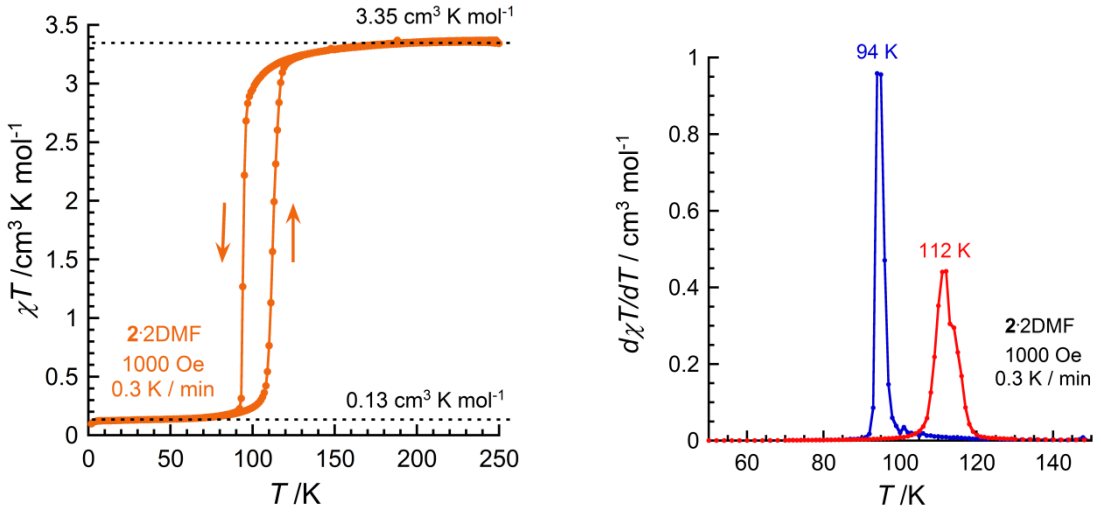

Figure III-11. (Left) χT versus T plots for polycrystalline samples of **2**•2DMF (in orange, from 250 to 1.8 K at 0.1 T) at 0.3 K/min; (right) derivative of the χT (i.e. $d\chi T/dT$) versus T curve at 0.1 T and 0.3 K/min for **2**•2DMF, in cooling (blue) and heating (red) modes. (the black dashed lines are guides for the eyes).

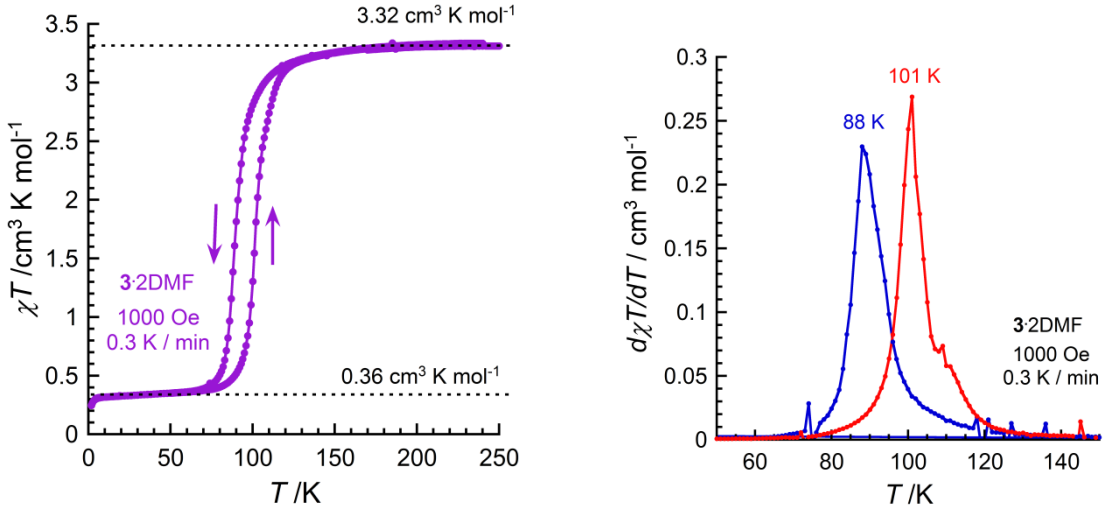

Figure III-12. (Left) χT versus T plots for polycrystalline samples of **3**•2DMF (in purple, from 250 to 1.8 K at 0.1 T) at 0.3 K/min; (right) derivative of the χT (i.e. $d\chi T/dT$) versus T curve at 0.1 T and 0.3 K/min for **3**•2DMF, in cooling (blue) and heating (red) modes. (the black dashed lines are guides for the eyes).

From the above data, it becomes obvious that the exchange of the counter ions from triflate in **1**•2DMF to hexafluorophosphate and hexafluoroarsenate in **2**•2DMF and **3**•2DMF, respectively, influenced the electron transfer behavior of the dinuclear unit. Firstly, the amount of pairs converted from the paramagnetic to the diamagnetic state is higher for compounds **2**•2DMF and **3**•2DMF and secondly, the electron transfer temperature has decreased by almost 70 K. All the data are summarized in Table III-3.

Table III-3. Summary of the temperatures of the thermally induced-electron transfer process in cooling and heating mode for compounds **1**•2DMF, **2**•2DMF and **3**•2DMF.

Compounds / *T* sweeping rate	$T_{1/2}$ cooling in K	$T_{1/2}$ heating in K
1•2DMF / 0.67 K/min	161 and 152	171 and 162
2•2DMF / 0.6 K/min	94	112
3•2DMF / 0.6 K/min	88	101

The investigation of the metastable $\{Fe^{III}_{LS}(\mu\text{-CN})Co^{II}_{HS}\}$ phase at low temperatures was performed by a fast cooling (>50 K/min) of the samples from 298 to 10 K and from 298 K to 5 K for **2**•2DMF and **3**•2DMF, respectively (Figure III-13). At 10 K, the χT product reaches a value of 1.59 cm^3 K mol^{-1} for **2**•2DMF and 1.66 cm^3 K mol^{-1} for **3**•2DMF, suggesting that about half of the compound was able to be thermally quenched under these conditions. In **2**•2DMF, from 2 to 50 K, the χT product of the partially quenched phase increased from 1.22 to 1.76 cm^3 K mol^{-1}, most likely due to the Co^{II} and Fe^{III} spin−orbit coupling[3,4] and/or antiferromagnetic interaction between the LS Fe^{III} and HS Co^{II} magnetic sites[5] in the $[Fe^{III}_{LS}(\mu\text{-CN})Co^{II}_{HS}]$ complex. Upon further heating, this metastable state relaxes rapidly into the thermodynamic diamagnetic phase at 61 K (Figure III-13, left with orange color). In **3**•2DMF, from 2 to 50 K, the χT product of the partially quenched phase increased similarly from 1.33 to 1.95 cm^3 K mol^{-1}. Upon further heating, this metastable state relaxes rapidly at 64 K and stabilizes into a new χT value (0. 25 cm^3 K mol^{-1}) at 74 K (Figure III-13, right with purple color), suggesting the stabilization of higher amount of diamagnetic pairs. Above 85 K, the χT product recovers the initial value for a paramagnetic $[Fe^{III}_{LS}(\mu\text{-CN})Co^{II}_{HS}]$ pair (Figure III-13, right with purple color).

The behavior observed for **2**•2DMF and **3**•2DMF by magnetic measurements (Figures III-11 and III-12), was evaluated by DSC measurements. Unfortunately, these studies were limited due to the minimum operational temperature of the instrument (97-100 K). Nevertheless, compound **2**•2DMF was characterized, since the temperature of electron transfer in cooling mode is occurring at 94 K (0.3 K / min). A phase transition was observed when the sample was cooled down and heated up at ca. 101 and 117 K respectively, in temperature sweeping rate of 1 K/min (Figure III-14). These peaks agree with a phase transition associated with the electron transfer process between the paramagnetic $\{Fe^{III}_{LS}(\mu\text{-CN})Co^{II}_{HS}\}$ and the diamagnetic $\{Fe^{II}_{LS}(\mu\text{-CN})Co^{III}_{LS}\}$ units. Integration of the DSC peak lead to an estimation of the transition enthalpy equal to ca. 3.84 and 4.33 kJ/mol, in cooling and heating mode, respectively, probably associated with a first order structural phase transition.

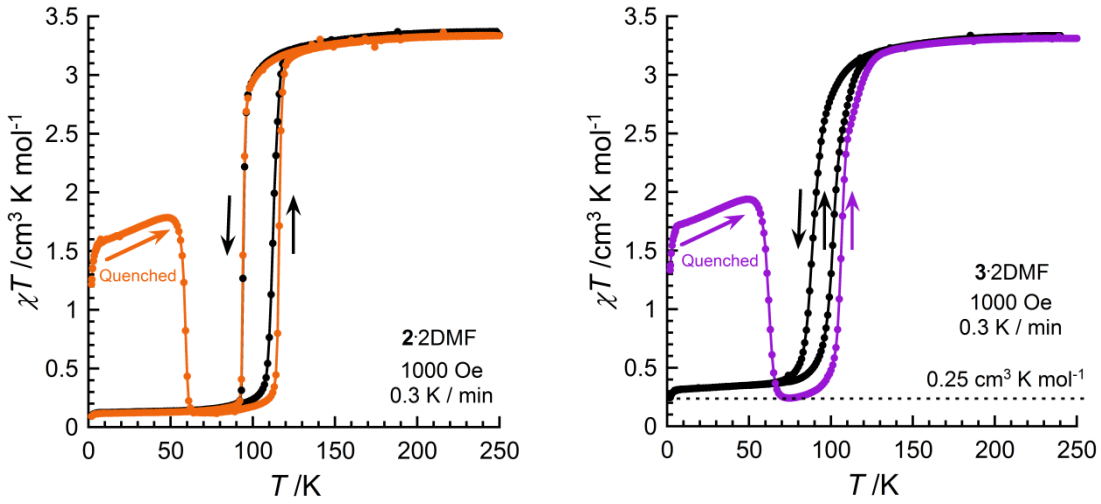

Figure III-13. (Left) χT versus T plots for polycrystalline samples of **2**•2DMF (in black, from 250 to 1.85 K at 0.1 T; in orange after thermal quench, from 1.8 to 65 K) at 0.3 K/min; (right) χT versus T plots for polycrystalline samples of **3**•2DMF (in black, from 250 to 1.85 K at 0.1 T; in purple after thermal quench, from 1.8 to 250 K) at 0.3 K/min (the black dashed lines are guides for the eyes).

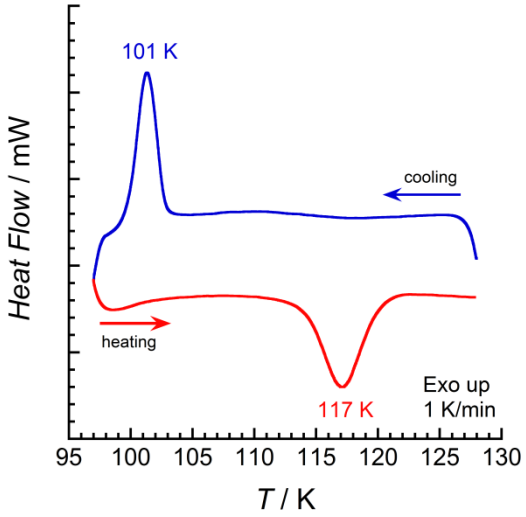

Figure III-14. DSC thermogram of **2**•2DMF at 1K/min.

III.2.4 Structural investigations at low temperature for compounds 2•2DMF and 3•2DMF

The appearance of a full and reversible electron transfer process for **2**•2DMF at 94 K (in cooling mode, Figure III-11) subsequently led to the performance of single-crystal X-ray diffraction studies at the lowest operational temperature of the instrument (82 K), in order to characterize the diamagnetic state of the pair. After collecting the crystal structure of **2**•2DMF at 220 K (see above, Figure III-3, Tables III-1 and III-2), the temperature of the cryostat was set at 82 K in a sweeping rate of 0.5 K / min. The first information obtained by comparing the data between the two temperatures, is the remarkable contraction of the unit cell volume

(5091.5(3) and 4769.5(3) $Å^3$ at 220 and 82 K, respectively; (Tables III-1, III-4)), evidencing more than a thermal effect. The second important information was obtained by looking closely the precession images collected in both temperatures (Figure III-15). The appearance of additional reflections peaks at 82 K (Figure III-15b; light blue squares), which were absent in the *P*nma phase (the space group at 220 K) indicate a lowering of the symmetry. This fact is proving a change of the space group and the presence of a phase transition. Moreover, the disappearance of these peaks when the crystal was heated up to 140 K with the same sweeping rate of 0.5 K/min, reinforced this hypothesis (Figure III-15c; light blue squares; Table S.III-1). The same experiment was repeated in order to verify the above mentioned results. By using PLATON, the space group selected to solve the crystal structure of **2**•2DMF at 82 K was the non-centrosymmetric orthorhombic $P2_12_12_1$ (Table III-4). In the cationic $[\{(Tp)Fe(CN)_3\}\{Co(PY5Me_2)\}]^+$ complex of **2**•2DMF, the Fe and Co metal ions are hexacoordinated with distorted octahedral geometries (Figure III-16) and their separation (Fe···Co) is 4.869(4) Å (Table III-5), slightly shorter that the one observed at 220 K for **2**•2DMF (5.056(1) Å, Table III-2). The same effect was also observed by the metal-cyanide ligand angle (Fe1−C1−N1 and C1−N1−Co1 angles are 177.0(5)° and 171.1(4)°, respectively, see Table III-5).

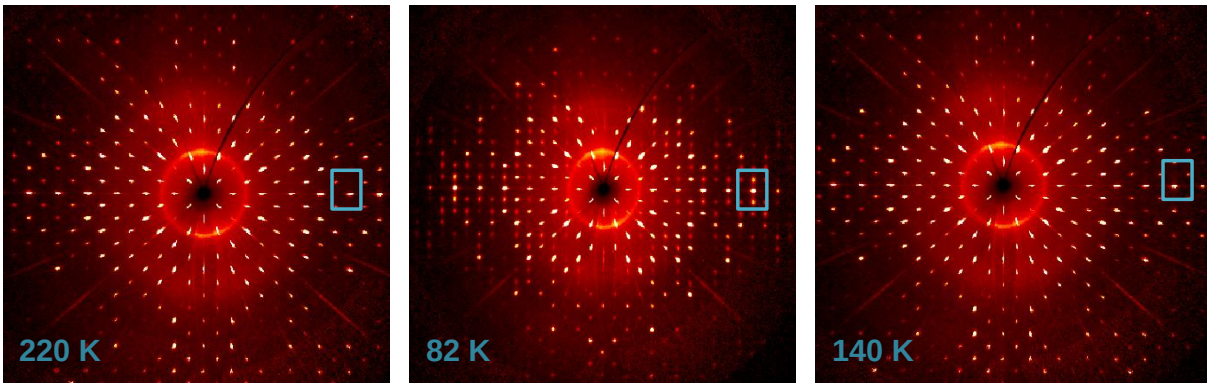

(a) **(b)** **(c)**

Figure III-15. *hk0* precision images of **2**•2DMF collected at (a) 220 K, (b) 82 K and (c) 140 K (the light blue squares are guides for the eyes).

The average Fe−C and Fe−N bonds are 1.890(8) and 2.007(6) Å, respectively (Table III-5). A preliminary comparison of the bond distances between the Fe and the donor atoms of the ligands at high and low temperatures can be used to establish the oxidation state of the metal center. The elongated Fe−C bond at 220 K (1.929(6) Å, see Table III-2) is due to the nature of the π bond between the $3d_{t2g}$ orbitals and the π* orbital of the cyanides. The lack of one bonding electron in Fe $3d_{t2g}$ orbitals for Fe^{III} results in a slight elongation of Fe-C distance in comparison with Fe^{II}-C bond. The average Co−N_{NC} and Co−N_{py} bonds at 82 K are 1.883(5) and 1.982(6) Å, respectively (Table III-5). The important contraction of the Co−N bonds at low temperature in comparison with those at high temperature (Co− N_{NC} and Co−N_{py} bonds at 250 K are 2.042(4) and 2.135(2) Å, respectively, see Table III-2) agrees with the fact that usually, higher-valent cations exhibit shorter metal-ligand bond distances due to a smaller

ionic radius. More specifically, in Co^{II}_{HS}, two e^- are present at the σ-antibonding $3d_{eg}$ levels, leading to a significant elongation of the Co-ligand bonds compared to that in the Co^{III}_{LS} state, where no e^- occupy the $3d_{eg}$ levels. These structural features confirm the presence of LS Fe^{II} and LS Co^{III} metal ions, leading to a diamagnetic complex **2**•2DMF at 82 K. This is the first time that the diamagnetic state of a dinuclear Fe/Co cyanide-bridged compound is studied by single-crystal X-ray diffraction.

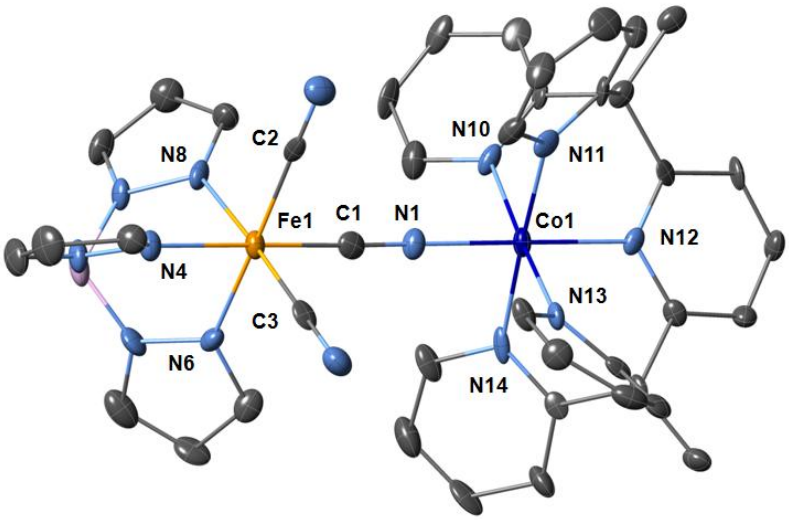

Figure III-16. ORTEP-type view of the cationic complex in **2**•2DMF at 82 K. Thermal ellipsoids are depicted at the 60% probability level. All anions, lattice solvents, and hydrogen atoms are omitted for clarity. Fe, Co, N, C, and B atoms are indicated in orange, dark blue, light blue, gray, and pink, respectively.

On the other hand, the evaluation of the crystal structure of the diamagnetic state of compound **3**•2DMF was not possible by following the same approach as for **2**•2DMF. This is not surprising, since the magnetic measurements of the compound (Figure III-12) revealed a value for the $\chi T \approx 1$ cm^3 K mol^{-1} at 82 K. The quasi-full electron transfer process is occurring actually at a lower temperature than the lowest operational temperature of the instrument (82 K; Figure III-12). For that reason, after collecting the crystal structure of **3**•2DMF at 250 K (see above Figure III-4, Table III-1 and 2), the crystal was cooled down to 82 K in a sweeping rate of 1 K / min following the thermal hysteresis and kept at this temperature for 12 hours in order to relax to its diamagnetic state before collecting the crystal structure. Finally, we were able to observe a remarkable contraction of the unit cell volume from 5161.0(5) to 4843.0(7) Å^3 at 250 and 82 K (12h), respectively, (Tables III-1 and III-4), showing more than a thermal effect. By closely analyzing the precession images collected at both temperatures, no additional reflections peaks were observed, and consequently the orthorhombic *Pnma* space group was used to refine the structure at 82 K (12h) (Table III-4). In the cationic $[\{(Tp)Fe(CN)_3\}\{Co(PY5Me_2)\}]^+$ complex of **3**•2DMF, the Fe and Co metal ions are hexacoordinated with distorted octahedral geometries (Figure III-17) and the Fe⋯Co separation is 4.880(2) Å (Table III-5), slightly shorter that the one observed at 250 K for **3**•2DMF (5.068(8) Å, Table III-2). It is worth noting that the metal-cyanide ligand angles for compound **3**•2DMF are not following the same tendency as for compound **2**•2DMF between

high and low temperatures, since the Fe1−C1−N1 angle is increasing to 179.2(12)° and the C1−N1−Co1 angle is decreasing to 168.9(10)° at 82 K (12h) (Tables III-2 and III-5). The average Fe−C and Fe−N bonds are 1.920(12) and 1.997(9) Å, respectively, while the average Co−N_{NC} and Co−N_{py} bonds are 1.888(9) and 1.998(8) Å, respectively (Table III-5). These structural features confirm the presence of LS Fe^{II} and LS Co^{III} metal ions and thus the stabilization of the diamagnetic complex **3**•2DMF after keeping the temperature at 82 K for 12 hours.

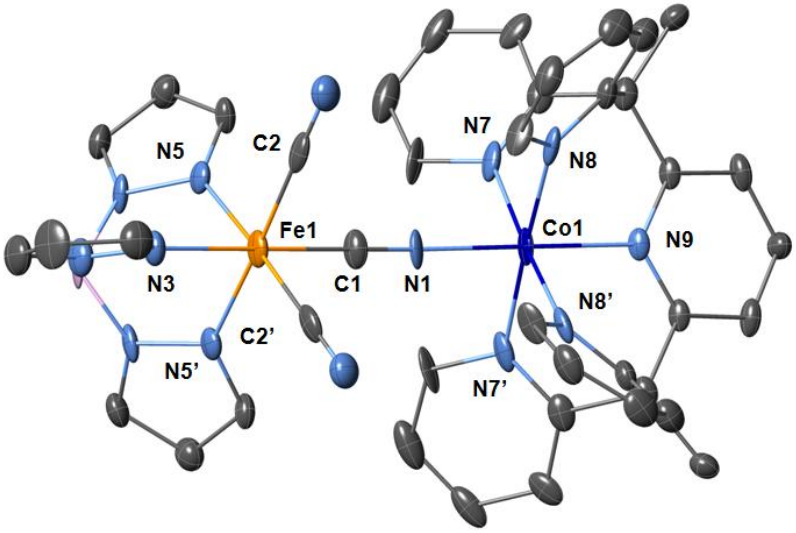

Figure III-17. ORTEP-type view of the cationic complex in **3**•2DMF at 82 K. Thermal ellipsoids are depicted at the 50% probability level. All anions, lattice solvents, and hydrogen atoms are omitted for clarity. Fe, Co, N, C, and B atoms are indicated in orange, dark blue, light blue, gray, and pink, respectively.

The crystal packing of **2**•2DMF at 82 K and **3**•2DMF at 82 K (12h) is similar with the one obtained at 220 K and 250 K, respectively (Figures III-5 to III-8), but it revealed slightly shorter interactions between the molecules in it, for both compounds. The degree of disorder of the two DMF molecules is again notable for both crystal structures at low temperature. In case of **2**•2DMF, the degree of disorder of one of the two DMF molecules is changing from high to low temperature. More specifically, at 220 K, one DMF was found to be disordered over two positions whereas the second DMF is disordered over four positions. When the temperature decreases to 82 K, the latter partially orders, leading to a disorder over two positions. This phenomenon was reversed when the crystal structure was heated up to 140 K. In the other hand, in compound **3**•2DMF the degree of disorder of the two DMF molecules is the same (one DMF is disordered over two positions and the second one over four positions) at both temperatures; 250 and 82 K (12h).

Table III-4. Crystallographic data for **2**•2DMF at 82 K and for **3**•2DMF at 82 K (12h).

Compound	**2**•2DMF	**3**•2DMF
Formula	$C_{47}H_{49}BCoF_6FeN_{16}O_2P$	$C_{47}H_{49}BCoF_6FeN_{16}O_2As$
FW / g·mol^{-1})	1140.58	1184.53
Crystal color	Orange	
Crystal size / mm	0.37 x 0.07 x 0.02	0.18 x 0.04 x 0.02
Crystal system	orthorhombic	
Space group	$P2_12_12_1$	*P*nma
Temperature / K	82	82
***a* / Å**	15.0351(6)	18.3827(14)
***b* / Å**	17.3813(6)	15.0915(14)
***c* / Å**	18.2510(7)	17.4572(12)
***V* / Å^3**	4769.5(3)	4843.0(7)
Z	4	
d_{calc}	1.588	1.625
μ / mm^{-1}	0.769	1.403
Absorp. Correction	SADABS	
$\theta_{min} - \theta_{max}$	2.23° - 25.36°	2.50° - 23.72°
Completeness to 2θ	0.991	0.995
R_{int}	0.0615	0.1343
Refined param./restr.	704 / 24	367 / 62
[a]R_1 ($I > 2\sigma(I)$)	0.0480	0.1107
[b]wR_2 (all data)	0.1070	0.2687
Goodness-of-fit	1.065	1.024
Flack Parameter	0.51(3)	

[a] $R_1 = \Sigma||F_0|-|F_C||/\Sigma|F_0|$, [b] $wR_2 = [\Sigma w(F_0^2-F_C^2)^2/\Sigma w(F_0^2)^2]^{1/2}$

Table III-5. Selected bond lengths, distances [Å] and angles [°] for **2**•2DMF at 82 K and for **3**•2DMF at 82 K (12h).

Compound	**2**•2DMF	**Compound**	**3**•2DMF
Temperature / K	82	**Temperature / K**	82
Average (Fe-C)	1.890(8)	**Average (Fe-C)**	1.920(12)
Fe1-C1	1.841(6)	**Fe1-C1**	1.869(12)
Fe1-C2	1.935(8)	**Fe1-C2**	1.945(12)
Fe1-C3	1.895(8)	**Fe1-C2'**	1.945(12)
Average (Fe-N)	2.007(6)	**Average (Fe-N)**	1.997(9)
Fe1-N4	2.007(4)	**Fe1-N3**	1.986(10)
Fe1-N6	1.994(6)	**Fe1-N5**	2.003(8)
Fe1-N8	2.021(6)	**Fe1-N5'**	2.003(8)
Co-N_{NC}	1.883(5)	**Co-N_{NC}**	1.888(9)
Average (Co-N_{py})	1.982(6)	**Average (Co-N_{py})**	1.998(8)
Co1-N10	2.006 (6)	**Co1-N7**	2.006(8)
Co1-N11	1.983(6)	**Co1-N7'**	2.006(8)
Co1-N12	1.974(4)	**Co1-N8**	1.998(8)
Co1-N13	1.965(6)	**Co1-N8'**	1.998(8)
Co1-N14	1.981(6)	**Co1-N9**	1.983(9)
Fe1-C1-N1	177.0(5)	**Fe1-C1-N1**	179.2(12)
C1-N1-Co1	171.1(4)	**C1-N1-Co1**	168.9 (10)
Fe1…Co1	4.869(4)	**Fe1…Co1**	4.880(8)

III.2.5 Optical measurements of compounds 2•2DMF and 3•2DMF

The signature of the electron transfer in **2**•2DMF and **3**•2DMF was also studied by solid-state optical reflectivity measurements. The set-up and the irradiation protocols that have been used to test the photosensitivity of both compounds were thoroughly presented in Chapter II.2.6 for complex **1**.

Figure III-18 shows the reflectivity spectra of compound **2**•2DMF between 286 and 10 K on cooling (top, left) and between 10 and 271 K on heating (top, right) with a sweeping temperature rate of 4 K/min. At 286 K, the spectrum is composed of two bands at 500 and 880 nm. Upon cooling, this spectrum is strongly modified in the 110−100 K temperature region, with a significant decrease in the reflectivity values above 700 nm, as expected due to the transition from the paramagnetic $[Fe^{III}_{LS}(\mu\ CN)Co^{II}_{HS}]$ to the diamagnetic $[Fe^{II}_{LS}(\mu\ CN)Co^{III}_{LS}]$ state.[6–10] The reflectivity spectra are very similar to the ones observed for the Fe/Co square complexes reported in reference 9 and also for **1** (Figure II-15, top), using the same reflectivity set-up. The thermal evolution of the absolute reflectivity at 850 nm helps to visualize the optical properties (Figure III-18, bottom) and reveals, as observed by magnetic measurements, a thermal hysteresis (ca. 20 K at 4 K/min) associated with the thermally induced electron transfer in **2**•2DMF. The small hysteresis appearing below 50 K indicates the possibility to photo-excite the compound at low temperature as discussed later in this paragraph.

Figure III-19 presents the reflectivity spectra of the compound **3**•2DMF between 285 and 10 K on cooling (top, left) and between 10 and 270 K on heating (top, right) with a sweeping temperature rate of 4 K/min. At high temperature, the spectrum related to the paramagnetic $[Fe^{III}_{LS}(\mu\text{-}CN)Co^{II}_{HS}]$ configuration of the complex is composed as expected of two bands at 500 and 880 nm. Upon cooling, this spectrum is strongly modified in the 100−70 K temperature region, especially in the reflectivity values above 700 nm. The wider temperature region of spectra modification (in comparison with those observed for **1** and **2**•2DMF), is confirming the transition observed by the magnetic studies at the same temperature region (Figure III-12). The thermal evolution of the absolute reflectivity at 850 nm helps to visualize the optical properties (Figure III-19, bottom) and to compare them with the magnetic measurements. In this case, a thermal hysteresis of 20 K at 4 K/min was observed, which can be associated with the thermally induced electron transfer in **3**•2DMF. The width and the shape of the hysteresis exhibit some differences with the one observed in the magnetic studies (Figure III-12). When the same experiment was repeated by using a 0.4 K / min temperature sweeping rate (close to the one used in the magnetic measurements, 0.3 K/ min), the optical properties are in agreement with the magnetic and the data obtained by single-crystal X-ray diffraction studies, demonstrating that the stabilization of the low temperature phase and the hysteresis width are depended as expected on the kinetics. It is worth mentioning that only when the stabilization of the diamagnetic state is achieved (or almost achieved), the photo-excitation of the compound is possible, fact that it is illustrated by the presence of a small hysteresis below 70 K for the curve of black dots in the bottom of Figure III-19.

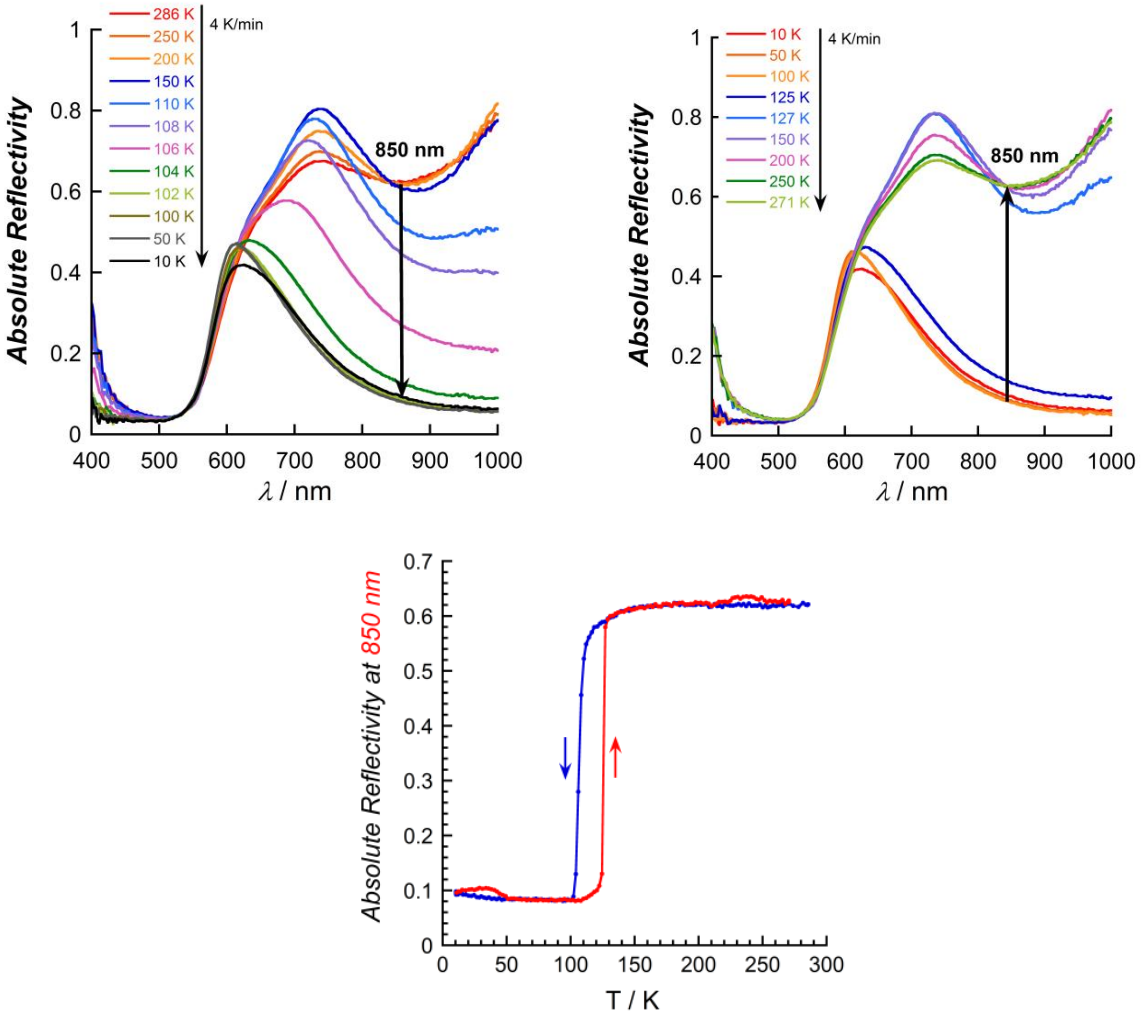

Figure III-18. Reflectivity spectra between 286 and 10 K as function of wavelength in cooling (top, left) and between 10 and 271 K in heating mode (top, right); (bottom) thermal evolution of reflectivity signal recorded at λ = 850 ± 5 nm (AR_{850}) in cooling mode (286-10 K, blue curve), and heating mode (10-271 K, red curve) at 4 K/min for **2**•2DMF.

A second set of measurements was realized in order to probe the photo-induced electron transfer process for compounds **2**•2DMF and **3**•2DMF. The first part includes the irradiation of the samples at 10 K with white light, as already described for **1** in section II.2.6. Compounds **2**•2DMF and **3**•2DMF, separately, are cooled to 10 K in the dark, and when the temperature is stable, the white light irradiation starts. After 90-100 min of white-light irradiation of the samples (0.4 mW/cm^2), the resulting spectra for each compound are resembling those recorded at 270 K (Figures III-20 and III-21, left), demonstrating the possibility to photo-induce the paramagnetic [Fe^{III}_{LS}(μ-CN)Co^{II}_{HS}] state, at least at the surface of the samples. Upon heating, the photo-induced state relaxes around 75 and 80 K for **2**•2DMF and **3**•2DMF, respectively, to the thermodynamic diamagnetic state (Figures III-20 and III-21, right) with temperature sweeping rate of 4 K / min.

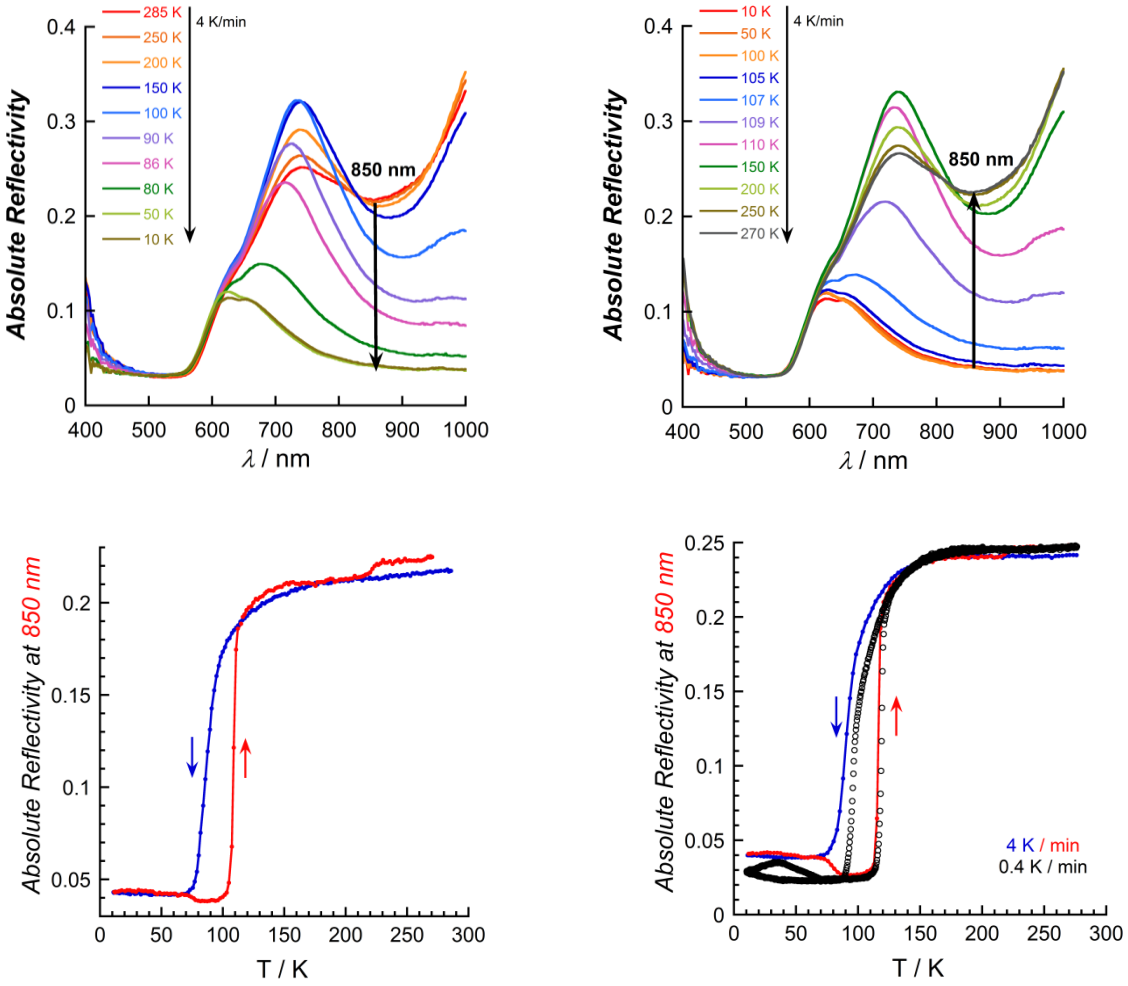

Figure III-19. Reflectivity spectra between 285 and 10 K as function of wavelength in cooling (top, left) and between 10 and 270 K in heating mode (top, right); (bottom, left) thermal evolution of reflectivity signal recorded at λ = 850 ± 5 nm (R_{850}) in cooling mode (285-10 K, blue curve), and heating mode (10-270 K, red curve) at 4 K/min; (bottom, right) thermal evolution of reflectivity signal recorded at λ = 850 ± 5 nm (AR_{850}) in cooling mode (285-10 K, blue curve), and heating mode (10-270 K, red curve) at 4 K/min and in cooling and heating mode (280 -10 K, black dots) at 0.4 K /min, for **3**•2DMF.

The reflectivity properties of **2**•2DMF and **3**•2DMF were further investigated by using a set-up of 14 different LEDs for irradiations. Detailed measurements were performed in order to find out the most efficient wavelength for irradiation, as described in section II.2.6. The most important changes in the spectra before and after 20 minutes of irradiation are observed with the 1050- and 940-nm LEDs (Figures S.III-13 and S.III-14 for **2**•2DMF and **3**•2DMF, respectively). The summarized results of the LEDs tests are presented in Figure III-22, which show clearly the ability of all 14 LEDs to excite the compounds. The most efficient wavelengths are in the 850-1050 nm range.

Then, the study with the most efficient wavelength of 940 nm was performed. Compounds **2**•2DMF and **3**•2DMF, separately, are cooled to 10 K in the dark, and the 940 nm irradiation at 5.5 mW/cm^2 starts. After 20 min of irradiation of the samples at 10 K, the resulting

spectrum for each compound is resembling those recorded at 270 K (Figures III-23 and III-24, left), demonstrating the possibility to photo-induce the paramagnetic [$Fe^{III}_{LS}(\mu$-CN)Co^{II}_{HS}] state, even with this specific wavelength. Finally, the thermal evolution of AR_{850} after the photo-excitation with the 940 nm LED at 5.5 mW/cm^2 is shown in Figure III-23 (right) for **2**•2DMF and in Figure III-24 (right) for **3**•2DMF. AR_{850} is nearly constant until 30 K, and shows a decrease from this temperature to 80 K approximately, for both samples. This decrease corresponds to the thermally-activated relaxation from the photo-excited state. Above 80 K, the same behavior for AR_{850} with the previous measurements is observed. These results demonstrate again the good reversibility after the photo-induced electron transfer in samples **2**•2DMF and **3**•2DMF.

To finish this reflectivity study with the LEDs, the eventual photo-reversibility at 10 K by cycling a photo-excitation at 940 nm (20 min with a power at 5.5 mW/cm^2) and a second irradiation (possible photo-deexcitation) with other LEDs (each irradiation for 10 min with a power at 2 mW/cm^2) was tested. Four LEDs at 365, 385, 405 and 455 nm (the less efficient to photo-excite the diamagnetic state; see Figure III-22) were selected for this deexcitation test. As for compound **1**, no photo-reversibility has been observed for **2**•2DMF and **3**•2DMF. In summary, the optical reflectivity studies demonstrate well the reversible thermally-induced electron transfer process within compounds **2**•2DMF and **3**•2DMF**.** Moreover, it was shown the possibility to fully photo-excited them by white light and 940-nm irradiation at least in the surface of the sample.

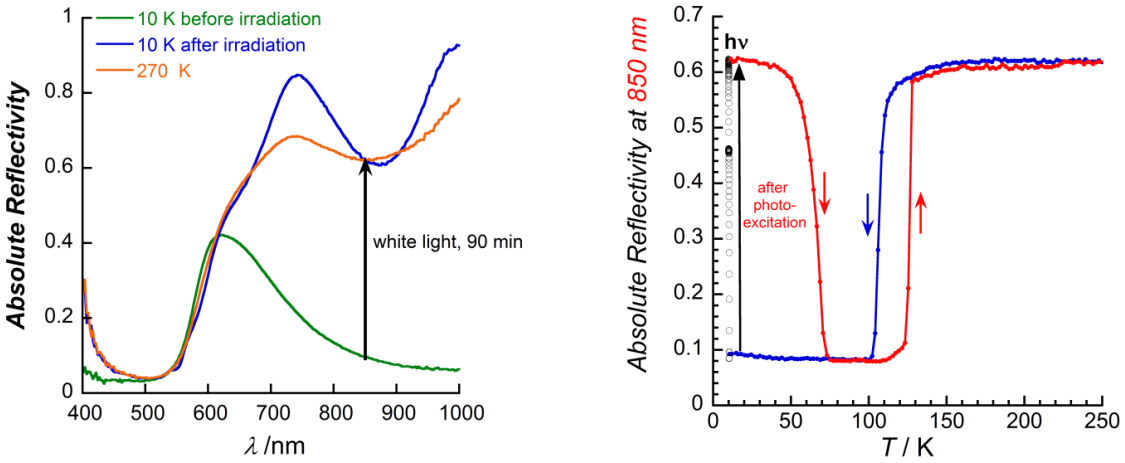

Figure III-20. (left) Reflectivity spectra at 270 K (orange) and 10 K (green) before irradiation and after white light irradiation 90 minutes (blue) with a temperature sweeping rate of 4 K/min; (right) thermal evolution of reflectivity signal recorded at λ= 850 ± 5 nm (AR_{850}) in cooling mode (250-10 K, blue curve), after white white-light irradiation (0.4 mW/cm^2, at 10 K, black circle markers) and in heating mode (10-250 K, red curve) at 4 K/min for **2**•2DMF.

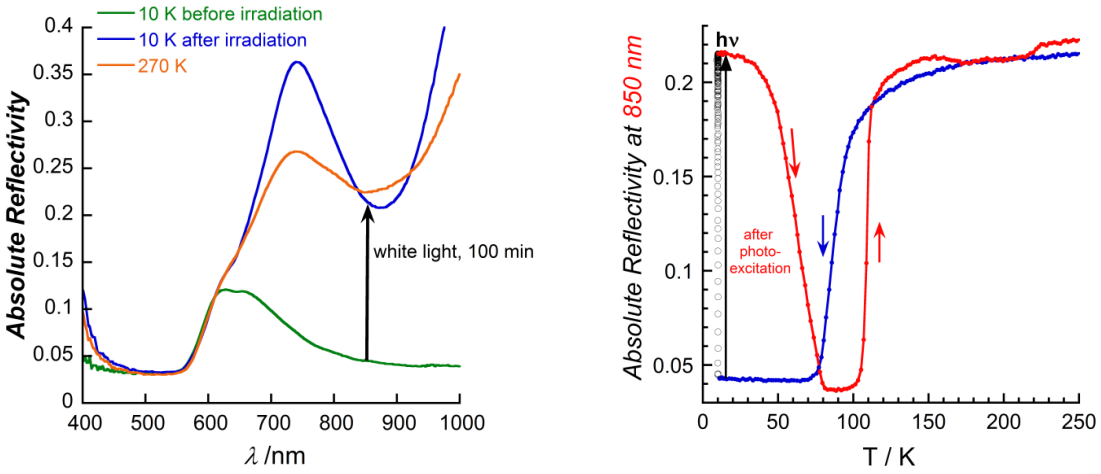

Figure III-21. (left) Reflectivity spectra at 270 K (orange) and 10 K (green) before irradiation and after white light irradiation 90 minutes (blue) with a temperature sweeping rate of 4 K/min; (right) thermal evolution of reflectivity signal recorded at λ = 850 ± 5 nm (AR_{850}) in cooling mode (250-10 K, blue curve), after white-light irradiation (0.4 mW/cm^2, at 10 K, black circle markers) and in heating mode (10-250 K, red curve) at 4 K/min for **3**•2DMF.

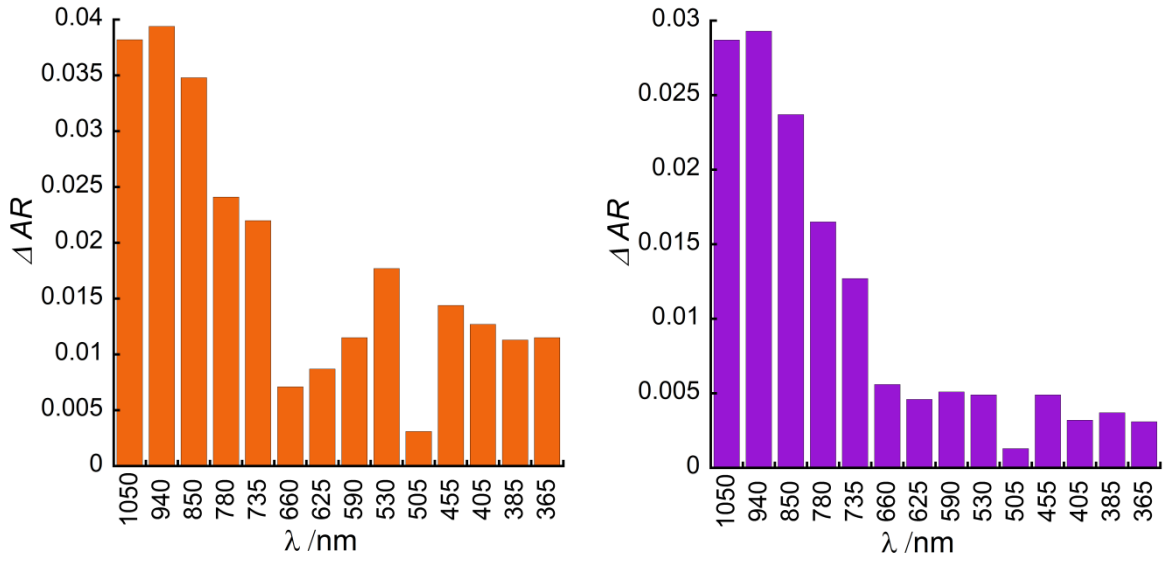

Figure III-22. Difference in absolute reflectivity (*ΔAR*) at 850 nm for **2**•2DMF (left) and **3**•2DMF (right), obtained before irradiation and after 20 min of irradiation with the 14 different LEDs (*P* = 0.2 mW/cm^2) at 10 K.

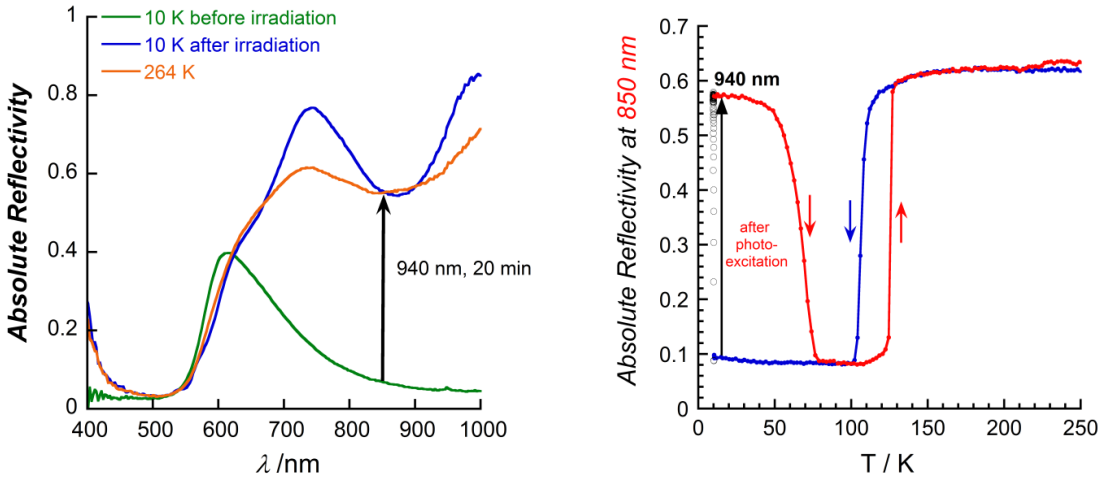

Figure III-23. (Left) Reflectivity spectra at 264 K (orange) and 10 K (green) before irradiation and after 940 nm irradiation 20 minutes (blue) with a temperature sweeping rate of 4 K/min; (right) thermal evolution of reflectivity signal recorded at λ = 850 ± 5 nm (AR_{850}) in cooling mode (250-10 K, blue curve), after 940 nm irradiation (5.5 mW/cm^2, at 10 K, black circle markers) and in heating mode (10-250 K, red curve) at 4 K/min for **2**•2DMF.

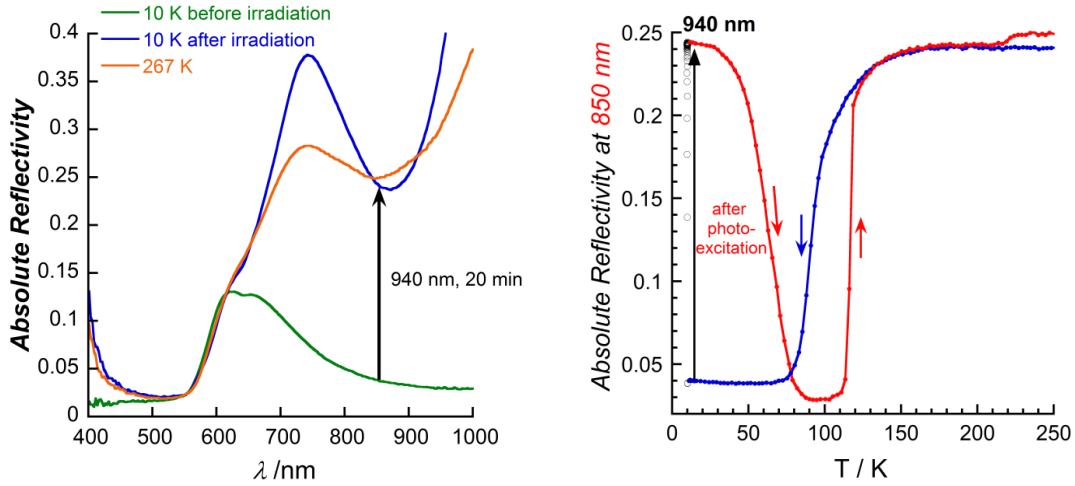

Figure III-24. (Left) Reflectivity spectra at 267 K (orange) and 10 K (green) before irradiation and after 940 nm irradiation 20 minutes (blue) with a temperature sweeping rate of 4 K/min; (right) thermal evolution of reflectivity signal recorded at λ = 850 ± 5 nm (AR_{850}) in cooling mode (250-10 K, blue curve), after 940 nm irradiation (5.5 mW/cm^2, at 10 K, black circle markers) and in heating mode (10-250 K, red curve) at 4 K/min for **3**•2DMF.

III.2.6 Photomagnetic measurements of compounds 2•2DMF and 3•2DMF

In order to confirm and further investigate the photo-induced electron transfer phenomenon observed at low temperatures in the bulk, compounds **2**•2DMF and **3**•2DMF were characterized by photomagnetic measurements (Figure III-25 and III-26, respectively).

In **2**•2DMF, under white-light irradiation (Figure III-25, red curves), the χT product at 10 K quickly increases and reaches a maximum of 3.24 cm^3 K mol^{-1} after 13 h (3 mW/cm^2), thus demonstrating that paramagnetic [Fe^{III}_{LS}(μ-CN)Co^{II}_{HS}] units are photogenerated in the bulk. If the sample is then cooled down to 2 K in the dark, the χT product of the photoinduced phase decreases to 1.8 cm^3 K mol^{-1}, most likely due to the Co^{II} and Fe^{III} spin−orbit coupling[3,4] and/or antiferromagnetic interaction between LS Fe^{III} and HS Co^{II} magnetic sites[5] in the [Fe^{III}_{LS}(μ-CN)Co^{II}_{HS}] complex (as already observed in **1**, Figure II-22). Upon heating (at 0.4 K/min), this metastable state relaxes rapidly into the thermodynamic diamagnetic phase at 53 K. The relaxation temperature differs from the one deduced from the optical reflectivity studies (Figure III-20, right) (≈ 75 K) likely due to the different temperaure sweeping rate used for the two techniques (4 K/min versus 0.4 K/min). The results obtained by irradiation of **2**•2DMF at 10 K with two different LEDs, 980 and 830 nm (8 mW/cm^2) (Figure III-25, blue and green curves, respectively), were very similar with those obtained with white light. The only difference lies in the efficiency of the irradiation in respect of time, since the 980 and 830 nm irradiations offer access in the metastable paramagnetic state in a few minutes (80 min), while the white-light irradiation needs ~13 hours (Figure III-25, left).

In this point, it is worth to mention that the white-light source used for these studies is the same as the one used for the optical reflectivity studies. The fact that we use higher power of light and longer time of exposure of the sample under irradiation now, lies on the different experiment set-up. In the reflectivity studies, we irradiate only the surface of the sample from less that 1 cm distance, whereas in the photomagnetic studies we wish to irradiate the totality of the sample (bulk measurements), which is 6 cm away from the optical fiber.

Since compound **3**•2DMF exhibits similar behavior under irradiation with compound **2**•2DMF (as shown by the reflectivity studies in Figure III-22), and the efficiency of 980 nm in respect of the irradiation time is high, (as demonstrated by the photomagnetic studies of **2**•2DMF in Figure III-25, right), the 980 nm LED was selected to investigate the photo-induced electron transfer phenomenon of **3**•2DMF. Indeed, under 980 nm irradiation (Figure III-26, red curve), the χT product at 10 K quickly increases and reaches a maximum of 3.24 cm^3 K mol^{-1} after 80 min (8 mW/cm^2), thus demonstrating that paramagnetic [Fe^{III}_{LS}(μ-CN)Co^{II}_{HS}] units are also photogenerated in the bulk. From 2 to 25 K in the dark, the χT product of the photoinduced phase increased from 1.82 to 3.32 cm^3 K mol^{-1}, most likely due to the Co^{II} and Fe^{III} spin−orbit coupling[3,4] and/or antiferromagnetic interaction between LS Fe^{III} and HS Co^{II} magnetic sites[5] in the [Fe^{III}_{LS}(μ-CN)Co^{II}_{HS}] complex (as already observed in **1** and **2**•2DMF, Figure II-22 and Figure III-25, respectively). Upon further heating (at 0.4 K/min), this metastable state relaxes rapidly into the thermodynamic diamagnetic phase at 57 K. As observed before, the relaxation temperature differs between the optical reflectivity

studies (Figure III-20, right) (≈ 80 K) and the photomagnetic studies, likely due to the different temperature sweeping rate used for the two techniques.

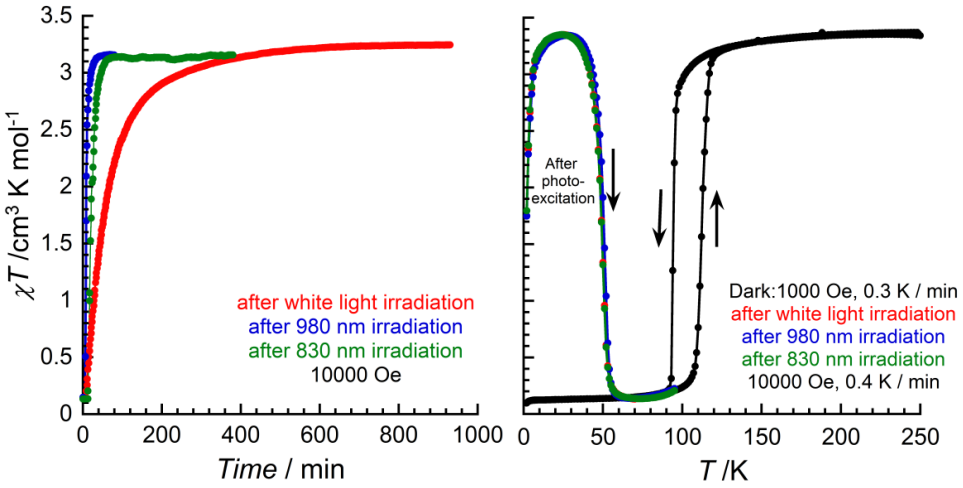

Figure III-25. (Left) χT versus time at 1 T under white-light irradiation (red curve, 3 mW/cm^2), 980 nm irradiation (blue curve, 8 mW/cm^2) and 830 nm irradiation (green curve, 8 mW/cm^2) at 10 K; (right) χT versus temperature plots at 0.1 T and 0.3 K/min for **2**•2DMF before (black) and after white-light irradiation (red; 3 mW/cm^2), 980 nm irradiation (blue; 8 mW/cm^2) and 830 nm irradiation (green; 8 mW/cm^2) at 10 K, from 1.8-100 K at 1 T and 0.4 K/min (the arrows are guides for the eye).

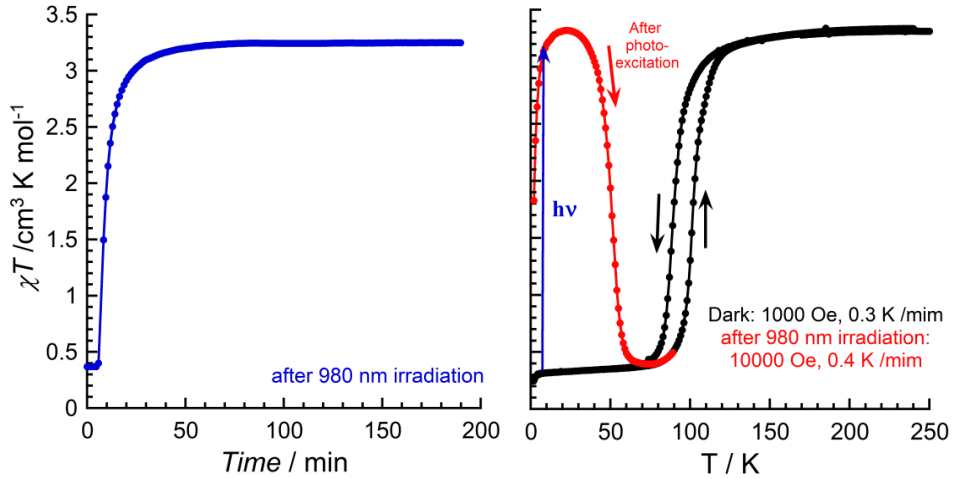

Figure III-26. (Left) χT versus time at 1 T under 980 nm irradiation (8 mW/cm^2) at 10 K; (right) χT versus temperature plots at 0.1 T and 0.3 K/min for **3**•2DMF before (black) and after (red) 980 nm irradiation (8 mW/cm^2) at 10 K, from 1.8-100 K at 1 T and 0.4 K/min (the arrows are guides for the eye).

It is worth mentioning that the relaxation temperature from the metastable state into the thermodynamic diamagnetic phase for these compounds is the lowest relaxation temperature observed for any molecular PBAs (120 K in a molecular square (2 Fe/Co pairs)[9] and 180 K in a molecular cube[8] (4 Fe/Co pairs)) and it seems to decrease with the miniaturization of the complex.

The population of the paramagnetic state of **2**•2DMF and **3**•2DMF at 10 K gave us the opportunity to study the magnetic properties of these systems by measuring the field dependence of the magnetization (*M*) at different low temperatures in order to probe the nature of the interaction between the metal centers. The two Fe/Co dinuclear complexes exhibit similar behavior as it is presented in Figures III-27 and S.III-17 for **2**•2DMF and **3**•2DMF, respectively. Thus, an increase of *M* at low fields is observed, which eventually saturates at values lower than 3 μ_B at 1.8 K and 7 T. The *M* versus *H* curves at 1.8 K were then compared with the corresponding curve from the sum of Fe(III) and Co(II) precursor used for the synthesis of the pairs (Figures III-28 and S.III-18, left, for **2**•2DMF and **3**•2DMF, respectively). The increase of *M* at low fields for the pairs resembles the one observed from the sum of the precursors, suggesting almost no interactions between the metal centers within the pairs. However, the saturation value at 1.8 K for the pairs is lower than the one observed from the sum of the precursors and it suggests the presence of weak antiferromagnetic interactions between the two metal centers and/or anisotropy. The presence of anisotropy is also supported by the non-superposed *M* versus *H*/*T* curves between 1.8 and 4 K (Figures III-27 and S.III-17). Additional measurements, like EPR (Electron Paramagnetic Resonance) spectroscopy at 10 K after light irradiation of the samples would allow us to determine the exact value and sign of this anisotropy. Moreover, the presence of weak antiferromagnetic interactions between the Fe^{III}_{LS} and Co^{II}_{HS} centers in the photo-induced paramagnetic state of the pairs is reinforced by the comparison of the low temperature region of the χT versus *T* plot for pairs and for the sum of Fe(III) and Co(II) precursor (Figures III-28 and S.III-18, right, for **2**•2DMF and **3**•2DMF, respectively). In order to confirm our interpretation, fitting of the low temperature χT data after photo-excitation is necessary to be obtained.

Finally, the dynamic properties of **2**•2DMF and **3**•2DMF in the photo-induced paramagnetic state were probed by using *ac* susceptometry. No signals of the out-of-phase component of the *ac* susceptibility, χ", were observed in the absence of a *dc* field at 1.8 K for both compounds.

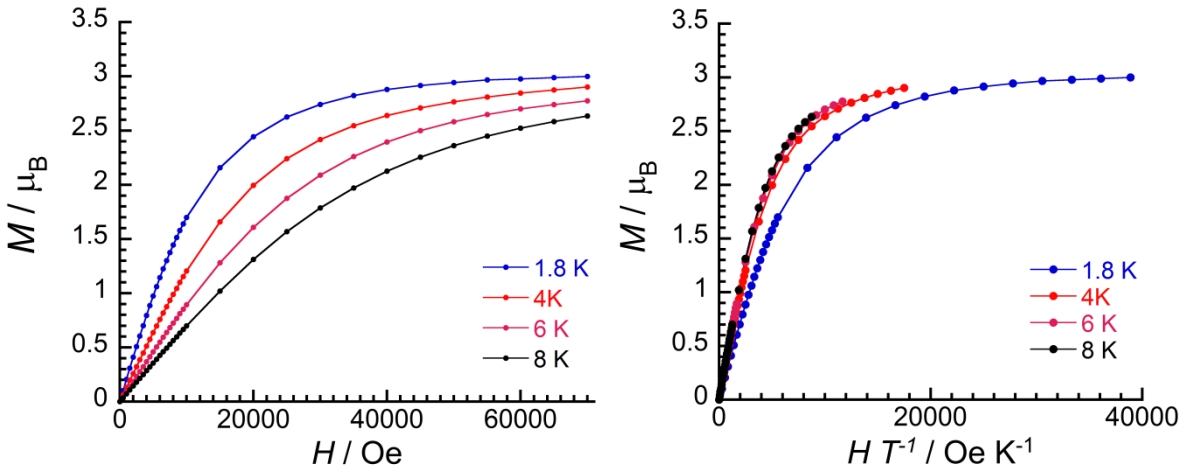

Figure III-27. (Left) *M* versus *H* and (right) *H*/*T* plots for complex **2**•2DMF at the indicated temperatures. Blue, 1.8 K; red, 4 K; pink, 6 K; black, 8 K.

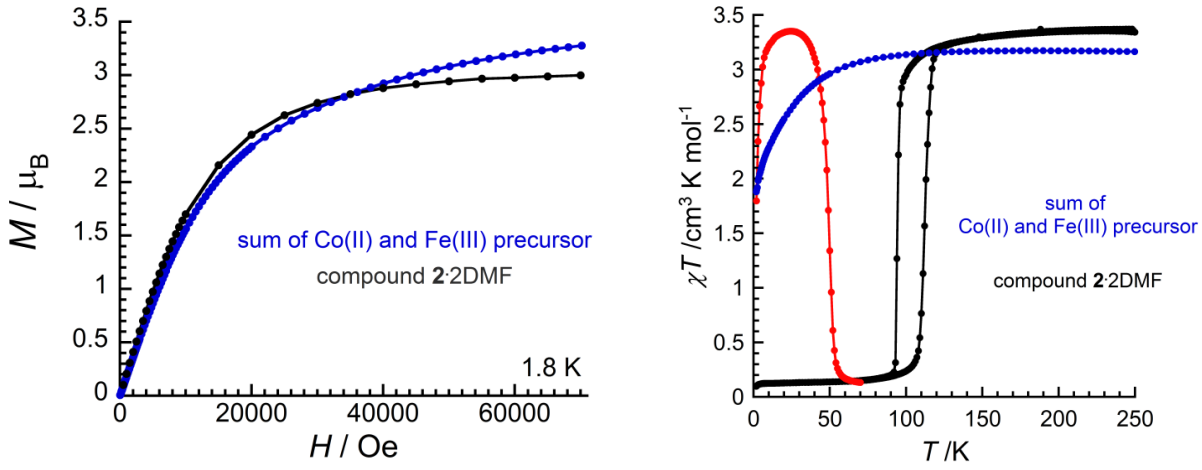

Figure III-28. (Left) *M* versus *H* plot for complex **2**•2DMF (black) and the sum of $(NBu_4)[(Tp)Fe^{III}(CN)_3]•3H_2O$ and $[Co^{II}(PY5Me_2)(H_2O)](BF_4)_2$ (blue), at 1.8 K; (right) χT versus temperature plot at 0.1 T from 250-1.8 K in the dark (black), after white-light irradiation at 10 K from 1.8-100 K at 1 T (red), for **2**•2DMF and at 0.1 T from 1.8-250 K for the sum of $(NBu_4)[(Tp)Fe^{III}(CN)_3]•3H_2O$ and $[Co^{II}(PY5Me_2)(H_2O)](BF_4)_2$ (blue).

In Figure III-29, we compare the thermally and light induced metastable paramagnetic state at low temperatures of compounds **2**•2DMF and **3**•2DMF. The fact that we managed to convert all the diamagnetic pairs into the paramagnetic by light treatment and only the half by thermal treatment is likely due to the presence of defects in the sample. These defects may promote the conversion from the diamagnetic state to the paramagnetic state of the pairs which starts form the surface of the sample during the irradiation, while they can be an obstacle to this direction in the case of the bulk thermal treatment. Moreover, we observe surprisingly that the partially quenched paramagnetic phases are relaxing about 10 K above the respective photo-induced paramagnetic states. Therefore, it will be interesting to compare the lifetime of these states, by following the relaxation process from the metastable paramagnetic state to the diamagnetic state of the compounds at different temperatures for both cases. In the next paragraphs, the relaxation study from the photo-induced paramagnetic state is presented.

This study includes several cycles of the beneath steps: a) irradiation of the sample and stabilization of the paramagnetic state of the compound at 10 K, b) increase of the temperature to the desired one while the light is switched on, c) switching off the light at the selected temperature and following the relaxation of the paramagnetic state to the thermodynamically stable diamagnetic state by squid measurements, d) increase of the temperature to 250 K and e) cooling back the sample at 10 K in order to repeat steps a) to d) for all the temperatures needed for the relaxation study.

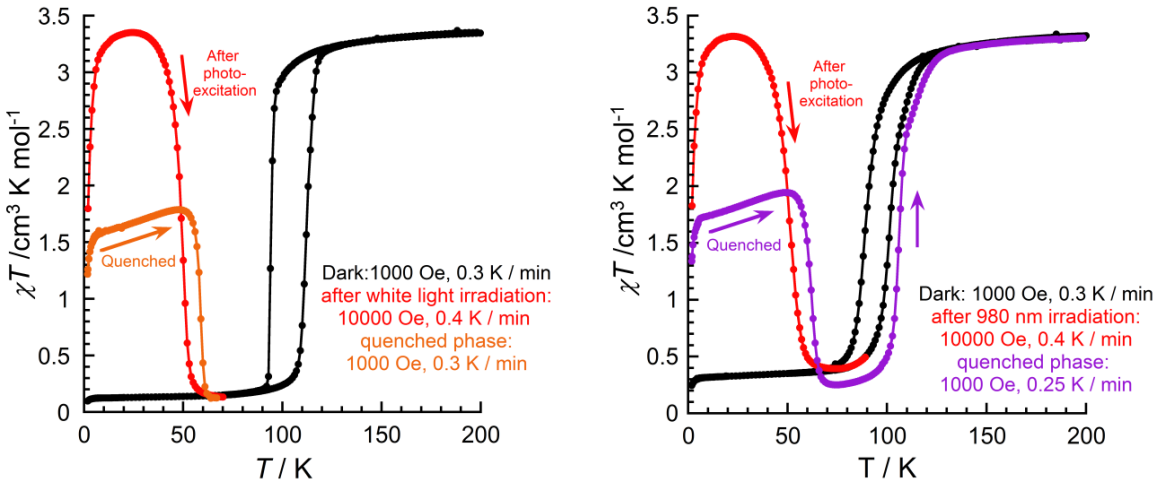

Figure III-29 (Left) χT versus temperature plot at 0.1 T and 0.3 K/min before (black), after (red) white-light irradiation (3 mW/cm^2) at 10 K, from 1.8-100 K at 1 T and 0.4 K/min and after (orange) quenching the paramagnetic state from 1.8-80 K at 0.1 T and 0.3 K/min, for **2**•2DMF; (right) χT versus temperature plot at 0.1 T and 0.3 K/min before (black), after (red) 980 nm irradiation (8 mW/cm^2) at 10 K, from 1.8-100 K at 1 T and 0.4 K/min and after (purple) quenching the paramagnetic state from 1.8-200 K at 0.1 T and 0.3 K/min, for **3**•2DMF.

Prerequisite of the experiment validity is the high chemically stability of the compound measured (i.e., unchanged magnetic properties between each cycle), which is fulfilled only by complex **2**•2DMF. In Figure III-30 is presented the set of temperatures used for the relaxation study of the compound and the evolution of the χT value at given temperature during this process. The selected relaxation curves (T = 45-54 K; Figure III-31) deviate from a mono-exponential behavior, indicating of distribution of the relaxation time. These relaxation curves follow a sigmoidal behavior, exhibiting a rapid initial decay followed by a long tail of a much slower process. The evolution of the normalized χ_{HS} values with the time for temperatures from 45 to 54 K, given in Figure III-31, have been fitted using the mean field macroscopic equation proposed in literature[11,12], Eq. III.1 and the mean lifetime τ has been estimated.

$$\chi_{HS} = \chi_{(t=0)} e^{-(t/\tau)^{\beta}} \qquad \text{III. 1}$$

Ln(τ) as a function of reciprocal temperature is plotted in Figure III-32. The linear dependence of the ln(τ) versus 1/T confirms the Arrhenius law and then a thermally activated process. The activation energy E_A/k_B = 972 K and relaxation time τ_0 = 7.6 10^{-6} s from the photoinduced paramagnetic state to the diamagnetic state in the dinuclear Fe/Co complex **2**•2DMF are comparable with the experimentally estimated energy barriers and relaxation times for other Prussian Blue molecular analogues : E_A/k_B = 2854 K and τ_0 = 9.1 10^{-9} s in a molecular square[9] (2 Fe/Co pairs) and E_A/k_B = 4455 K and τ_0 = 2.6 10^{-8} s in a molecular cube[8] (4 Fe/Co pairs).

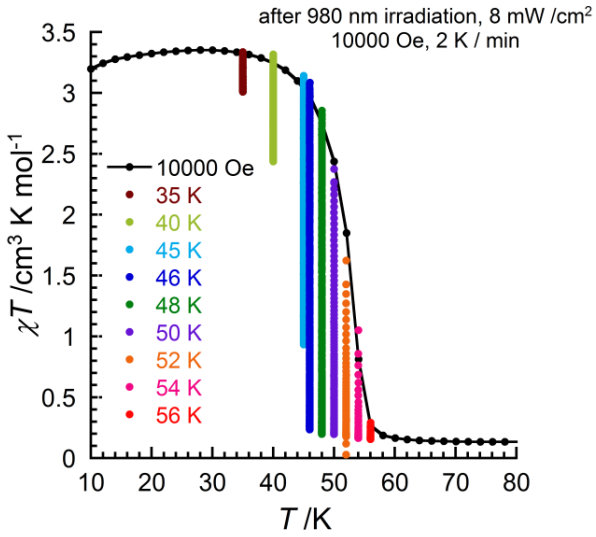

Figure III-30. The evolution of the χT value as a function of temperature, at various temperatures from 35 to 56 K, and the χT value as a function of temperature (black dots) after 25 min irradiation of the diamagnetic state of the sample with 980 nm LED (8 mW/cm^2) at 10 K with temperature increasing (at 2 K/min) from 10 to 80 K, for complex **2**•2DMF.

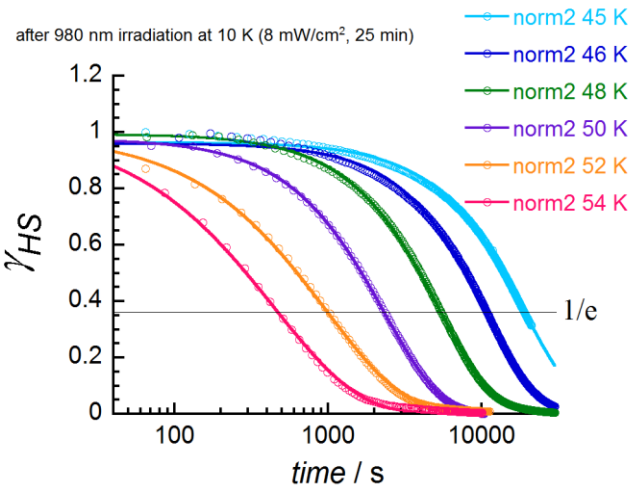

	$\chi_{HS} = \chi_{(t=0)} e^{-(t/\tau)^{\beta}}$		
T (K)	$\chi_{HS\ (t=0)}$	τ	β
45	0.97987	16949	1.34
46	0.95925	10926	1.31
48	0.99274	5396	1.26
50	0.97644	2331	1.18
52	0.99443	979	0.85
54	1.0194	451	0.71

Figure III-31. (Left) The evolution of the normalized χ_{HS} values with the time for the fitted temperatures from 45 to 54 K (empty dots) and the fit by Eq. III.1 (solid lines); (right) the results of the fit by Eq. III.1, for complex **2**•2DMF.

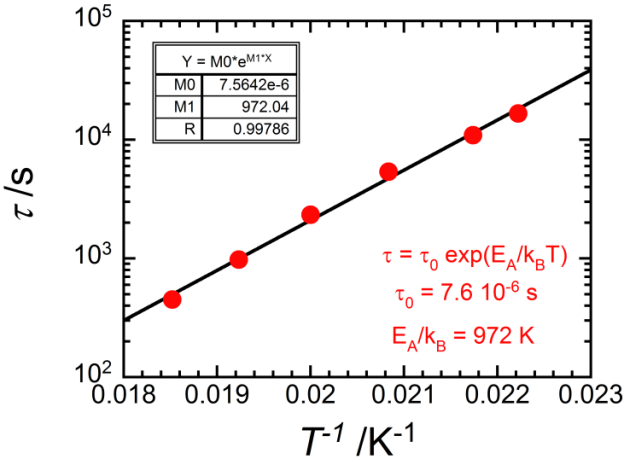

Figure III-32. Arrhenius plot ln(τ) as a function of 1/T for complex **2**•2DMF by estimation of τ from Eq. III.1.

III.2.7 Preparation and Physical Characterization of [{(Tp)Fe(CN)$_3$}{Co(PY5Me$_2$)}](PF$_6$) (2) and [{(Tp)Fe(CN)$_3$}{Co(PY5Me$_2$)}](AsF$_6$) (3)

III.2.7.1 Preparation and FT-IR characterizations of compounds 2 and 3

The revelation of the fascinating properties of **1**•2DMF and its desolvated form **1**, encouraged us to study the properties of the desolvated form of the two new compounds, **2**•2DMF and **3**•2DMF. The preparation of the desolvated form of compounds **2**•2DMF and **3**•2DMF was based on the preparation of **1**•2DMF in Chapter II.5.1. Thus, to avoid any decomposition during the desolvation process, the dinuclear complexes**,** **2**•2DMF and **3**•2DMF, were successively sonicated in diethyl ether (30 min) and kept for 24 h under vacuum at 50 °C. Complete removal of the lattice DMF solvent was confirmed by the disappearance of the intense $\tilde{\nu}_{C=O}$ stretching absorption band at 1678 cm^{-1} in the solid-state IR spectrum at room temperature (Figure III-33, pale color spectra) of the microcrystalline powders of **2** and **3**. The rest of the spectrum (Figure III-33) for **2** and **3** is almost identical with the spectrum collected for **2**•2DMF and **3**•2DMF, respectively, suggesting the stability of the dinuclear moieties, even in their desolvated form.

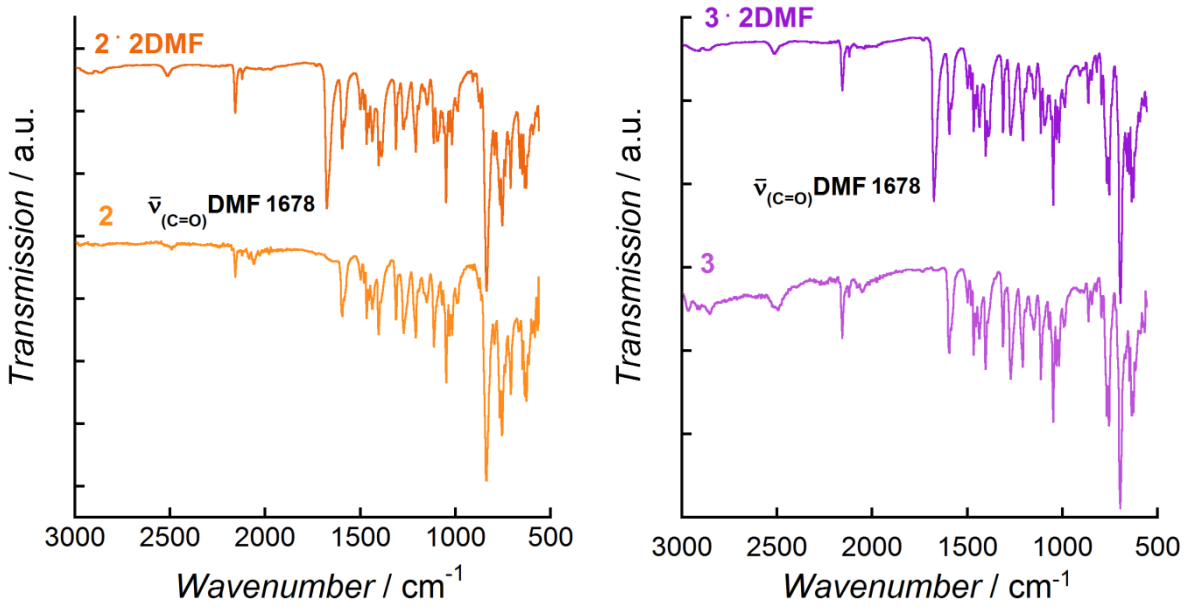

Figure III-33. FT-IR spectra of **2**•2DMF (left, orange), **2** (left, pale orange), **3**•2DMF (right, purple) and **3** (right, pale purple) at 298 K for comparison. The $\tilde{\nu}_{C=O}$ stretching absorption band at 1678 cm^{-1} for DMF is indicated at the spectra of **2**•2DMF and **3**•2DMF.

II.2.7.2 Magnetic measurements of compounds 2 and 3

Magnetic susceptibility measurements were performed for complexes **2** and **3** between 1.8 and 240 K (Figures III-34 and III-35). At 240 K, the χT product is 3.11 cm^3 K mol^{-1} and 3.05 cm^3 K mol^{-1} for **2** and **3**, respectively, which corresponds to the isolated magnetic centers, i.e., one LS Fe^{III} (S = 1/2) and one HS Co^{II} (S = 3/2) in an octahedral coordination environment. Indeed, this value is close to the value measured for the related dinuclear $[\{(BBP)Fe(CN)_3\}\{Co(PY5Me_2)\}]$[1] complex (3.1 cm^3 K mol^{-1}) and ~ 0.25 cm^3 K mol^{-1} lower than the value measured for **2**•2DMF and **3**•2DMF. Lowering the temperature, the χT product is constant down to 180 K and then decreases sharply in one step (at 170 and 156 K for **2** and **3**, respectively; Figures III-34 and III-35, right), until 0.20 cm^3 K mol^{-1} for **2** and 0.06 cm^3 K mol^{-1} for **3**. The value of 0.20 cm^3 K mol^{-1} at 150 K for **2**, suggests the stabilization of the diamagnetic $\{Fe^{II}_{LS}(\mu\text{-CN})Co^{III}_{LS}\}$ state by a quasi-full electron transfer, while the value of 0.06 cm^3 K mol^{-1} at the same temperature for **3**, confirms the stabilization of the diamagnetic $\{Fe^{II}_{LS}(\mu\text{-CN})Co^{III}_{LS}\}$ state by full electron transfer process. In heating mode, a sharp transition at 182 K for **2** and at 164 K for **3** (Figures III-34 and III-35, right), reveals a thermal hysteresis of about 12 and 8 K, respectively, at 0.3 K/min. The reversibility of the magnetic properties for both compounds is confirmed above these temperatures, when the magnetic susceptibility recovers its initial value. As mentioned before for **2**•2DMF and **3**•2DMF, the width of the hysteresis loop for both compounds **2** and **3**, is not changing by increasing the sweeping rate of temperature from 0.3 to 0.6 and 1.2 K /min (Figure S.III-6). It is worth to mention that the temperature range of 156-182 K of the occurring electron transfer process for

the desolvated complexes **1**, **2** and **3** is comparable. This result reveals the important role of the solvent content in the electron transfer process for these species. The solvent loss may cause notable changes in the packing of the cationic dinuclear species, which influence their magnetic properties to the same direction independently the counter ions that used.

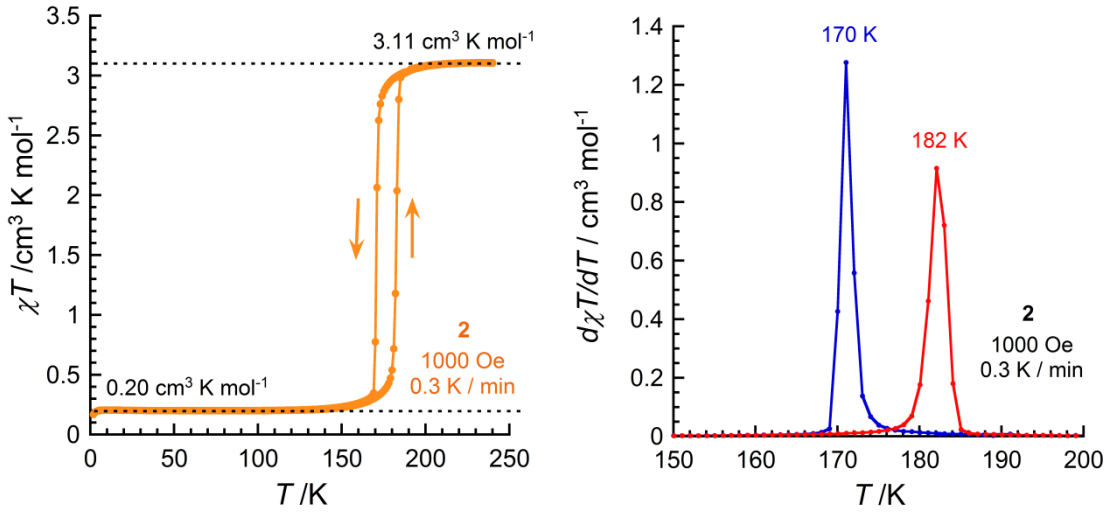

Figure III-34. (Left) χT versus T plots for **2** (in pale orange, from 240 to 1.8 K at 0.1 T) at 0.3 K/min; (right) derivative of the χT (i.e. $d\chi T/dT$) versus T curve at 0.1 T for **2** in cooling (blue) and heating (red) modes (the black dashed lines are guides for the eyes).

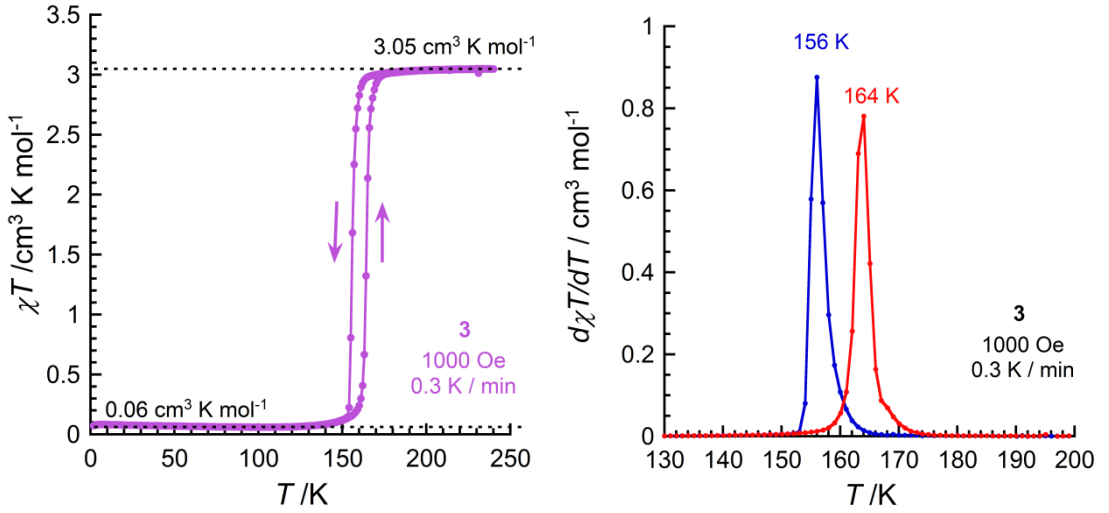

Figure III-35. (Left) χT versus T plots for **3** (in pale purple, from 240 to 1.8 K at 0.1 T) at 0.3 K/min; (right) derivative of the χT (i.e. $d\chi T/dT$) versus T curve at 0.1 T for **3** in cooling (blue) and heating (red) modes (the black dashed lines are guides for the eyes).

The results obtained by the magnetic characterization of the three desolvated new Fe/Co dinuclear complexes, **1**, **2** and **3** are summarized in Table III-6 and demonstrate well the importance of the environment of the molecular objects and the developing intermolecular interactions, in respect to their electron transfer properties.

Table III-6. Summary of the temperatures of the thermally induced-electron transfer process in cooling and heating mode for compounds **1**, **2** and **3**.

Compounds / *T* sweeping rate	$T_{1/2}$ cooling in K	$T_{1/2}$ heating in K
1 / 0.67 K/min	165	170
2 / 0.6 K/min	170	182
3 / 0.6 K/min	156	164

III.2.7.3 Optical measurements of compounds 2 and 3

Beneath we summarize the results obtained by solid-state optical reflectivity measurements for compounds **2** and **3**.

Figures III-36 and III-37 shows the reflectivity spectra of compounds **2** and **3**, respectively, between high temperatures and 10 K on cooling (left) and then on heating (right) with a sweeping temperature rate of 4 K/min. The thermal evolution of the reflectivity values observed in the temperature regions of 160-190 K for **2** and 150-180 K in **3**, can be associated with the thermally induced electron transfer process described by the magnetic studies above.

The photo-induced electron transfer for compounds **2** and **3** was probed firstly by using white-light source of irradiation at 10 K (P = 0.4 mW/cm^2): after 160 min and 200 min of irradiation for **2** and **3**, respectively, the resulting spectra for each compound are resembling those recorded at high temperature (Figures III-38 and III-39, left), demonstrating the possibility to photo-induce the paramagnetic [Fe^{III}_{LS}(μ-CN)Co^{II}_{HS}] state, at least at the surface of the samples. Upon heating (temperature sweeping rate of 4 K/min), the photo-induced state relaxes around 48 K to the thermodynamic diamagnetic state, for both compounds (Figures III-38 and III-39, right). At this point, we must mention that the relaxation temperature of 48 K is also the one estimated for **1,** highlighting the molecular origin of the phenomenon in these compounds, which consist of the same {Fe(μ-CN)Co} unit "decorated" by three different counter ions, $CF_3SO_3^-$, PF_6^- and AsF_6^-.

The reflectivity properties of **2** and **3** were further investigated by using a set-up of 14 different LEDs for irradiations, and as before the 940-nm LED was chosen as the most efficient one for further studies (Figure III-40). It is worth to note that the LEDs in the near-UV spectral region show less efficiency in samples **2** and **3** than **2**•2DMF and **3**•2DMF (Figure III-40 versus Figure III-22). Finally, the study with the optimum wavelength of 940-nm (P = 5.5 mW/cm^2) for samples of **2** and **3** revealed the possibility to effectively photo-induce the paramagnetic [Fe^{III}_{LS}(μ-CN)Co^{II}_{HS}] state (Figure III-41). Photomagnetic studies of these compounds have been planned in order to confirm these properties at the bulk level.

The results obtained by the magnetic, photomagnetic and optical characterization of the three new Fe/Co dinuclear complexes **1**•2DMF, **2**•2DMF and **3**•2DMF, and their desolvated forms, **1**, **2** and **3** are summarized in Table III-7.

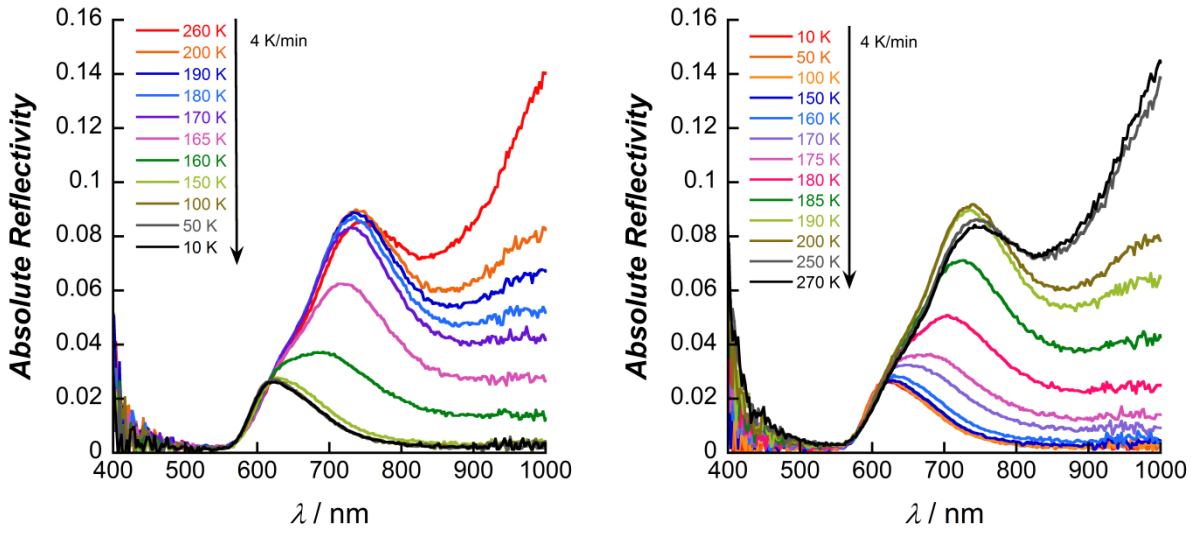

Figure III-36. Reflectivity spectra between 260 and 10 K as function of wavelength in cooling (left) and between 10 and 270 K in heating mode (right) at 4 K/min for **2**.

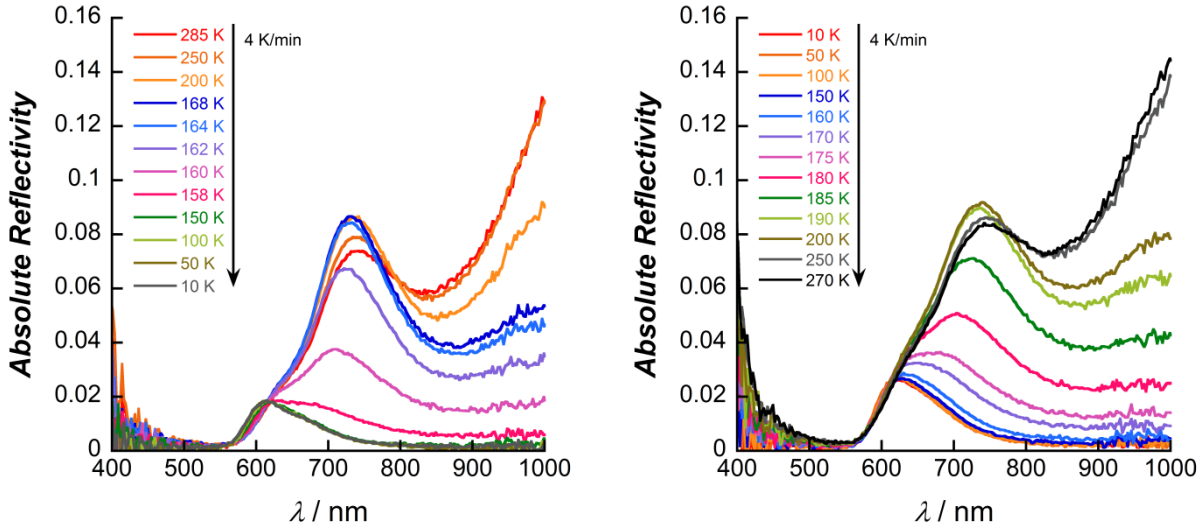

Figure III-37. Reflectivity spectra between 285 and 10 K as function of wavelength in cooling (left) and between 10 and 270 K in heating mode (right) at 4 K/min for **3**.

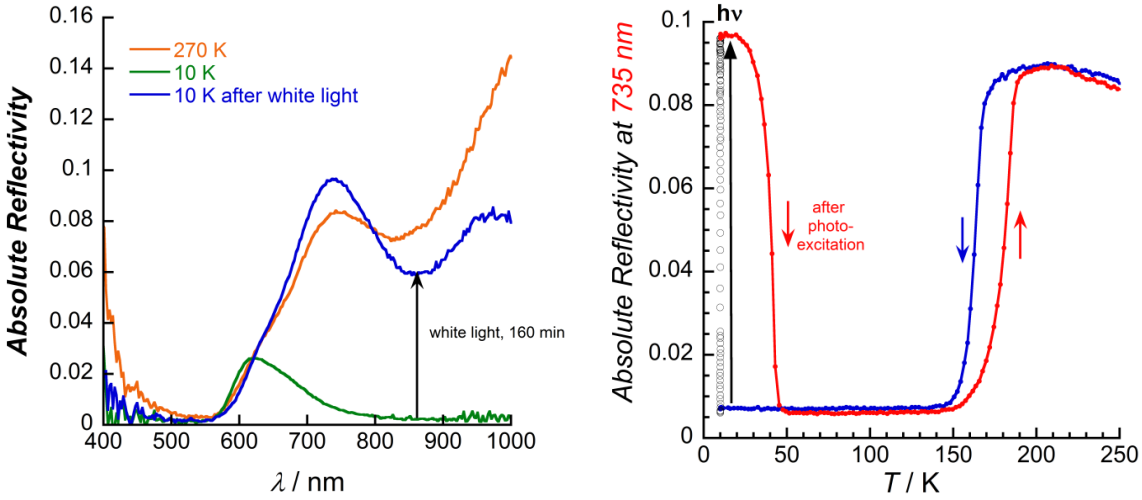

Figure III-38. (Left) Reflectivity spectra at 270 K (orange) and 10 K (green) before irradiation and after white light irradiation 160 minutes (blue); (right) thermal evolution of reflectivity signal recorded at λ = 735 ± 5 nm (AR_{735}) in cooling mode (250-10 K, blue curve), after white light irradiation (0.4 mW/cm^2, at 10 K, black circle markers) and in heating mode (10-250 K, red curve) at 4 K/min for **2**.

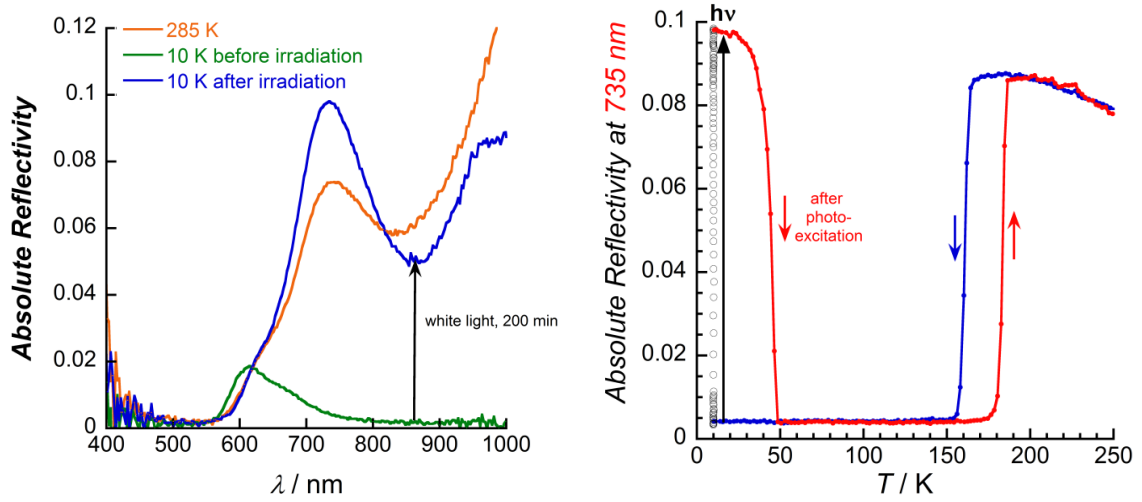

Figure III-39. (Left) Reflectivity spectra at 285 K (orange) and 10 K (green) before irradiation and after white light irradiation 200 minutes (blue); (right) thermal evolution of reflectivity signal recorded at λ = 735 ± 5 nm (AR_{735}) in cooling mode (250-10 K, blue curve), after white light irradiation (0.4 mW/cm^2, at 10 K, black circle markers) and in heating mode (10-250 K, red curve) at 4 K/min for **3**.

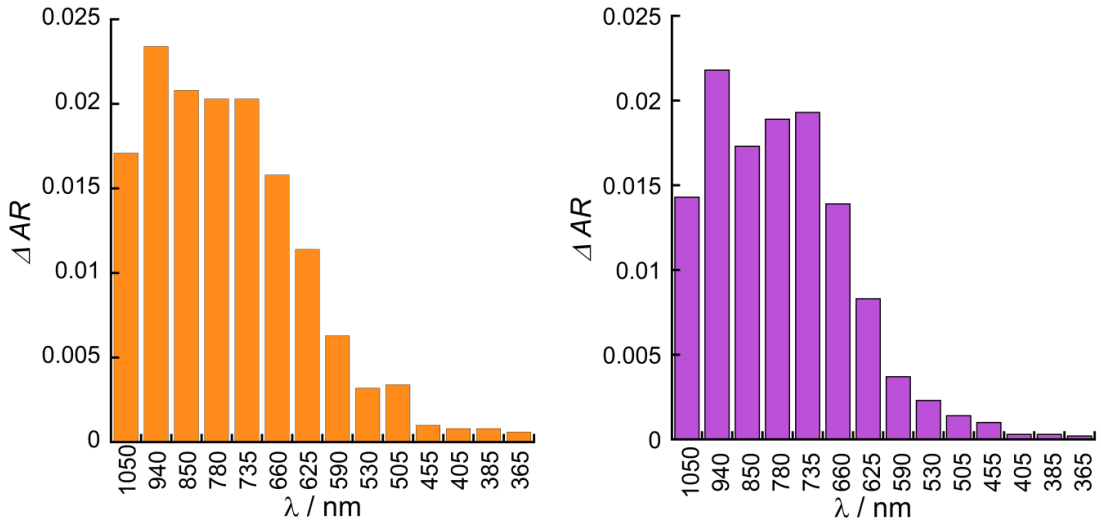

Figure III-40. Difference in absolute reflectivity (*ΔAR*) at 735 nm for **2** (left) and **3** (right), obtained before and after 20 min of irradiation with the 14 different LEDs (P = 0.2 mW/cm^2) at 10 K.

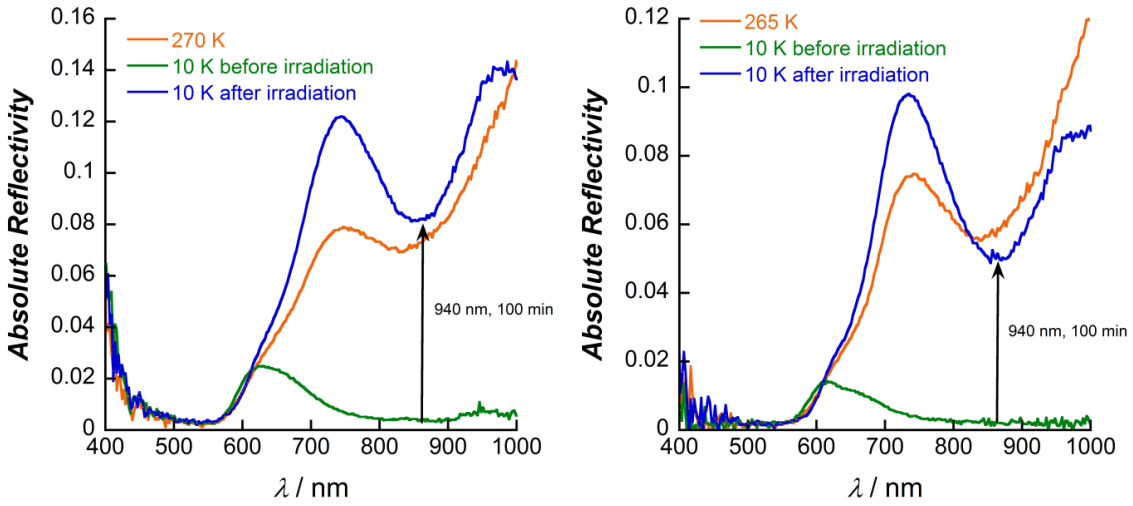

Figure III-41. Reflectivity spectra at high temperature (orange), at 10 K before irradiation (green) and after 940 nm irradiation (P = 5.5 mW/cm^2, 100 min at 10 K, blue) for **2** (left) and **3** (right).

Table III-7. Summary of the temperatures of the thermally induced-electron transfer process in cooling and heating mode and the relaxation temperatures from the metastable paramagnetic state to the diamagnetic state for compounds **1**•2DMF, **2**•2DMF and **3**•2DMF and their desolvated forms **1**, **2** and **3**.

Compounds	$T_{1/2}$ cooling in K	$T_{1/2}$ heating in K	T relaxation in K
1•2DMF	161 and 152	171 and 162	
1	165	170	45
2•2DMF	94	112	53
2	170	182	48
3•2DMF	88	101	57
3	156	164	48

III.3 XAS and XMCD Investigations for [{(Tp)Fe(CN)$_3$}{Co(PY5Me$_2$)}](PF$_6$)•2DMF (2•2DMF)

III.3.1 Introduction

As we have already seen in Chapter II (part II.3), the synthesis of the simplest reported molecular analogue of the FeCo PBAs, the dinuclear cyanido-bridged {FeCo} complex **1**, offered us the possibility to investigate in depth the electronic states involved in the thermal and photo-switching process using X-ray absorption spectroscopy (XAS) and X-ray magnetic circular dichroism (XMCD) on the $L_{2,3}$-edges of cobalt and iron ions. X-rays with the energy of a few keV (~ 1.0- 10 keV), used in ID12 beamline of ESRF synchrotron (Grenoble, France), are efficient for excitation of a *1s* electron to the *4p* or *3d* levels, giving information about the electronic states of the metals, from the *K*-edges viewpoint. One major difference in the experimental set-up between the XAS and XMCD investigations at *L*-edges at Soleil synchrotron and this experiment, is the absence of ultra-high vacuum conditions (UHV: 10^{-10} mbar range) in the experimental chambers of the latter. That allows the study of the properties of the new member in the Fe/Co electron transfer family, which contains lattice solvent molecules, compound **2**•2DMF.

In collaboration with Sadaf Fatima, Marie-Anne Arrio and Philippe Sainctavit from IMPMC (University of Paris VI), and Andrei Rogalev and Fabrice Wilhelm from ESRF, we performed studies at the *K*- edges of cobalt (~ 7.709 keV) and iron (~ 7.112 keV) ions with the following aims: (a) to observe the thermally and photo-induced ET in the dinuclear cyanido-bridged {FeCo} complex **2**•2DMF using these techniques; (b) to determine/confirm the spin and oxidation numbers of the Co and Fe ions in the different states; and (c) to determine the exact nature of the magnetic coupling between Fe and Co ions in the metastable light-induced paramagnetic state.

III.3.2 Experimental results

As it has been mentioned in the previous paragraphs of this chapter, the loss of lattice solvent molecules in complexes **2**•2DMF and **3**•2DMF influences significantly the temperature in which the ET is occurring. The experimental set-up of XAS investigations on *K*-edges in ID12 beamline in Grenoble synchrotron doesn't use ultra-high vacuum conditions (UHV: 10^{-10} mbar range), but still the investigations are performed under vacuum of 10^{-5} mbar range. In order to avoid the solvent loss during XAS and XMCD studies, the analyzed sample of compound **2**•2DMF was taken fast from its mother liquor solution (DFM/Et_2O) and covered with Kapton film on the sample holder (Figure III-42, left). The sample holder was then adapted to the cryostat (Figure III-42, middle) and inserted in the experimental chamber.

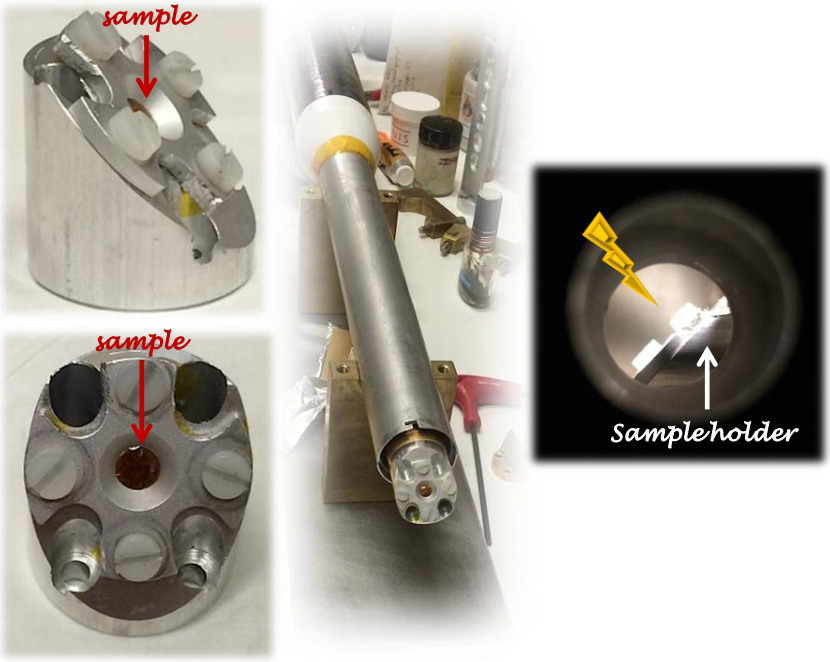

Figure III-42. (Left) The sample holder where compound **2**•2DMF was deposited; (middle) the cryostat and (right) the view of the sample holder from the window of the experimental chamber, while the sample is irradiated with 940 nm LED (*P* = 5 mW) at 2 K for 8 hours.

For a systematic study of **2**•2DMF by XAS/XMCD, the detailed study of Fe(III) and Co(II) precursors used for the synthesis is required. Microcrystalline powders of $[(PY5Me_2)Co^{II}(H_2O)](BF_4)_2$ and $(Bu_4N)[(Tp)Fe^{III}(CN)_3]$ were deposited on the sample holder in the same ways as **2**•2DMF, before they were inserted in the experimental chamber. XAS spectra at Co *K*-edges for $[(PY5Me_2)Co^{II}(H_2O)](BF_4)_2$ (Figure III-43, left) and Fe *K*-edges for $(Bu_4N)[(Tp)Fe^{III}(CN)_3]$ (Figure III-43, right) were recorded at 2 K. In the cobalt *K*-edge absorption spectrum of $[(PY5Me_2)Co^{II}(H_2O)](BF_4)_2$ at 2 K (Figure III-43, left), the energy of the absorption maximum observed at 7712 eV (pre-edge) corresponds to the forbidden *1s* (a_{1g}) → *3d* ($t_{2g,eg}$) transition, while the intense absorption maximum at 7728 eV to the allowed *1s* (a_{1g}) → *4p* (t_{1u}) transition, indicating the presence of Co^{II} ions.[13] In the iron *K*-edge absorption spectrum of $(Bu_4N)[(Tp)Fe^{III}(CN)_3]$ at 2 K (Figure III-43, right), the energy of the weak pre-edge at 7114.8 eV and the energy of the absorption maxima at 7131.8 eV indicate that the oxidation state of iron ion is +III.[13] XMCD signals were observed at the same temperature by applying external magnetic field of +/- 17 T. These XMCD signals were found to present successively two negative peaks and one positive peak in the Co precursor and three positive peaks in the Fe precursor (Figure III-44). The meaning of the XMCD data signs as well as information for the spin and orbital magnetic moment of the metal centers will be part of the Ph.D. work of Sadaf Fatima at IMPMC and they won't be discussed in the thesis.

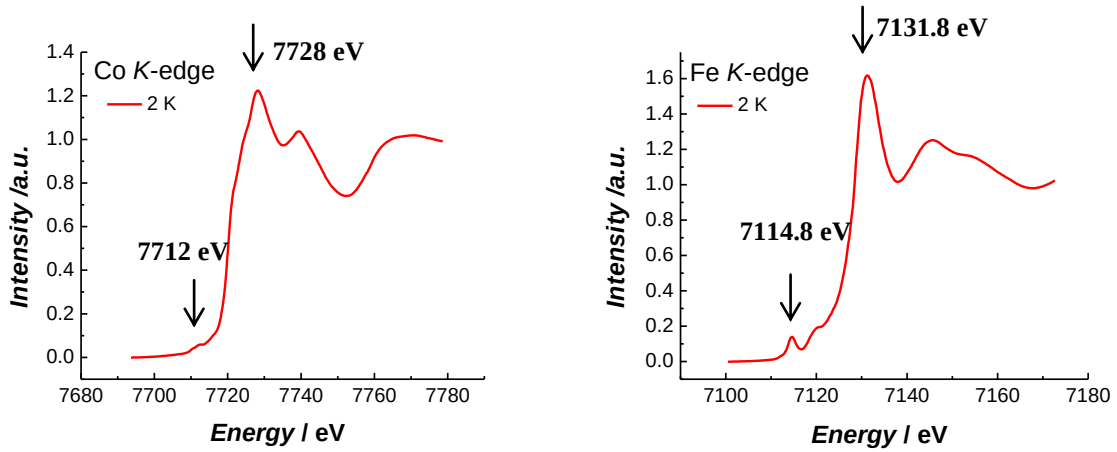

Figure III-43. XAS at Co *K*-edge (left) for $[(PY5Me_2)Co^{II}(H_2O)](BF_4)_2$ and Fe *K*-edge (right) for $(Bu_4N)[(Tp)Fe^{III}(CN)_3]$ at 2 K.

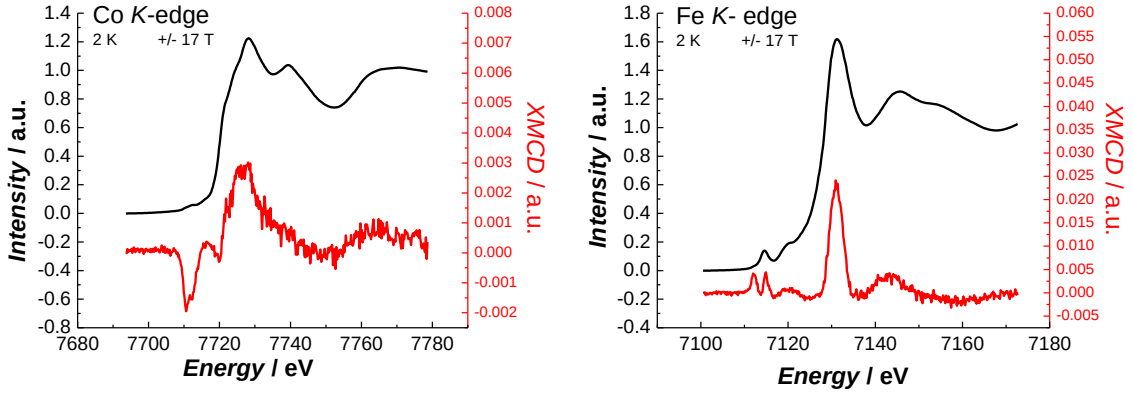

Figure III-44. Isotropic (average, black) and dichroic (XMCD, red) absorption spectra at Co *K*-edges for $[(PY5Me_2)Co^{II}(H_2O)](BF_4)_2$ (left) and at Fe *K*-edges for $(Bu_4N)[(Tp)Fe^{III}(CN)_3]$ (right) at 2 K.

Having in mind the results obtained from the precursors, we will focus on the results obtained for compound **2**•2DMF. The first series of experiments include the investigation of the thermal induced electron transfer process, as well as its reversibility probed by X-ray absorption spectroscopy. Co and Fe *K*-edge XAS spectra were recorded for the complex **2**•2DMF at 300 K and 2 K, in order to obtain the signature of the paramagnetic and the diamagnetic states, respectively, as suggested by the magnetic measurements (Figure III-11). The cobalt *K*-edge absorption spectrum of **2**•2DMF at 300 K (Figure III-45, left, red), shows a maximum absorption at 7728 eV (allowed *1s* (a_{1g}) → *4p* (t_{1u}) transition) and a weak pre-edge at 7711.8 eV (forbidden *1s* (a_{1g}) → *3d* ($t_{2g,\ eg}$) transition), indicating the presence of Co^{II} ions.[13] At 2 K (Figure III-45, left, gray), the Co *K* edge maximum is shifted by 2 eV to higher energy (7730 eV) compared to that at 300 K and fits the energy of the absorption maximum of Co^{III} ions.[13,14] The high-energy shift of the EXAFS (extended X-ray absorption fine structure) oscillations observed above 7740 eV clearly demonstrates the presence of shorter Co^{III}-to-ligand bonds in **2**•2DMF at 2 K (as reported for EXAFS oscillations in 3D Fe/Co PBAs).[14] The iron *K*-edge spectra of **2**•2DMF exhibit weaker changes regarding the thermally induced

ET (Figure III-45, right).[13,14] The pre-edge energy shifts from 7117.8 eV at 300 K to 7113.9 eV at 2K, while the absorption maximum shifts from 7131.8 eV at 300 K to 7130.5 eV at 2 K. These weak changes are not surprising, given the similarity of the electronic configuration of the low spin state (LS) and the similar Fe coordination sphere observed in the crystal structures at 220 and 82 K (Tables III-2 and III-5). The energy of the *K*-edge absorption maximum (7131.8 eV) at 300 K indicates that the oxidation state of the iron ion is +III.[13,14] This 1 eV low-energy shift of the pre-edge and of the absorption maxima between 300 and 2 K is characteristic of the decrease of the oxidation state for +III to +II.[13]

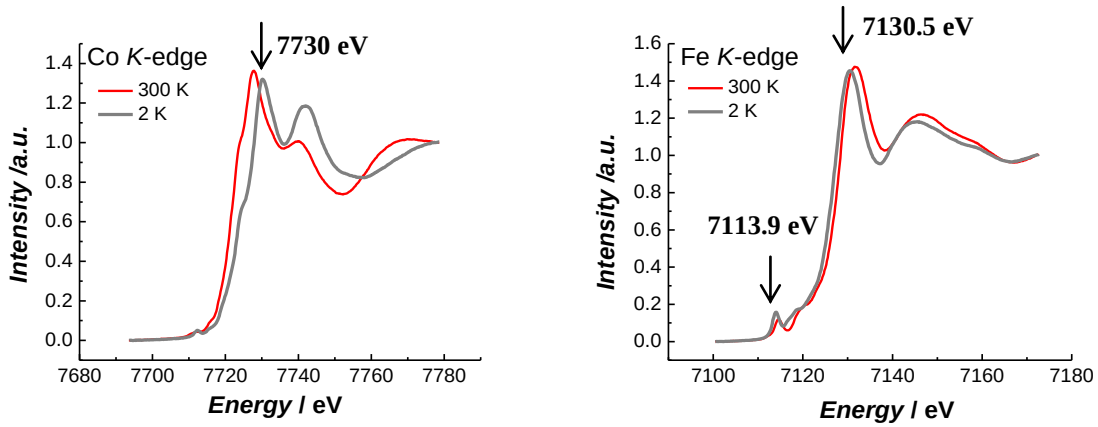

Figure III-45. XAS at Co (left) and Fe (right) *K*-edge at 300 K (red) and 2 K (gray) for **2**•2DMF.

The second series of experiments concern the investigation of the photoinduced paramagnetic state of **2**•2DMF at low temperature. The Co and Fe *K*-edge XAS spectra were recorded at 2 K before irradiation and after irradiation with a LED at 940 nm, P = 5 mW for 8 hours. The choice of the 940-nm LED for irradiation was based on the reflectivity results obtained (Figure III-22, left). The Co and Fe *K*-edge XAS spectra at 2 K after the irradiation of **2**•2DMF (Figure III-46, black spectra) are **identical** with those obtained at 300 K (Figure III-46, red spectra), confirming the photoinduced electron transfer from the diamagnetic $\{Fe^{II}_{LS}Co^{III}_{LS}\}$ state of the pair at low temperature to the paramagnetic $\{Fe^{III}_{LS}Co^{II}_{HS}\}$ state after irradiation. After the photo-excitation experiment, the reversibility of the photo- and thermally induced intramolecular ET was verified. The photo-excited system recovered its diamagnetic state at 70 K and then its initial paramagnetic state when it was warmed up to 300 K.

Since the light-induced metastable state in compound **2**•2DMF is paramagnetic, weak XMCD signals were observed at Co and Fe *K*-edges at 2 K under applied magnetic field of +/- 17 T (Figure III-47). These XMCD data exhibited several negative and positive peaks, for both Co and Fe ions. The sign of the XMCD peaks at the Co and Fe *K*-edges in **2**•2DMF is different than the sign observed in the Co and Fe precursors (Figure III-44). Keeping in mind that the bulk photomagnetic studies of this compound (part III.2.6) suggested the presence of weak antiferromagnetic interactions between the metal centers (Figure III-28), the above phenomenon can be attributed to the alignment of the spins at 17 T.

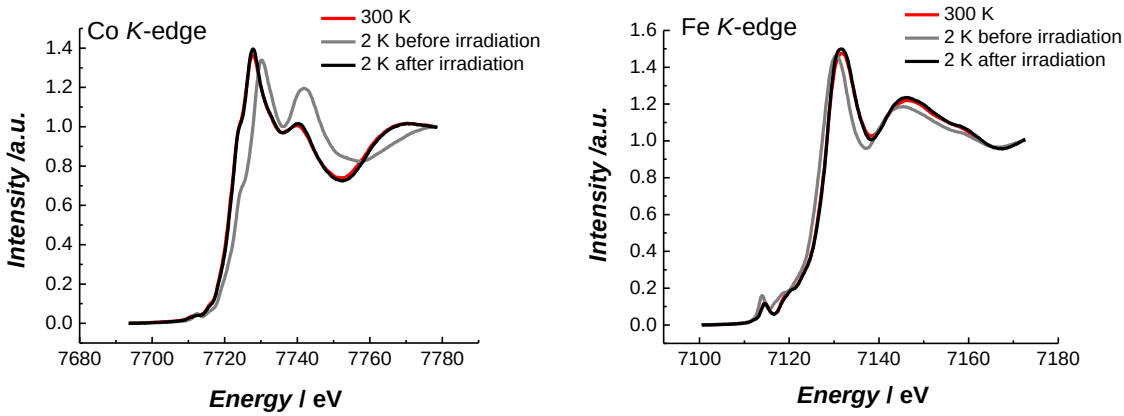

Figure III-46. XAS at Co (left) and Fe (right) *K*-edge for **2**•2DMF at 300 K (red), 2 K (gray) and at 2 K (black) after irradiation of the 940-nm LED (*P* = 5 mW) for 8 hours.

The magnetization of the light-induced paramagnetic state of **2**•2DMF, at the Co (7725 eV) and Fe (7114 eV) energies (the energies where the most prominent changes in the Co and in the Fe *K*-edges between the high and low temperature spectra were observed) was estimated by the XMCD data at 2 K, under applied magnetic field of +/- 8 and +/- 17 T (Figure S.III-19). As it is shown in Figure III-48, the normalized magnetization curves for Co and Fe, are superposed to each other, as well as to the normalized magnetization of the pair **2**•2DMF from bulk photomagnetic studies of the photo-induced paramagnetic state at 1.8 K, suggesting the absence of interactions between the metal sites within the complex. This is not surprising, since the interactions expected are very weak and only by performing this experiment at much lower temperature (< 1 K) and under weak magnetic field (< 1 T), we may achieve to confirm the sign and determine the value of the interactions between the Fe and Co ions in the photo-induced paramagnetic state of the pair.

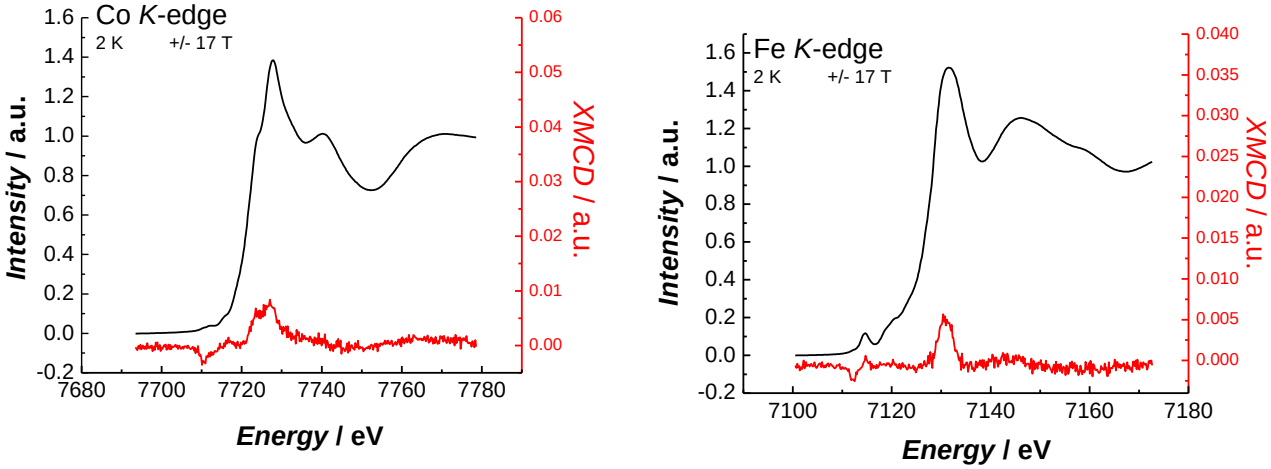

Figure III-47. Isotropic (average, black) and dichroic (XMCD, red) absorption spectra at Co *K*-edges (left) and Fe *K*-edges (right) at 2 K under applied magnetic field of +/- 17 T, for **2**•2DMF, after 940 nm irradiation (*P* = 5 mW, 2 K) for 8 hours.

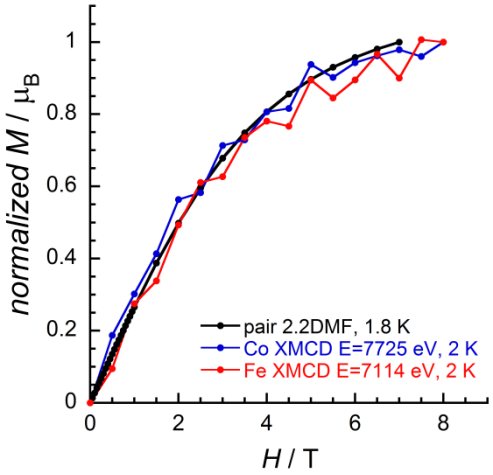

Figure III-48. *M versus H* plot (black dots) for complex **2**•2DMF at 1.8 K from bulk photomagnetic studies; normalized XMCD signal of the light-induced paramagnetic state of **2**•2DMF as a function of the field, at the Co (7725 eV, blue) and Fe (7114 eV, red) *K*-edges, under applied magnetic field of +/- 8 T at 2 K.

The electron transfer phenomenon was also followed as a function of temperature by XAS. The temperature dependence of the paramagnetic $\{Fe^{III}_{LS}(\mu\text{-}CN)Co^{II}_{HS}\}$ fractions was deduced from the thermal variation of the absorption at the characteristic energies (Co and Fe *K*-edges of energy 7725 and 7114 eV, respectively; Figure III-49). For the Fe *K*-edge, the temperature dependence of the XAS intensity was followed in cooling mode from 300 to 70 K in a temperature sweeping rate of 2.8 K / min (Figure III-49, right, blue circle dots) and it is almost similar with the magnetic properties of **2**•2DMF from magnetic susceptibility measurements (Figure III-49, right, black curve). The transition associated with the electron transfer process was clearly observed, while the small deviation from the susceptibility measurements (regarding the ET temperature) can be ascribed to the different temperature sweeping rates and experimental set-up used. The results obtained for the Co *K*-edge in cooling mode (Figure III-49 left, blue circle dots), evidence the concurrent electron transfer process in the Co and Fe ions at the local level. In addition, the XAS intensity was followed in heating mode form 70 to 300 K in a temperature sweeping rate of 1.9 K / min (Figure III-49 left, blue square dots) for the Co *K*-edge and the obtained XAS data correlate very well with the data obtained from the magnetic susceptibility measurements (Figure III-49, left, black curve). Finally, the relaxation from the metastable paramagnetic state to the thermodynamically stable diamagnetic state was followed at the Co *K*-edge, in heating mode at 0.23 K / min (Figure III-49 left, red dots) and the results are in a perfect agreement with the photomagnetic studies (Figure III-49, left, black curve).

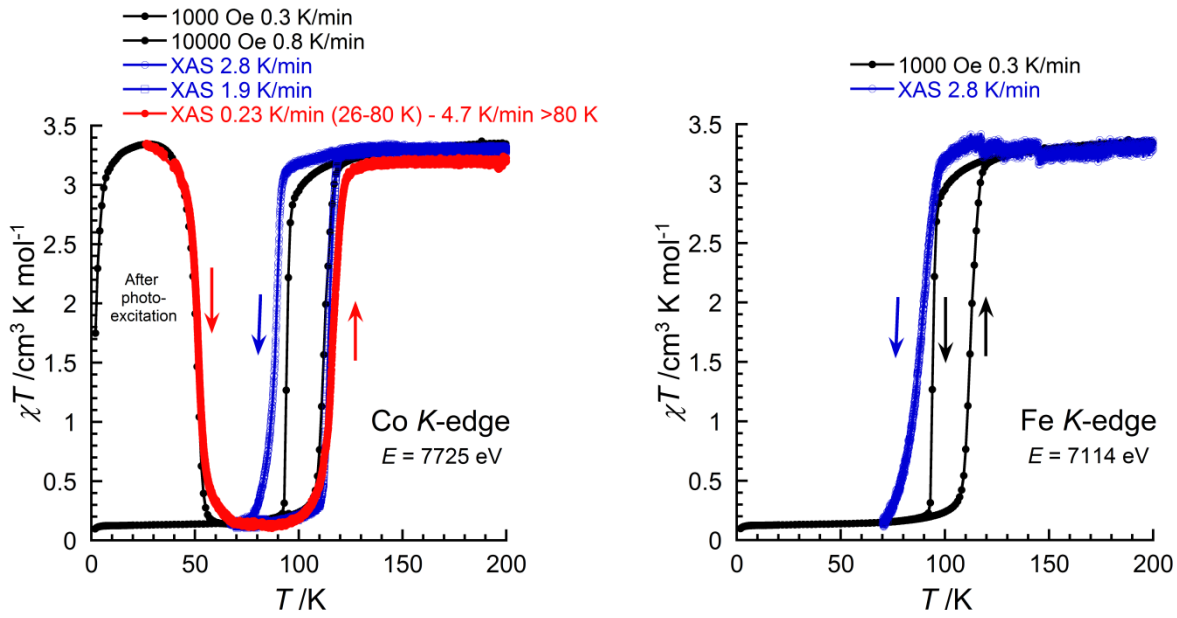

Figure III-49. (Left) χT versus T plots for **2**•2DMF (in black, from 200 to 1.8 K at 0.1 T and 0.3 K/min and from 1.8 to 200 K in heating mode at 1 T and 0.8 K/min after irradiation of the diamagnetic state at 10 K with 940 nm LED); Thermal dependence of the normalized XAS data in the Co *K*-edge (E = 7725 eV) for **2**•2DMF (in blue circle dots, in cooling mode from 200 to 70 K at 2.8 K/min; in blue square dots, in heating mode from 70 to 200 K at 1.9 K/min and in red dots, in heating mode from 26 to 80 K at 0.23 K/min and from 80 to 200 K at 4.7 K/min). (Right) χT versus T plots for **2**•2DMF (in black, in cooling and heating mode from 200 to 1.8 K at 0.1 T and 0.3 K/min); thermal dependence of the normalized XAS data in the Fe *K*-edge (E = 7114 eV) for **2**•2DMF (in blue circle dots, in cooling mode from 200 to 70 K at 2.8 K/min).

III.4 Investigations of the Electron Transfer Phenomenon in the Dinuclear {Fe(*μ*-CN)Co} Complexes under Applied Electric Field

III.4.1 Introduction

In response to the challenge of designing and synthesizing multiresponsive molecular systems that may find applications in future devices, we presented up to now a new family of molecular PBAs, which consists of the simple Fe/Co dinuclear unit. These compounds exhibit magnetic bistability under a thermal and light treatment due to an intramolecular metal-to-metal ET process. The fact that the origin of this phenomenon is the transfer of one electron from one metal site to the other, opens the possibility to investigate the switchable properties of these compounds by applying electric field as an external stimuli. An interplay between electric field, temperature and Co(II)↔Fe(III) electron transfer was observed in some 3-D and 1-D [FeCo] PBAs,[15-17] but the link between ET and dielectric properties is as-yet an unexplored area for molecular cyanide-bridged systems. With this in mind, we investigated the dielectric properties of the dinuclear compounds **2**•2DMF and **3**•2DMF, by measuring the

real and the imaginary parts of dielectric permittivity, ε' and ε'', respectively, as a function of frequency of the applied electric field at given temperatures from 300 to 50 K.

The permittivity (ε_r) describes the response of a material introduced to an electric field. ε_r is a complex quantity, $\varepsilon_r = \varepsilon' + i\,\varepsilon''$: the real part of permittivity (ε') is a measure of how much energy from an external electric field is stored in a material, while the imaginary part of permittivity (ε'') (or "loss factor") is a measure of how dissipative is the material when it is introduced to an external electric field. In a molecular material, atoms are assembled to each other, sharing one or more of their electrons. These rearrangements of electrons are creating a permanent dipole moment. These moments are oriented in a random manner in the absence of an electric field so that no polarization exists. When an electric field is applied, the dipoles will rotate to align with it, inducing a polarization, which contributes to the overall permittivity of the material. The dipolar/dielectric friction accompanying the orientation of the dipole will contribute to the dielectric losses, causing a variation in both ε' and ε'', associated with a relaxation effect (relaxation barrier and time). If an electron transfer process is occurring inside the molecular material due to another external parameter (i.e. temperature), a new dipole is created, which will rotate to align in the direction of the applied electric field, and that will affect the permittivity values, as it has been proposed for heterometallic PBAs.[18,19]

III.4.2 Experimental results

In collaboration with Hitoshi Miyasaka and Wataru Kosaka from IMR-Tohoku University in Japan, we studied the real and the imaginary parts of dielectric permittivity of compounds **2**•2DMF and **3**•2DMF as a function of frequency of the applied electric field at given temperatures in order to probe their electron transfer behavior. The measurements were performed in the PPMS using the conventional three-terminal method (or parallel plate method). A few mg from each sample filtrated from their mother liquor (DMF/Et_2O), were gently grinded and finally transformed to a pellet (10 mm diameter) by applying pressure of 2 kN for 60 sec. For each compound, a pellet was placed between two stainless plates (electrodes), where Au wires were attached by Au paste and epoxy resin, to finally form a capacitor. This capacitor was attached to the PPMS sample holder and inserted in the PPMS dewar (under 1 atm of He). The temperature was controlled with the PPMS program, while the sample temperature was monitored by Si diode sensor attached near the pellet (Figure III-50). The properties of the compounds in the form of a pellet in respect to the thermally induced electron transfer process are necessary to be investigated before the experiment. Thus, the optical reflectivity properties of **2**•2DMF in the form of a pellet are shown in Figure S.III-15, where the thermally induced electron transfer process was probed in the same temperature region (100-120 K) as for the fresh filtrated crystals of **2**•2DMF by the same studies.

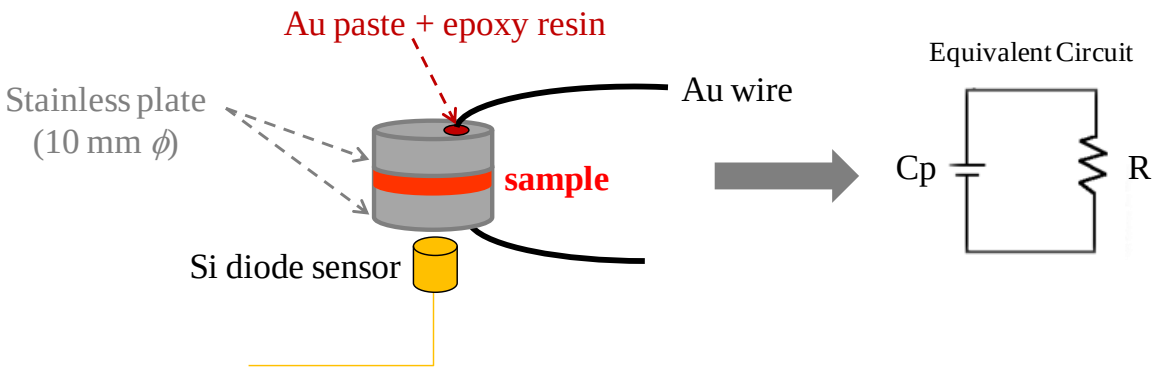

Figure III-50. Capacitor used at the three-terminal method (or parallel plate method) and the equivalent circuit formed.

The temperature dependence of the real and the imaginary parts of dielectric permittivity, ε' and ε'', (T = 300-50 K, in cooling and heating modes, at 0.09 K/min) under applied oscillating electric field of 1.5 V at 100 Hz and 15 V at 1000 and 10000 Hz are shown in Figures III-51 and III-52, for **2**•2DMF and **3**•2DMF, respectively. These curves allow us to visualize easily the temperature region where the signal variations in the dielectric constant appear. Moreover, these data are plotted in a similar way with the magnetic properties in order to compare the electron transfer behavior discussed in our systems. Indeed, as the temperature was decreased from 300 to 50 K (Figures III-51 and III-52, left, for **2**•2DMF and **3**•2DMF, respectively), one sharp and frequency-dependent ε'signal and several frequency-dependent ε''signals were observed for both compounds in two temperature regions (160 and 195 K and 130-70 K). In heating mode from 50 to 300 K (Figures III-51 and III-52, right, for **2**•2DMF and **3**•2DMF, respectively), the frequency-dependent ε' and ε''signals appear again, but we note different shapes for the peaks in the low temperature region. This corresponds to a hysteresis behavior in temperature.

In order to analyze deeper and extract information from these studies, the frequency dependence of the real and the imaginary parts of dielectric permittivity, ε' and ε''(Figures III-53 and III-55, for **2**•2DMF and **3**•2DMF, respectively), at the different temperature regions, was evaluated for both cooling and heating. These plots illustrated the relaxation behavior of the above mentioned relaxation processes. It is worth mentioning that the signals observed at high temperatures for both compounds are identical in both cooling and heating processes, thus for this relaxation event only the data derived from the cooling process will be presented.

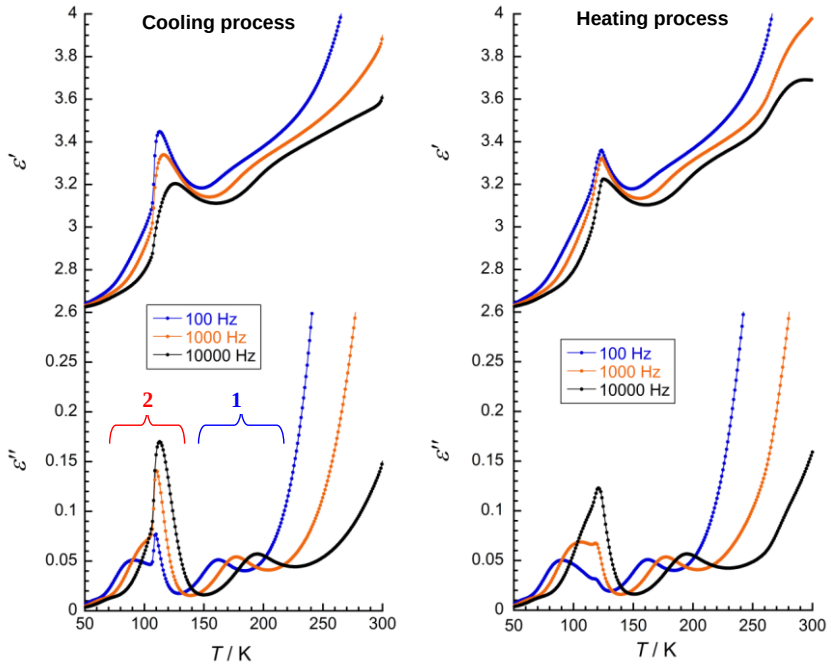

Figure III-51. Temperature dependence of the real and imaginary parts of the dielectric permittivity, ε' and ε'', respectively, at 100, 1000 and 10000 Hz, in cooling (left) and heating (right), between 300 and 50 K, at 0.09 K/min, for compound **2**•2DMF; the region of the two observed modes are marked with different colors and numbered for clarity.

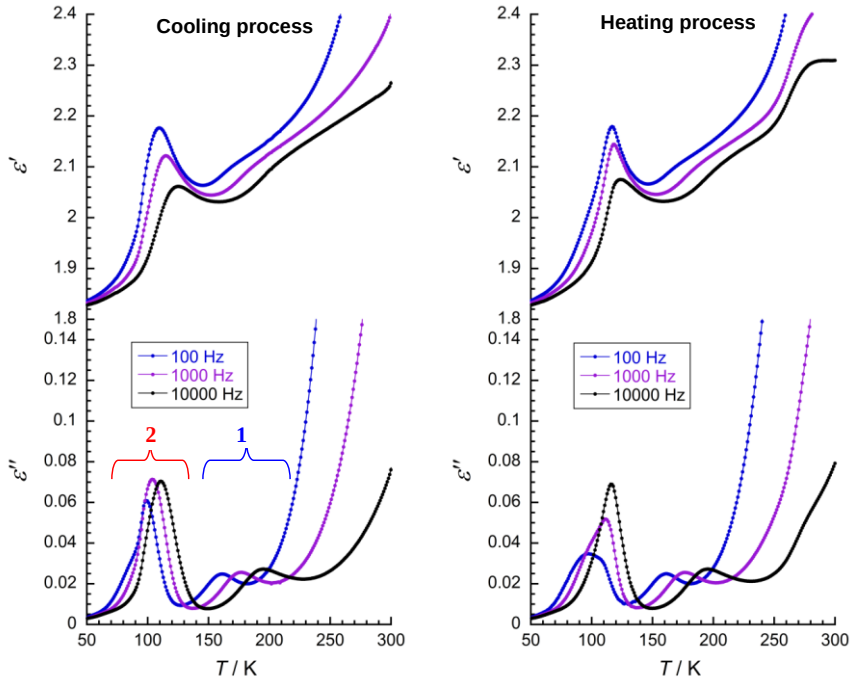

Figure III-52. Temperature dependence of the real and imaginary parts of the dielectric permittivity, ε' and ε'', respectively, at 100, 1000 and 10000 Hz, in cooling (left) and heating (right), between 300 and 50 K, at 0.09 K/min, for compound **3**•2DMF; the region of the two observed modes are marked with different colors and numbered for clarity.

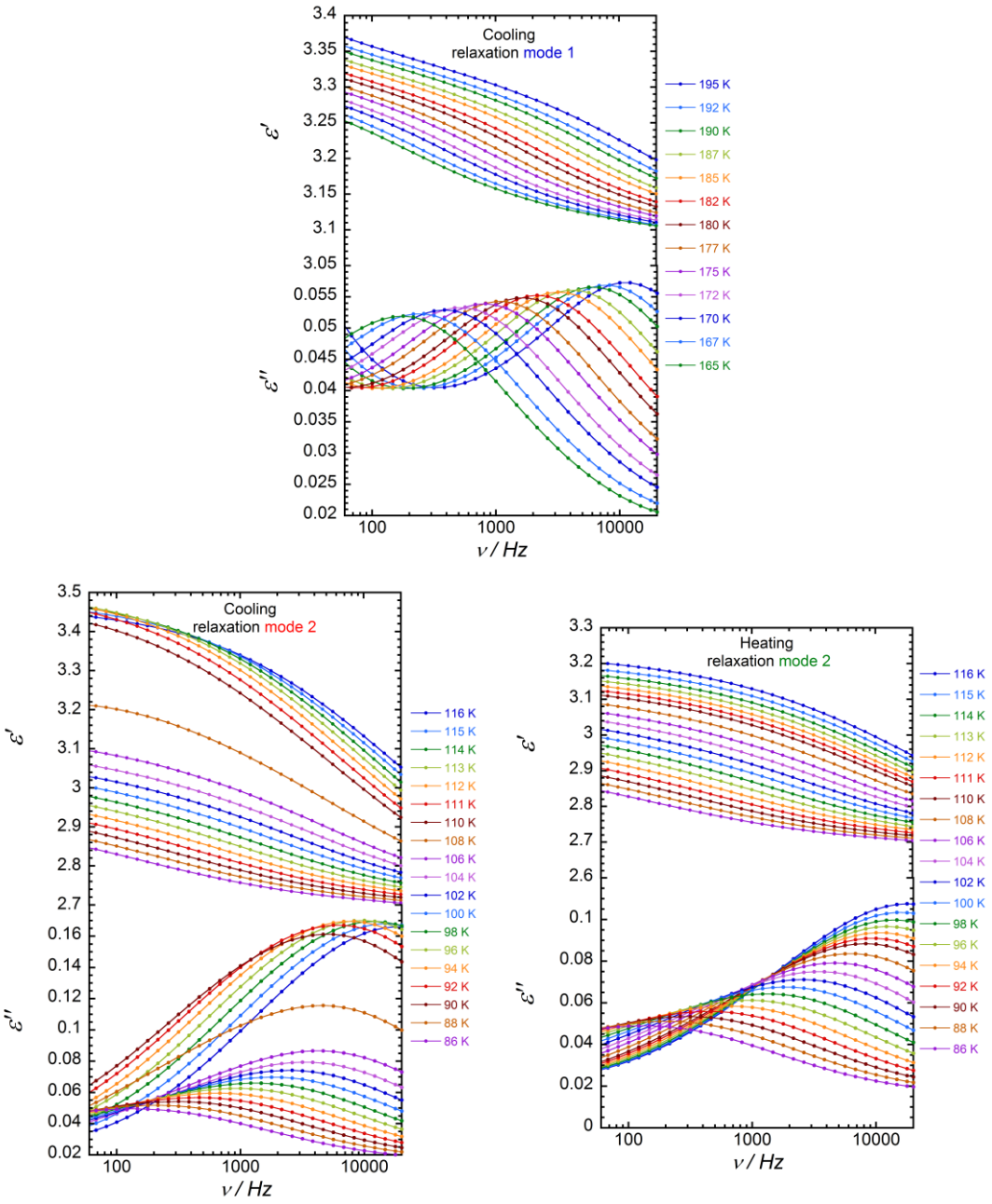

Figure III-53. Frequency dependence of the real and imaginary parts of dielectric permittivity, ε' and ε'', respectively, at the given temperatures, in cooling for relaxation mode 1 (top), mode 2 (bottom, left) and in heating for relaxation mode 2 (bottom, right), for compound **2**•2DMF.

With the assumption that the frequencies of the peak maxima correspond to the relaxation time constant τ of the dipolar reorientations, the Arrhenius plots were constructed (Figures III-54 and III-56 for **2**•2DMF and **3**•2DMF, respectively) and the values of energy barriers (E_A/k_B) and relaxation time (τ_0) were derived in cooling and heating process.

For compound **2**•2DMF in the cooling process, the energy barrier of mode 1 was found to be equal to E_A/k_B = 4414 K and the τ_0 = 2.1 10^{-15} s. For mode 2 the data are not following the Arrhenius law, but a crossover between two thermally activated regimes is appearing, giving

rise to two values for the energy barrier and τ_0: E_A/k_B = 2710 K and τ_0 = 6.2 10^{-16} s, and a second E_A/k_B = 1599 K and τ_0 = 1 10^{-11} s. It is important to keep in mind that this phenomenon is appearing in the temperature region where the first order transition associated with the electron transfer process is taking place in compound **2**•2DMF (Figure III-54, right the light blue area). In the heating process, mode 2 seems to follow an Arrhenius law and values for relaxation barrier and time are obtained: E_A/k_B = 1623 K and τ_0 = 7.5 10^{-12} s.

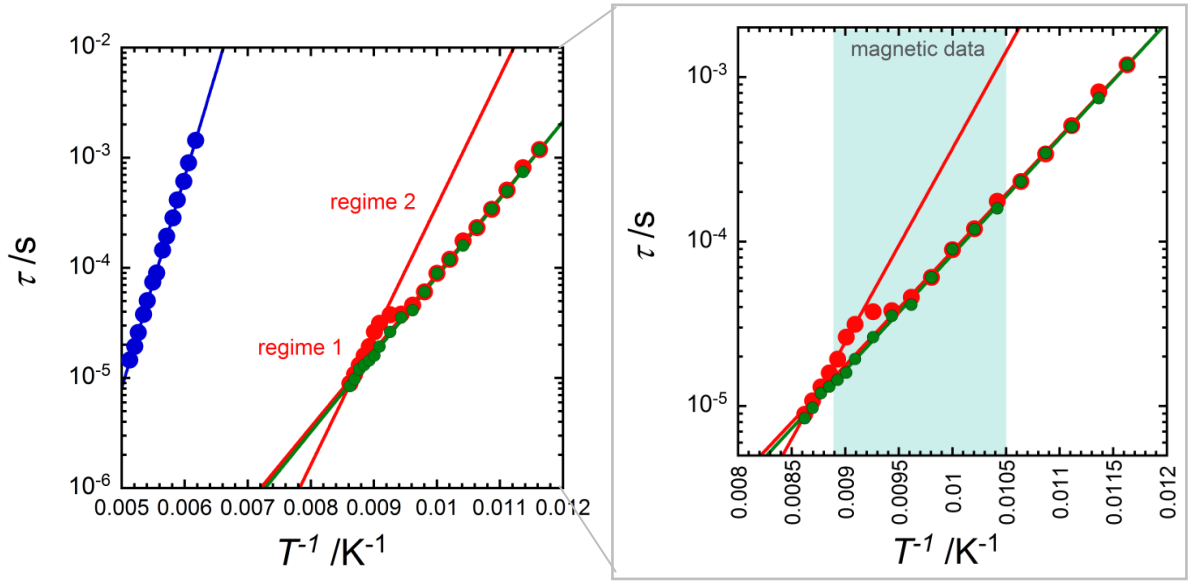

Figure III-54. (Left) τ as a function of 1/T plot in semi logarithmic scale, from the data in cooling (blue and red circles), and heating (green circles); (right) zoom of the Arrhenius plot for mode 2 in cooling (red circles) and heating (green circles), for complex **2**•2DMF. The crosshatch area in light blue color, indicates the temperature region where the first order transition is taking place in compound **2**•2DMF, from the magnetic data (0.3 K/min).

Table III-8. The values for the energy barrier and relaxation time of the two modes in cooling and heating for compound **2**•2DMF.

	$\tau = \tau_0 e^{C/T}$		
modes	***regime***	τ_0	$C = E_A/k_B$
1		2.1 10^{-15} s	4414 K
2	1	6.2 10^{-16} s	2710 K
	2	1 10^{-11} s	1599 K
2		7.5 10^{-12} s	1623 K

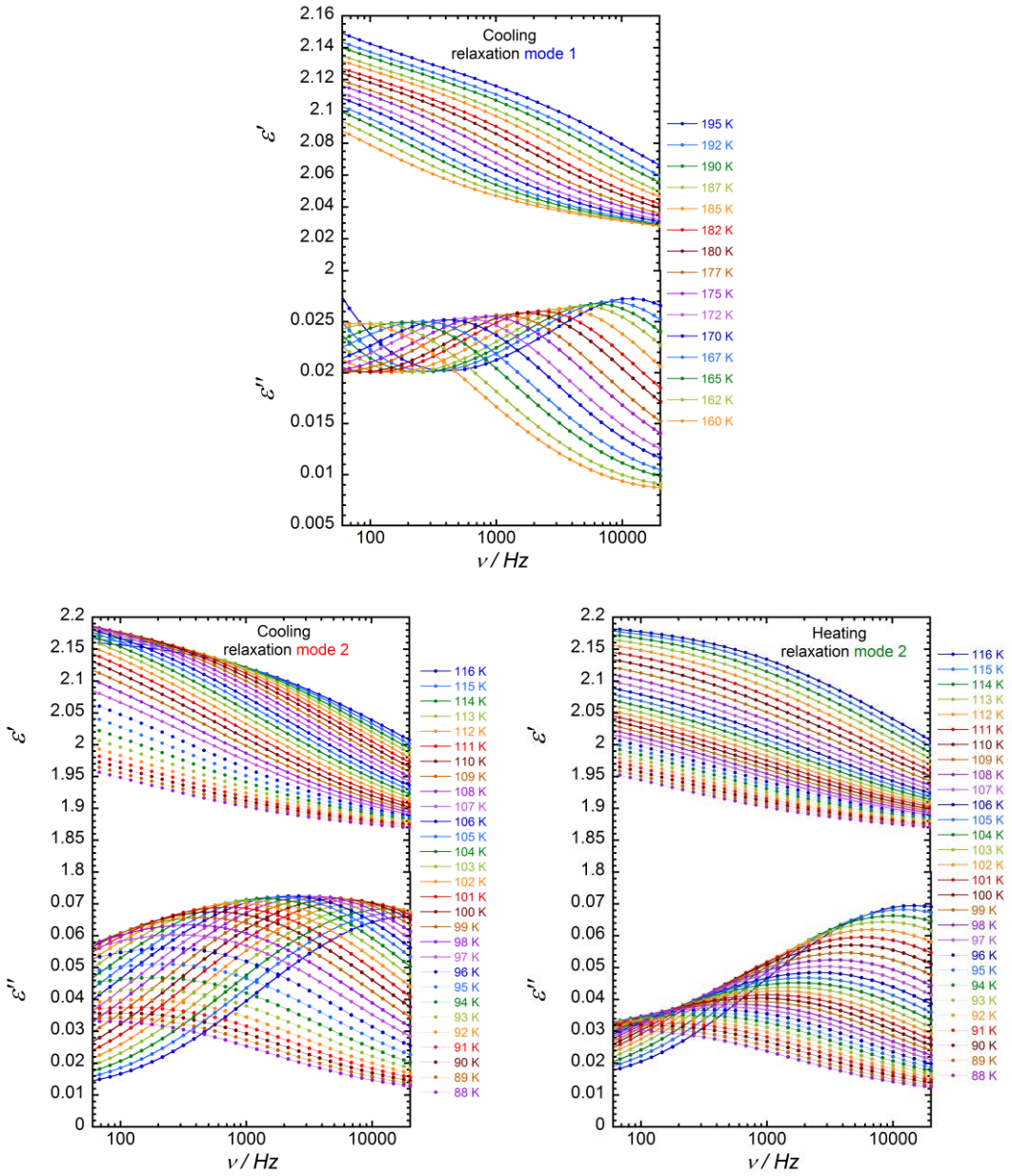

Figure III-55. Frequency dependence of the real and imaginary parts of dielectric permittivity, ε' and ε'', respectively, at the given temperatures, in cooling for relaxation mode 1 (top), mode 2 (bottom, left) and in heating for relaxation mode 2 (bottom, right), for compound **3**•2DMF.

For compound **3**•2DMF in the cooling process, the energy barrier of the relaxation mode 1 was found to be equal to E_A/k_B = 4441 K and the τ_0 = 1.8 10^{-15} s. For mode 2, the data are not following an Arrhenius law, but again with a crossover between two thermally activated regimes, giving rise to two values for the energy barrier and relaxation time: E_A/k_B = 2539 K and τ_0 = 2.6 10^{-15} s, and a second E_A/k_B = 1377 K and τ_0 = 3.6 10^{-10} s. As mentioned before, this phenomenon is appearing in the temperature region where the first order transition is taking place in compound **3**•2DMF (Figure III-56, light blue area). In heating, mode 2 seems

to follow an Arrhenius law and values for relaxation barrier and time are obtained: E_A/k_B = 1928 K and τ_0 = 7.7 10^{-13} s.

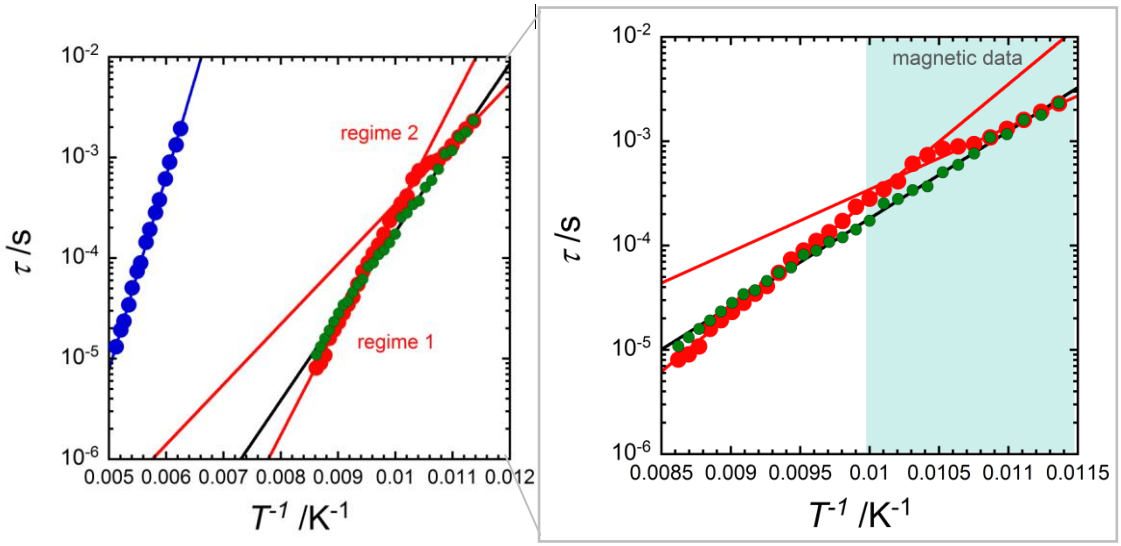

Figure III-56. (Left) τ as a function of 1/T plot in semi logarithmic scale, from the data in cooling (blue and red circles), and heating (green circles); (right) zoom of the Arrhenius plot for mode 2 in cooling (red circles) and heating (green circles), for complex **3**•2DMF. The crosshatch area in light blue color, indicates the temperature region where the first order phase transition is taking place in compound **3**•2DMF, from the magnetic data (0.3 K/min).

Table III-9. The values for the energy barrier and relaxation time of the two modes in cooling and heating for compound **3**•2DMF.

	$\tau = \tau_0 e^{C/T}$		
modes	***regime***	τ_0	$C = E_A/k_B$
1		1.8 10^{-15} s	4441 K
2	1	2.6 10^{-15} s	2539 K
	2	3.6 10^{-10} s	1377 K
2		7.7 10^{-13} s	1928 K

Compounds **2**•2DMF and **3**•2DMF exhibit similarly complicated behavior under an oscillating electric field. In an effort to explain the origin of mode 1 in the high temperature region, we propose that the molecules of DMF in the lattice of the compound can act as dipoles and thus create a response in the permittivity, due to a disorder close to the their freezing point (≈ 213 K). The proof of this suggestion will be the lack of this mode in a compound with no DMF lattice molecules. The best candidates for this investigation are the desolvated forms of **2**•2DMF and **3**•2DMF, compounds **2** and **3**. Compound **2** was chosen for our investigations. At this point it is important to remind that this compound is exhibiting electron transfer behavior at 170 K in cooling mode and a hysteresis of 12 K for temperature sweeping rate 0.3 K / min (Figure III-34).

The temperature dependence of the real and the imaginary parts of dielectric permittivity, ε' and ε'', (T = 300-50 K, in cooling and heating, at 0.09 K/min) under applied oscillating

electric field of 1.5 V at 100 Hz and 15 V at 1000 and 10000 Hz for compound **2** is presented in Figure III-57. In cooling (Figure III-57, left) two frequency-dependent ε'' signals were observed: mode 1 (blue area in Figure III-57) around 170 K and mode 2 (red area in Figure III-57) at low temperatures. As the temperature increases from 50 to 300 K, we observe again mode 2 unchanged, while mode 1 is appearing more clearly and it is shifted 15 K higher in temperature. The frequency dependence of the real and the imaginary parts of dielectric permittivity, ε' and ε'' for compound **2** (Figure III-58), at the different temperature regions (see Figure III-57), allowed us to construct the Arrhenius plot (Figure III-59) and extract the values for the energy barrier and relaxation time of mode 2. In the other hand, for mode 1 (Figure III-57) we weren't able to extract the relaxation barrier and time, since the frequencies of the peak maxima, corresponding to the relaxation time constant τ, were out of the window of the frequency range used. Moreover, the ε''peak maximum (shape and presence of hysteresis) of mode 1 is appearing where the first order phase transition is expected for the desolvated compound **2** (Figure III-34). These results are suggesting that this mode is coupled with the electron transfer behavior of the compound, reinforcing our hypothesis of the DMF disorder in the solvated [FeCo] pairs at high temperatures. For mode 2, the values of E_A/k_B = 1612 K and τ_0 = 2.2 10^{-12} s were extracted. Astonishingly, the values obtained for the relaxation barrier and time in compound **2**, are comparable with those obtained from the second regime of mode 2 in compounds **2**•2DMF and **3**•2DMF (Figures III-54 and III-56).

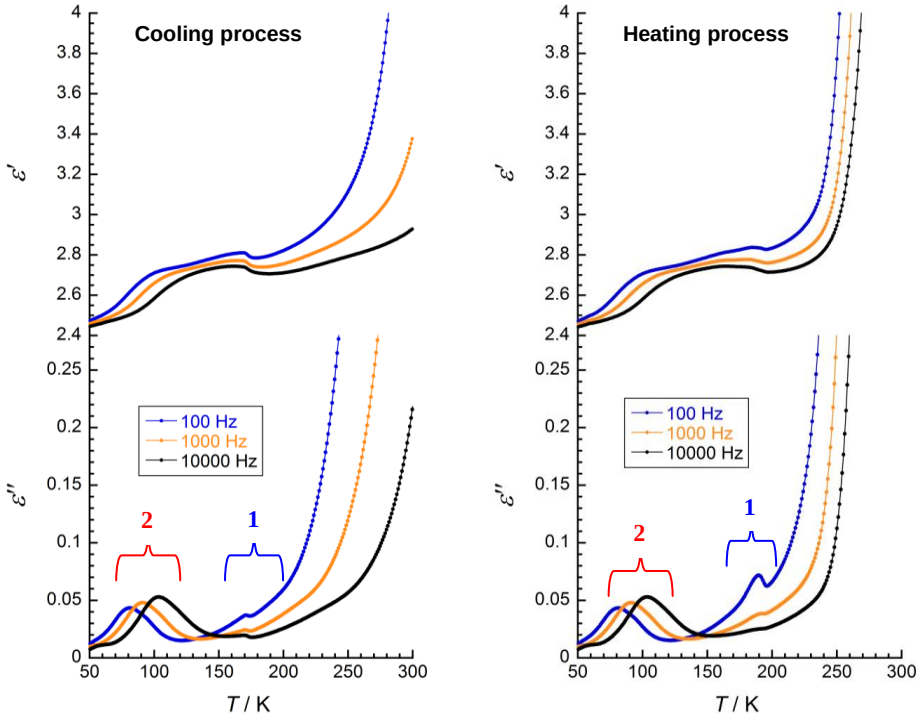

Figure III-57. Temperature dependence of the real and imaginary parts of the dielectric permittivity, ε' and ε'', respectively, at 100, 1000 and 10000 Hz, in cooling (left) and heating (right), between 300 and 50 K, at 0.09 K/min, for compound **2**; the region of the two observed relaxation modes are marked with different colors and numbered for clarity.

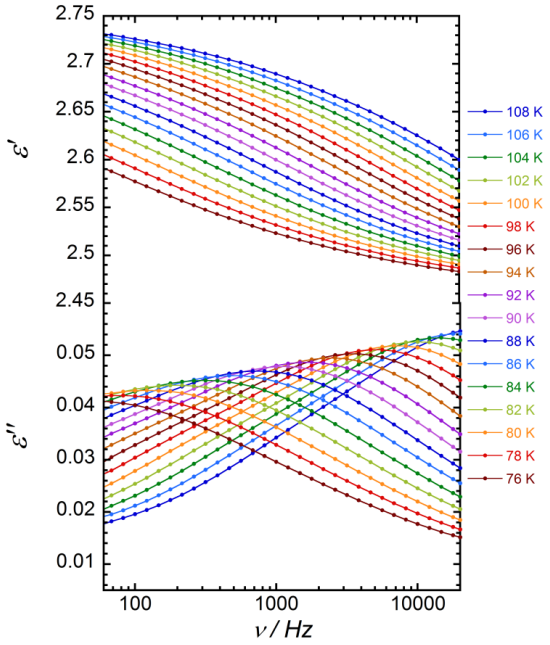

Figure III-58. Frequency dependence of the real and imaginary parts of dielectric permittivity, ε' and ε'', respectively, at the given temperatures in cooling, for compound **2**.

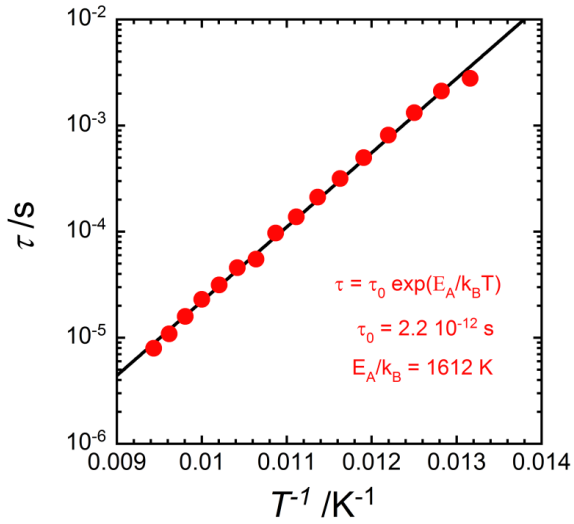

Figure III-59. τ as a function of 1/T plot in semi logarithmic scale, from the data in cooling mode, for compound **2**.

Summarizing the results obtained from compounds **2**•2DMF, **3**•2DMF and **2**, concerning the presence of mode 2 for the three systems at low temperatures, we suggest that it is probably associated with a dipolar relaxation of the asymmetric dinuclear unit inside the oscillating electric field. This relaxation is affected by the first order phase transition presented in **2**•2DMF and **3**•2DMF in the same temperature region. In other words, the dipolar relaxation of the paramagnetic {FeCo} dinuclear unit is different than the one of the diamagnetic {FeCo} dinuclear unit. This is not surprising, since when the electron transfer

process is occurring, a new dipole is created and thus its relaxation properties must be affected. In the case of compounds **2**•2DMF and **3**•2DMF, where the first order phase transition is observed at the same temperature region as the dipolar relaxation of the molecule, we were able to observe this effect, by a crossover between two regimes. These regimes were characterized by different values of the relaxation barrier and time. In the case of compound **2**, which is already in its diamagnetic state at this temperature region, only one regime of mode 2 was observed and showed similar values of relaxation time and barrier as the diamagnetic state of **2**•2DMF and **3**•2DMF.

In order to further study the role of the electron transfer in the dipolar relaxation, we synthesized the isostructural dinuclear Fe/Ni cyanide-bridged complex $[\{(Tp)Fe(CN)_3\}\{Ni(PY5Me_2)\}](PF_6)$•2DMF (**4**•2DMF), which doesn't exhibit electron transfer properties. Its synthesis, crystal structure and interesting magnetic properties in respect to Single-Molecule-Magnet behavior (SMM) are presented in the Supporting Material part III.6.

As for compounds **2**•2DMF, **3**•2DMF and **2**, the temperature dependence of the real and the imaginary parts of dielectric permittivity, ε' and ε'' under applied oscillating electric field (Figure III-60) were plotted for compound **4**•2DMF. As the temperature was decreasing from 300 to 50 K (Figure III-60, left), two broad and frequency-dependent ε' and ε''signals were observed. The high temperature mode observed in ε'' (mode 1, blue area) shows peaks between 160 and 220 K and can be associated with mode 1 in compounds **2**•2DMF and **3**•2DMF (Figures III-51 and III-52, for **2**•2DMF and **3**•2DMF, respectively). The second mode (mode 2, red area) shows peaks between 76 and 95 K, a temperature range very close to those observed for mode 2 in **2**•2DMF and **3**•2DMF. In heating process (Figure III-60, right) the data are identical with those obtained in cooling process.

The frequency dependence of the real and the imaginary parts of dielectric permittivity, ε' and ε'' for compound **4**•2DMF (Figure III-61), at the different temperature regions where the two modes were observed (Figure III-60), allowed us to construct the Arrhenius plots (Figure III-62) and extract the values for the energy barriers and relaxation times for mode 1 and 2. More specifically, for mode 1 we obtained E_A/k_B = 4489 K and τ_0 = 1.8 10^{-14} s, while for mode 2 we obtained E_A/k_B = 1985 K and τ_0 = 4.8 10^{-15} s. As it was anticipated, the values obtained for the relaxation barrier and time for mode 2, are comparable with those obtained from the first regime of mode 2 in compounds **2**•2DMF and **3**•2DMF (Figures III-54 and III-56). These results confirm that the origin of mode 2 in all four pairs is the same (probably associated with the dipolar relaxation of the molecule) and that the electron transfer behavior of the [FeCo] pairs is influencing the physical properties of this relaxation. Moreover, the reappearance of mode 1 in **4**•2DMF, expressed in the same way as in the solvated compounds **2**•2DMF and **3**•2DMF, is confirming our hypothesis of the DMF disorder generating a relaxation at high temperature region. The values for the energy barriers and relaxation times of the different modes for the four compounds are summarized in Table III-10.

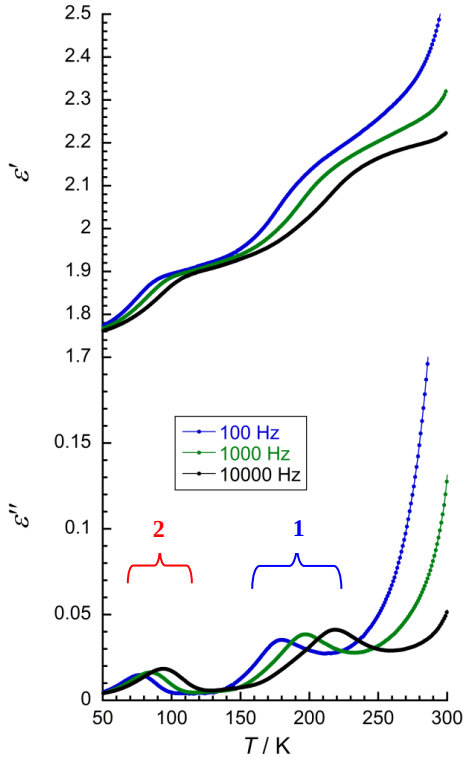

Figure III-60. Temperature dependence of the real and imaginary parts of the dielectric permittivity, ε' and ε'', respectively, at 100, 1000 and 10000 Hz, in cooling, between 300 and 50 K, at 0.09 K/min, for compound **4**•2DMF; the region of the two observed modes are marked with different colors and numbered for clarity.

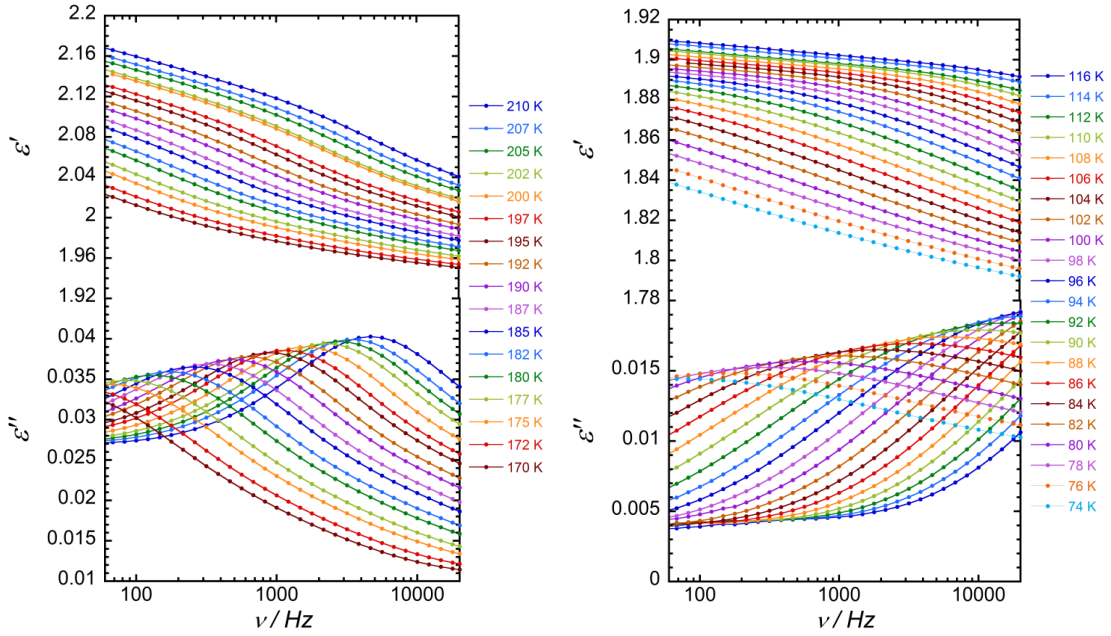

Figure III-61. Frequency dependence of the real and imaginary parts of the dielectric permittivity, ε' and ε'', respectively, at the given temperatures in cooling, for compound **4**•2DMF.

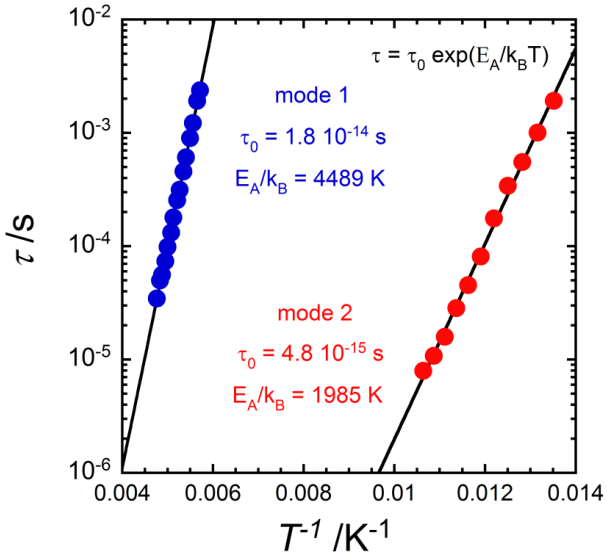

Figure III-62. τ as a function of $1/T$ plot in semi logarithmic scale, from the data in cooling, for complex **4**•2DMF.

Table III-10. The values for the energy barrier and relaxation time of the different modes for the compounds **2**•2DMF, **3**•2DMF, **4**•2DMF and **2**.

	2•2DMF		**3**•2DMF		**2**	**4**•2DMF	
modes							**origin**
1	τ_0 = 2.1 10^{-15} s E_A/k_B = 4414 K		τ_0 = 1.8 10^{-15} s E_A/k_B = 4441 K			τ_0 = 1.8 10^{-14} s E_A/k_B = 4489 K	disordered DMF
	T↓	**T↑**	**T↓**	**T↑**			
2	τ_0 = 6.2 10^{-16} s E_A/k_B = 2710 K		τ_0 = 2.6 10^{-15} s E_A/k_B = 2539 K			τ_0 = 4.8 10^{-15} s E_A/k_B = 1985 K	Relaxation of the paramagnetic pair
	τ_0 = 1 10^{-11} s E_A/k_B = 1599 K	τ_0 = 7.5 10^{-12} s E_A/k_B = 1623 K	τ_0 = 3.6 10^{-10} s E_A/k_B = 1377 K	τ_0 = 7.7 10^{-13} s E_A/k_B = 1928 K	τ_0 = 2.2 10^{-12} s E_A/k_B = 1612 K		Relaxation of the diamagnetic pair

III.5 Conclusions and Perspectives

Two new dinuclear cyanido-bridged {FeCo} molecular systems, compounds **2**•2DMF and **3**•2DMF, were synthesized and their properties associated to the metal-to-metal electron transfer phenomenon were investigated in the solid state by structural, spectroscopic, optical, magnetic and photomagnetic methods. The synthesis of compounds **2**•2DMF and **3**•2DMF was based on the synthesis of compound **1**•2DMF described in Chapter II, but using different counter ions for their crystallization: hexafluorphosphates for **2**•2DMF and hexafluoroarsenates for **3**•2DMF. Structural investigations on single-crystals of **2**•2DMF and **3**•2DMF at high temperatures, confirmed the presence of paramagnetic pairs and revealed the isostructural character of the three dinuclear complexes **1**•2DMF, **2**•2DMF and **3**•2DMF. The magnetic studies of **2**•2DMF and **3**•2DMF revealed a quasi-complete and reversible electron

transfer process around 94 and 88 K, respectively, in cooling mode. The electron transfer behavior observed in complexes **2**•2DMF and **3**•2DMF, was followed also by single-crystal X-ray diffraction at 82 K. It is worth to mention that we managed to modulate via anion exchange the electron transfer properties of the {Fe(*μ*-CN)Co} moiety, since in the case of compounds **2**•2DMF and **3**•2DMF, we don't have to dry them, like in compound **1**•2DMF in order to reveal a complete and reversible electron transfer behavior. Moreover, this behavior was shifted of about 70-80 K lower in temperature, in respect to the properties of **1**.

Optical reflectivity and photomagnetic studies demonstrate unambiguously that the diamagnetic state of **2**•2DMF and **3**•2DMF can be photo-converted into the paramagnetic one by applying a simple white-light or a 940-nm LED irradiation at 10 K. When the light is switched off and the temperature increases, compounds **2**•2DMF and **3**•2DMF are relaxing from the photo-induced paramagnetic state to the diamagnetic one at 53 and 57 K, respectively. The chemically stable compound **2**•2DMF gave us the opportunity to investigate the photo-induced electron transfer process by different light sources, and study the lifetime of the photo-induced paramagnetic state in terms of activation energy and relaxation time.

Another important feature of the photo-induced paramagnetic state is the nature of the coupling between the Fe^{III}_{LS} and Co^{II}_{HS} sites. The comparison of the field dependence of magnetization at 1.8 K and the temperature dependence of susceptibility at low temperatures for the photo-induced paramagnetic state of the pair with the corresponding curves for the sum of the Fe(III) and Co(II) precursor, suggested the presence of weak antiferromagnetic interactions between the Fe^{III}_{LS} and Co^{II}_{HS} sites. X-ray absorption spectroscopy (XAS) and X-ray magnetic circular dichroism (XMCD) experiments on the *K*-edges of Fe and Co have been performed for compound **2**•2DMF. The thermally- induced electron transfer process and the relaxation from the light-induced paramagnetic state in **2**•2DMF were followed as a function of temperature by XAS in the Fe and Co *K*-edges, proving the concurrent ET in Co and Fe ions at the local level. Moreover, the magnetization of the light-induced paramagnetic state of **2**•2DMF, at the Co and Fe *K*-edges was estimated by the XMCD data at 2 K, under applied magnetic field of +/- 8 and +/- 17 T. The normalized magnetization curves for Co and Fe, are superposed to each other, as well as to the normalized magnetization of the pair **2**•2DMF from the bulk photomagnetic studies of the photo-induced paramagnetic state at 1.8 K, suggesting the absence of interactions between the metal sites within the complex. Since the interactions expected are very weak only by performing this experiment at much lower temperature (< 1 K) and under weak magnetic field (< 1 T), we may achieve to confirm the sign and determine the value of the interactions between the Fe and Co ions in the photo-induced paramagnetic state of the pair.

The fascinating properties of **1**•2DMF and its desolvated form **1** in chapter II, encouraged us to study the properties of the desolvated form of **2**•2DMF and **3**•2DMF. The magnetic studies of **2** and **3** revealed a complete and reversible electron transfer process for both compounds around 170 K and 156 K, respectively, in cooling mode. Optical reflectivity studies demonstrate unambiguously that the diamagnetic state of **2** and **3** can be photo-converted into the paramagnetic one by applying a simple white-light or 940 nm irradiation at

10 K. When the light is switched off and the temperature increases, the compounds **2** and **3** are relaxing at 48 K back to the thermodynamically diamagnetic state.

Last but not least, we presented the first investigations of the electron transfer phenomenon in the dinuclear {Fe(μ−CN)Co} complexes under applied electric field. We studied the dielectric properties of the dinuclear compounds **2**•2DMF and **3**•2DMF, by measuring the real and the imaginary parts of dielectric permittivity, ε' and ε'', respectively, as a function of the frequency of applied oscillating electric field at given temperatures. Two modes, associated with relaxation phenomena, are present in both compounds. The mode observed at high temperature region (160-195 K) was associated to the DMF disorder close to its freezing point, since it is observed only in the solvated pairs **2**•2DMF and **3**•2DMF, and not when we perform the same measurements for the desolvated compound **2**. Taking into account the results obtained from compounds **2**•2DMF, **3**•2DMF and **2**, we suggested that the presence of the low temperature mode (130-70 K) is probably associated with a dipolar relaxation of the asymmetric dinuclear unit when it is introduced to the oscillating electric field. In the case of compounds **2**•2DMF and **3**•2DMF, where the first order phase transition is present in the same temperature region as the dipolar relaxation of the molecule, we were able to observe a crossover between two thermally activated regimes that were characterized by different values of the relaxation barrier and time. This result is suggesting that the dipolar relaxation of the paramagnetic {FeCo} dinuclear unit is different than the one of the diamagnetic {FeCo} dinuclear unit. In the case of compound **2**, that is already in its diamagnetic state in this temperature region, only one regime was observed and characterized by similar values of relaxation time and barrier as in the diamagnetic states of **2**•2DMF and **3**•2DMF. The study of the isostructural, paramagnetic Fe/Ni cyanide-bridged complex also revealed this mode in the same temperature region, but characterized by similar values of relaxation time and barrier as in the paramagnetic states of **2**•2DMF and **3**•2DMF. These results confirm that the origin of the low temperature mode in all pairs is the same, probably associated with the dipolar moment of the asymmetric molecules and that the electron transfer behavior in the [FeCo] pairs is influencing the physical characteristics of this relaxation.

III.6 Supporting Material

III.6.1 Experimental protocols

The ligands PY5Me2 and KTp were prepared using a procedure described in the literature.[20,21] The synthesis of **2**•2DMF and **3**•2DMF were performed under argon atmosphere using glovebox techniques, while the synthesis of **4**•2DMF and $[Ni^{II}(PY5Me_2)(MeCN)](CF_3SO_3)_2$•2MeCN under aerobic conditions. The DMF solvent and the KPF_6 and $NaAsF_6$ salts were used as received from Aldrich. Diethylether was dried on and collected from a solvent purification system (PSMD5(2012)/Innovative Technology) before being stored under an argon atmosphere prior to use. The $Co^{II}(CF_3SO_3)_2$ and $(Bu_4N)[(Tp)Fe^{III}(CN)_3]$[22] were synthesized as it was described in section II.5.1. Distilled water used as solvent for the synthesis of $Ni^{II}(CF_3SO_3)_2$.

Synthesis of $[\{(Tp)Fe^{III}(CN)_3\}\{Co^{II}(PY5Me_2)\}](X)$•2DMF (X = PF_6 for 2•2DMF; X = AsF_6 for 3•2DMF). To a DMF solution (4 ml) of $PY5Me_2$ (11.2 mg, 0.027 mmol) was added simultaneously 13 mg (0.035 mmol) of $Co^{II}(CF_3SO_3)_2$ and the salt with the desired counter ion (for **2**•2DMF, 13 mg of KPF_6; for **3**•2DMF, 15 mg of $NaAsF_6$; 0.070 mmol). The resulting pale yellow solution was stirred for 1 hour before adding 15.3 mg (0.027 mmol) of $(Bu_4N)[(Tp)Fe^{III}(CN)_3]$. The solution turned dark red and was stirred for four additional hours and then filtrated. Slow diffusion of diethylether vapor afforded orange needles of: **2**•2DMF (Yield 70 %); MW = 1140.58 g/mol; **3**•2DMF (Yield 50 %); MW = 1184.53 g/mol; FT-IR data (ATR, cm^{-1}) (**2**•2DMF): 3095 (m), 2953 (m), 2513 (w), 2158 (m) 2122 (w), 1678 (s), 1594 (m), 1500 (w), 1466 (m), 1434(m), 1403 (m), 1388 (m), 1314 (m), 1270 (s), 1201 (m), 1146 (m), 1111 (m), 1092 (m), 1046 (m), 1030 (s), 1015 (m), 987 (w), 870 (w), 837 (s), 793 (w), 765 (m), 750 (m), 707 (w), 650 (w), 648 (w), 629 (m), 590 (w), 555 (m); FT-IR data (ATR, cm^{-1}) (**3**•2DMF): 3095 (m), 2953 (m), 2514 (w), 2158 (m) 2122 (w), 1676 (s), 1594 (m), 1497 (w), 1466 (m), 1438(m), 1403 (m), 1388 (m), 1310 (m), 1271 (s), 1208 (m), 1150 (m), 1116 (m), 1092 (m), 1046 (m), 1034 (s), 1018 (m), 987 (w), 866 (w), 847 (w), 793 (w), 765 (m), 754 (m), 695 (s), 629 (m), 590 (w); Elemental analysis calc. for C47H49N16CoFeO2BF6P (**2**•2DMF): C 49.5, H 4.3, N 19.7; found: C 50.1, H 4.6, N 20.3 %. Elemental analysis calc. for C47H49N16CoFeO2BF6As (**3**•2DMF): C 49.7, H 4.2, N 18.9; found: C 49.0, H 3.2, N 19.0 %.

Preparation of $[\{(Tp)Fe^{III}(CN)_3\}\{Co^{II}(PY5Me_2)\}](X)$ (X = PF_6 for 2; X = AsF_6 for 3). Orange needles of **2**•2DMF or **3**•2DMF were kept in diethylether and sonicated for 30 minutes. The resulting orange microcrystalline powders were filtered and dried in a vacuum oven (at a few mbars and 50°C) for 24 hours, resulting in dark orange powders. FT-IR data (ATR, cm^{-1}) (**2**), MW = 994.40 g/mol: 2502 (w), 2158 (m) 2122 (w), 2086 (w), 2057 (w), 1596 (m), 1498 (w), 1466 (m), 1438(m), 1403 (m), 1312 (m), 1270 (s), 1211 (m), 1151 (m), 1113 (m), 1070 (m), 1049 (m), 1032 (s), 1018 (m), 985 (w), 870 (w), 835 (s), 792 (w), 764 (m), 754 (m), 740 (w), 709 (w), 666 (w), 649 (w), 635 (m), 628 (m), 614 (m); FT-IR data

(ATR, cm^{-1}) (**3**), MW = 1038.40 g/mol: 3099 (m), 2966 (m), 2853 (w), 2503 (w), 2157 (m) 2123 (w), 2078 (w), 2056 (w), 1595 (m), 1497 (w), 1468 (m), 1436(m), 1407 (m), 1312 (m), 1271 (s), 1210 (m), 1149 (m), 1113 (m), 1071 (m), 1050 (m), 1034 (s), 1018 (m), 989 (w), 862 (w), 847 (w), 792 (w), 768 (m), 756 (m), 695 (s), 649 (m), 633 (m), 625 (m); Elemental analysis calc. for C41H35N14CoFeBF6P (**2**+3.8H_2O): C 46.3, H 4.0, N 18.5; found: C 46.7, H 4.0, N 18.3; Elemental analysis calc. for C41H35N14CoFeBF6As (**3**+2H_2O): C 45.9, H 3.7, N 18.3; found: C 45.6, H 3.9, N 18.2. As **2** and **3** are highly hydroscopic, the water molecules considered in the elemental analysis are most likely the result of the solvatation of **2** and **3** by the atmosphere during the preparation of the sample for elemental analysis.

Preparation of $Ni^{II}(CF_3SO_3)_2$. 0.2 g of $NiCO_3$ (1.6 mmol) were added in 10 ml of trifluoromethanesulfonic acid (0.5 g, 3.2 mmol) solution in water (30 ml). The mixture was stirred until CO_2 gas stopped to form. Then the solution was filtered and concentrated under reduced pressure, where $Ni^{II}(CF_3SO_3)_2$ was precipitated as a light green powder. The compound was collected and dried in vacuum at 323 K. Yield: 0.51 g (90 %); MW = 462 g/mol; FT-IR (ATR, cm^{-1}): 1225 (vs), 1191 (vs), 1023 (vs), 626 (m), 593 (m).

Preparation of $[Ni^{II}(PY5Me_2)(MeCN)](CF_3SO_3)_2$•2MeCN. To an acetonitrile solution (10 ml) of ligand $PY5Me_2$ (50 mg, 0.12 mmol) was added $Ni^{II}(CF_3SO_3)_2$ (42 mg, 0.12 mmol). The pale purple colored solution was stirred for 2 hours, and then filtrated. The slow diffusion of ether vapor afforded pale purple crystals in 2 days. Yield 87 mg (80 %); MW = 964.58 g/mol; FT-IR (ATR, cm-1): 3316 (w), 3231 (w), 2924 (w), 2307 (w), 2280 (w), 2250 (w), 1597 (m), 1468 (m), 1453 (m), 1440 (m), 1253 (s), 1224 (s), 1153 (s), 864 (w), 794 (w), 757 (s), 629 (s), 572 (m); Elemental analysis calc. for C33H28N6NiO6S2F6 (**5**•2H_2O): C 45.2, H 3.7, N 9.6; found: C 45.2, H 3.4, N 9.3 %.

Synthesis of $[\{(Tp)Fe^{III}(CN)_3\}\{Ni^{II}(PY5Me_2)\}](PF_6)$•2DMF (4•2DMF). To a DMF solution (8 ml) of $[Ni^{II}(PY5Me_2)(MeCN)](CF_3SO_3)_2$•2MeCN (58 mg, 0.06 mmol) was added 26 mg (0.12 mmol) of KPF_6. The resulting pale purple solution was stirred for 15 minutes before adding 31 mg (0.06 mmol) of $(Bu_4N)[(Tp)Fe^{III}(CN)_3]$. The solution turned bright orange and was stirred for four additional hours and then filtrated. Slow diffusion of diethylether vapor afforded bright orange needles of **4**•2DMF. Yield 90 %; MW = 1140.36 g/mol; FT-IR data (ATR, cm^{-1}): 3095 (m), 2953 (m), 2513 (w), 2165 (m) 2120 (w), 1675 (s), 1594 (m), 1500 (w), 1466 (m), 1434(m), 1403 (m), 1388 (m), 1314 (m), 1270 (s), 1201 (m), 1146 (m), 1111 (m), 1092 (m), 1046 (m), 1030 (s), 1015 (m), 987 (w), 870 (w), 834 (s), 793 (w), 765 (m), 750 (m), 707 (w), 650 (w), 648 (w), 629 (m), 590 (w), 555 (m); Elemental analysis calc. for C47H49N16NiFeO2BF6P (**4**•2DMF): C 49.5, H 4.3, N 19.7; found: C 50.0, H 4.8, N 21.0 %.

III.6.2 Physical methods of characterization

Elemental analysis. Elemental analysis for C, H and N were performed following the classical Pregl-Dumas technique for fluorine samples on a Thermo Fischer Flash EA 1112 equipment at Institut de Chimie de la Matière Condensée de Bordeaux (ICMCB).

FT-IR spectroscopy. FT-IR spectra were recorded in the 400–4000 cm^{-1} range on a Thermal Scientific Nicolet 6700 ATR (attenuated total reflection) spectrometer equipped with a smart iTR diamond window, housed at the Centre de Recherche Paul Pascal.

Crystallographic data. Single crystals of **2**•2DMF, **3**•2DMF, **4**•2DMF and $[Ni^{II}(PY5Me_2)(MeCN)](CF_3SO_3)_2$•2MeCN were mounted in CargilleTM NHV immersion oil on a 50 mm MicroMounts^{TM} rod at different temperatures 220,82 and 140 K for **2**•2DMF, 250 and 82 K for **3**•2DMF, 250 K for **4**•2DMF and 120 K for $[Ni^{II}(PY5Me_2)(MeCN)](CF_3SO_3)_2$•2MeCN. The crystallographic data were collected with Bruker APEX II Quasar diffractometers, housed at the Centre de Recherche Paul Pascal and at the Institut de Chimie de la Matière Condensée de Bordeaux, and equipped with a graphite monochromator centered on the MoK_α path. The program SAINT was used to integrate the data, which was thereafter corrected for absorption using SADABS.[23] All structures were solved by direct methods and refined by a full-matrix least-squares method on F^2 using SHELXL-2013.[24] All non-hydrogen atoms were refined anisotropically. Hydrogen atoms were assigned to ideal positions and refined isotropically using suitable riding models. Reflections were merged by SHELXL according to the crystal class for the calculation of statistics and refinement. Figures III-3 to III-6, III-16 and III-17 and S.III-1 to S.III-4 were generated using CrystalMaker® (CrystalMaker Software Ltd, www.crystalmaker.com). Figures III-1 and III-7 to III-10 were generated using Mercury version 3.3.

Table S.III-1. Crystallographic data, selected bond lengths and distances [Å] and angles [°] for **2**•2DMF at 140 K, in heating mode from 82 K.

Compound	**2**•2DMF
Temperature / K	140
Formula	$C_{47}H_{49}BCoF_6FeN_{16}O_2P$
FW / g·mol^{-1}	1140.58
Crystal color	Orange
Crystal size / mm	0.37 x 0.07 x 0.02
Crystal system	orthorhombic
Space group	*P*nma
***a* / Å**	18.451(2)
***b* / Å**	15.3326(19)
***c* / Å**	17.6747(19)
***V* / Å^3**	5000.2(10)
Z	4
Completeness to 2*θ*	0.971
R_{int}	0.0772
[a]R_1 ($I > 2\sigma(I)$)	0.0529
[b]wR_2 (all data)	0.1306
Goodness-of-fit	1.102
Average (Fe-C)	1.904(4)
Fe1-C1	1.871(3)
Fe1-C2	1.921(4)
Average (Fe-N)	1.965(4)
Fe1-N3	1.972(5)
Fe1-N5	1.962(3)
Co-N_{NC}	2.030(5)
Average (Co-N_{py})	2.122(3)
Co1-N7	2.122(3)
Co1-N8	2.134(3)
Co1-N9	2.098(4)
Fe1-C1-N1	176.6(5)
C1-N1-Co1	172.8(4)
Fe1…Co1	5.038(4)

[a] $R_1 = \Sigma||F_0|-|F_C||/\Sigma|F_0|$, [b] $wR_2 = [\Sigma w(F_0^2-F_C^2)^2/\Sigma w(F_0^2)^2]^{1/2}$

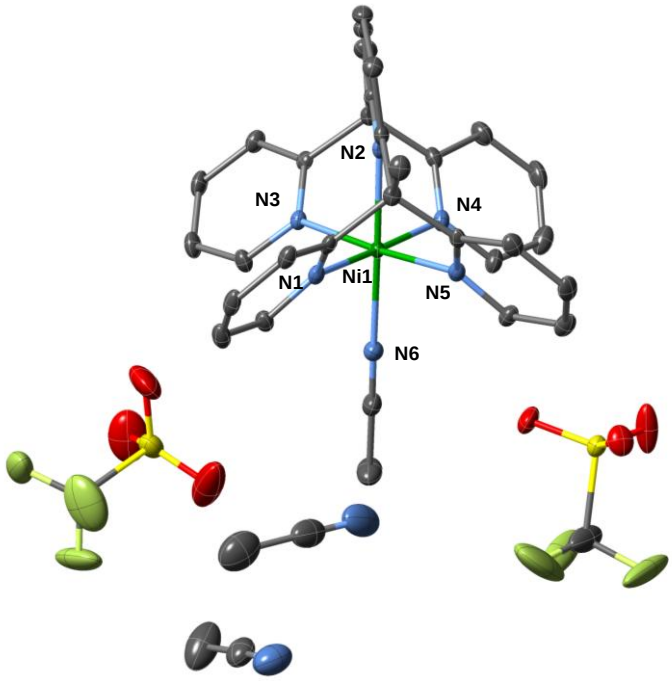

Figure S.III-1. ORTEP-type view of the complex $[Ni^{II}(PY5Me_2)(MeCN)](CF_3SO_3)_2$•2MeCN at 120 K. Thermal ellipsoids are depicted at the 40% probability level. All hydrogen atoms are omitted for clarity. Ni, N, C, O, F and S atoms are indicated in green, light blue, gray, red, light green and yellow, respectively.

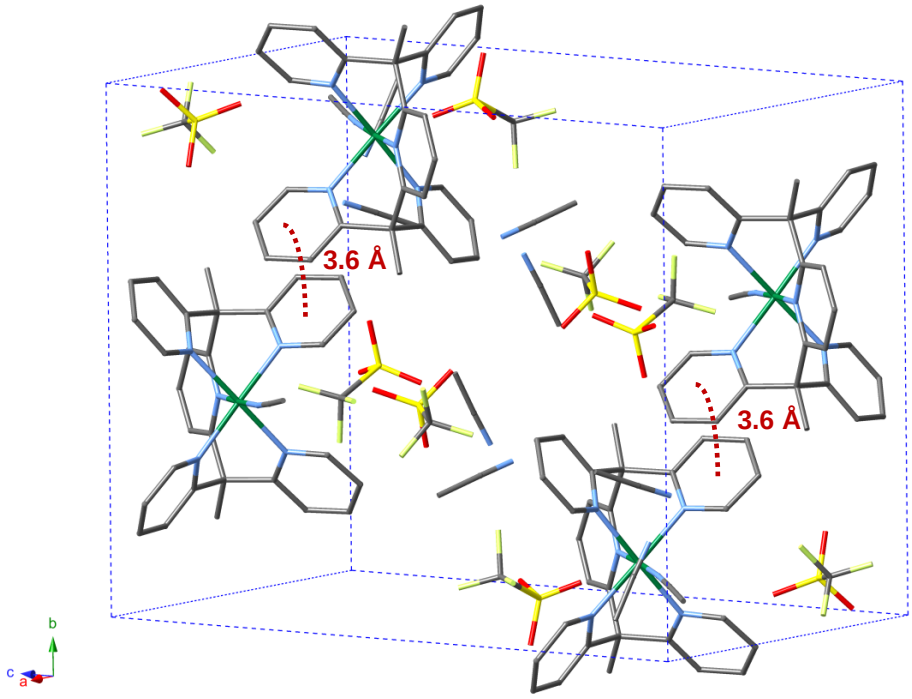

Figure S.III-2. Projection view of the crystal structure of $[Ni^{II}(PY5Me_2)(MeCN)](CF_3SO_3)_2$•2MeCN at 120 K showing the packing of the cationic complexes, the triflate anions, the lattice MeCN molecules and the π-π stacking interactions between the neighboring cationic complexes. Ni, N, C, O, S and F atoms are indicated in green, light blue, dark gray, red, yellow and light green, respectively.

Table S.III-2. Crystallographic data, selected bond lengths and distances [Å] and angles [°] for $[Ni^{II}(PY5Me_2)(MeCN)](CF_3SO_3)_2$•2MeCN at 120 K.

Compound	$[Ni^{II}(PY5Me_2)(MeCN)](CF_3SO_3)_2$•2MeCN
Formula / FW / g·mol^{-1}	$C_{39}H_{37}NiF_6N_9O_6S_2$ / 964.58
Crystal color	light purple
Crystal system	monoclinic
Space group	P 21/n
Temperature / K	120
***a* / Å**	12.5161(3)
***b* / Å**	15.8447(4)
***c* / Å**	20.1390(6)
***α* = *γ* / °**	90
***β* / °**	90.9210(10)
***V* / Å^3**	3993.33(18)
Z	4
Ni1-N1	2.094(3)
Ni1-N2	2.055(3)
Ni1-N3	2.111(3)
Ni1-N4	2.086(3)
Ni1-N5	2.107(3)
Ni1-N6	2.087(3)
[a] R_1 ($I > 2\sigma(I)$)	0.0550
[b] wR_2 (all data)	0.1603
R_{int}	0.0308

[a] $R_1 = \Sigma||F_0|-|F_C||/\Sigma|F_0|$, [b] $wR_2 = [\Sigma w(F_0^2-F_C^2)^2/\Sigma w(F_0^2)^2]^{1/2}$

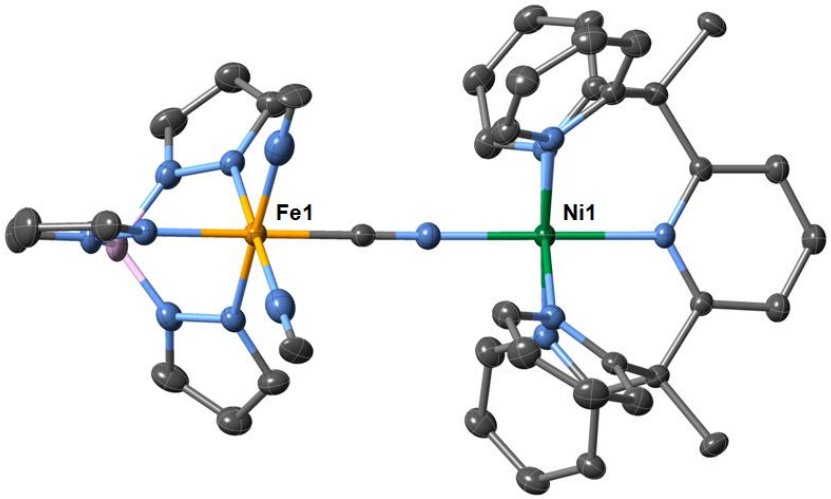

Figure S.III-3. ORTEP-type view of the cationic complex in **4**•2DMF at 250 K. Thermal ellipsoids are depicted at the 40% probability level. All anions, lattice solvents, and hydrogen atoms are omitted for clarity. Fe, Ni, N, C, and B atoms are indicated in orange, green, light blue, gray, and pink, respectively.

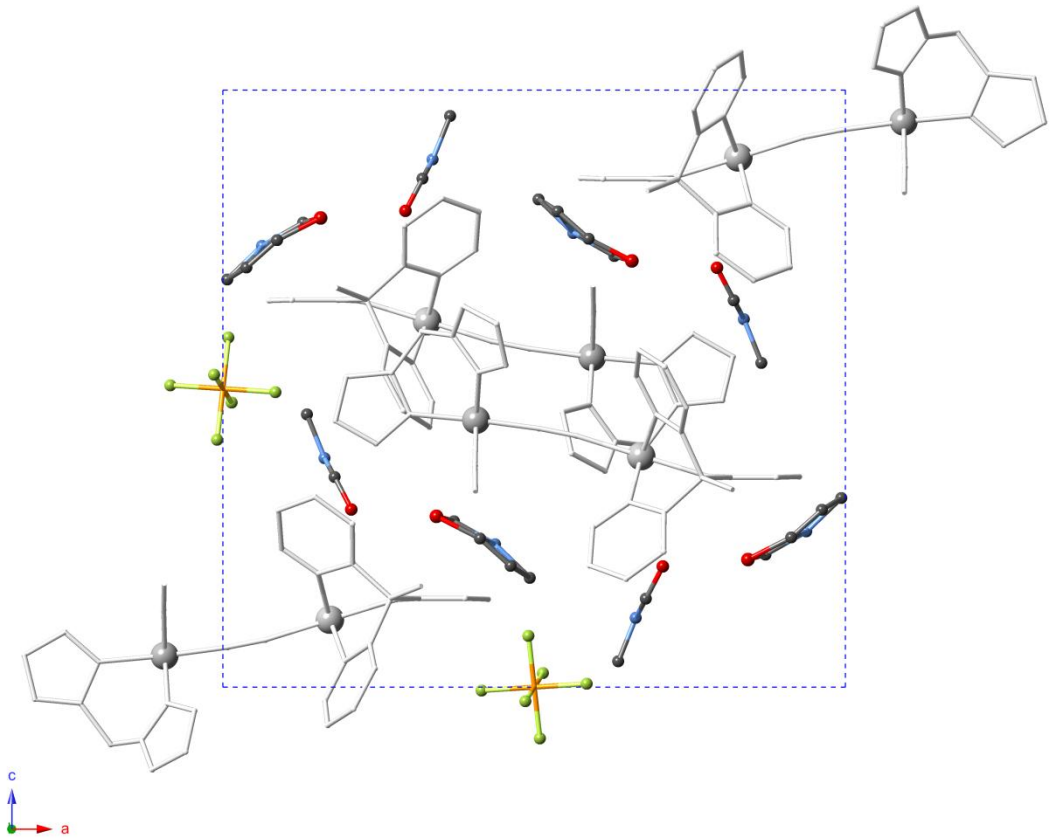

Figure S.III-4. Projection view of the crystal structure of **4**•2DMF at 250 K showing the packing of the cationic complexes, the PF_6^- anions and the lattice DMF molecules in the (*ac*) plane. All the atoms of the cationic complexes are in light grey color for clarity. The PF_6^- anions, the lattice DMF molecules and the metal centers are visualized in balls and sticks for clarity. N, C, P, O and F atoms are indicated in light blue, dark grey, orange, red and light green, respectively.

Table S.III-3. Crystallographic data, selected bond lengths and distances [Å] and angles [°] for **4**•2DMF at 250 K.

Compound	**4**•2DMF
Temperature / K	250
Formula	$C_{47}H_{49}BNiF_6FeN_{16}O_2P$
FW / g·mol^{-1}	1140.36
Crystal color	Orange
Crystal size / mm	0.18 x 0.04 x 0.02
Crystal system	orthorhombic
Space group	*P*nma
***a* / Å**	18.6218(7)
***b* / Å**	15.3937(5)
***c* / Å**	17.8707(7)
***V* / Å^3**	5122.8(3)
Z	4
Completeness to 2*θ*	0.999
R_{int}	0.0768
[a]R_1 ($I > 2\sigma(I)$)	0.0550
[b]wR_2 (all data)	0.1614
Goodness-of-fit	1.117
Average (Fe-C)	1.917(4)
Fe1-C1	1.898(6)
Fe1-C2,2'	1.927(4)
Average (Fe-N)	1.980(4)
Fe1-N3,3'	1.976(3)
Fe1-N5	1.989(3)
Co-N_{NC}	2.028(5)
Average (Co-N_{py})	2.101(3)
Co1-N7,7'	2.111(3)
Co1-N8,8'	2.106(3)
Co1-N9	2.072(4)
Fe1-C1-N1	176.7(5)
C1-N1-Co1	173.6(5)
Fe1…Co1	5.058(5)

[a] $R_1 = \Sigma||F_0|-|F_C||/\Sigma|F_0|$, [b] $wR_2 = [\Sigma w(F_0^2-F_C^2)^2/\Sigma w(F_0^2)^2]^{1/2}$

Magnetic studies. Magnetic susceptibility measurements were performed on a Quantum Design SQUID magnetometer MPMS-XL housed at the Centre de Recherche Paul Pascal at temperatures between 1.8 and 300 K and dc magnetic fields ranging from -7 to 7 T. In the absence of light, measurements were reproducibly performed using polycrystalline samples. Crystals of **2**•2DMF (14.84 mg) and **3**•2DMF (12.88 mg) filtrated fast form their mother liquor and then introduced in sealed polyethylene bags (3 × 0.5 × 0.02 cm). Complexes **2** and **3** were measured on samples obtained by keeping **2**•2DMF and **3**•2DMF in diethylether with sonication for 30 minutes, before filtering and drying in a vacuum oven (at a few mbars and 50°C) for 24 hours. The resulting dark orange powders (21.67 mg for **2** and 19.70 mg for **3**) were then introduced in sealed polyethylene bags. Crystals of **4**•2DMF (28.00 mg) and $[Ni^{II}(PY5Me_2)(MeCN)](CF_3SO_3)_2$•2MeCN (25.52 mg) filtrated fast form their mother liquor and then introduced in sealed polyethylene bags, which were containing 13.19 mg and 9.48

mg of paraton oil, respectively. Prior to the experiments, the field-dependent magnetization was measured at 100 K on each sample in order to detect the presence of any bulk ferromagnetic impurities. In fact, paramagnetic or diamagnetic materials should exhibit a perfectly linear dependence of the magnetization that extrapolates to zero at zero dc field. The samples appeared to be free of any significant ferromagnetic impurities. The magnetic data were corrected for the sample holder, solvent, paraton oil and the intrinsic diamagnetic contributions.

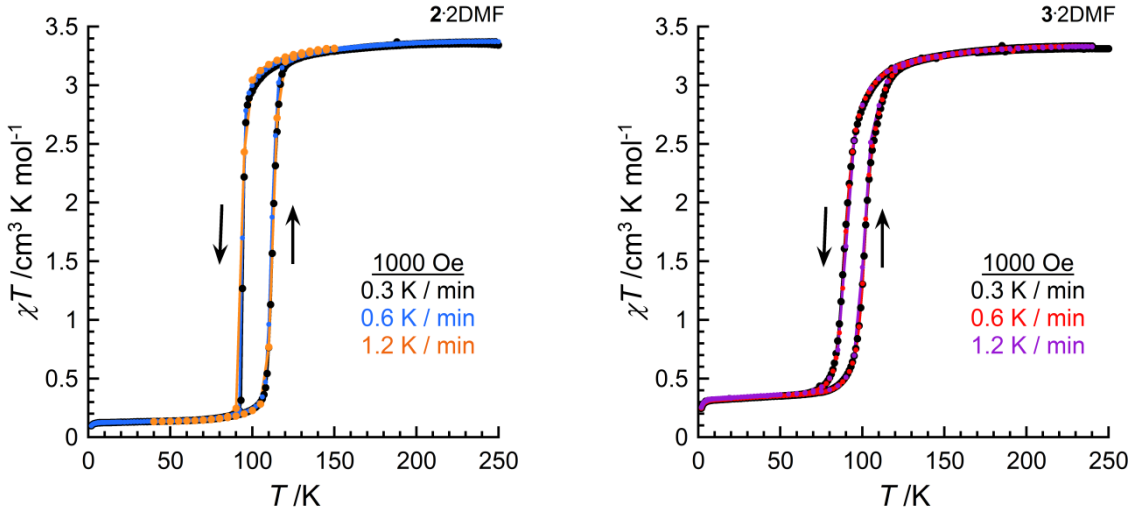

Figure S.III-5. (Left) χT versus T plots for polycrystalline samples of **2**•2DMF (from 250 to 1.8 K at 0.1 T) at 0.3 K/min (black), 0.6 K/min (blue) and 1.2 K/min (orange); (right) χT versus T plots for polycrystalline samples of **3**•2DMF (from 250 to 1.8 K at 0.1 T) at 0.3 K/min (black), 0.6 K/min (red) and 1.2 K/min (purple).

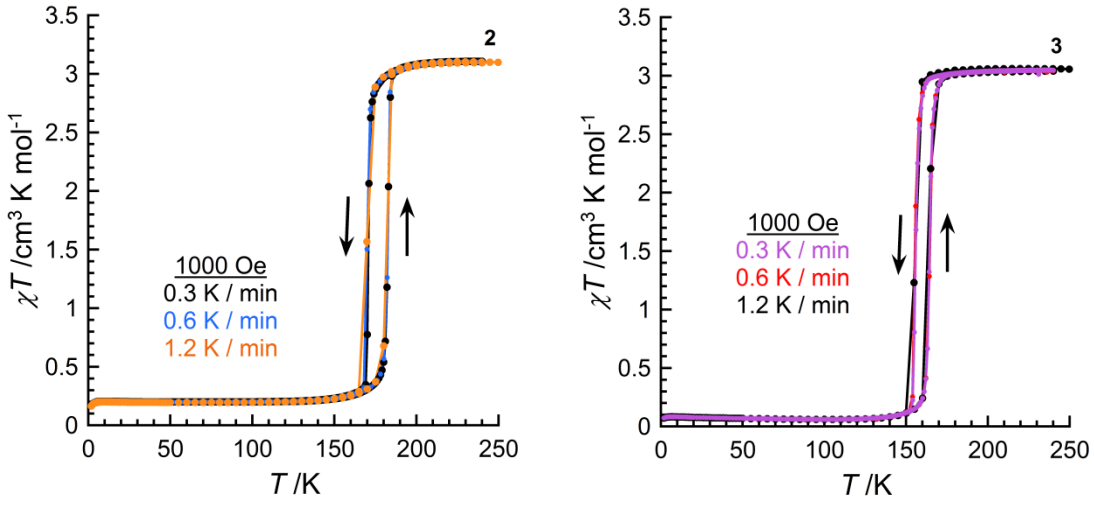

Figure S.III-6. (Left) χT versus T plots for polycrystalline samples of **2** (from 250 to 1.8 K at 0.1 T) at 0.3 K/min (black), 0.6 K/min (blue) and 1.2 K/min (orange); (right) χT versus T plots for polycrystalline samples of **3** (from 250 to 1.8 K at 0.1 T) at 0.3 K/min (purple), 0.6 K/min (red) and 1.2 K/min (black).

Complex $[Ni^{II}(PY5Me_2)(H_2O)](CF_3SO_3)_2$•2MeCN was synthesized as a precursor for the synthesis of compound **4**•2DMF. Direct current (dc) magnetic susceptibility data χT on fresh filtered crystals of $[Ni^{II}(PY5Me_2)(H_2O)](CF_3SO_3)_2$•2MeCN were collected in the 1.8-280 K range under applied field of 1000 Oe and plotted as a function of temperature (Figure S.III-7, top). The χT value of 1.29 cm^3 K mol^{-1} at 280 K is in agreement with the expected value for one Ni^{II} (S =1, g = 2.2-2.3) ion. Upon cooling, the χT value remains stable in the temperature range 280-20 K and then increases reaching the value of 1.39 cm^3 K mol^{-1} at 10 K. From 10 to 1.8 K, the χT product is decreasing rapidly to 1.1 cm^3 K mol^{-1}. The increase of the χT between 20 and 10 K is suggesting the presence of ferromagnetic interactions between neighboring mononuclear complexes through π-π stacking interactions, as it has proposed from the crystal structure (Figure S.III-2). Finally the decrease observed at very low temperatures can be attributed to the anisotropy of the system. The field dependence of the magnetization and the M versus H/T plot confirm that the complex exhibits magnetic anisotropy below 5 K, due to the non-superimposable M versus H/T curves on a single master curve (Figure S.III-7, bottom).

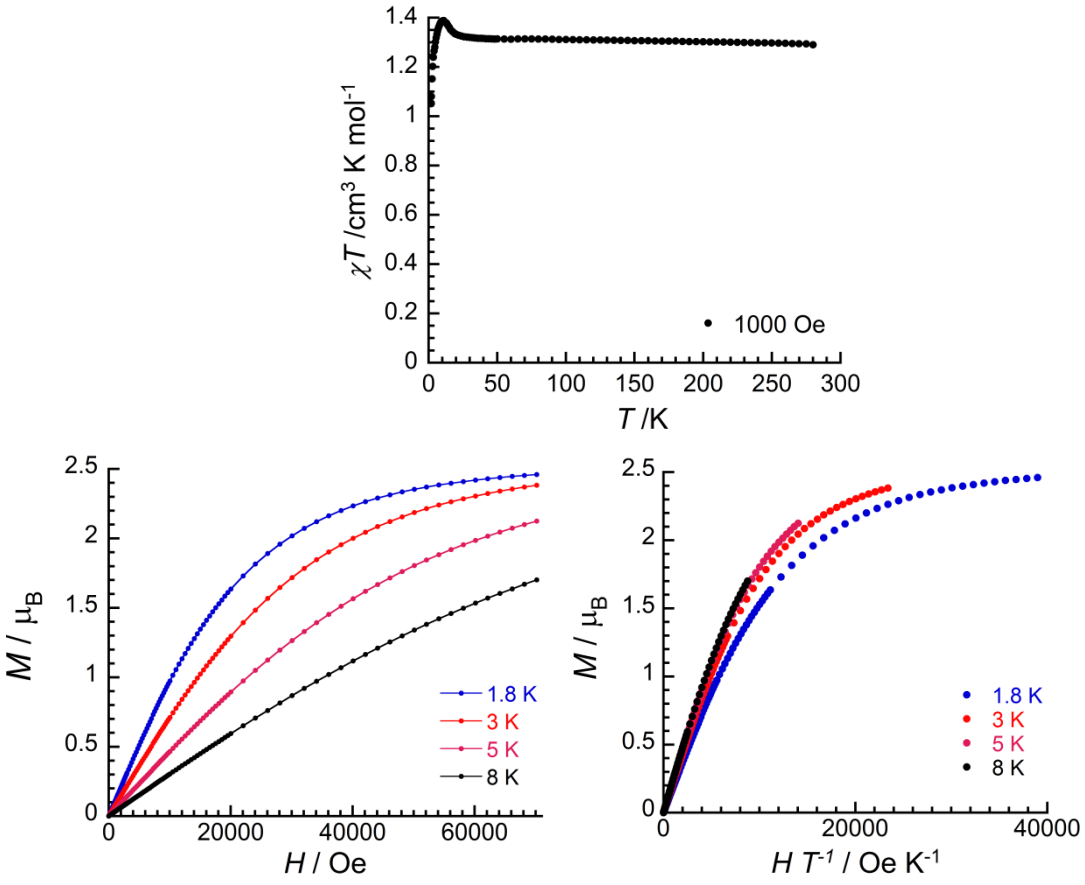

Figure S.III-7. (top) χT versus T curve at 0.1 T from 280 to 1.8 K, (bottom left) the magnetization versus field H, and (bottom right) the reduced magnetization curve for $[Ni^{II}(PY5Me_2)(H_2O)](CF_3SO_3)_2$•2MeCN at different temperatures; blue, 1.8 K; red, 3 K; pink, 5 K; black, 8 K.

The dinuclear Fe/Ni cyanide-bridged complex [{(Tp)Fe(CN)$_3$}{Ni(PY5Me$_2$)}](PF$_6$)•2DMF (**4**•2DMF) exhibits interesting magnetic properties in respect to Single-Molecule Magnet behavior (SMM). Direct currect (dc) magnetic susceptibility data χT on fresh filtered crystals of **4**•2DMF were collected in the 1.8-280 K range under applied field of 1000 Oe and plotted as a function of temperature (Figure S.III-8, top). The χT value of 1.6 cm^3 K mol^{-1} at 280 K is in agreement with the expected value for one Fe$^{III}_{LS}$ (S = 1/2, g =2.6-2.8) ion and one Ni^{II} (S =1, g = 2.2-2.3) ion, assuming that significant orbital contributions are present on the Fe$^{III}_{LS}$ ion.[25] Upon cooling, the χT value remains stable in the temperature range 280-100 K, then increases slowly until 50 K and finally more rapidly reaching the value of 2.05 cm^3 K mol^{-1} at 7 K. From 7 to 1.8 K, the product of the χT is decreasing rapidly to 1.7 cm^3 K mol^{-1}.

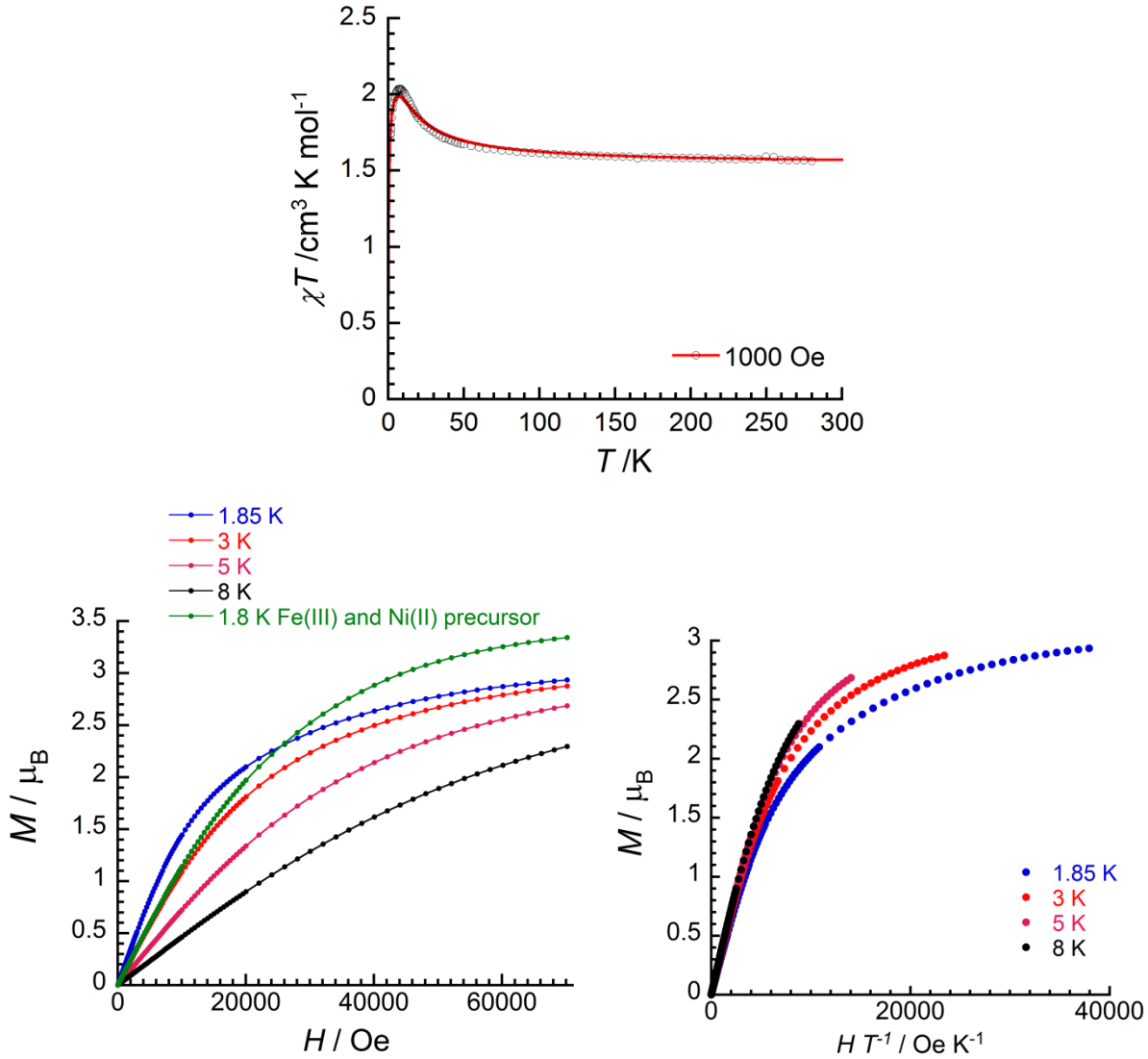

Figure S.III-8. (top) The χT versus T curve at 0.1 T and the fitting (with red solid line), (bottom left) the magnetization versus field H for **4**•2DMF at different temperatures; blue, 1.85 K; red, 3K; pink, 5 K; black, 8 K and green for the sum of (NBu$_4$)[(Tp)Fe^{III}(CN)$_3$]•3H$_2$O and [Ni^{II}(PY5Me$_2$)(MeCN)](CF$_3$SO$_3$)$_2$•2MeCN at 1.8 K; (bottom right) the reduced magnetization curve for **4**•2DMF at different temperatures; blue, 1.85 K; red, 3 K; pink, 5 K; black, 8 K.

The increase of the χT between 50 and 7 K is suggesting the presence of ferromagnetic interactions between the two metal centers trough the CN^- bridge, as it has been already observed in the literature for [FeNi] cyanide bridged squares and related complexes.[25] Finally the decrease observed at very low temperatures can be attributed to antiferromagnetic interactions developing between neighboring pairs. The magnetic data were modelised and fitted by the Hamiltonian presented here:

$$\mathcal{H} = -2J\left(\vec{S}_{Fe} \bullet \vec{S}_{Ni}\right) + g\mu_B \vec{S}_{Total} \cdot \vec{H} - 2zJ' < S_{Total} > \vec{S}_{Total} \qquad SIII.1$$

where J is the exchange interaction between Fe^{III}_{LS} and Ni^{II} sites inside the pair, zJ' the interactions between neighboring pairs, $< S_{Total} >$ the mean value of the $\vec{S}_{Total}$ component of the spin operator. Subsequent application of the van Vleck equation to Kambe's vector coupling scheme allowed for analytical expression (Eq. SIII.2) of the magnetic susceptibility in the low field approximation[26].

$$\chi T = T\,\frac{N{g^2}{\mu_B}^2}{k_B T - 2zJ'F(x)}F(x) \qquad with \qquad F(x) = \frac{1 + 10exp(3x)}{4(1 + 2exp(3x))} \quad and \quad x = {J}/{k_B T}$$

So,
$$\chi T = \frac{N{g^2}{\mu_B}^2}{k_B}\left\{\frac{1+10\exp(3x)}{4+8\exp(3x)}\left[1 - \frac{2zJ\prime}{k_B T}\frac{1+10\exp(3x)}{4+8\exp(3x)}\right]^{-1}\right\} \qquad SIII.2$$

Finally, we obtained values for g_{av} = 2.1, J/k_B = 7.9 K and zJ'/k_B = -0.12 K. The exchange parameter J/k_B is close to those obtain for the [FeNi] square.[25a] The field dependence of the magnetization and the M versus H/T plot confirm that the [FeNi] pair exhibits significant magnetic anisotropy below 8 K, due to the non-superimposable M versus H/T curves on a single master curve (Figure S.III-8, bottom).

The dynamic properties of **4**•2DMF were probed by *ac* measurements. Tails of the out-of-phase component of the *ac* susceptibility χ'', were observed in the absence of a *dc* field at 1.9 K. Then, *ac* susceptometry measurements at 1.9 K as a function of the frequency were performed in the presence of external fields from 0 to 10000 Oe and the optimum field of 3000 Oe was selected in order to continue our studies (Figure S.III-9).

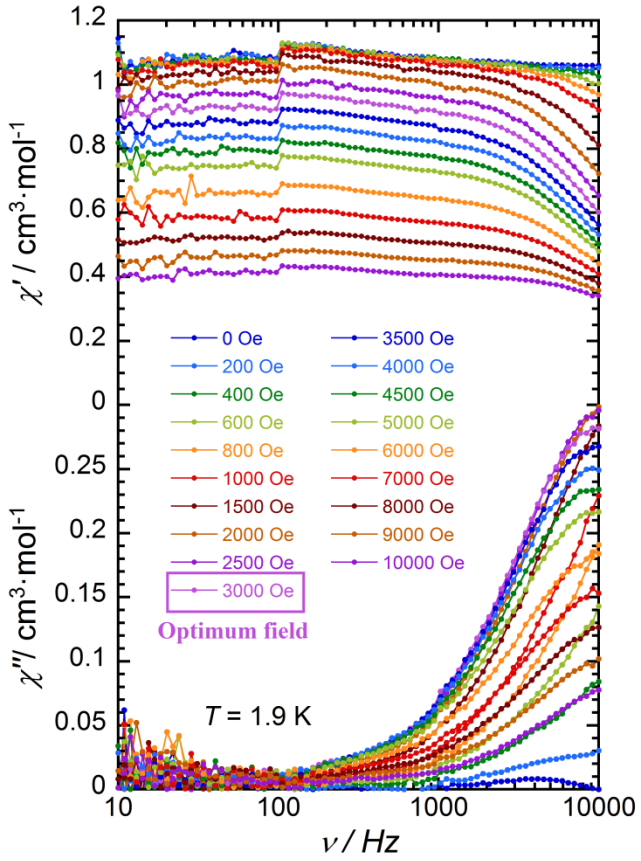

Figure S.III-9. Plots of the in-phase (top), χ', and out-of-phase (bottom), χ'', components of the *ac* magnetic susceptibility *versus* the frequency, *ν*, of the oscillating field at 1.9 K for compound **4**•2DMF in the presence of the indicated *dc* fields from 0 to 10000 Oe.

Indeed, strong frequency dependence of the in-phase and out-of phase *ac* susceptibilities with varying temperatures was observed under *dc* field of 3000 Oe (Figure S.III-10, left). Unfortunately, we weren't able to see all the frequency maxima in the experimental window in order to extract the characteristic experimental time τ_{exp} ($\tau_{exp} = (2\pi\nu_{exp})^{-1}$). In order to obtain the τ_{exp} we scaled the χ''/χ_0'' curves (for temperatures from 1.9 to 3 K) to the χ''/χ_0'' curve at 1.8 K, that exhibits a frequency maximum, by a factor of α (Figure S.III-11). The frequency maximum at 1.8 K was multiplied by the corresponding factor α for each temperature (1.9 to 3 K) and the experimental time τ_{exp} was estimated. The Arrhenius plot was built (Figure S.III-10, inset) and the linear regression fits of the experimental ln(τ) versus 1/*T* data, afforded an estimation of an energy barrier of E_A/k_B = 9.5 K and τ_0 = 1.1 10^{-7} s in Figure S.III-10 (inset). These values are comparable with the values of the relaxation barrier and time extracted for the [FeNi] square.[25a]

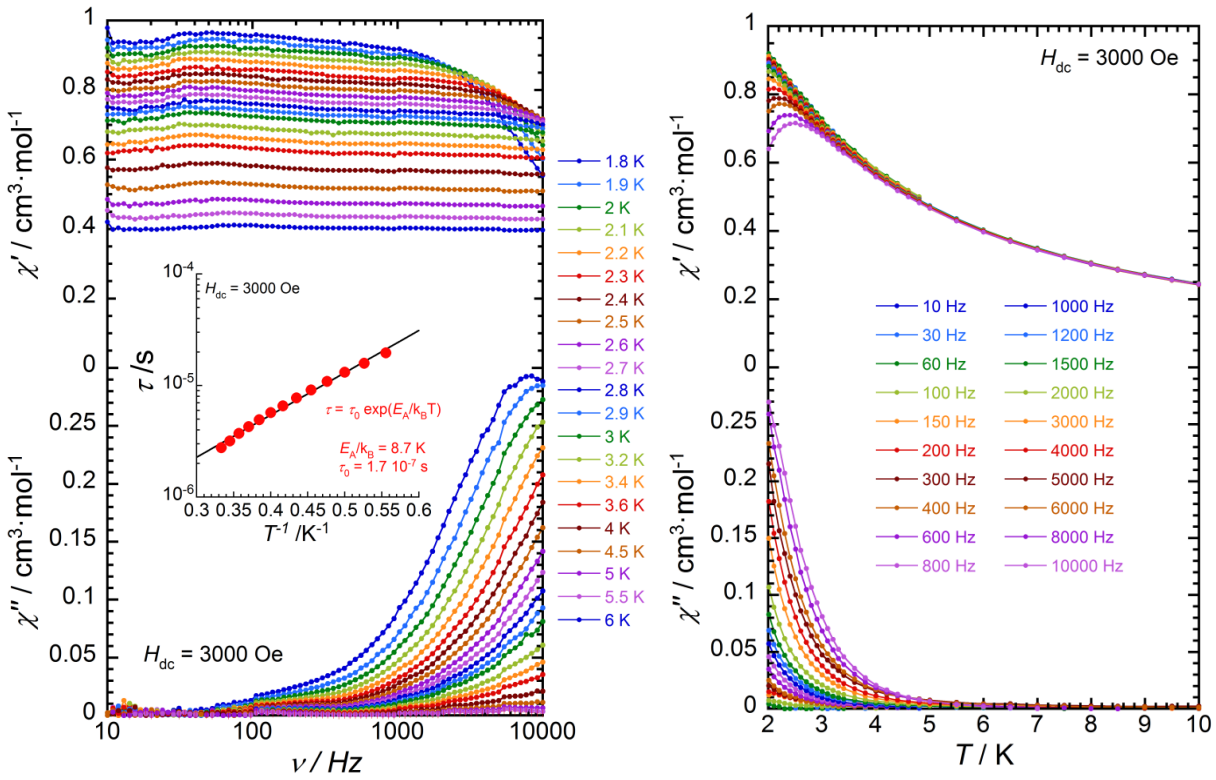

Figure S.III-10. (Left) Plots of the in-phase (top), χ', and out-of-phase (bottom), χ'', components of the *ac* magnetic susceptibility *versus* the frequency, ν, under an external *dc* field of 3000 Oe at the indicated temperatures, and the τ versus $1/T$ plot in semi logarithmic scale (inset); (right) *p*lots of the in-phase (top), χ', and out-of-phase (bottom), χ'', components of the *ac* magnetic susceptibility versus the temperature, *T*, under an external *dc* field of 3000 Oe at different frequencies between 10 and 10000 Hz , of complex **4**•2DMF.

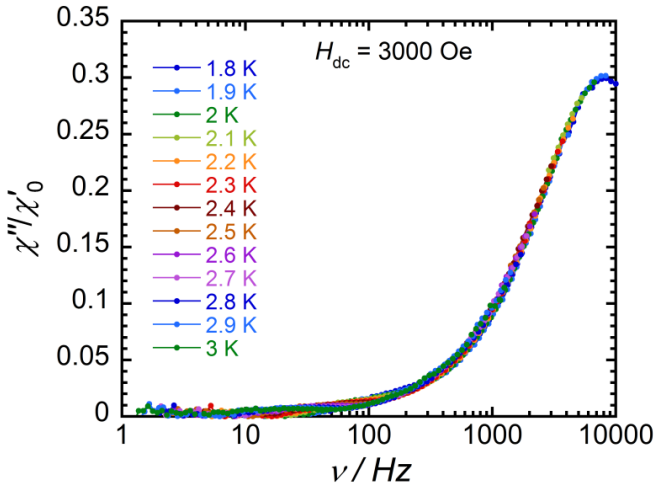

Figure S.III-11. Plot of the, χ''/χ_0' versus the frequency, ν, under an external *dc* field of 3000 Oe at the indicated temperatures, showing the scaling of the curves (at 1.9 to 3 K) to the 1.8 K curve that exhibits frequency maximum, for complex **4**•2DMF.

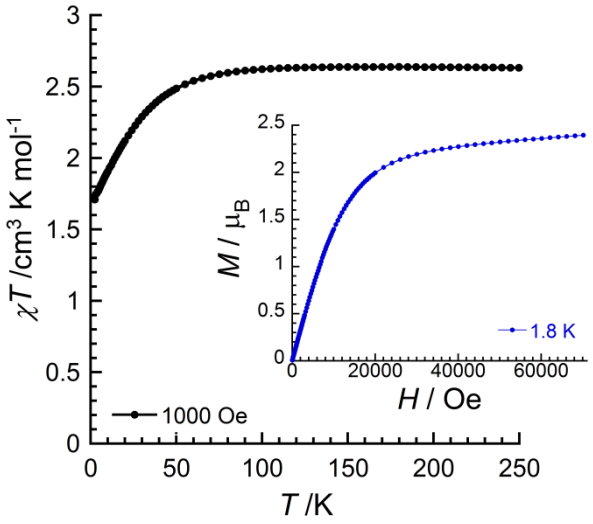

Figure S.III-12. χT versus T curve at 0.1 T (black) and inset the magnetization versus field H at 1.8 K (blue) for $[Co^{II}(PY5Me_2)(H_2O)](BF_4)_2$.[27]

Differential scanning calorimetry srudies of compound 2•2DMF (DSC). The DSC measurements were carried out on freshly filtered crystals of **2**•2DMF using the thermogravimetric analyser DSC Modulée Q200 from TA Instruments, housed at the Centre de Recherche Paul Pascal. The DSC measurements were carried out using 11 mg of **2**•2DMF inside an aluminum hermetically closed capsule in order to avoid the evaporation of solvent. The liquid Nitrogen cooling source was used.

Optical measurements. Surface reflectivity measurements were performed on a home built system, housed at the Centre de Recherche Paul Pascal, at temperatures ranging between 10 and 300 K. A tungsten-halogen light source was used (Leica CLS 150 XD, adjustable up to 1 W/cm^2) at wavelengths between 400 and 1000 nm. All measurements were calibrated against a NIST traceable reflectance standard (sphereOptics, ref SG3054).

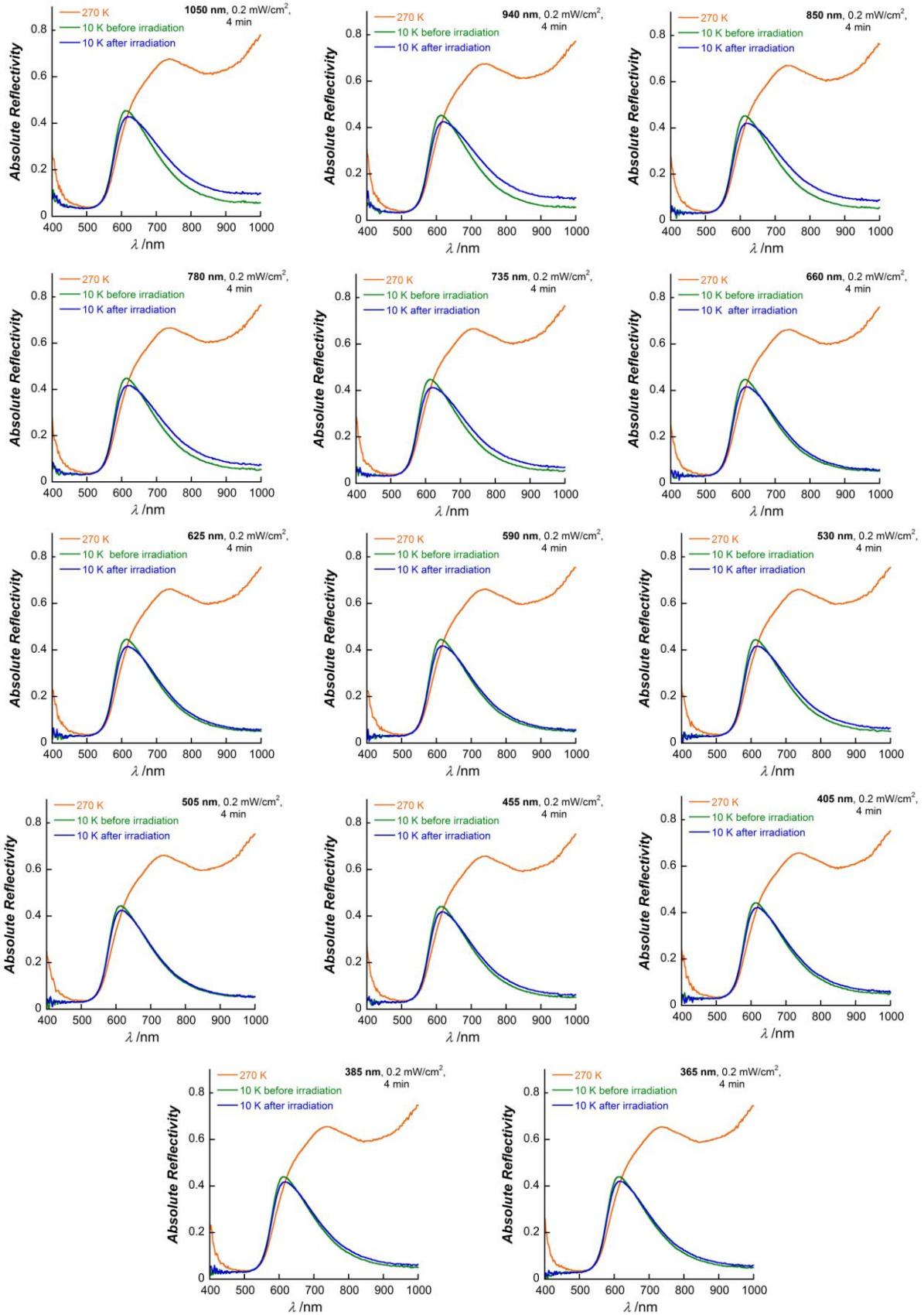

Figure S.III-13. Reflectivity spectra of **2**•2DMF at 270 K and 10 K obtained before irradiation and after 4 min of irradiation (0.2 mW/cm^2) at different wavelengths delivered by 14 LEDs.

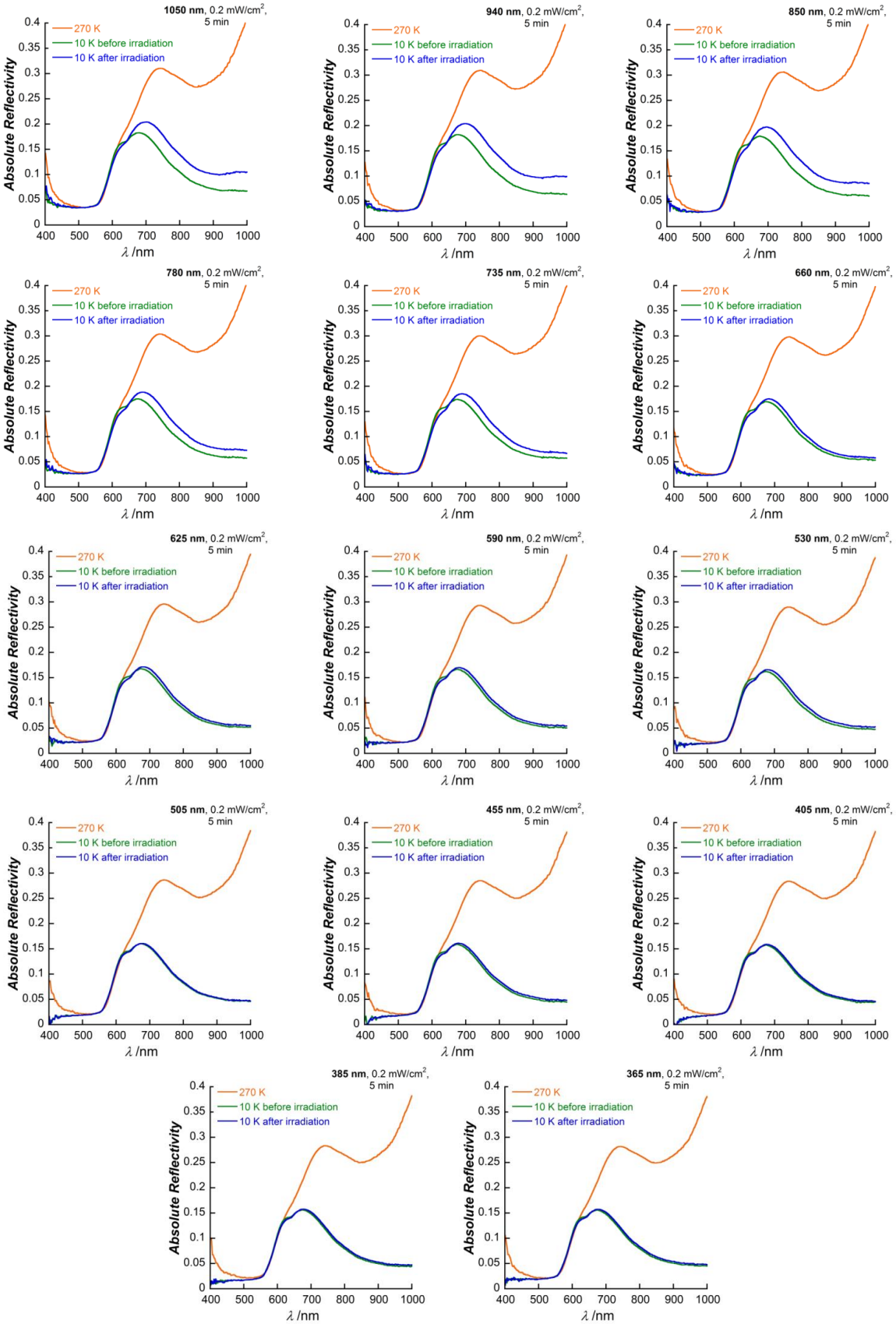

Figure S.III-14. Reflectivity spectra of **3**•2DMF at 270 K and 10 K obtained before irradiation and after 5 min of irradiation (0.2 mW/cm^2) at different wavelengths delivered by 14 LEDs.

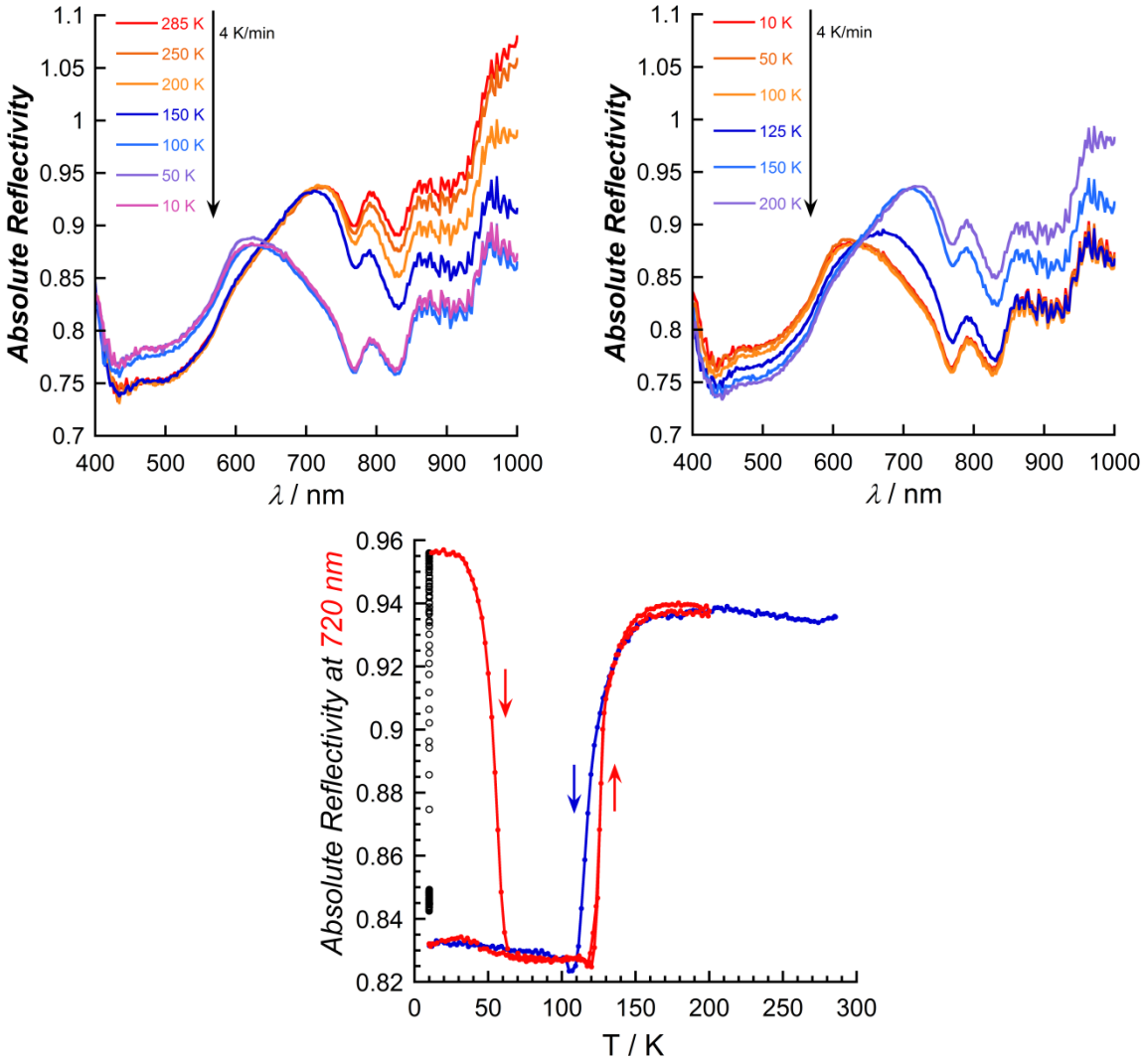

Figure S.III-15. Reflectivity spectra between 285 and 10 K as function of wavelength in cooling (top, left) and between 10 and 200 K in heating mode (top, right); (bottom) thermal evolution of reflectivity signal recorded at λ = 850 ± 5 nm (AR_{850}) in cooling mode (286-10 K, blue curve), after white light irradiation (0.4 mW/cm^2, at 10 K, black circle markers) and heating mode (10-200 K, red curve) at 4 K/min for **2**•2DMF in the form of a pellet from pure compound.

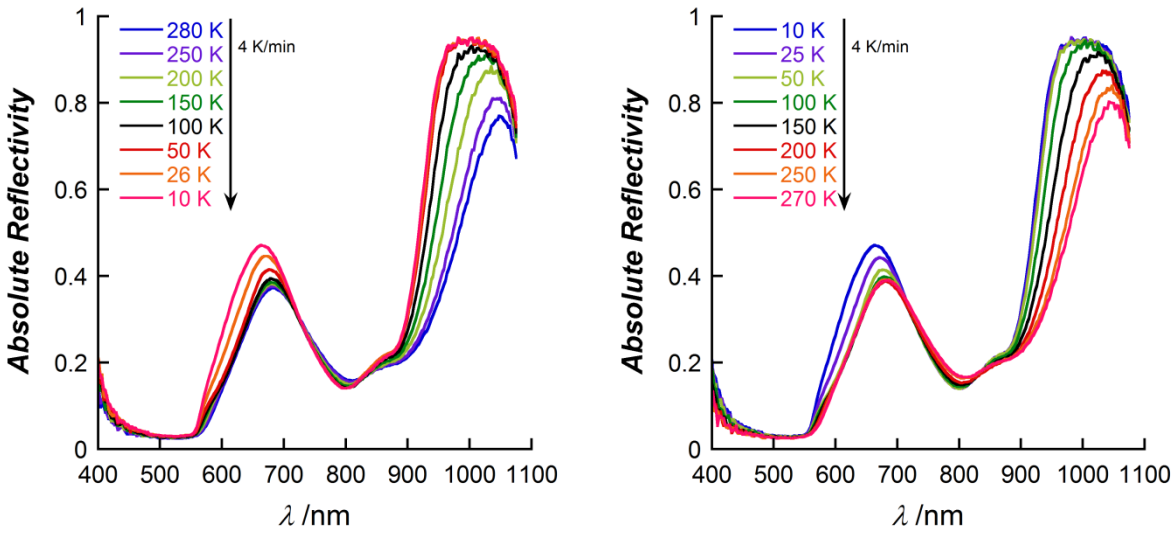

Figure S.III-16. Reflectivity spectra as function of wavelength between 280 and 10 K in cooling mode (left) and between 10 and 270 K in heating mode (right) for **4**•2DMF.

Photomagnetic measurements. Photomagnetic experiments were carried out at Institut de Chimie de la Matière Condensée de Bordeaux (ICMCB) and utilized a Quantum Design SQUID magnetometer MPMS-XL and a 150 W halogen lamp (LEICA CLS 150X) coupled to an optical fiber that was directed into the magnetometer cavity. For **2**•2DMF: 3.8 mg of sample and for **3**•2DMF: 3.5 mg of sample were introduced into a preformed straw at a distance of 6 cm from the optical fiber end [incident light flux = 3 mW/cm^2]. Sample temperatures were corrected for light-induced heating (avg. +2 K with light) by calibrating the experimental sample temperatures to the data collected in the absence of light.

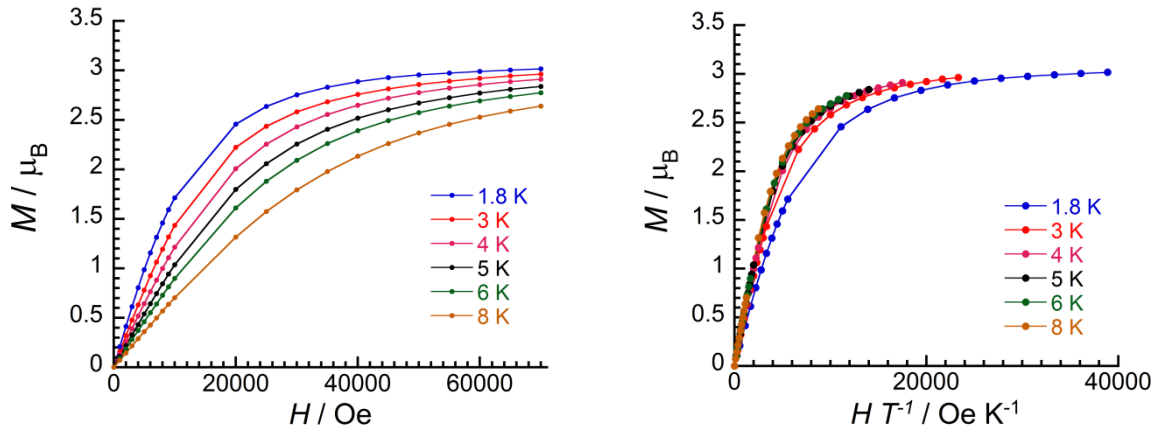

Figure S.III-17. (Left) *M* versus *H* and (right) *H*/*T* plots for complex **3**•2DMF after 980 nm irradiation (8 mW/cm^2, at 10 K) at the indicated temperatures. Blue, 1.8 K; red, 3 K; pink, 4 K; black, 5 K, green, 6 K; black, 8 K.

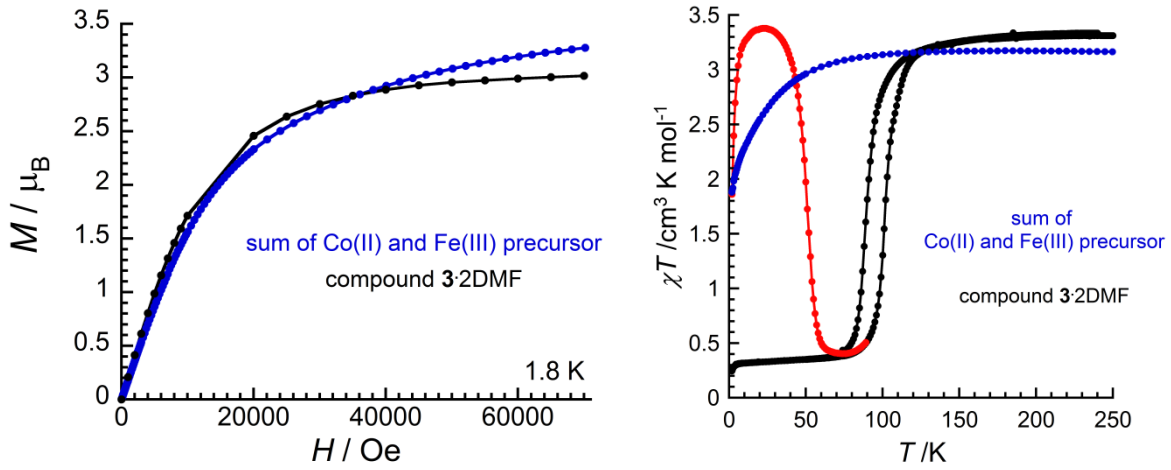

Figure S.III-18. (Left) *M* versus *H* plot for complex **3**•2DMF (black) and the sum of $(NBu_4)[(Tp)Fe^{III}(CN)_3]•3H_2O$ and $[Co^{II}(PY5Me_2)(H_2O)](BF_4)_2$ (blue), at 1.8 K; (right) χT versus temperature plot at 0.1 T from 250-1.8 K in the dark (black), after 980 nm irradiation at 10 K from 1.8-100 K at 1 T (red), for **3**•2DMF and at 0.1 T from 1.8-250 K for the sum of $(NBu_4)[(Tp)Fe^{III}(CN)_3]•3H_2O$ and $[Co^{II}(PY5Me_2)(H_2O)](BF_4)_2$ (blue).

XAS/XMCD studies.

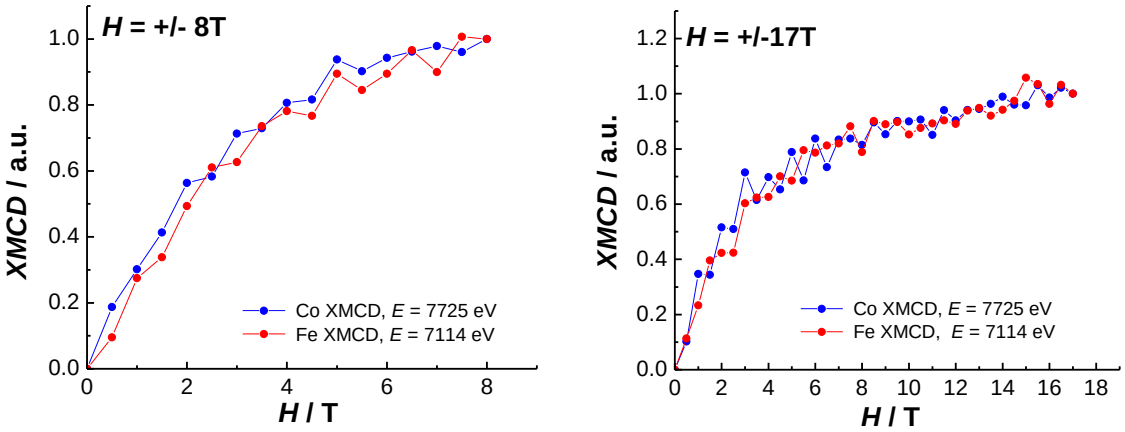

Figure S.III-19. XMCD signal of the light-induced paramagnetic state of **2**•2DMF as a function of the field, at the Co (7725 eV, blue) and Fe (7114 eV, red) energies, under applied magnetic field of +/- 8 T (left) and +/- 17 T (right) at 2 K.

Dielectric constant measurements. Studies of permittivity versus frequency at given temperatures from 300 to 50 K (1 K increment) in cooling and heating modes, under applied electric field for compounds **2**•2DMF, **3**•2DMF, **2** and **4**•2DMF were performed on a PPMS, housed at IMR in Tohoku University in Japan. The measurements are using the conventional three-terminal method (or parallel plate method) and an Andeen-Hagerling 2700A Capacitance bridge. Compounds **2**•2DMF, **3**•2DMF and **4**•2DMF were manipulated in air, while compound **2** under N_2 atmosphere in order to avoid the absorption of water. 4-5 mg from each sample (filtrated from their mother liquor DMF/Et_2O in the case of **2**•2DMF,

3•2DMF and **4**•2DMF), were gently grinded and finally transformed to a pellet (10 mm diameter and 0.005 mm thickness) by applying pressure of 2 kN for 60 sec. The pellet of each sample was placed between two stainless plates (electrodes), were Au wire was attached by Au paste and epoxy resin, to finally form a capacitor. This capacitor was attached to the PPMS sample holder and inserted in the PPMS dewar (under 1 atm of He). The temperature was controlled with PPMS function, while the sample temperature was monitored by Si diode sensor attached near the pellet.

III.7 References

(1) Jeon, I.-R.; Calancea, S.; Panja, A.; Piñero Cruz, D. M.; Koumousi, E. S.; Dechambenoit, P.; Coulon, C.; Wattiaux, A.; Rosa, P.; Mathonière, C.; Clérac, R. *Chem. Sci.* **2013**, *4*, 2463.
(2) Koumousi, E. S.; Jeon, I.-R.; Gao, Q.; Dechambenoit, P.; Merzeau, P.; Buisson, L.; Jia, B.; Li, D.; Woodruff, D. N.; Voltaron, F.; Mathonière, C.; Clérac, R. *J. Am. Chem. Soc*., **2014**, *136*, 15461**.**
(3) Zadrozny, J. M.; Freedman, D. E.; Jenkins, D. M.; Harris, T. H.; Iavarone, A. T.; Mathonière, C.; Clérac, R.; Long, J. R. *Inorg. Chem.* **2010**, *49*, 8886.
(4) (a) Lescouëzec, R.; Vaissermann, J.; Lloret, F.; Julve, M.; Verdaguer, M. *Inorg. Chem.* **2005**, *41*, 5943. (b) Li, D.; Parkin, S.; Wang, G.; Yee, G. T.; Holmes, S. M. *Inorg. Chem.* **2006**, *45*, 1951.
(5) (a) Champion, G.; Escax, V.; Cartier dit Moulin, C.; Bleuzen, A.; Verdaguer, M. J. Am. Chem. Soc. **2001**, 123, 12544. (b) Goujon, A.; Roubeau, O.; Varret, F.; Dolbecq, A.; Bleuzen, A.; Verdaguer, M. *Eur. Phys. J. B* **2000**, *14*, 115.
(6) (a) Berlinguette, C.; Dragulescu-Andrasi, A.; Sieber, A.; Galàn- Mascaròs, J. R.; Güdel, H.-U.; Achim, C.; Dunbar, K. R. *J. Am. Chem. Soc*. **2004**, *126*, 6222. (b) Berlinguette, C.; Dragulescu-Andrasi, A.; Sieber, A.; Güdel, H.-U.; Achim, C.; Dunbar, K. R. *J. Am. Chem. Soc*. **2005**, *127*, 6766.
(7) Later, in 2011, this complex was reported to display a photoinduced intramolecular electron transfer: Funck, K. E.; Prosvirin, A. V.; Mathonière, C.; Clérac, R.; Dunbar, K. R. *Inorg. Chem.* **2011**, *50*, 2782.
(8) Li, D.; Clérac, R.; Roubeau, O.; Harté, E.; Mathonière, C.; Le Bris, R.; Holmes, S. M. *J. Am. Chem. Soc.* **2008**, *130*, 252.
(9) Zhang, Y.; Li, D.; Clérac, R.; Kalisz, M.; Mathonière, C.; Holmes, S. M. *Angew. Chem., Int. Ed.* **2010**, *49*, 3752.
(10) (a) Siretanu, D.; Li, D.; Buisson, L.; Bassani, D. M.; Holmes, S. M.; Mathonière, C.; Clérac, R. *Chem.-Eur. J.* **2011**, *17*, 11704. (b) Zhang, Y.-Z.; Ferko, P.; Siretanu, D.; Ababei, R.; Rath, N. P.; Shaw, M. J.; Clérac, R.; Mathonière, C.; Holmes, S. M. *J. Am. Chem. Soc.* **2014**, *136*, 16854.
(11) Hauser, A.; Alder, J.; Gütlich, P. *Chem. Phys. Lett.* **1988**, *152*, 468.
(12) Hauser, A.; Gütlich, P.; Spiering, H. *Inorg. Chem.* **1986**, **25**, 4245.
(13) Bleuzen, A.; Lomenech, C.; Escax, V.; Villain, F.; Varret, F.; Cartier dit Moulin, C.; Verdaguer, M. *J. Am. Chem. Soc.* **2000**, *122*, 6648.
(14) Champion, G.; Escax, V.; Cartier dit Moulin, C.; Bleuzen, A.; Villain, F.; Baudelet, F.; Dartyge, E.; Verdaguer, M. *J. Am. Chem. Soc.* **2001**, *123*, 12544.
(15) Itkis, M. E.; Chi, X.; Cordes, A. W.; Haddon, R. C. *Science* **2002**, *296*, 1443.
(16) Sato, O.; Kawakami, T.; Kimura, M.; Hishiya, S.; Kubo, S.; Einaga, Y. *J. Am. Chem. Soc*. **2004**, *126*, 13176.
(17) Hoshino, N.; Iijima, F.; Newton, G. N.; Yoshida, N.; Shiga, T.; Nojiri, H.; Nakao, A.; Kumai, R.; Murakami, Y.; Oshio, H. *Nat. Chem*. **2012**, *4*, 921.
(18) Ohkoshi, S.; Nuida, T.; Matsuda, T.; Tokoro, H.; Hashimoto, K. *J. Mater. Chem.* **2005**, *15*, 3291.

(19) Molnár, G.; Cobo, S.; Mahfoud, T.; Vertelman, E. J. M.; van Koningsbruggen, P. J. *J. Phys. Chem. C* **2009**, *113*, 2586.
(20) Bechlars, B.; D'Alessandro, D. M.; Jenkins, D. M.; Iavarone, A. T.; Glover, S. D.; Kubiak, C. P.; Long, J. R. *Nat. Chem.* **2010**, *2*, 362.
(21) Trofimenko, S. *Inorg. Synth.* **1970**, *12*, 99.
(22) Kim, J. I.; Han, S.; Cho, I.-K.; Choi, K. Y.; Heu, M.; Yoon, S.; Suh, B. *Polyhedron* **2004**, *23*, 1333.
(23) Sheldrick, G. M. SADABS, version 2.03, Bruker Analytical X-Ray Systems, Madison, WI, **2000**.
(24) Sheldrick, G. M. *Acta Cryst.* **2008**, *A64*, 112.
(25) (a) Zhang, Y.-Z.; Mallik, U.P.; Clérac, R.; Rath, N.P.; Holmes, S.M. *Polyhedron* **2013**, *52*, 115 and references wherein; (b) Li, D.-F.; Clérac, R.; Parkin, S.; Wang, G.-B.; Yee, G.T.; Holmes, S.M. *Inorg. Chem.* **2000**, *45*, 5251.
(26) Kambe, K. *J. Phys. Soc. Jpn.* **1950**, *5*, 48.
(27) Jeon, I.-R. *PhD thesis, Bordeaux University* **2012**.

Chapter IV

Preliminary investigations of the electron transfer phenomenon of {Fe(*μ*-CN)Co} pairs in solution

Table of Contents for Chapter IV:

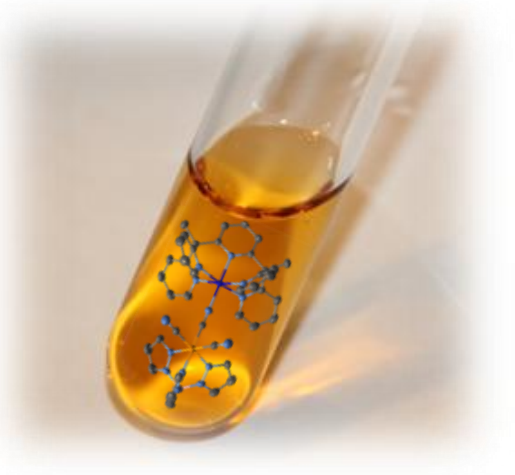

IV.1 Introduction

In Chapters II and III, the synthesis of three novel electron transfer pairs[1] and the characterization of their switchable properties in solid state were described. In this chapter, we will present some preliminary investigations of their properties in solution. The importance of designing and synthesizing soluble, well-defined molecular fragments of the 3D Prussian Blue analogues (PBAs)[2] lies on their potential technological applications in the form of films or molecular layers.

The possibility of transferring the electron transfer phenomenon from solid state to solution has been investigated thoroughly for several Fe/Co molecular square complexes by means of temperature depended UV-Vis spectroscopy, cyclic voltammetry and magnetic studies.[3-8] The diverse functionalization of the ligands capping the metal ion centers in these moieties allows the tuning of the electronic properties of the final complexes as well as their solubility. Interestingly, the thermally induced electron transfer conversion was found to be strongly influenced by the nature of the solvent and a general tendency showed that $T_{1/2}$ values (temperature where the ratio between paramagnetic and diamagnetic configuration is 1:1) increased with the solvent polarity. These results are very promising in the frame of technological applications since they are allowing a fine tuning of the electron transfer properties simply by a judicious choice of the solvent or by adjusting the composition of a solvent mixture.[5,7,8] Furthermore, the electron transfer process has been observed by UV-Vis spectroscopy upon addition of trifluoroacetic acid in a solution of an Fe/Co molecular square at fixed temperature. This remarkable result demonstrated for the first time the possibility of inducing an electron transfer in these Fe/Co PBAs by protonation in solution.[4]

In 2013, the first dinuclear Fe/Co PBAs exhibiting tunable magnetic and optical properties depending on its physical state was published.[9] In this system, the spin-crossover phenomenon occurring at the cobalt site of the pair in solid state was lost when the compound was dissolved in DMSO, as the magnetic susceptibility measurements revealed. Inspired by the work reported on molecular square analogues,[4] the properties of the pair in solution, treated with trifluoroacetic acid, were investigated. The systematic study of the pair and its precursors upon addition of acid by UV-Vis spectroscopy, ^{1}H-NMR and electrochemistry demonstrated the occurrence of an intramolecular electron transfer triggered by protonation in solution at room temperature.

Motivated by these results, we focused our efforts to the study of the properties of **1**•2DMF, **2**•2DMF and **3**•2DMF in solution. Amongst various organic solvents tested, acetonitrile (MeCN) was chosen as the most efficient dilution media, allowing reasonable concentration of the pairs in solution. One of the main concerns of this chapter is the stability of the dinuclear complexes in solution. This has been investigated by various spectroscopic techniques based on the previous work done for the tetra- and dinuclear Fe/Co species.[5,7-9]

IV.2 Experimental Results

IV.2.1 Mass spectroscopy studies of compounds 1•2DMF, 2•2DMF and 3•2DMF

The stability of the complexes **1**•2DMF, **2**•2DMF and **3**•2DMF in solution has been examined by positive and negative ion electrospray (ESI^+ and ESI^-, respectively) mass spectroscopy, using MeCN as dilution media and as eluent. For all complexes, the mass spectra are similar and the presence of the dinuclear $[\{(Tp)Fe(CN)_3\}\{Co(PY5Me_2)\}]^+$ unit was found in solution by the appearance of the peak at 848.96 for **1**•2DMF, 848.94 for **2**•2DMF and 849.01 for **3**•2DMF (Figures IV-1, S.IV-1 and S.IV-2, respectively). The experimental isotopic distribution of this peak is in agreement with the simulated one for the cationic species $[\{(Tp)Fe(CN)_3\}\{Co(PY5Me_2)\}]^+$, demonstrating the presence of the compound in MeCN solution (Figure IV-2). The peak at 251.30 observed in Figure IV-1 and 251.32 and 251.34 in Figures S.IV-1 and S.IV-2, left, can be attributed to the cationic species $\{Co(PY5Me_2)\}^{2+}$, while the origin of the rest of the peaks is still under investigation. The main peak observed in the negative (ESI^-) spectra at 346.94 for **1**•2DMF and **2**•2DMF and at 347.15 for **3**•2DMF (Figures IV-1, S.IV-1 and S.IV-2, respectively), is attributed to the anionic species of $\{(Tp)Fe(CN)_3\}^-$. The presence of the peaks attributed to the $\{Co(PY5Me_2)\}^{2+}$ and $\{(Tp)Fe(CN)_3\}^-$ species can be due to the experimental conditions (fragmentation of molecular species to pseudo molecular ions due to the ionization process), although a partial dissociation of the pair in MeCN cannot be excluded.

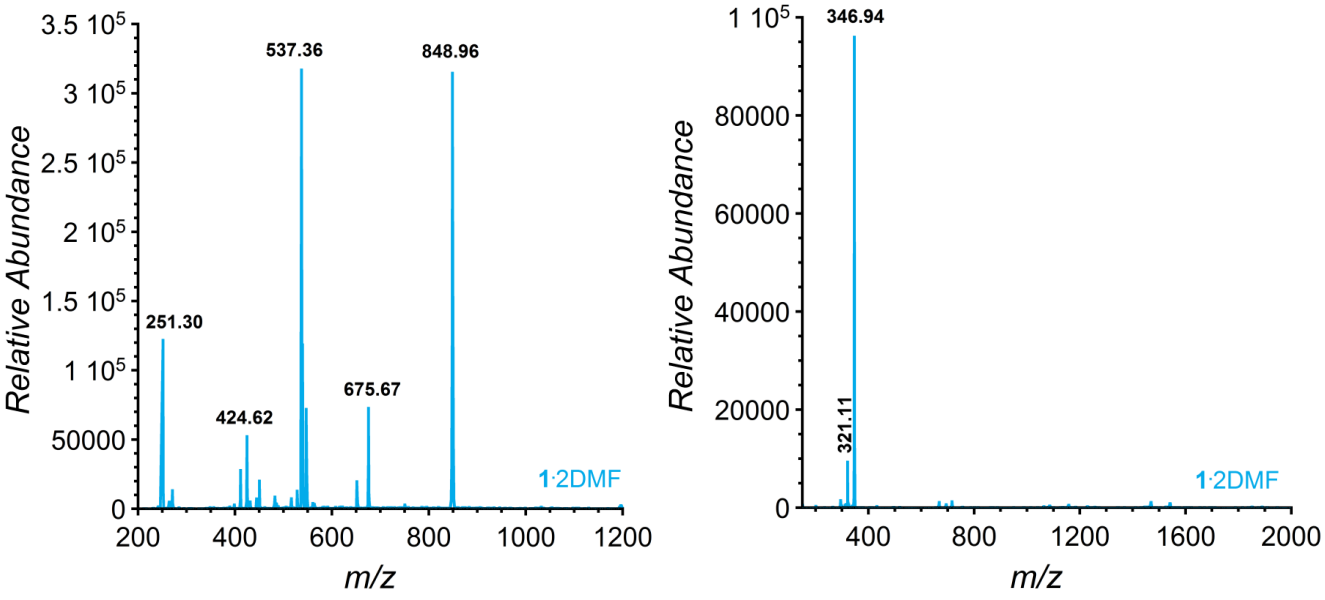

Figure IV-1. (Left) Positive and (right) negative mass spectrograms of **1**•2DMF in MeCN.

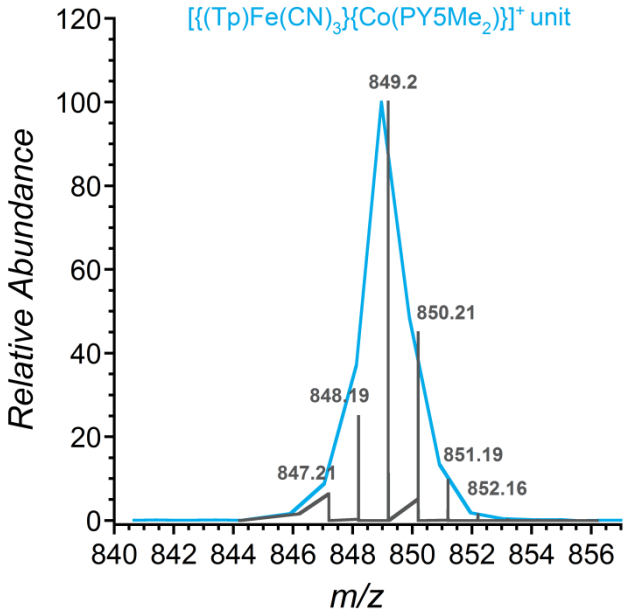

Figure IV-2. Experimental (light blue) and calculated (gray) isotopic distribution of the peak at 848.96, showing the presence of the cationic $[\{(Tp)Fe(CN)_3\}\{Co(PY5Me_2)\}]^+$ unit, in MeCN.

IV.2.2 ^{1}H-NMR spectroscopy in solution of compound 1•2DMF and its precursors

^{1}H-NMR spectroscopy is a useful technique for this study as it can detect the occurrence of dissociation of the pair, by comparing the spectra of the pair and the ones of the precursors. Moreover, this technique allows the detection of an electron transfer process in solution, as it is sensitive to the presence of paramagnetic ($[Fe^{III}_{LS}(\mu\text{-}CN)Co^{II}_{HS}]$) or diamagnetic ($[Fe^{II}_{LS}(\mu\text{-}CN)Co^{III}_{LS}]$) species.

Based on the work done for the dinuclear complex $[\{(BBP)Fe(CN)_3\}\{Co(PY5Me_2)\}]$, [**FeCo**],[9] (BBP: 2,6- bis(benzimidazol-2-yl)pyridine)), we expect paramagnetic shifts of all resonances for paramagnetic ($[Fe^{III}_{LS}(\mu\text{-}CN)Co^{II}_{HS}]$) species. That should be different that the sum of the spectra of the precursors. On the other hand, for diamagnetic ($[Fe^{II}_{LS}(\mu\text{-}CN)Co^{III}_{LS}]$) species the absence of the paramagnetic shift is accompanied by the assignment of all resonances to the ligands in 1:1 ratio.

The ^{1}H-NMR spectrum of **1**•2DMF at room temperature (Figure IV-3, light blue) shows various weak resonances above and below the diamagnetic region, indicative of the presence of paramagnetic species in solution. These resonances are shifted compared to the NMR resonances for the original building blocks (Figure IV-3, light blue versus red and blue NMR spectra). The shift can be attributed to the coordination of the precursors to form the dinuclear complex and suggests the presence of the pair in its paramagnetic state at room temperature. The NMR spectrum of **1**•2DMF in the diamagnetic area (Figure IV-4, light blue) is very simple in comparison with the spectra of the capping ligands (Figure IV-4, light blue versus red and blue spectra, Figures S.IV-3 and S.IV-4). Therefore, we cannot conclude on the

eventual presence of diamagnetic dinuclear complexes in solution at room temperature, which if exist, they are in lower concentration than the paramagnetic dinuclear complexes.

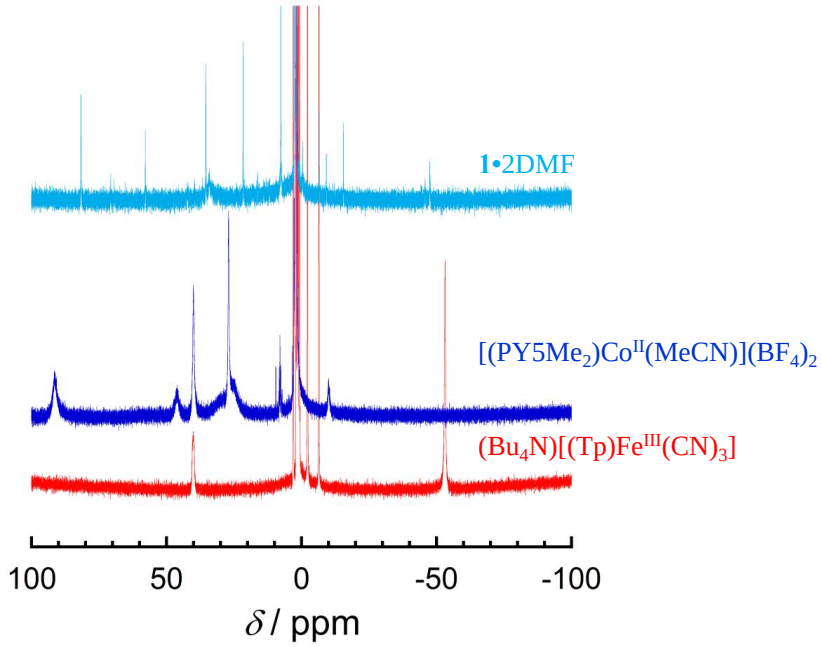

Figure IV-3. ^{1}H-NMR spectra in d-MeCN at 298 K of **1**•2DMF (light blue), $[(PY5Me_2)Co^{II}(MeCN)](BF_4)_2$ (blue) and $(Bu_4N)[(Tp)Fe^{III}(CN)_3]$ (red).

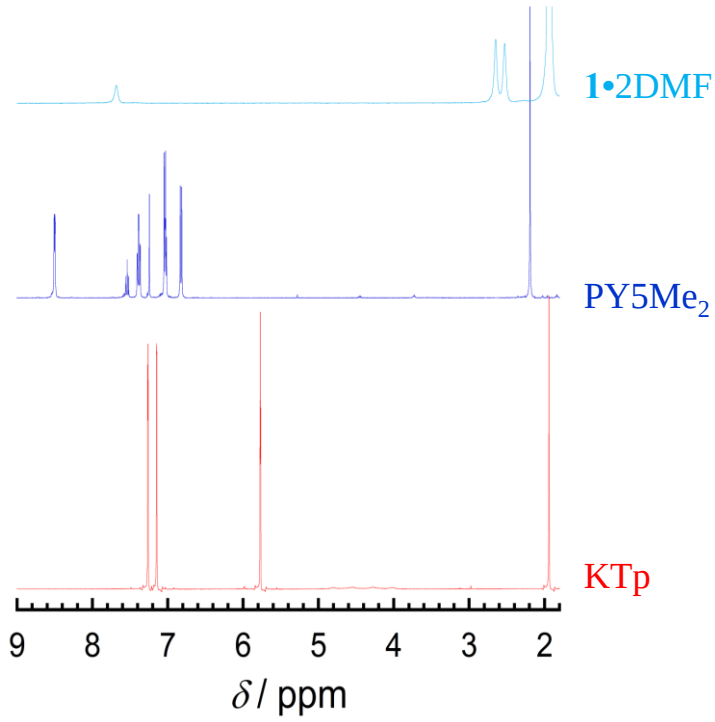

Figure IV-4. Portion of the ^{1}H-NMR spectra in d-MeCN at 298 K of **1**•2DMF (light blue) in comparison with the ligand hydridotris(pyrazol-1-yl)borate (Tp^{-}) (red) and the ligand 2,6-bis(1,1-di(pyridin-2-yl)ethyl)pyridine ($PY5Me_2$) (blue) in d-$CHCl_3$.

IV.2.3 IR spectroscopy in solution of compounds 1•2DMF, 2•2DMF and 3•2DMF

As already shown in Chapters II and III, IR spectroscopy is a useful technique to investigate cyanido compounds, in particular in the region of the $\tilde{\nu}_{CN}$ stretching band that is sensitive to the stretching mode of the -CN groups (terminal or bridging) and the oxidations states of the coordinated metal ions. We used IR spectroscopy in Attenuated Total Reflection (ATR) in order to study the pairs in solution (MeCN) (Figure IV-5). Blank experiment has been performed on pure MeCN and the IR spectrum of the $(Bu_4N)[(Tp)Fe^{III}(CN)_3]$ dissolved in MeCN has been collected for guidance (Figures S.IV-6 and S.IV-7, respectively). The analysis of the spectra of the pairs in solution (black spectra for **1**•2DMF, **2**•2DMF and **3**•2DMF in Figure IV-5) at the cyanide region, compared with those obtained in solid state (light blue, orange and purple spectra for **1**•2DMF, **2**•2DMF and **3**•2DMF, respectively, in Figure IV-5) allows the attribution of the bands at ~2144-2146 cm^{-1} to the bridging cyanides within $\{Fe^{III}_{LS}(\mu\text{-CN})Co^{II}_{HS}\}$ units and the one at 2120 cm^{-1} to the terminal cyanide groups. The appearance of bands at 2093 and 2063 cm^{-1} was attributed to the bridging cyanides within $\{Fe^{II}_{LS}(\mu\text{-CN})Co^{III}_{LS}\}$ units and to the terminal cyanide groups coordinating to the LS Fe(II) ions, respectively, as it has been observed for the diamagnetic state of [FeCo] squares in literature.[3-8] This demonstrates the coexistence of paramagnetic $[Fe^{III}_{LS}(\mu\text{-CN})Co^{II}_{HS}]$ and diamagnetic $[Fe^{II}_{LS}(\mu\text{-CN})Co^{III}_{LS}]$ species in solution, suggesting a partial electron transfer process at room temperature. This result is reinforced by the analysis of the spectra of the [FeNi] pair (**4**•2DMF) below 2120 cm^{-1}. The lack of additional $\tilde{\nu}_{CN}$ stretching bands below these wavenumbers is in agreement with the absence of electron transfer in this molecule. Summary of the values of the $\tilde{\nu}_{CN}$ stretching bands discussed above is included in Table IV-1.

Table IV-1. Summary of the values of the $\tilde{\nu}_{CN}$ stretching bands for compounds $(Bu_4N)[(Tp)Fe^{III}(CN)_3]$, **1**•2DMF, **2**•2DMF, **3**•2DMF and **4**•2DMF in solid state and in MeCN solutions.

	$\tilde{\nu}_{CN}$ **in solid state**	$\tilde{\nu}_{CN}$ **in MeCN solutions**		
		MeCN origin	***Paramagnetic compound***	***Diamagnetic compound***
$(Bu_4N)[(Tp)Fe^{III}(CN)_3]$	2117	2293, 2253	2119	
1•2DMF	2155, 2120		2144, 2120	2093, 2063
2•2DMF	2158, 2120		2146, 2121	
3•2DMF	2158, 2120		2144, 2120	
4•2DMF	2165, 2120		2151, 2121	

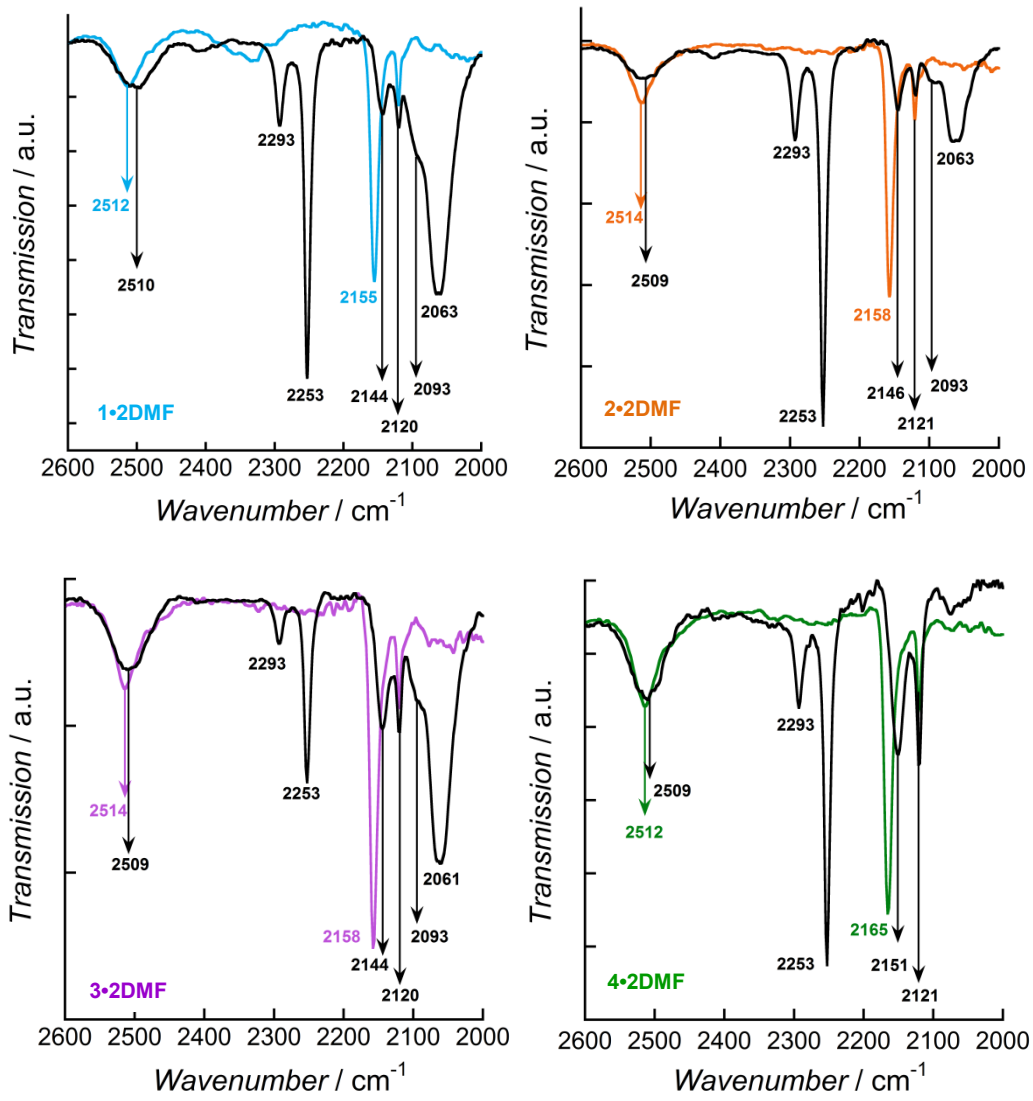

Figure IV-5. Portion of the FT-IR spectra of **1**•2DMF (top, left), **2**•2DMF (top, right), **3**•2DMF (bottom, left) and **4**•2DMF (bottom, right) in solid state (light blue, orange, purple and green, respectively) and in MeCN solutions (black), at 298 K.

IV.2.4 UV-Vis spectroscopy in solution of compounds 1•2DMF, 2•2DMF and 3•2DMF

The electron transfer process is accompanied by reversible changes in the color of the studied compounds due to changes in their electronic properties in the UV-visible area. These changes are mainly associated to charge transfer (CT) transitions between the ligands and the metals (MLCT/LMCT) and between the two metals (MMCT), which can be easily detected by UV-Vis spectroscopy.

UV-Vis spectroscopy, performed at different temperatures, has been successfully used in order to probe the thermally-induced electron transfer process in solution for several Fe/Co squares.[3-8] Moreover, the UV-Vis spectra of the dinuclear complex [{(BBP)Fe(CN)$_3$}{Co(PY5Me$_2$)}] ([**FeCo**]),[9] before and after acidic addition in DMSO

solution, in combination with the spectra obtained for the $\{(BBP)Fe^{III}(CN)_3\}$ and $\{(H_2BBP)Fe^{II}(CN)_3\}$ species, revealed that an electron transfer process occurs in a dinuclear [FeCo] complex in solution, triggered by the protonation.

The conversion of the color from orange to green in MeCN solutions of **1**•2DMF, **2**•2DMF and **3**•2DMF, when they were immersed in liquid nitrogen bath, reinforced the conclusions obtained by the IR spectroscopy studies and motivated us to study the solutions of these complexes by UV-Vis spectroscopy.

Spectra of compounds **1**•2DMF, **2**•2DMF and **3**•2DMF, dissolved in MeCN, were first measured at room temperature. As it is shown in Figure IV-6, left, the electronic spectra of the three dinuclear complexes (**1**•2DMF, **2**•2DMF and **3**•2DMF in light blue, orange and purple, respectively) are similar, suggesting that in solution these compounds have similar properties independently from the counter ion used for their crystallization. Therefore, only the UV-Vis spectrum of compound **1**•2DMF is compared with those of Fe(III) and Co(II) precursors in Figure IV-6, right (red and blue spectrum, respectively). The spectrum of compound **1**•2DMF (light blue spectrum, Figure IV-6, right), exhibits an intense band at 418 nm, which is attributed to the LMCT of the Fe(III) unit in the pair. This transition is shifted 10 nm higher (587 cm^{-1} lower in energy) compared to the LMCT band of the Fe(III) precursor (red spectrum, Figure IV-6, right), due to the coordination with the $\{Co(PY5Me_2)\}$ species. This shift is in agreement with the results obtained for the [**FeCo**] pair.[9] The small shoulder at ≈ 480 nm and the broad and weak transition around 800 nm observed in **1**•2DMF are not present in the spectra of the two precursors, thus their origin has to be investigated further. Based on the results obtained for the Fe/Co squares in solution,[3-8] the small shoulder around 480 nm can be attributed to a MMCT ($Co^{II} \rightarrow Fe^{III}$) band and the broad signal around 800 nm to a MMCT ($Fe^{II} \rightarrow Co^{III}$) band. As the [FeNi] pair (**4**•2DMF) doesn't exhibit electron transfer properties, these two transitions should not be observed in the solution spectrum of this compound. Indeed, the broad band around 800 nm is absent in the spectrum of **4**•2DMF (green spectrum, Figure IV-6), reinforcing the attribution of a MMCT ($Fe^{II} \rightarrow Co^{III}$) band in the spectrum of **1**•2DMF. To confirm the existence of the MMCT ($Fe^{II} \rightarrow Co^{III}$) band in our [FeCo] pairs, and thus the occurrence of an electron transfer process at room temperature in solution, the temperature dependence of the UV-Vis spectra has to be followed, where an increase of the intensity of the band around 800 nm with decrease of temperature is expected (as observed for the [FeCo] squares[3-8]). It is worth to mention that recently theoretical calculations have been performed for a [FeCo] square that support the presence of a MMCT ($Fe^{II} \rightarrow Co^{III}$) band at 770 nm.[10] Although the broad band around 800 nm is absent in the spectra of **4**•2DMF (green spectrum, Figure IV-5), the presence of the small shoulder at 480 nm is discarding its attribution to a MMCT ($Co^{II} \rightarrow Fe^{III}$) band in **1**•2DMF. This hypothesis is reinforced by the study of the UV-Vis spectra of the Fe(III) precursor in different solvents (Figure S.IV-8), since the small shoulder around 480 nm is also present in the spectrum of the Fe(III) precursor in MeOH.

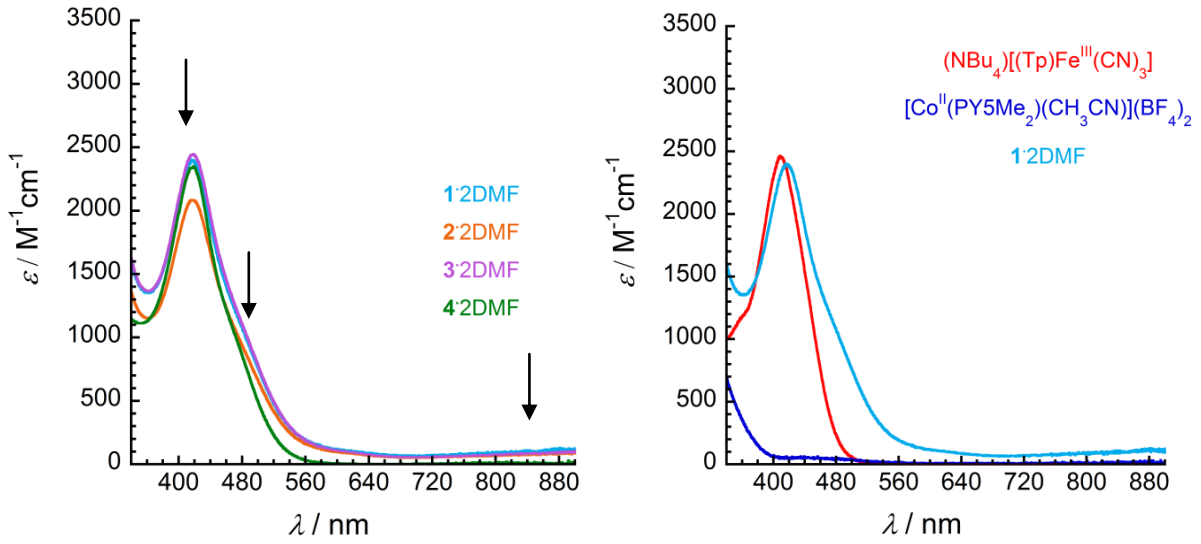

Figure IV-6. (Left) UV-Vis spectra of compounds **1**•2DMF (light blue), **2**•2DMF (orange), **3**•2DMF (purple) and **4**•2DMF (green) in MeCN solution with C = 0.005 M; (right) UV-Vis spectra of compound **1**•2DMF (light blue), $(Bu_4N)[(Tp)Fe^{III}(CN)_3]$ (red) and $[(PY5Me_2)Co^{II}(MeCN)](BF_4)_2$ (blue) in MeCN solution and C = 0.005 M. The arrows show the different transitions.

IV.2.5 Cyclic Voltammetry studies in solution of compounds 1•2DMF, 2•2DMF and 3•2DMF

Keeping in mind that the electron transfer is governed by the redox potential difference (ΔE) between the metal ion sites, the redox properties of compounds **1**•2DMF, **2**•2DMF and **3**•2DMF in MeCN solutions and their precursors $(Bu_4N)[(Tp)Fe^{III}(CN)_3]$ and $[(PY5Me_2)Co^{II}(MeCN)](BF_4)_2$ were investigated. All compounds were dissolved in MeCN (1 mM), supplemented with 0.1 M $Bu_4N(BF_4)$. These results are very preliminary and their interpretation should be taken with precaution.

Before discussing these results, we remind the reader of the electrochemistry results obtained for the [**FeCo**] in DMSO solution.[9] When this pair is in its paramagnetic state two reversible redox waves appear and they have been attributed to the Fe^{II}/Fe^{III} and Co^{II}/Co^{III} couples in the pair. The comparison with the redox waves of the Fe and Co precursors shows that these two waves are shifted, due to their coordination, reducing slightly the ΔE between them. When the diamagnetic state of this pair is induced by an electron transfer process, the two redox waves described above for the Fe^{II}/Fe^{III} and Co^{II}/Co^{III} couples in the pair are reversed.

The $(Bu_4N)[(Tp)Fe^{III}(CN)_3]$ precursor shows a reversible redox wave at -0.81 V, which is attributed to the $\{Fe^{II}/Fe^{III}\}$ couple (Figure IV-7, red voltammogram). On the other hand, the $[(PY5Me_2)Co^{II}(MeCN)](BF_4)_2$ compound exhibits a reversible redox wave at +0.13 V related to the $\{Co^{II}/Co^{III}\}$couple (Figure IV-7, blue voltammogram).

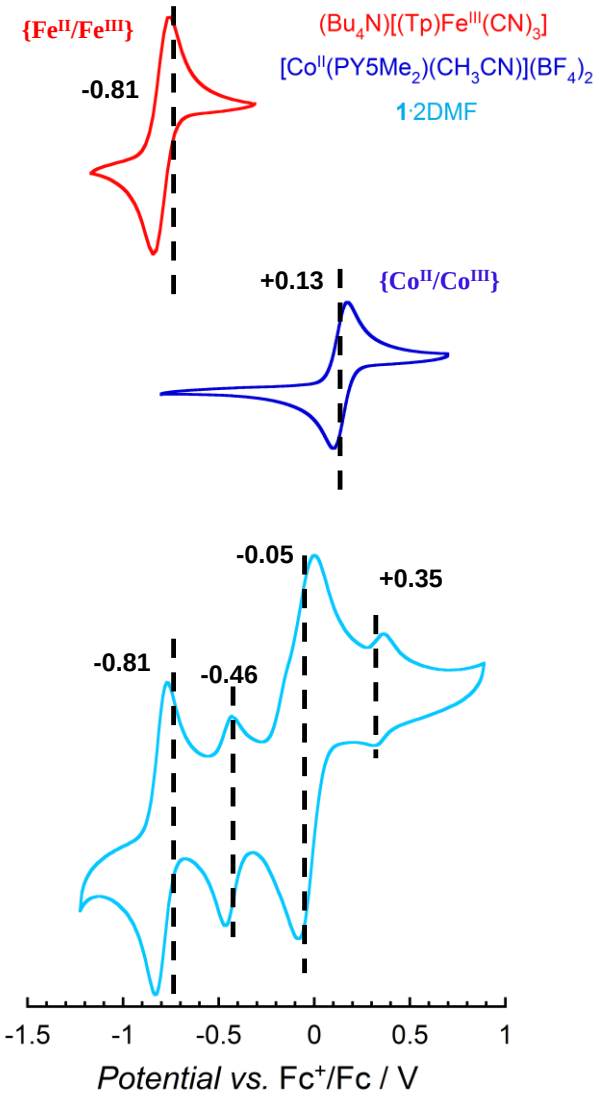

Figure IV-7. Cyclic voltammograms of $(Bu_4N)[(Tp)Fe^{III}(CN)_3]$ (red), $[(PY5Me_2)Co^{II}(MeCN)](BF_4)_2$ (blue) and compound **1**•2DMF (light blue) (~1 mM), collected in a 0.1 M solution of $Bu_4N(BF_4)$ in MeCN, with a scan rate of 0.1 V s^{-1}. Potentials were referenced to the $[Cp_2Fe]^{1+/0}$ couple. The dashed lines are guides for the discussion in the text.

Compounds **1**•2DMF, **2**•2DMF and **3**•2DMF exhibit similar behavior (see Figure IV-8), with multiple reversible redox waves at -0.81, -0.46, -0.05, +0.35 V and a small shoulder at -0.16 V. The presence of the reversible redox wave at -0.81 V, in the same position as in the Fe precursor, suggests a dissociation of the dinuclear complexes in MeCN in the highly ionic solution. The reversible wave at -0.46 V can be attributed to the $\{Fe^{II}/Fe^{III}\}$ couple of the Fe site of the pair, shifted towards a higher potential due to the coordination with the Co unit, as also seen in the [**FeCo**] pair.[9] The wave at -0.05 V may be attributed to the $\{Co^{II}/Co^{III}\}$ couple of the Co site of the pair, shifted towards a lower potential due to the coordination with the Fe unit, again as previously observed.[9] It is worth to note that this interpretation suggests a ΔE of

0.40 V between the Fe and Co parts of the pair, 0.54 V smaller than the Δ*E* between the Fe and Co precursors under the same conditions. This hypothesis is reinforced by the results obtained in a second electrochemistry experiment, which involved the addition of the Fe(III) precursor in five parts to an electrolyte solution of the Co(II) precursor until an equimolar ratio was obtained (Figure IV-9). When about 0.4 eq. of Fe(III) precursor were added, the intensity of the Co(II) precursor peak decreased, while two peak appeared at lower (around -0.05 V and -0.45 V) and one at higher potential (+0.35 V). Previous work on the [**FeCo**][9] suggests that the peak at -0.05 V belongs to the cobalt coordinated to the iron via a cyanide bridge, while that at -0.45 V corresponds to the coordinated iron. However, the higher potential peak has not yet been identified. When 0.8 eq. of Fe(III) precursor were added, the Co(II) precursor peak had completely disappeared, the coordinated cobalt and iron peaks had increased, while a new peak was seen (around -0.80 V), probably corresponding to uncoordinated Fe species. Surprisingly, the peak attributed to the cobalt in the pair is much more intense than that of the putative iron moiety in the pair. This observation, combined with the presence of uncoordinated Fe species, suggests that the Fe:Co ratio of the species in solution is not 1:1. It is highly likely that a complex equilibrium is established within the highly ionic solution, which will require further study to be elucidated.

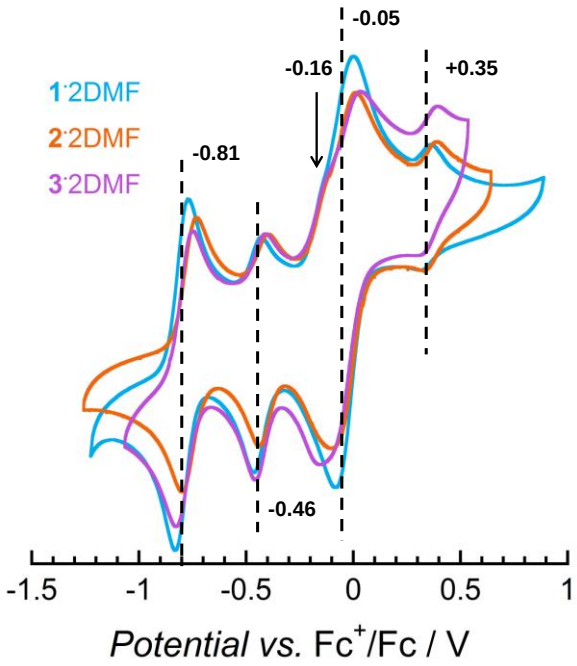

Figure IV-8. Cyclic voltammograms of compounds **1**•2DMF (light blue), **2**•2DMF (orange) and **3**•2DMF (purple) in MeCN solution (~1 mM), collected in a 0.1 M solution of $Bu_4N(BF_4)$ in MeCN with a scan rate of 0.1 V s^{-1}. Potentials were referenced to the $[Cp_2Fe]^{1+/0}$ couple. The dashed lines and the arrow are guides for the discussion in the text.

In an effort to explain the presence of the small shoulder at -0.16 V (Figure IV-8), variable scan rate experiments in MeCN solution of **1**•2DMF were performed (Figure IV-10). These CVs demonstrated that the redox events at -0.46 (**II**) and -0.16 V (**II'**), are not independent of each other, and display opposite behavior scan rate. At a low scan rate (Figure IV-10, 50 mV/s), the current passing in the oxidation **II** is low, while that passing in the oxidation **II'** is relatively strong. Conversely, at fast scan rates (10 V/s), the current ratio for the oxidation and reduction in **II** approaches one, characteristic of a reversible process, while the redox wave **II'** disappears (Figure IV-10, 10 V/s). Therefore, this shoulder likely results from the decomposition of the product electrochemically produced during the reduction event **II**, in a classic ECE (Electrochemical-Chemical-Electrochemical) reaction sequence. Further evidence to this effect is shown Figure IV-10c. When the potential window is restricted to only include peak **III**, no shoulder is observed. However, when the window is enlarged to include peak **II**, the shoulder appears. Thus, the shoulder at -0.16 V is a result of the reduction process in the redox wave at -0.46 V.

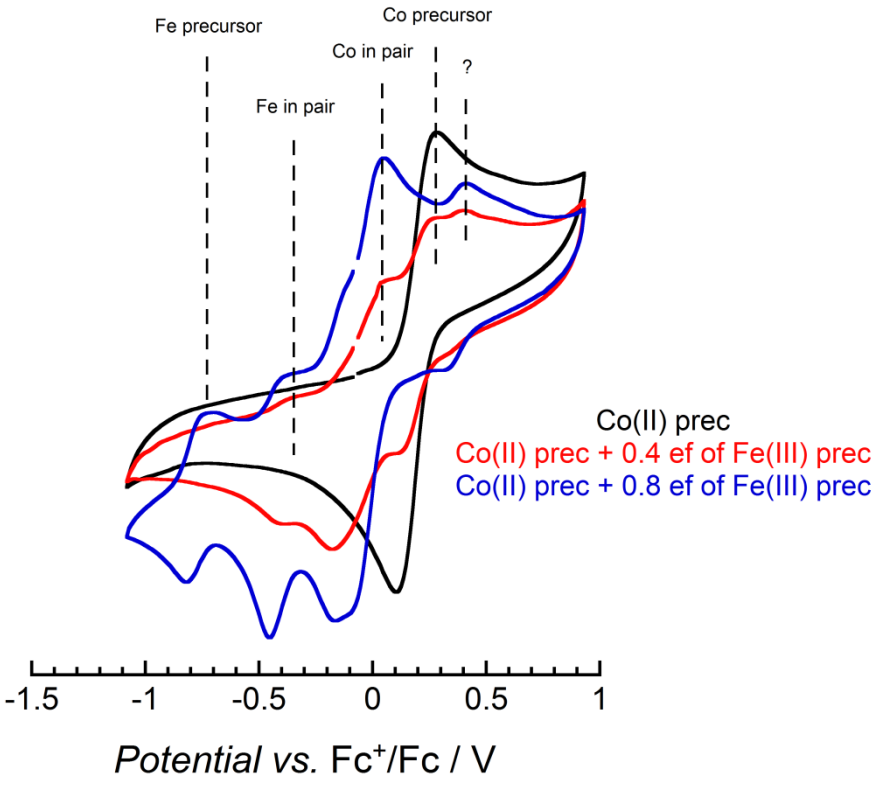

Figure IV-9. Cyclic voltammograms of $[(PY5Me_2)Co^{II}(MeCN)](BF_4)_2$ (black), $[(PY5Me_2)Co^{II}(MeCN)](BF_4)_2$ and 0.4 eq of $(Bu_4N)[(Tp)Fe^{III}(CN)_3]$ (red) $[(PY5Me_2)Co^{II}(MeCN)](BF_4)_2$ and 0.8 eq of $(Bu_4N)[(Tp)Fe^{III}(CN)_3]$ (red) in MeCN solution (~1 mM), collected in a 0.1 M solution of $Bu_4N(BF_4)$ in MeCN with a scan rate of 0.5 V s^{-1}. Potentials were referenced to the $[Cp_2Fe]^{1+/0}$ couple. The dashed lines and the arrow are guides for the discussion in the text.

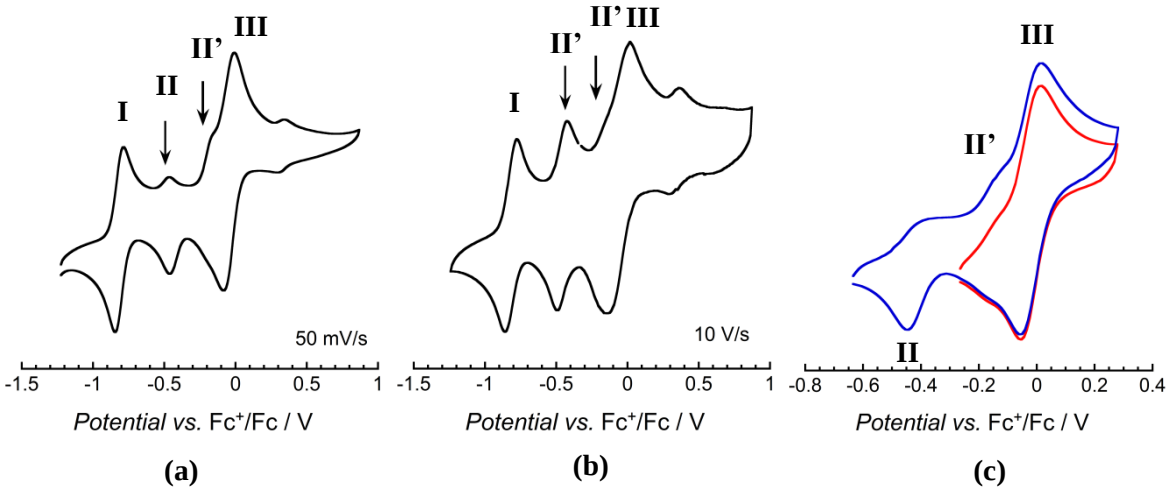

Figure IV-10. Cyclic voltammograms of compounds **1**•2DMF in MeCN solution (~1 mM), collected in a 0.1 M solution of $Bu_4N(BF_4)$ in MeCN with a scan rate of 0.05 V s^{-1} (a) and 10 V s^{-1} (b); (c) demonstration that the oxidation **II'** is a result of the reduction **II**. Potentials were referenced to the $[Cp_2Fe]^{1+/0}$ couple. The arrows are guides for the discussion in the text.

IV.3 Conclusions and Perspectives

In conclusion, in this chapter the possibility to transfer the electron transfer phenomenon from solid state to solution for the three dinuclear complexes **1**•2DMF, **2**•2DMF and **3**•2DMF was investigated. The importance of designing and synthesizing soluble, well-defined molecular fragments of the 3D Prussian Blue analogues (PBAs)[2] lies on their potential technological applications in the form of films and coatings. One of the main concerns of this chapter is the stability of the pairs in MeCN solution. This has been investigated by various spectroscopic techniques, like mass, ^{1}H-NMR, IR and UV-Vis spectroscopic methods. The presence of a peak corresponding to the dinuclear $[\{(Tp)Fe(CN)_3\}\{Co(PY5Me_2)\}]^+$ unit in the mass spectrum of the pairs, the presence of various resonances above and below the diamagnetic region in the ^{1}H-NMR spectrum of **1**•2DMF, shifted from those observed for the original building blocks and the $\tilde{\nu}_{CN}$ stretching band of the -CN group attributed to the $\{Fe^{III}_{LS}(\mu\text{-}CN)Co^{II}_{HS}\}$ units in the IR spectra of the pairs in solution, are concluding to that direction. At the same time, in IR spectroscopy an equilibrium between the paramagnetic and diamagnetic species inside the solution was detected by the appearance of the $\tilde{\nu}_{CN}$ stretching band of the -CN group attributed to the $\{Fe^{II}_{LS}(\mu\text{-}CN)Co^{III}_{LS}\}$ units, suggesting the partial occurrence of a electron transfer process even at room temperature. This fact was supported by the UV-vis spectroscopic studies for the solution of pairs at room temperature, where the MMCT ($Fe^{II} \rightarrow Co^{III}$) band around 800 nm was detected. But this has to be confirmed by following the temperature dependence of the UV-Vis spectra. Finally, the electrochemical properties of the [FeCo] pairs in MeCN were investigated by cyclic voltammetry. In an effort to explain the complicated obtained behavior, the electrochemistry of the Fe and Co precursors, separately and upon addition of the Fe precursor in a MeCN solution of the Co

precursor, was also investigated. The results of these experiments suggested the existence of a complex equilibrium inside the highly ionic solution, such as an equilibrium between the dinuclear complex and its precursors and/or an equilibrium between the dinuclear complex and other species. Furthermore, the dinuclear complex does not appear to be stable to reduction of the iron. Additional experiments, such as spectroelectrochemistry can be performed in order confirm the results discussed above.

IV.4 Supporting Material

Mass Spectroscopy. Positive and Negative ion electrospray mass spectroscopy (ESI^+ and ESI^-, respectively), using MeCN as dilution media and as well as eluent were performed for 1 mg of compounds **1**•2DMF, **2**•2DMF and **3**•2DMF in 1 mL of MeCN, on a Thermo Fischer LCQ Fleet with attached a Dionex 3000 LC equipment at Centre de Recherche Paul Pascal. The positive spectra were collected after treatment of the MeCN solution with one drop of acetic acid and the negative spectra were collected after treatment of the MeCN solution with one drop of ammonia.

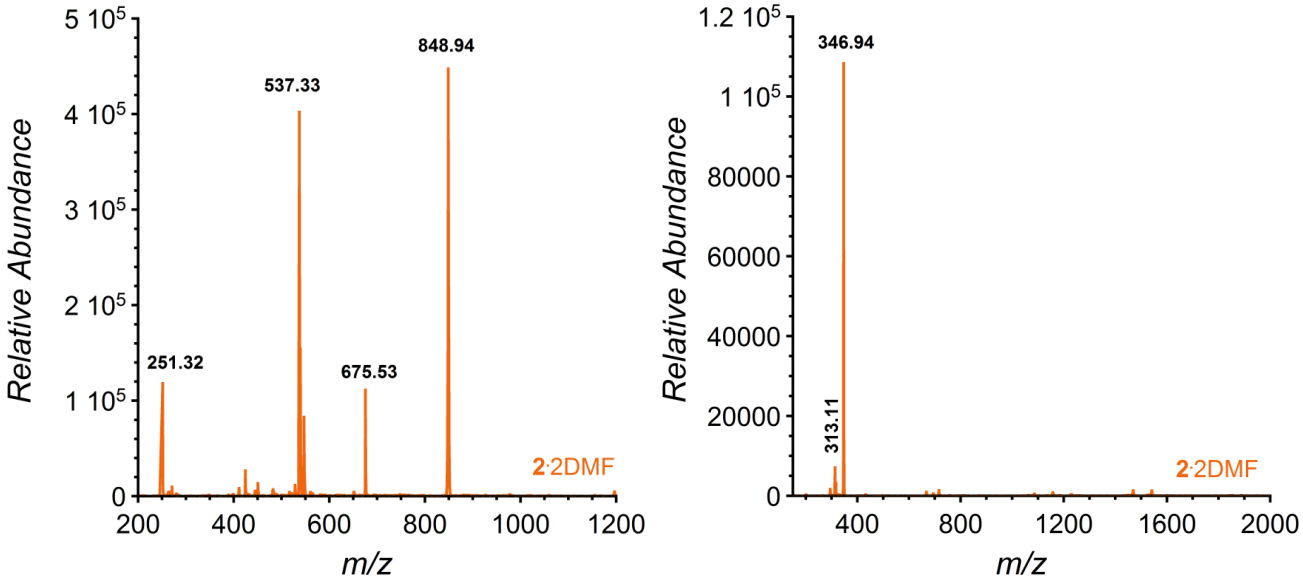

Figure S.IV-1. (Left) Positive and (right) negative mass spectrograms of **2**•2DMF, in MeCN.

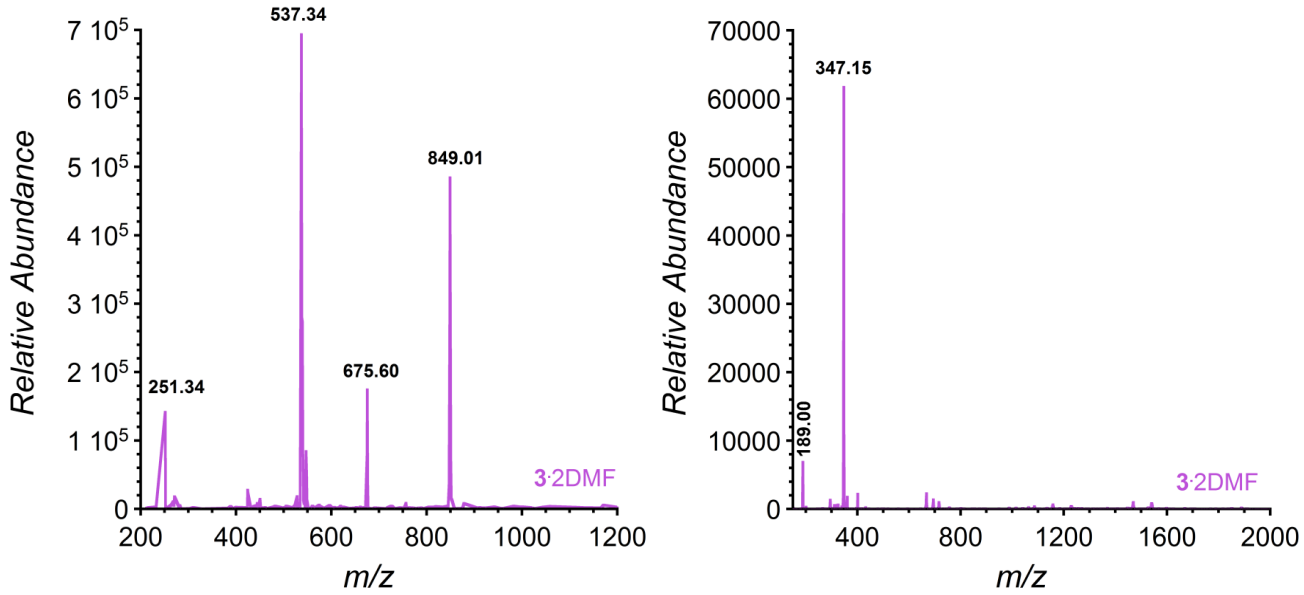

Figure S.IV-2. (Left) Positive and (right) negative mass spectrograms of **3**•2DMF, in MeCN.

Nuclear magnetic resonance spectroscopy. NMR spectra were obtained by JEOL JMN-ECS 400, housed at the Centre de Recherche Paul Pascal.

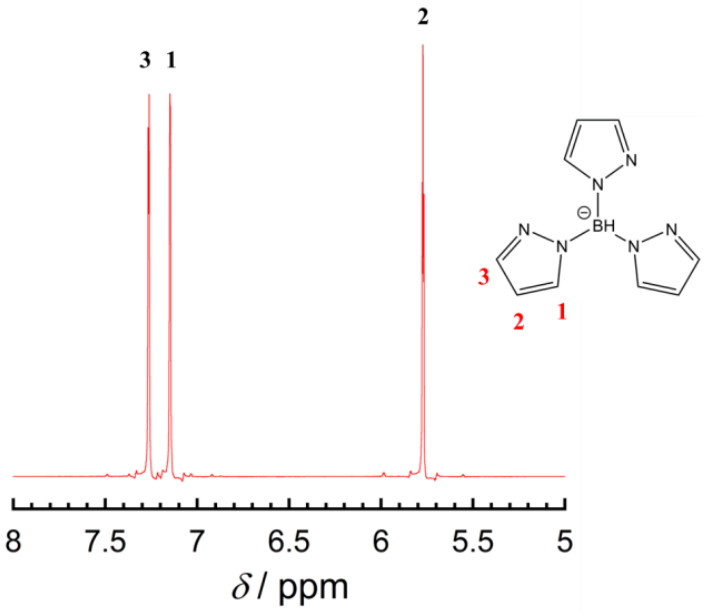

Figure S.IV-3. Portion of the ^{1}H-NMR spectra in d-MeCN at 298 K of the ligand hydridotris(pyrazol-1-yl)borate (Tp^{-}).

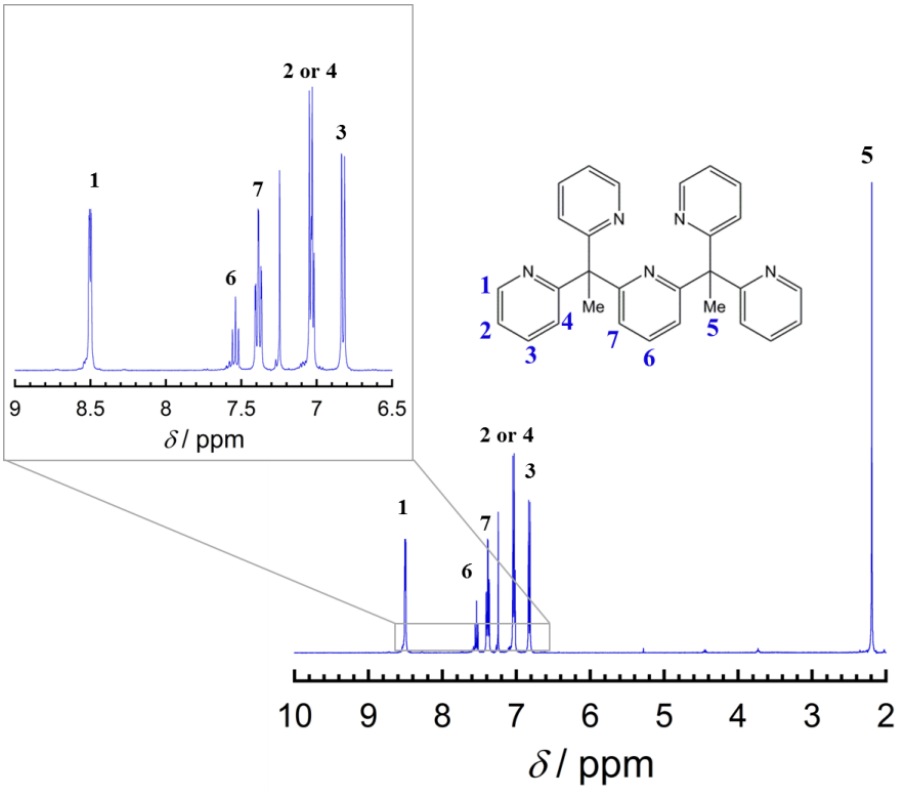

Figure S.IV-4. ^{1}H-NMR spectra (zoom in the aromatic region) in d-$CHCl_3$ at 298 K of the ligand 2,6-bis(1,1-di(pyridin-2-yl)ethyl)pyridine ($PY5Me_2$).

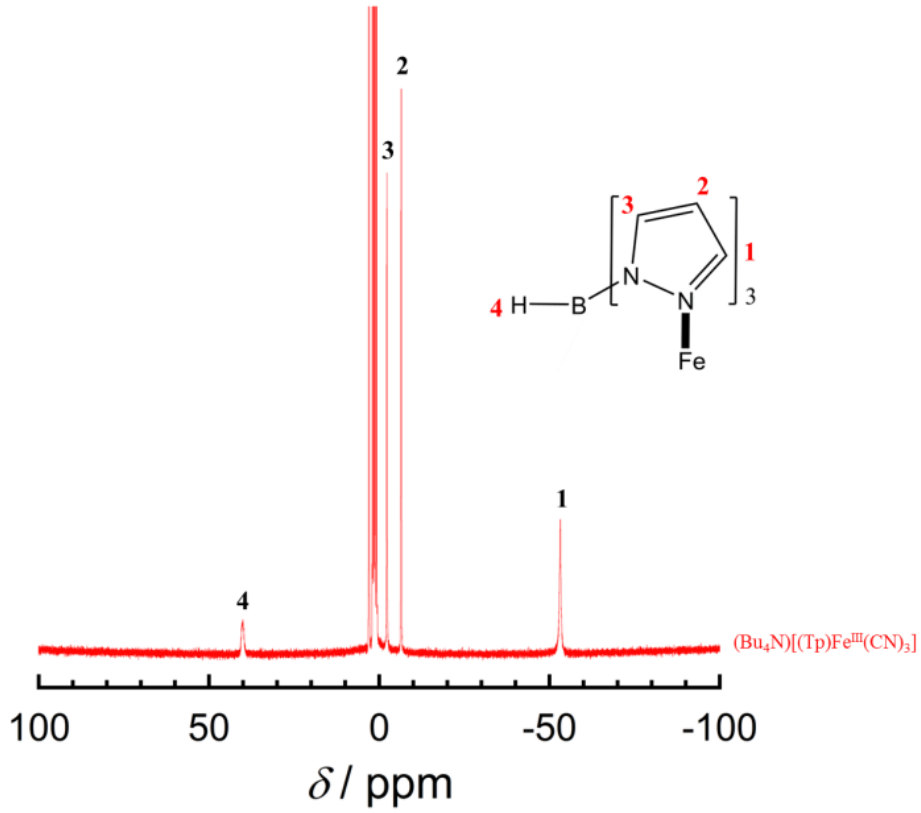

Figure S.IV-5. ^{1}H-NMR spectra in d-MeCN at 298 K of $(Bu_4N)[(Tp)Fe^{III}(CN)_3]$.

FT-IR spectroscopy. FT-IR spectra were recorded in the range 500–3500 cm^{-1} on a Thermal Scientific Nicolet 6700 ATR (attenuated total reflection) spectrometer equipped with a smart iTR diamond window, housed at the Centre de Recherche Paul Pascal.

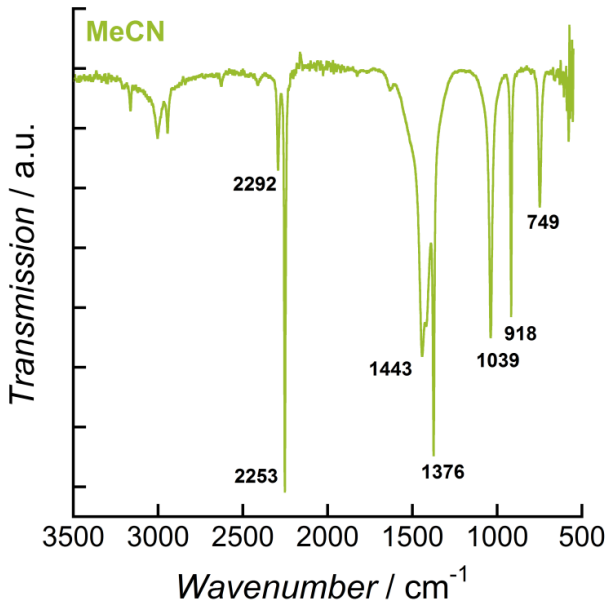

Figure S.IV-6. The FT-IR spectra of MeCN at 298 K.

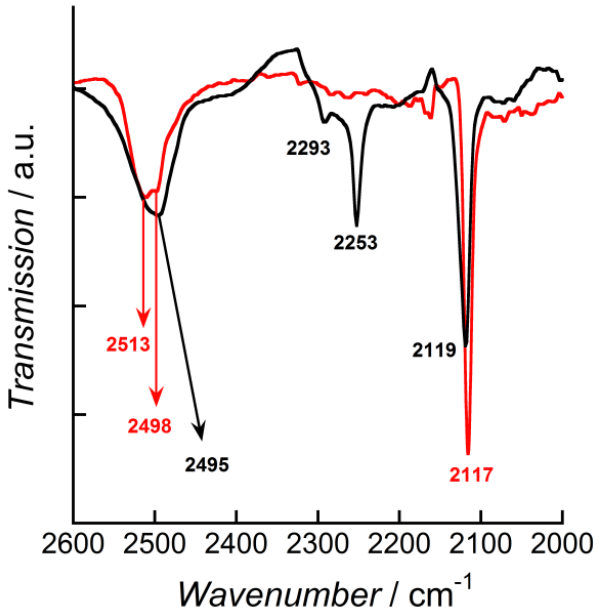

Figure S.IV-7. Portion of the FT-IR spectra of $(Bu_4N)[(Tp)Fe^{III}(CN)_3]$ in solid state (red) and in MeCN solution (black), at 298 K.

UV-Vis spectroscopy. UV-Vis spectra were recorded in the range 300-900 nm on a UNICAM/UV4 spectrometer, housed at the Centre de Recherche Paul Pascal.

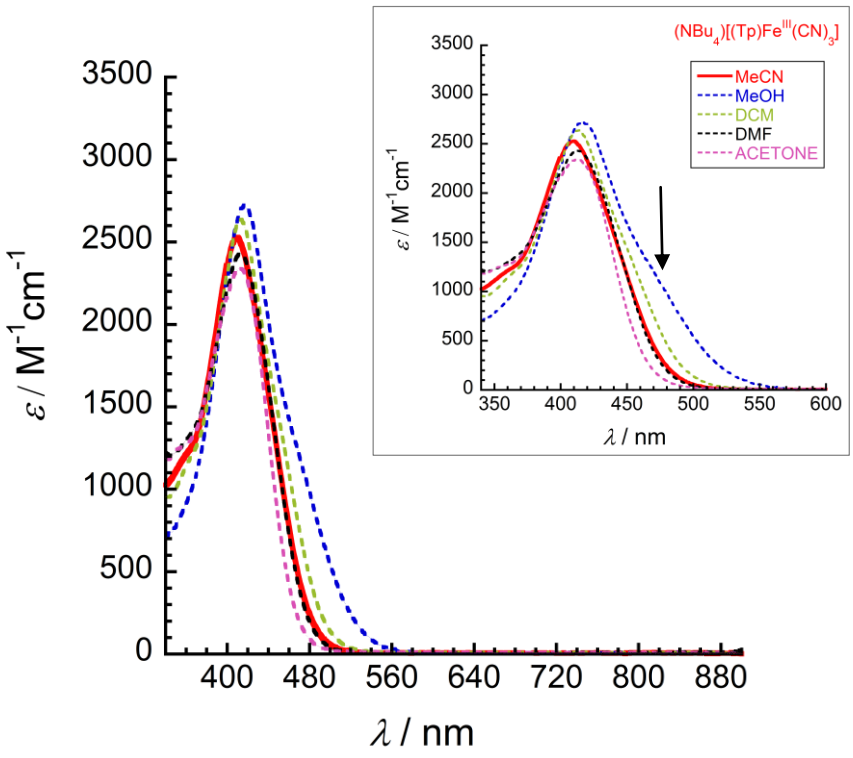

Figure S.IV-8. UV-Vis spectra (zoom in the characteristic band) of $(Bu_4N)[(Tp)Fe^{III}(CN)_3]$ in MeCN (red), MeOH (dashed blue line), dichloromethane (dashed green line), DMF (dashed black line) and Me_2CO (dashed pink line), for C = 0.005 M. The arrow is guide for the eyes.

Electrochemistry. Cyclic voltammograms (CVs) were obtained in a three electrode cell, utilizing an Autolab PGStat20 potentiostat, driven by GPES software (General Purpose Electrochemical System, Version 4.4, EcoChemie B.V., Utrecht, the Netherlands), a platinum wire counter electrode, a 1.6mm platinum disc working electrode, and a non-aqueous reference electrode comprised of a silver wire in a 0.01 M solution of $AgNO_3$and 0.1 M tetrabutylammonium perchlorate in acetonitrile. The analytes (1 mM) were dissolved in acetonitrile supplemented with 0.1 M tetrabutylammonium tetrafluoroborate and degassed prior to measurement. CVs were obtained at scan rate of 0.1 V/s. $E_{1/2}$ values for reversible or quasi-reversible processes were determined by cyclic voltammetry using the relation $E_{1/2} = (E_p^a + E_p^c)/2$.

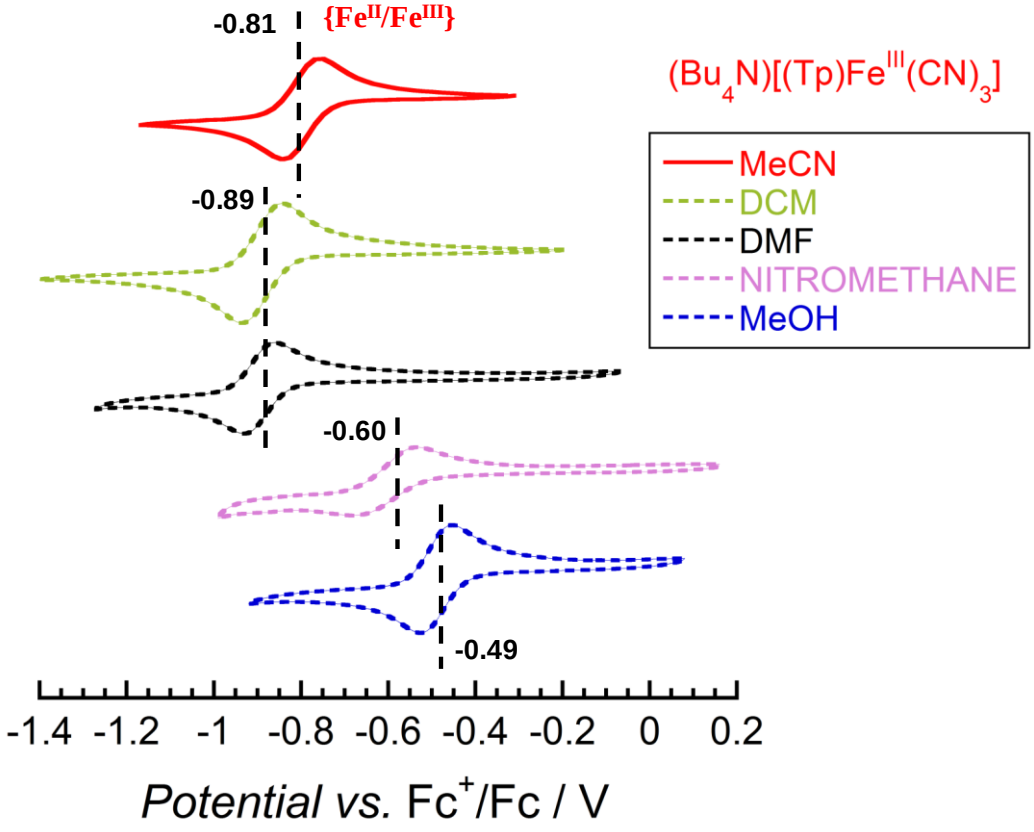

Figure S.IV-9. Cyclic voltammograms of $(Bu_4N)[(Tp)Fe^{III}(CN)_3]$ in MeCN (red), MeOH (dashed blue line), dichloromethane (dashed green line), DMF (dashed black line) and $MeNO_2$ (dashed pink line) solutions (~1 mM), collected in a 0.1 M solution of $Bu_4N(BF_4)$ in each solvent with a scan rate of 0.1 V s^{-1}. Potentials were referenced to the $[Cp_2Fe]^{1+/0}$ couple. The dashed lines are guides for the eyes.

IV.5 References

(1) Koumousi, E. S.; Jeon, I.-R.; Gao, Q.; Dechambenoit, P.; Merzeau, P.; Buisson, L.; Jia, B.; Li, D.; Woodruff, D. N.; Voltaron, F.; Mathonière, C.; Clérac, R. *J. Am. Chem. Soc*., **2014**, *136*, 15461**.**
(2) Sato, O.; Iyoda, T.; Fujishima, A.; Hashimoto, K. *Science* **1996**, *272*, 704.
(3) Zhang, Y.; Li, D.; Clérac, R.; Kalisz, M.; Mathonière, C.; Holmes, S. M. *Angew. Chem., Int. Ed.* **2010**, *49*, 3752.
(4) Nihei, M.; Sekine, Y.; Suganami, N.; Nakazawa, K.; Nakao, A.; Nakao, H.; Murakami, Y.; Oshio, H. *J. Am. Chem. Soc.* **2011**, *133*, 3592.
(5) Siretanu, D.; Li, D.; Buisson, L.; Bassani, D. M.; Holmes, S. M.; Mathonière, C.; Clérac, R. *Chem.-Eur. J.* **2011**, *17*, 11704.
(6) Li, D.; Parkin, S.; Wang, G.; Yee, G. T.; Prosvirin, A. V.; Holmes, S. M. *Inorg. Chem.* **2005**, *44*, 4903.
(7) Codreanu Siretanu, D. *PhD thesis*, *Bordeaux University*, **2011**.
(8) Mitcov, D., *PhD thesis*, *Bordeaux University*, **2014**.
(9) Jeon, I.-R.; Calancea, S.; Panja, A.; Piñero Cruz, D. M.; Koumousi, E. S.; Dechambenoit, P.; Coulon, C.; Wattiaux, A.; Rosa, P.; Mathonière, C.; Clérac, R. *Chem. Sci.* **2013**, *4*, 2463.
(10) Kitagawa, Y.; Asaoka, M.; Miyagi, K.; Matsui, T.; Nihei, M.; Oshio, H.; Okamura, M.; Nakano, M. *Inorg. Chem. Front.* **2015**, *2*, 771.

General Conclusions and Perspectives

The control of the magnetic properties by an external stimulus such as temperature, light, pressure or electric field has attracted great attention in the last two decades within the scientific community. In that sense, systems with photo-switchable physical properties based on a reversible transfer of one electron between two metals, such as Fe/Co Prussian Blue Analogues (PBAs), are of particular interest. When these fascinating magneto-optical bistabilities are present in molecular systems, which can be easily manipulated and studied, the fundamental and technological interest becomes even greater. Therefore, the aim of this thesis work has been the design of novel dinuclear Fe/Co complexes, which can represent the smallest molecular system featuring electron transfer properties in solid state and in solution. Herein we summarize the principal results obtained during this thesis and our perspectives in order to complete this work and enrich the field of molecular magnetism.

In Chapter I, we presented the most representative examples of Fe/Co PBAs, focusing on the techniques used to understand their photomagnetic properties and the synthetic strategies employed in order to obtain these systems with different dimensionalities. The theoretical aspects of this important class of magnetic materials were also described. By this chapter, we aimed to introduce to the readers the importance of our research motivation and offer them an opportunity to understand easily the following Chapters II-IV.

In Chapter II, we presented how the use of the building block approach allows us to predict the structure and the switchable properties of the final product. We succeed to crystallize a new dinuclear Fe/Co cyanide-bridged complex, the smallest {Fe(μ-CN)Co} moiety at the origin of the remarkable physical properties of the high dimensionality Fe/Co Prussian blue analogues. Combined structural and magnetic studies of compound $[\{(Tp)Fe^{III}(CN)_3\}\{Co^{II}(PY5Me_2)\}](CF_3SO_3)\bullet 2DMF$ (**1**•2DMF) reveal that a partial metal-to-metal electron transfer process can be triggered for first time in solid state by temperature. The desolvated form of this system, **1**, was studied by optical and magnetic methods evidencing a complete and reversible thermally induced electron transfer process between 165 and 170 K. Photomagnetic and optical reflectivity studies demonstrated unambiguously that the diamagnetic state of **1** can be photoconverted into the paramagnetic one by applying white-light irradiation at 10 K. When the light is switched off and the temperature is increased, the compound relaxes at 45 K back to the thermodynamically diamagnetic state. This relaxation temperature is the lowest relaxation temperature observed for any molecular PBA, suggesting that it decreases with the miniaturization of the complex. The thermally and light-induced electron transfer process in **1** was confirmed at the local level by X-ray absorption spectroscopy (XAS) and X-ray magnetic circular dichroism (XMCD) measurements, performed at synchrotron facilities. The effect of the solvent contents of the pair on the electron transfer properties opened the possibility of manipulating this phenomenon by changing the chemical environment of it. These results suggest the crystallization of the dinuclear complex from different reaction/crystallization solvents and the study of the properties of the new products.

In Chapter III, we studied the influence of the counter ions on the occurrence of the thermally and/or photo-induced electron transfer in solid state for this type of systems. Two new Fe/Co complexes, $[\{(Tp)Fe^{III}(CN)_3\}\{Co^{II}(PY5Me_2)\}](PF_6)\bullet 2DMF$ (**2**•2DMF) and $[\{(Tp)Fe^{III}(CN)_3\}\{Co^{II}(PY5Me_2)\}](AsF_6)\bullet 2DMF$ (**3**•2DMF) were obtained, featuring a different anion in the environment. The influence of the new anions around the

{Fe(μ−CN)Co} moiety was indeed revealed in the electron transfer properties, since a complete and reversible conversion (associated to a first order phase transition) was observed without the need of desolvating the compounds, like for **1**•2DMF/**1** system. Moreover, this behavior was shifted 70-80 K lower in temperature in respect to the properties of **1**. This behavior was confirmed by single crystal X-ray diffraction at high and low temperatures, magnetic and optical studies. It is worth mentioning that the electron transfer process in compound **2**•2DMF was accompanied by a change of the space group, which was revealed by X-ray diffraction studies at high and low temperatures. Curiously, this phenomenon wasn't observed for compound **3**•2DMF. Keeping in mind that the temperature where the electron transfer is occurring for this compound is lower than the temperature limit of our diffractometer, we are planning to perform structural measurements of **3**•2DMF at 50 K in synchrotron installations. The desolvated forms of **2**•2DMF and **3**•2DMF are exhibiting electron transfer behavior between 170 and 182 K for compound **2** and 156 and 164 K for compound **3**, as it was observed by magnetic and optical studies. Optical and photomagnetic studies for compounds **2**•2DMF and **3**•2DMF and optical studies for compounds **2** and **3**, showed the possibility to photo-induce the paramagnetic state of the compounds under white-light and 940-nm irradiation at 10 K. The relaxation temperature from the metastable paramagnetic state to the thermodynamically diamagnetic state was found to be similar for all the complexes (with and without DMF) and comparable with the one obtained for **1**, demonstrating the molecular origin of the light-induced electron transfer phenomenon in these compounds. On the other hand, the results obtained for compounds **1**•2DMF, **2**•2DMF, **3**•2DMF and **1**, **2** and **3** in respect to the thermally-induced electron transfer phenomenon evidence its dependence on the environment of the molecule, like the solvents and the counter ions. It is worth to mention that the relaxation temperature from the metastable paramagnetic state to the thermodynamically diamagnetic state for these dinuclear Fe/Co systems is the lowest relaxation temperature observed for any molecular Fe/Co PBA. In an effort to explain this decrease and understand the mechanism of the light-induced electron transfer process, we suggest the study of the metastable state of our compounds, as well as of the Fe/Co square and cube analogues, by ultrafast laser spectroscopy at low temperatures. This technique studies the dynamics of the molecules on extremely short time scales (femtoseconds) and may reveal the different states involved in the relaxation process of the metastable paramagnetic state. Another important feature of the photo-induced paramagnetic state, the nature of the coupling between the Fe^{III}_{LS} and Co^{II}_{HS} sites, was studied by photomagnetic measurements. As preliminary result we can mention the presence of weak antiferromagnetic interactions between the cobalt and iron. Finally, the lifetime of the photo-induced paramagnetic state of compound **2**•2DMF was studied in terms of activation energy and relaxation time. The values obtained are comparable with those obtained for other molecular PBAs. Once more, the thermally and light-induced electron transfer process in **2**•2DMF was confirmed at the local level by X-ray absorption spectroscopy (XAS) and X-ray magnetic circular dichroism (XMCD) studies, performed at synchrotron facilities. By this technique the nature of the coupling between the Fe^{III}_{LS} and Co^{II}_{HS} sites was also studied, but the absence of interactions between the metal sites within the complex was suggested. Since the interactions expected are very weak only by performing this experiment at much lower temperature (< 1 K) and under weak magnetic field

(< 1 T), we may achieve to confirm the sign and determine the value of the interactions between the Fe and Co ions. Thus, new experiments at very low temperature (400 mK) are initiated at SLS synchrotron in Switzerland, where a specific cryostat can reach this temperature. At last, we presented the first investigations of the electron transfer phenomenon for dinuclear {Fe(μ−CN)Co} complexes under applied electric field, by measuring the real and the imaginary parts of the dielectric permittivity as a function of the frequency at given temperatures for compounds **2**•2DMF, **3**•2DMF and **2**. The obtained dipolar relaxation of the moiety was expressed in different ways for the paramagnetic and the diamagnetic state of the pairs, offering us a new bistable phenomenon related to the electron transfer behavior under applied electric field.

Finally in Chapter IV, the possibility of transferring the electron transfer phenomenon of the studied [FeCo] pairs from solid state to solution was investigated. Combined mass, ^{1}H-NMR, IR and UV-vis spectroscopic studies of MeCN solution of the [FeCo] pairs, their precursors and the non-ET transfer [FeNi] pair (**4**•2DMF), suggested the existence of an equilibrium between the paramagnetic and diamagnetic dinuclear complexes. To confirm this hypothesis, additional measurements in the solution of the pairs are necessary such as the temperature dependence of the UV-vis spectra and magnetic susceptibility measurements. Electrochemistry studies of the [FeCo] dinuclear complexes **1**•2DMF, **2**•2DMF and **3**•2DMF in MeCN solution revealed their complex redox behavior, which can be associated with an equilibrium between the dinuclear species and their precursors in the highly ionic solution.

Except the fundamental interest arising from the synthesis of the smallest {Fe(μ-CN)Co} Prussian Blue Analogue, the two free cyanide groups, bearing by the Fe site of the pair, opens the possibility of using these compounds as building blocks for further coordination with interesting magnetic molecules. Thus, we propose the use of the photo-switchable compounds **1**•2DMF, **2**•2DMF and **3**•2DMF as linker between Single-Molecule Magnets (SMMs). At low temperatures, the diamagnetic pairs-linkers will promote “isolated” (or weakly coupled) SMM behavior in these systems, whereas “enhance” SMM, or Single-Chain Magnet (SCM (one dimensional systems)) behavior, when the pair-linker is switched by photo-excitation in its paramagnetic state (Scheme 1). By this approach, organization of SMMs will be succeeded and it may lead to a new generation of photo-switchable magnets.

The first step to this direction was succeeded during the post-doctoral fellowship of Yoann Prado, who connected two [{(BBP)Fe(CN)$_3$}{Co(PY5Me$_2$)}] complexes with a mononuclear Mn(III) complex through the terminal cyanide groups of the former compound. The [{(BBP)Fe(CN)$_3$}{Co(PY5Me$_2$)}] complex by itself doesn’t exhibit electron transfer properties in solid state. Interestingly, the coordination with the mononuclear Mn(III) complex tuned the redox properties of the Fe site and a thermally and light-induced electron transfer process was revealed for the {Fe(μ-CN)Co} units within the pentanuclear complex.

Another way to tune the redox difference between the metal sites in the dinuclear Fe/Co complexes is the functionalization of the capping ligands (BBP, Tp and PY5). In the case of [{(BBP)Fe(CN)$_3$}{Co(PY5Me$_2$)}] complex, the protonation on the ligand belonging to the Fe center played an important role to induce a positive shift of the redox potential on the Fe site, and consequently trigger an intramolecular electron transfer in solution. Therefore, it is worth

trying to functionalize the BBP ligand by alkyl- or nitro- groups, crystallize the functionalized Fe precursors and Fe/Co complexes and study their electrochemical properties. This work is part of the post-doctoral fellowships of Abhishake Mondal and Yoann Prado in the M_3 group.

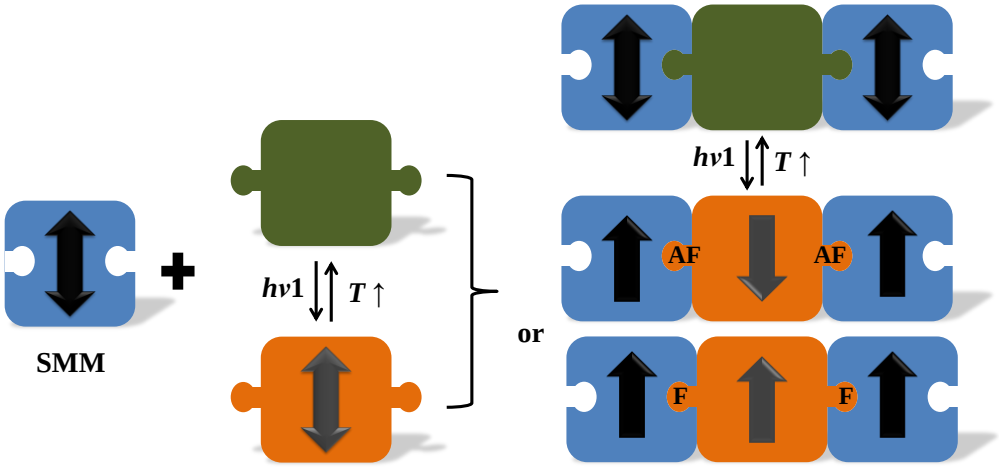

Scheme 1. Scheme of the SMM arrangement with different possible magnetic couplings, through photo-switchable linkers. The arrows indicate the total spin of each molecule; the double arrow indicates that the spin orientation is not fixed by magnetic interactions.

Annex

A1: List of abbreviations

1D	One-dimensional
2D	Two-dimensional
3D	Three-dimensional
ac	Alternating current
AsF_6^-	hexafluoroarsenate
CVs	Cyclic voltammograms
CRPP	Centre de Recherche Paul Pascal
dc	Direct current
DMF	N,N-dimethylformamide
DSC	Differential scanning calorimetry
EA	Elemental analysis
ECE	Electrochemical-Chemical-Electrochemical
ESRF	European synchrotron radiation facility
ET	Electron transfer
EXAFS	Extended X-ray absorption fine structure
FT-IR	Fourier transform infrared spectroscopy
HS	High spin
HT	High temperature
ICMCB	Institut de Chimie de la Matière Condensée de Bordeaux
IMPMC	Institut de Minéralogie, de Physique des Matériaux et de Cosmochimie
IMR	Institute for Materials Research
IPCMS	Institut de Physique et de Chimie de Strasbourg
LED	Light emitting diode
LMCT	Ligand-to-metal charge transfer
LS	Low spin
LT	Low temperature
M_3	Molecular materials & magnetism
MeCN	Acetonitrile
MMCT	Metal-to-metal charge transfer
NBu_4^+	Tetrabutylammonium
NMR	Nuclear magnetic resonance
OTf^-	Trifluoromethanesulfonate ($CF_3SO_3^-$)
P	Power

PB	Prussian blue
PBAs	Prussian blue analogues
PF_6^-	hexafluorophosphate
$PY5Me_2$	2,6-bis(1,1-bis(2-pyridyl)ethyl)pyridine
SCO	Spin crossover
SCM	Single-chain magnet
SLS	Swiss Light Source
SMM	Single-molecule magnet
TGA	Thermogravimetric analysis
Tp	tri(pyrazol-1-yl)hydroborate
XANES	X-ray absorption near-edge spectra
XAS	X-ray absorption spectroscopy
XMCD	X-ray magnetic circular dichroism
XRD	X-ray diffraction

A2: Physical constants

	Symbol	Value	Units SI	CGS
Avogadro constant	N_A	6.02217	10^{23} mol^{-1}	
Boltzmann constant	k_B	1.38062	10^{-23} J·K^{-1}	10^{-21} erg·G^{-1}
Bohr magneton	μ_B	9.27410	10^{-24} J·T^{-1}	10^{-16} erg·K^{-1}
Electron volt	eV	1.60219	10^{-19} J	10^{-11} erg
Molar gas constant	R	8.31446	J·mol^{-1}·K^{-1}	10^{7} erg·mol^{-1}·K^{-1}

Résumé

Résumé

Synthèse et caractérisation de complexes binucléaires de type {Fe(μ-CN)Co} présentant des propriétés de transfert d'électron intermétalliques

Introduction : Dans ce domaine en pleine croissance qu'est la science des matériaux, les matériaux moléculaires connaissent un intérêt relativement récent et émergent, qui est motivé par le développement rapide de nouvelles technologies qui requièrent des matériaux toujours plus performants. Les systèmes moléculaires présentent des avantages synthétiques par rapport aux matériaux traditionnels puisqu'ils utilisent des précurseurs bien définis avec une géométrie contrôlée et ne nécessitent pas de méthodes de production couteuses en énergie. Le choix rationnel des briques moléculaires permet un contrôle efficace de la structure finale des matériaux et ainsi de leurs propriétés physiques. Le développement de matériaux construits à partir de motifs moléculaires, assemblés et conçus pour induire des propriétés magnétiques intéressantes et parfois préméditées, a donné naissance au domaine du magnétisme moléculaire. Ces composants magnétiques sont omniprésents dans nos vie comme par exemple dans les générateurs, les moteurs, les haut-parleurs, les microphones, les commutateurs, les capteurs, **les systèmes de stockage de l'informations**, et bien d'autres. Durant ces dernières années, des efforts de recherche considérables ont été dédiés à la synthèse de systèmes à l'échelle nanométrique, afin par exemple de réduire la taille des unités magnétiques dans les dispositifs de stockage de l'information. Différentes approches ont été utilisées pour obtenir des mono-domaines de particules magnétiques, mais le début des années 90 a été marquée par le découverte des molécules-aimants.[1,2] Ces composés paramagnétiques ont suscité de grands espoirs de coder l' information sur une molécule unique et donc de réduire considérablement la taille des unités de stockage magnétiques en réduisant la taille des bits. Cependant, dans un avenir proche, cette voie sera confrontée à des limitations fondamentales concernant l'adressage des bits. Comme la taille des bits d'information diminue, mais la densité de bits, elle, augmente, le champ magnétique utilisé pour écrire l'information aura une influence sur les bits voisins, conduisant à des erreurs systématiques.[3] Par conséquent, d'autres façons de réaliser l'adressage de bits seront nécessaires , tels que les mémoires basées de sur la commutation assistée thermiquement ou par transfert de spin.[4,5] En parallèle, la recherche industriel ainsi que fondamentale ont mis l'accent sur le contrôle des propriétés magnétiques par stimulus externe autre que le champ magnétique, tel que la température, la lumière, la pression ou le champ électrique.[6,7]

À cet égard, les composés Fe/Co, analogue de Bleu de Prusse (PBAs), avec la formule générale, $A_xCo_y[Fe(CN)_6]\bullet nH_2O$ (A=ions alcalins)[8] ont émergé comme les systèmes les plus intéressants en raison de leurs exceptionnelles propriétés physiques photo-commutables. Dans de tels systèmes, le transfert réversible d'un électron entre deux sites (ions métalliques), se produit par le changement de température et/ou par la photo-excitation à basse température. La modification des états optiques et magnétiques donne lieu à la bistabilité magnéto-optique. D'autre part, l'introduction de cette bistabilité remarquable dans les systèmes à dimensionnalité inférieure (2D, 1D ou 0D) représente objectif de recherche attractif pour développer de nouveaux matériaux pouvant être facilement manipulés et étudiés.[9]

Cette thèse porte sur la synthèse de nouveaux complexes binucléaires à ponts cyanures de type {Fe(μ-CN)Co}, qui reproduisent au sein d'une seule molécule les propriétés originales du réseau de coordination d'analogue de bleu de Prusse $A_xCo[Fe(CN)_6]_y \bullet nH_2O$ (A = ions alcalins), i.e. un transfert d'électron intramoléculaire thermo- et photo-induit à l'état solide. Au sein de ce travail, nous nous sommes intéressés à l'étude des propriétés physiques des paires moléculaires Fe/Co, avec l'objectif de comprendre les mécanismes du phénomène de transfert d'électrons.

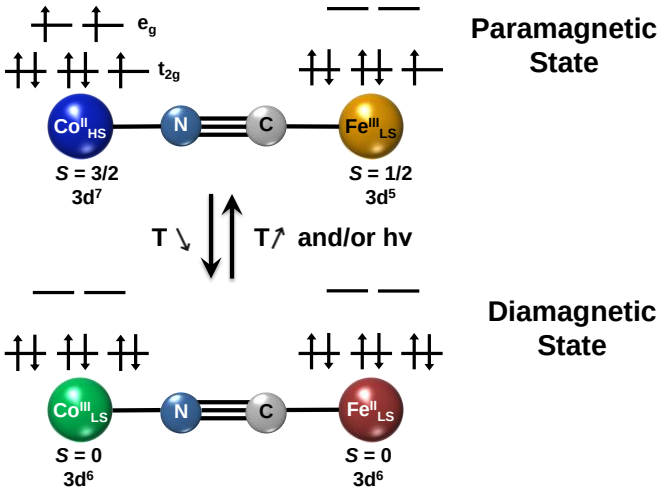

Schéma R-1. Interconversion entre les configurations électroniques paramagnétique (Fe^{III}_{LS}-CN-Co^{II}_{HS}) et diamagnétique (Fe^{II}_{LS}-CN-Co^{III}_{LS}) grâce au transfert d'électron intermétallique thermo- et photo-induit.

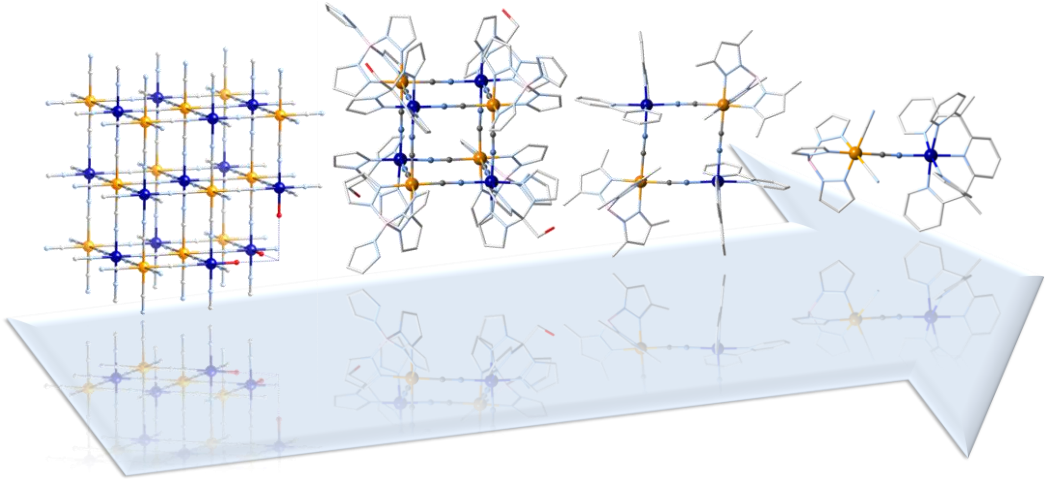

Schéma R-2. Schéma illustrant les différents systèmes Fe/Co, présentant des propriétés de transfert d'électron: du réseau 3D de la d'analogue de Bleu de Prusse en 1996, à sa cellule 'unitaire, un cube Fe/Co, à une face de la cellule unitaire cubique, un Fe/Co carré et enfin l'unité fondamentale des composés mentionnés précédemment, une paire Fe/Co, en 2013.[9]

Resultats: Dans le chapitre II, nous avons présenté comment l'approche « building block » nous permet de prédire la structure et les propriétés commutables du produit final. Nous avons réussi à cristalliser de nouveaux complexes binucléaires Fe/Co à ponts de cyanures, le plus petit étant {Fe(μ-CN)Co}, fragment à l'origine des propriétés physiques remarquables de la haute dimensionnalité Fe/Co d'analogue de Bleu de Prusse. Les études structurelles et magnétiques combinées du composé $[\{(Tp)Fe^{III}(CN)_3\}\{Co^{II}(PY5Me_2)\}](CF_3SO_3)$•2DMF (**1**•2DMF)[10] (Figure R-1, gauche) révèlent pour la première fois, un processus de transfert d'électron intermétallique partiel peut être déclenchée par la température à l'état solide (Figure R-1, droit, rouge). L'état désolvaté de ce système, **1**, a été étudié par des méthodes optiques et magnétiques attestant un processus de transfert d'électron complet et réversible thermo-induit entre 165 et 170 K (Figure R-1, droite, courbe noire).

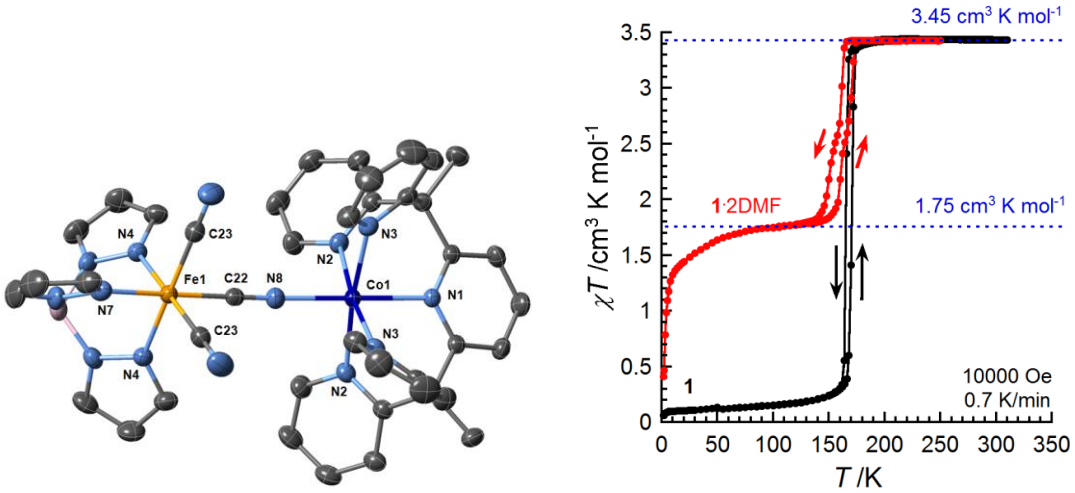

Figure R-1. (Gauche) Représentation ORTEP du complexe cationique **1**•2DMF à 180 K. Tous les anions, les solvants et les atomes d'hydrogène ont été omis pour plus de clarté. Les atomes Fe, Co, N, C, et B sont indiquées en orange, bleu foncé, bleu clair, gris, et rose, respectivement; (droite) χT en fonction de la température pour les échantillons polycristallins de **1**•2DMF (en rouge, de 250 à 100 K à 1 T et en dessous de 100 K à 0.1 T) et **1** (en noir, 300 à 1.8 K à 1 T) 0.67 K / min (les lignes bleues pointillées servent de guides).

Les études photomagnétiques et de réflectivité optique démontrent sans ambiguïté que l'état diamagnétique de **1,** à 10 K, peut être photo-converti en paramagnétique en appliquant un rayonnement de lumière blanche (Figure R-2). Lorsque la lumière est éteinte et la température est augmentée, le composé se détend à 45 K et retourne à l'état thermodynamique diamagnétique. Cette température de relaxation est la température de relaxation la plus faible observée pour n'importe quel PBA moléculaire, ce qui suggère qu'elle diminue avec la miniaturisation du complexe. Le processus de transfert d'électron thermo- et photo-induit en **1** a été confirmé au niveau local par spectroscopie d'absorption des rayons-X (XAS) et par dichroïsme circulaire magnétique des rayon-X (XMCD), réalisée en synchrotron.

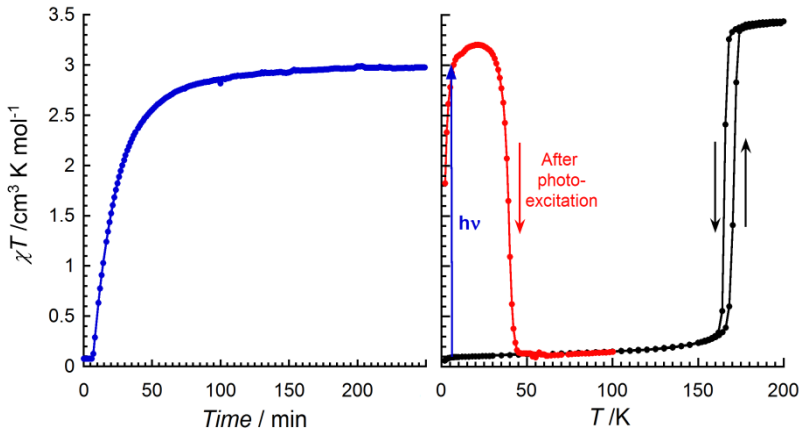

Figure R-2. (Gauche) χT en fonction du temps pour 1 T sous irradiation de lumière blanche (3 mW/cm^2) à 10 K; (droit) χT en fonction de la température pour 1 T et 0.4 K / min pour **1** avant (courbe noire) et après (courbe rouge) irradiation de lumière blanche (3 mW/cm^2) à 10 K (les flèches servent de guide).

Dans le chapitre III, nous avons étudié l'influence du contre-ion sur l'occurrence du transfert d'électron thermo- et/ou photo-induit à l'état solide pour ce type de systèmes. Deux nouveaux complexes binucléaires à ponts cyanures de type {Fe(μ-CN)Co}, [{(Tp)Fe(CN)$_3$}{Co(PY5Me$_2$)}](PF$_6$)•2DMF (**2**•2DMF) et [{(Tp)Fe(CN)$_3$}{Co(PY5Me$_2$)}](AsF$_6$)•2DMF (**3**•2DMF), ont été synthétisés et leurs propriétés associées au phénomène de transfert d'électron intramoléculaire ont été étudiés à l'état solide par des études cristallographique, spectroscopique, optique, photomagnétiques et magnétiques. L'influence des anions présent autour de la paire {Fe(μ-CN)Co} sur les propriétés de transfert d'électron a été révélé, puisqu' une conversion complète et réversible (associée à une transition de phase du premier ordre) a été observée sans qu'il soit nécessaire de désolvaté les composés, comme dans le cas des complexes **1**•2DMF/**1**. En outre, le phénomène de transfert d'électron a été décalé de 70 à 80 K en dessous de la température obtenue dans le cas du complexe **1** (Figure R-3). Ce comportement a été confirmé par diffraction des rayons-X sur monocristal à basse et haute températures, ainsi que par les études magnétiques et optiques. Les complexes désolvatés **2** et **3** présentent un transfert d'électron complet entre 170 et 182 K et 156 et 164 K, respectivement, comme il a été montré par les mesures magnétiques et optiques. Les études optiques et photomagnétiques des composés **2**•2DMF et **3**•2DMF ainsi que les études optiques des composés **2** et **3**, ont montré qu'il est possible de photo-induire l'état métastable paramagnétique a basse température (10 K) sous irradiation avec la lumière blanche ou de 940 nm. La température de relaxation de l'état paramagnétique métastable vers l'état thermodynamiquement stable (diamagnétique) est similaire pour tous les complexes (avec et sans DMF) et comparable à celle obtenue pour **1**. Ceci démontre que le phénomène de transfert d'électron photo-induit est d'origine moléculaire dans ces composés. En revanche, les résultats obtenus pour cette série de complexes montrent clairement que le phénomène de transfert d'électron thermo-induit est fortement dépendant de l'environnement de la molécule, en particulier les solvants et les contre-ions.

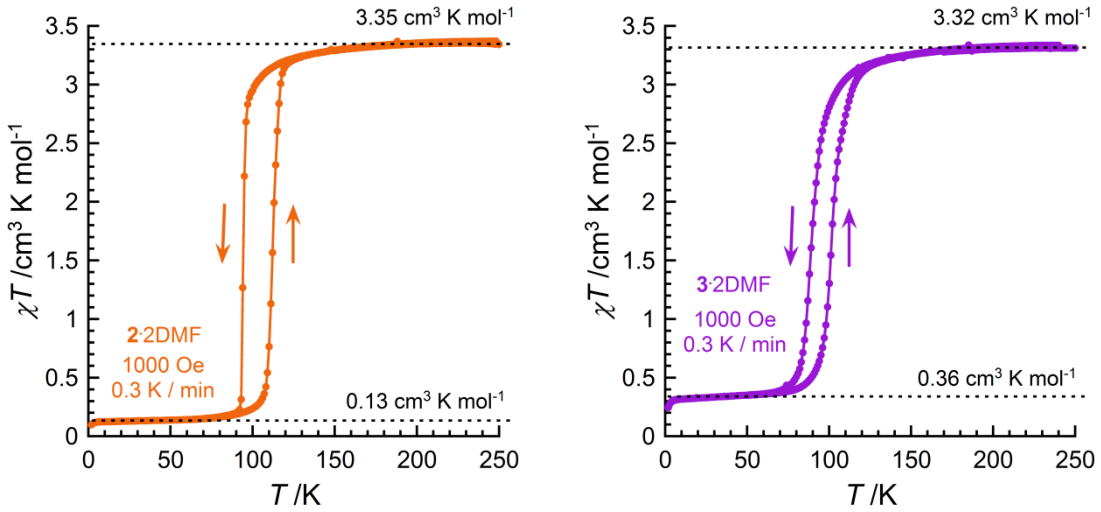

Figure R-3. Courbes de χT en fonction de la température (250 à 1.8 K à 0.1 T et à 0.3 K/min) pour les échantillons polycristallins de **2**•2DMF (gauche) et pour **3**•2DMF (droite); les flèches servent de guide.

La nature du couplage entre les Fe^{III}_{LS} et Co^{II}_{HS} dans l'état paramagnétique photo-induit, a été étudiée par des mesures photomagnétiques. Les résultats préliminaires suggèrent la présence de faibles interactions antiferromagnétiques entre le cobalt et le fer. Enfin, la durée de vie de l'état paramagnétique photo-induit du composé **2**•2DMF a été étudiée en termes d'énergie d'activation et temps de relaxation. Les valeurs obtenues sont comparables à celles obtenues pour les autres analogues moléculaires. Une fois de plus, le processus de transfert d'électron thermo- and photo-induit dans **2**•2DMF a été confirmé au niveau local via des mesures de spectroscopie d'absorption des rayons-X (XAS) et dichroïsme circulaire magnétique (XMCD), réalisées dans les installations du synchrotron. Enfin, nous avons effectué les premières étude du phénomène de transfert d'électron pour complexes binucléaires {Fe(μ-CN)Co} sous champ électrique. Ceci a été réalisé pour les composés **2**•2DMF, **3**•2DMF et **2**, en mesurant la partie réelle et imaginaire de la permittivité diélectrique en fonction de la fréquence à une température donnée. La relaxation dipolaire obtenue s'exprime différemment pour l'état paramagnétique et diamagnétique des paires, offrant ainsi une nouvelle façon d'observer le transfert d'électron sous l'application d'un champ électrique.

Le quatrième chapitre rapporte l'étude des propriétés de commutation des trois dimères en solution. Une étude des complexes de coordination par une combinaison de techniques est présentée: spectrométrie de masse, spectroscopies ^{1}H-RMN, IR, UV-visible et voltamétrie cyclique. L'ensemble des résultats montre un comportement complexe des dimères en solution. Ces résultats posent de nouvelles questions quant aux équilibres en solution et à la stabilité des espèces et des caractérisations complémentaires seront nécessaires avant de conclure.

Table R-1. Résumé des températures de transfert d'électron thermo-induit et des températures de relaxation de l'état paramagnétique métastable vers l'état diamagnétique pour les composés **1**•2DMF, **2**•2DMF et **3**•2DMF et leurs formes désolvatés **1**, **2** et **3**.

Composés	$T_{1/2}$ cooling in K	$T_{1/2}$ heating in K	*T* relaxation in K
1•2DMF	161 and 152	171 and 162	
1	165	170	45
2•2DMF	94	112	53
2	170	182	48
3•2DMF	88	101	57
3	156	164	48

Conclusions: Dans ce travail de thése, nous avons synthétise de nouveaux composés binucléaires à ponts cyanures Fe/Co, avec l'utilisation des briques moléculaires employées et l'étude de leurs potentiels redox. Ces sont le premières complexes binucléaires qui imite les propriétés de commutation dans le blues de Prusse. Des études structurales, spectroscopiques, magnétiques, photomagnétiques, diélectriques et d'absorption des rayons-X révèlent qu'un transfert d'électron métal-métal peut être déclenché à l'état solide en faisant varier la température et par application de la lumière.

References:

(1) (a) Boyd, P. D. W.; Li, Q.; Vincent, J. B.; Folting, K.; Chang, H. R.; Streib, W. E.; Huffman, J. C.; Christou, G.; Hendrickson, D. N. *J. Am. Chem. Soc.* **1988**, *110*, 8537; (b) Caneschi, A.; Gatteschi, D.; Sessoli, R.; Barra, A. L.; Brunel, L. C.; Guillot, M. *J. Am. Chem. Soc.* **1991**, *113*, 5873; (c) Sessoli, R.; Gatteschi, D.; Caneschi, A.; Novak, M. A. *Nature* **1993**, *365*, 141.

(2) (a) Caneschi, A.; Gatteschi, D.; Lalioti, N.; Sangregorio, C.; Sessoli, R.; Venturi. G.; Vindigni. A.; Rettori. A.; Pini, M. G.; Novak, M. A. *Angew. Chem. Int. Ed.* **2001,** *40*, 1760; (b) Clérac, R.; Miyasaka, H.; Yamashita, M.; Coulon, C. *J. Am. Chem. Soc.* **2002,** *124*, 12837.

(3) Chappert, C.; Fert, A.; Van Dau, F. N. *Nat. Mater.* **2007**, *6*, 813.

(4) Kahn, O.; Jay Martinez, C. *Science* **1998**, *279*, 44.

(5) Ralph, D. C.; Stiles, M. D. *Journal of Magnetism and Magnetic Materials* **2008**, *320*, 1190.

(6) Sato, O.; Tao, J.;. Zhang, Y.-Z *Angew. Chem., Int. Ed.* **2007**, *46*, 2152.

(7) Sato, O. *J. Photochem. Photobiol. C Photochem. Rev.* **2004**, *5*, 203.

(8) Sato, O.; Iyoda, T.; Fujishima, A.; Hashimoto, K. *Science* **1996**, *272*, 704.

(9) Aguilà, D.; Prado, Y.; Koumousi, E. S.; Mathonière, C.; Clérac, R. *Chem. Soc. Rev.* **2016**, DOI: 10.1039/c5cs00321k.

(10) Koumousi, E. S.; Jeon, I.-R.; Gao, Q.; Dechambenoit, P.; Merzeau, P.; Buisson, L.; Jia, B.; Li, D.; Woodruff, D. N.; Voltaron, F.; Mathonière, C.; Clérac, R. *J. Am. Chem. Soc.*, **2014**, *136*, 15461**.**

List of Publications :

1. Jeon, I.-R.; Calancea, S.; Panja, A.; Piñero Cruz, D. M.; **Koumousi, E. S.**; Dechambenoit, P.; Coulon, C.; Wattiaux, A.; Rosa, P.; Mathonière, C.; Clérac, R. "Spin Crossover or Intra-Molecular Electron Transfer in a Cyanido-Bridged Fe/Co Dinuclear Dumbbell: A Matter of State", *Chem. Sci.* **2013**, *4*, 2463.

2. **Koumousi, E. S.**; Jeon, I.-R.; Gao, Q.; Dechambenoit, P.; Merzeau, P.; Buisson, L.; Jia, B.; Li, D.; Woodruff, D. N.; Voltaron, F.; Mathonière, C.; Clérac, R. "Metal-to-Metal Electron Transfer in Co/Fe Prussian Blue Molecular Analogues: The Ultimate Miniaturization", *J. Am. Chem. Soc.* **2014**, *136*, 7569.

3. Aguilà, D.; Prado, Y.; **Koumousi, E. S.**; Mathonière, C.; Clérac, R. "Switchable Fe/Co Prussian blue networks and molecular analogues" *Chem. Soc. Rev.* **2016**, DOI: 10.1039/c5cs00321k.

Synthèse et caractérisation de complexes binucléaires de type {Fe(μ-CN)Co} présentant des propriétés de transfert d'électron intermétalliques

Cette thèse porte sur la synthèse de nouveaux complexes binucléaires à ponts cyanures de type {Fe(μ-CN)Co}, qui reproduisent au sein d'une seule molécule les propriétés originales du réseau de coordination d'analogue de bleu de Prusse $A_xCo[Fe(CN)_6]_y \bullet nH_2O$ (A=ions alcalins), i.e. un transfert d'électron intramoléculaire thermo- et photo-induit à l'état solide. Au sein de ce travail, nous nous sommes intéressés à l'étude des propriétés physiques des paires moléculaires Fe/Co, avec l'objectif de comprendre les mécanismes du phénomène de transfert d'électrons. Le chapitre I contient les exemples les plus représentatifs des réseaux de coordination d'analogues de bleu de Prusse et de leurs analogues moléculaires Fe/Co, en se concentrant sur les techniques utilisées pour comprendre leurs propriétés photomagnétiques et les stratégies synthétiques employées pour contrôller leur dimensionnalité et obtenir ces analogues moléculaires. Les bases théoriques du transfert d'électron ainsi que la motivation de ce travail sont décrites à la fin du chapitre. Après une introduction sur l'utilisation des briques moléculaires employées au cours de ce travail à travers l'étude de leurs potentiels redox, le chapitre II est consacré à la synthèse et la caractérisation de nouveaux composés dinucléaires à ponts cyanures Fe/Co. Des études structurales, spectroscopiques, magnétiques, photomagnétiques, diélectriques et d'absorption des rayons-X révèlent qu'un transfert d'électron métal-métal peut être déclenché à l'état solide en faisant varier la température et par application de la lumière. Dans le chapitre III est présenté l'influence de l'environnement des complexes binucléaires Fe/Co, à savoir les contre-ions, sur le transfert d'électron thermo- et / ou photo-induit à l'état solide. Enfin le chapitre IV porte sur la possibilité de transférer le phénomène de transfert d'électron des paires Fe/Co étudiées de l'état solide à la solution.

Mot clés: magnétisme moléculaire; photomagnétisme; transfert d'électron métal-métal; complexes binucléaires Fe/Co à pont cyanure; commutation moléculaire

---

Synthesis and characterization of dinuclear {Fe(μ-CN)Co} complexes exhibiting metal-to-metal electron transfer properties

This thesis is dedicated to the synthesis of new dinuclear cyanido-bridged Co/Fe complexes, which mimics on a single molecule the original properties of the coordination network of Prussian Blue Analogues $A_xCo[Fe(CN)_6]_y \bullet nH_2O$ (A= alkaline ions), i.e. intramolecular thermal and photo-induced electron transfer in the solid state. We focus on the study of the physical properties of the simplest Fe/Co PBA, a dinuclear complex, with the hope to understand the fundamental concepts of this fascinating phenomenon. Chapter I contains the most representative examples of Fe/Co PBAs, focusing on the synthetic strategies employed in order to obtain Fe/Co PBAs of different dimensionalities and the techniques used to understand their photomagnetic properties. The theoretical background of the electron transfer phenomenon and the motivation of our work are described in the end of the chapter. After introducing the choice of the building blocks used in this work through the study of their redox potential properties, chapter II is devoted to the synthesis and the characterization of a novel dinuclear Fe/Co cyanido-bridged complex, which exhibits metal-to-metal electron transfer properties in solid state triggered by temperature and light. The ET phenomenon has been also studied by X-ray absorption spectroscopy and dielectric measurements. In Chapter III is illustrated the influence of the environment content of the dinuclear Fe/Co complexes, such as the counter ions, on the occurrence of the thermally and/or photo-induced electron transfer in solid state, thus highlighting the versatility of these molecular materials. Finally in chapter IV, the possibility of transferring the electron transfer phenomenon of the studied Fe/Co pairs from solid state to solution is investigated.

Keywords: molecular magnetism; photomagnetism; metal-to-metal electron transfer; dinuclear cyanido-bridged Fe/Co complexes; molecular switches

Thèse préparée au:
Centre de Recherche Paul Pascal UPR 8641 / CNRS - Université de Bordeaux
115 av. Albert Schweitzer, 33600 PESSAC (France)
http://www.crpp-bordeaux.cnrs.fr/